

Dissertation
submitted to the
Combined Faculty of Natural Sciences and Mathematics
of Heidelberg University, Germany
for the degree of
Doctor of Natural Sciences

Put forward by
Giada Peron
born in Mirano, Italy
Oral examination: 17.12.2020

Probing the Spatial and Spectral Distribution of Galactic Cosmic Rays with High-Energy Gamma-Rays

Referees:

Prof. Dr. Felix Aharonian

Prof. Dr. Andreas Quirrenbach

ABSTRACT

Gamma-ray astronomy provides a unique tool to study Galactic cosmic rays far from Earth. Cosmic rays in fact, during their propagation, interact with the interstellar medium, producing high-energy gamma rays that can be detected from Earth. These gamma rays carry the information on the origin and the energetics of the parent cosmic rays at the location of interaction. The detection is facilitated in regions with enhanced gas density, like giant molecular clouds, or in regions with enhanced cosmic-ray flux, for example near an accelerator.

In this thesis, I studied both scenarios by analyzing the data accumulated by the Fermi Large Area Telescope between a few tens of MeV up to almost 1 TeV. Firstly, the gamma-ray emission arising from giant molecular clouds, distributed all over the Milky Way, has been investigated, obtaining an unprecedented mapping of the cosmic-ray distribution in the Galaxy. Secondly, the emission that originates in the medium surrounding the supernova remnant W44 has been studied, confirming the presence of recently accelerated particles and unveiling evidence for anisotropic escape. Finally, the potential of the current and future gamma-ray instruments in detecting the radiation emitted from the interstellar medium, both in correspondence of clouds and in the vicinity of accelerators, is evaluated and discussed.

ZUSAMMENFASSUNG

Die Gammastrahlen-Astronomie bietet ein einzigartiges Mittel zur Untersuchung der galaktischen kosmischen Strahlung fern von der Erde. Während der Propagation interagiert die kosmische Strahlung mit dem interstellaren Medium und erzeugt hochenergetische γ -Strahlung, die von der Erde aus nachgewiesen werden konnte. Diese Strahlung trägt die Information über den Ursprung und die Energetik der ursprünglichen kosmischen Strahlung am Ort der Wechselwirkung. Der Nachweis ist einfacher in Regionen mit erhöhter Gasdichte, wie in Riesenmolekülwolken, oder in Regionen mit erhöhtem kosmischen Strahlungsfluss, zum Beispiel in der Nähe eines Beschleunigers.

In dieser Arbeit habe ich beide Szenarien untersucht, indem ich die vom Fermi Large Area Telescope zwischen Energien von einigen zehn MeV und fast 1 TeV angesammelten Daten analysierte. Zunächst wurde die Gammastrahlenemission untersucht, die von über die ganze Milchstraße verteilten riesigen Molekülwolken ausgeht. Dadurch wurde eine noch nie dagewesene Kartierung der kosmischen Strahlungsverteilung in der Galaxie erzielt. Danach wurde die Emission untersucht, die aus dem Medium stammt, das den Supernova-Überrest W44 umgibt, was die Anwesenheit kürzlich beschleunigter Teilchen bestätigt und Beweise für anisotrope Diffusion liefert. Schließlich wurde auch das Potenzial der gegenwärtigen und zukünftigen γ -Strahlungsinstrumente zum Nachweis der Strahlung, die vom interstellaren Medium sowohl durch erhöhte Gasdichte als auch durch erhöhte Strahlungsdichte hervorgerufen wird, untersucht und diskutiert.

"It always seems impossible, until it is done."

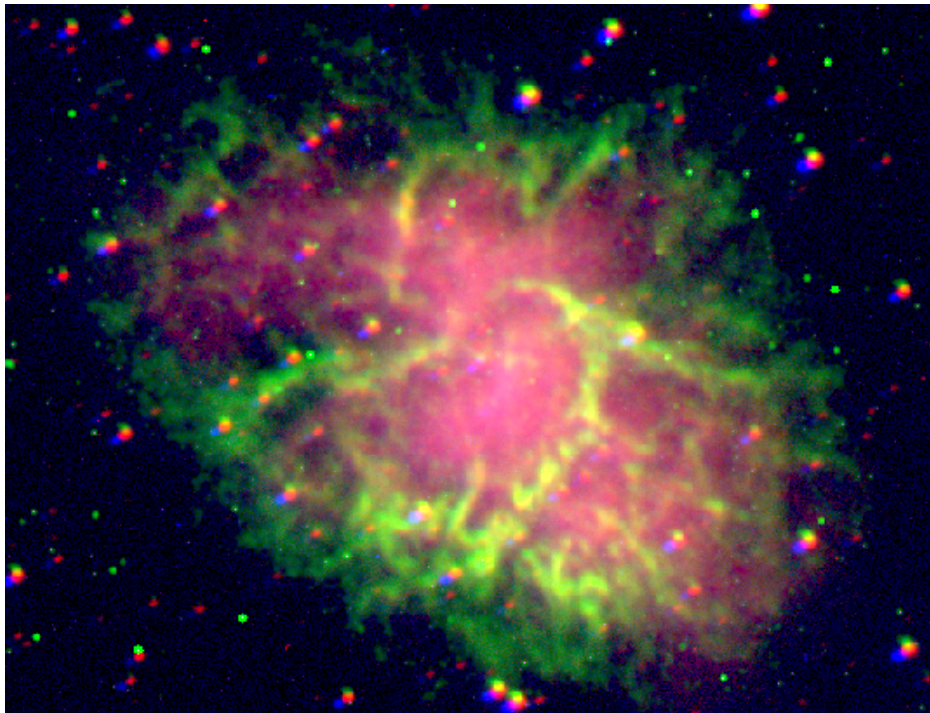


Fig. 1 The Crab nebula (M1) as seen from Heidelberg. The image has been obtained with the 70-cm telescope at the Landessternwarte observatory of Heidelberg during the Astrolab praktikum WS2018-2019 and it is a superposition of three different images obtained with a B (blue), R (red) and $H\alpha$ (green) filter.

TABLE OF CONTENTS

List of figures	xiii
List of tables	xxiii
1 Introduction	1
1.1 Cosmic Rays	2
1.1.1 Local Cosmic Rays	3
1.1.2 Galactic Cosmic Rays	9
1.1.3 Cosmic-ray accelerators	13
1.2 The Interstellar Medium	22
1.2.1 Molecular hydrogen	23
1.2.2 Molecular Clouds in the Milky Way	26
1.2.3 Neutral atomic hydrogen	28
1.2.4 Interstellar dust	31
1.3 Diffuse gamma-ray emission	33
1.3.1 Main radiation mechanism of the Interstellar Medium	33
1.3.2 Observations of the gamma-ray diffuse component	37
2 Giant Molecular Clouds as probes of Galactic Cosmic Rays	45
2.1 Cosmic Rays from Molecular Clouds	45
2.2 Analysis technique	49
2.3 Results from Molecular Clouds	56
2.3.1 Gould Belt and nearby Molecular Clouds	56
2.3.2 Molecular Clouds in the Galactic Disk	60
2.3.3 Molecular Clouds in the inner (1.5–4.5 kpc) region	67
2.3.4 The Central Molecular Zone	74
2.4 Discussion of the results	76
3 Cosmic-ray accelerators and their surroundings	83
3.1 The Supernova Remnant W44	83

3.1.1	Gamma-ray emission from the Remnant	84
3.1.2	Gamma-ray emission from the surrounding gas	92
3.2	Discussion	97
4	A new instrument for Cosmic-ray astrophysics	101
4.1	Sensitivity	102
4.2	Current and next-future gamma-ray instruments	103
4.2.1	The sea of Galactic Cosmic Rays with current gamma-ray instruments	105
4.2.2	Accelerators and their surroundings with current gamma-ray instruments	108
4.3	Beyond the Fermi-LAT	111
4.3.1	Expected results from improved sensitivity	114
4.4	Discussion	116
5	Summary and Conclusions	121
	Acknowledgments	125
	Personal Bibliography	127
	References	129

LIST OF FIGURES

1.1	Energy distribution, $J(E)$, of the local population of cosmic rays as measured by different experiments (see figure's legend). The points are multiplied by E^2 to emphasize the spectral features. The figure is from ref. [43].	6
1.2	Spectra of cosmic-ray protons (upper panels) and cosmic-ray electrons (lower panels) as a function of their kinetic energy. In the right panels the spectra have been multiplied to $E^{2.7}$ and E^3 respectively for protons and electrons, to emphasize the spectral features. The points are from refs. [17–19, 22, 26, 28, 44]	8
1.3	The differential cross section of proton-proton interaction as derived by ref. [49] as a function of the proton kinetic energy with different fixed photon energies (left panel) and as a function of the photon energy with different fixed values for the proton energy (right panel).	12
1.4	Classes of galactic sources contained in the fourth Fermi-LAT (4FGL) catalog [51] and the H.E.S.S. galactic plane survey (HGPS) [52]	14
1.5	Spectral energy distribution of several supernova remnants of the Galaxy. In particular the spectra of the youngest (< 1000 yr) SNRs (Tycho and Cas A) are plotted in cyan, slightly older (~ 2000) SNRs (RX J1713.7-3946 and RX J0852.0-4622) are plotted in red and middle-age (~ 10000 yr) remnants (W44, IC443 and W51C) are displayed in blue. The fluxes of the youngest ones reaches higher energy, however they all show a tendency to cut-off before 100 TeV. Figure is from ref. [60].	17
1.6	Galacto-centric distribution of potential cosmic-ray accelerators (pulsars, supernova remnants and HII regions), from Stahler & Palla [67]. The distributions of pulsars from Yusifov & Küçük 2004 [68] and of supernova remnants from Green (2015) [69] are also plotted.	19

-
- 1.7 Spectra of protons escaping from an impulsive accelerator, calculated at different distances $R=10$ pc (red), $R=100$ pc (blue) and for different times 10^3 yr (solid), 10^4 yr (dashed) 10^5 yr (dotted). The curves are from ref. [48]. For comparison the local spectrum of protons is plotted as grey points (as in Fig. 1.2). 20
- 1.8 Angular resolution of the main surveys of the molecular medium and their coverage of the galactic plane. The features of the HI4PI survey of galactic HI are also shown. For comparison, the resolution and coverage of several gamma-ray instruments are also plotted. 25
- 1.9 Main physical properties of the clouds reported in [87]. From top left to bottom right: the A parameter, defined as the ratio between $M_5 \equiv M/10^5 M_\odot$ and $d_{kpc}^2 \equiv (d/1 \text{ kpc})^2$, which characterizes the γ -ray flux of a molecular cloud, the mass, the angular size and the velocity dispersion. In the plot, the clouds are divided into inner-galaxy clouds ($R_{gal} < 6$ kpc; grey bars) and outer-galaxy clouds ($R_{gal} > 6$ kpc; green-contoured bars). 29
- 1.10 Fermi-LAT counts map (left panel) collected above 1 GeV and the Planck 353 GHz dust opacity map (right panel) for the central 30° of the Milky Way ($|l| < 30^\circ$, $|b| < 30^\circ$). In both maps not only the galactic plane is well distinguishable, but also the regions of the molecular clouds ρ -Ophiuchi [$(l, b) = (353.7, 17.7)^\circ$] and RCrA [$(l, b) = (359.9, -17.8)^\circ$] are well visible. Fermi-LAT data have been retrieved from [113], Planck data from [114]. 34
- 1.11 Model of the gamma-ray energy spectrum of the Galactic Disk between latitudes -5° and 5° as measured by Fermi-LAT [110]. The relative contribution of the main radiation mechanism, namely synchrotron, inverse Compton, bremsstrahlung and pion decay are shown. They have been calculated with the `naima` python package [121] and have been adjusted to interpolate the gamma-ray data points. 38

1.12	Sensitivity and angular resolution of the Fermi-LAT. The values have been taken from the Fermi-LAT performance's web page [122]. The two sensitivity curves refer to the outer (dark red) and inner (light red) Galaxy. The angular resolution curves refer to photon converted at the front (light green) or at the back (dark green) of the instrument, while the average resolution when using photons converted both in the front and in the back of the detector is plotted in black.	39
1.13	Upper panel: radial distribution of the gamma-ray emissivity per H atom of the diffuse gas as measured by EGRET [109] and Fermi-LAT by different authors [111, 130, 131]. The values are normalized to the value observed in the local region (~ 8 kpc). For comparison, the radial distribution of supernova remnants from [69] is also plotted. Lower panel: radial distribution of the derived CR spectral indexes from the same works. Two model predictions for the radial distribution of the spectral index are also plotted: one takes into account the effect of turbulence [132], the other assumes anti-correlation between the sources and the diffusion coefficient [133], see the text for more details.	41
2.1	Gamma-ray flux expected for molecular clouds of different A parameter (0.2, orange; 0.4, green; 1, blue) illuminated by cosmic rays of spectrum similar to the one measured by the local direct experiments. For comparison, the sensitivity of Fermi-LAT for the inner (light red) and outer (dark red) longitudes are plotted as areas, to account for the different worsening due to the observed source extension, θ , from a value relative to $\theta = 0.2^\circ$, to $\theta = 1^\circ$	48
2.2	The customized templates used in the analyses both for the background gas (left panels) and the clouds of interest (right panels). The top panel shows the template derived from CO and H _I for the cloud R877 from the catalog in [86]; the lower panel shows the template derived from dust opacity for the Gould Belt molecular cloud Orion A.	55
2.3	Position on the (X_{gal}, Y_{gal}) plane of the analyzed nearby clouds. The position of the Sun is indicated as yellow star.	57
2.4	(l, b) and (l, v) maps of the gas traced by CO [73] in the region of the considered Gould Belt clouds.	58

2.5	Same as in Fig. 2.4, for the other nearby clouds.	59
2.6	Residual maps in terms of σ (see text) after the subtraction of all the sources in the region of interest. The black contours refer to dust opacity at 353 Hz traced by Planck [101]. The figure has been adapted from [151].	61
2.7	Spectral energy distributions extracted from the six selected nearby molecular clouds. The blue regions show the expected flux for each cloud assuming the proton spectrum measured locally by AMS02 [18] up to 1 TeV and DAMPE [17] at higher energies. The area represents the 20% uncertainty on the flux normalization that derives from the uncertainty on the gas column density. In the case of Taurus and Orion A, the SED extracted by Yang et. al. 2013 [148] is also shown as grey crosses, renormalized in order to have the same value of A . The figure has been adapted from [151].	62
2.8	Position on the (X_{gal}, Y_{gal}) plane of the analyzed clouds of the catalog of Rice et al. 2016 [86]. The position of nearby and Gould Belt clouds are indicated as open circles. The position of the Sagittarius B complex is also shown as a black triangle.	64
2.9	Gas along the line of sight of the selected clouds. The gas densities have been summed over the area of the clouds. The blue curves show the contribution of molecular hydrogen and have been obtained from CO-datacubes. The orange ones show the abundance of the atomic hydrogen traced by the H α line. The position and extension on the line of sight of the cloud under analysis are indicated as a green area.	66
2.10	Residual maps in terms of σ after the subtractions of all the sources in the region of interest. The black contours refer to the CO gas in the region $(\Delta l \times \Delta b \times \Delta v)$ of the cloud. The figure has been adapted from [151].	68

2.11	The spectral energy distributions of the analyzed clouds are shown and compared to the expected gamma-ray flux derived from a local (as measured by AMS and Dapne) proton spectrum. The fluxes have been normalized to $A = 1$ and the curves have been multiplied by different factors (10,100,1000,10000) to separate the clouds belonging to different regions. The errorbars represent the systematic uncertainties derived as described in the text. The grey area represents the 30% uncertainty that affects the predicted flux, deriving from the uncertainty on the CO-to-H ₂ conversion factor. The figure has been adapted from [151].	69
2.12	Position on the (X_{gal}, Y_{gal}) plane of the analyzed molecular clouds of the 1.5–4.5 kpc region. The numeration corresponds to the indexes reported in the MD-catalog.	70
2.13	Spectral energy distribution derived from the analyzed regions corresponding to the named clouds (black points). The expected γ -ray fluxes in case of a uniform and a radial emissivity are shown as yellow and red areas, respectively. The local γ -ray flux derived from direct CR measurements is also shown in blue. The area represents the 20% uncertainty that derives from the column density. The fluxes expected from each ring in the given direction are also plotted as dashed lines, respectively: 0–1.5 kpc (magenta), 1.5–4.5 kpc (cyan), 4.5–5.5 kpc (green), 5.5–6.5 kpc (yellow), 6.5–7 kpc (orange), 7–8 kpc (red), 8–10 kpc (brown), 10–16.5 kpc (violet), 16.5–50 kpc (blue).	75
2.14	Left panel: spectral energy distributions derived for the Sagittarius B complex by Fermi-LAT [151] (black bullets) and by H.E.S.S. [155] (black squares), compared to the flux expected from a local spectrum of cosmic rays (see previous sections). Right panel: spectral points of Sagittarius B compared to the one extracted in the clouds of the Gould Belt [151]. Fluxes have been normalized to $A = 1$	76

-
- 2.15 The γ -ray and CR parameters are shown for each cloud against their distance from the Galactic Center. The top panel shows the gamma-ray emissivity at 2 GeV, the middle panel shows the cosmic-ray density at 30 GeV and the bottom panel shows the CR power law spectral index. The grey points indicate the corresponding values obtained from the ring analysis, in ref. [111]. The values for the clouds in the 1.5–4.5 kpc regions are indicated as upper limits, since they are characteristic of the entire column of gas. The red points instead indicate the derived value for these clouds after subtraction of the corresponding fraction of gas, assuming that it emits as the local (8–10 kpc) ring. The orange area highlights the local spectrum of cosmic rays, derived from the points of AMS02. 81
- 3.1 RGB image of the supernova remnant W44 observed in radio at 324 GHz by the Very Large Array (red), in X-rays by CHANDRA between 0.3 and 2.1 keV (green) and in γ -rays in the energy range 1 GeV–1 TeV as seen by the Fermi-Large area telescope (blue). The radio and X-ray maps have been taken from the online-available catalog of supernova remnants from ref. [165]. 86
- 3.2 Fermi-LAT count maps of the supernova remnant W44 for different energy ranges after the subtraction of all the background sources. The images have been smoothed, using a bicubic interpolation method included in the python library matplotlib.pyplot. 87

- 3.3 Spectral energy distribution of the supernova remnant W44 as obtained from ~ 10 years of observation with the Fermi-LAT above 60 MeV. The red curves show the hadronic models that best represent the data, the area corresponds to a broken power law in total energy with indices 2.40 ± 0.02 and 3.87 ± 0.14 below and above 39 ± 3 GeV. The area corresponds to the 1σ confidence level of the model. A power law with an exponential cutoff at 71 ± 6 GeV and index of 2.30 ± 0.02 also fits the data and is plotted as red dashed line. The best leptonic model is displayed in green and it corresponds to bremsstrahlung radiation originating from a broken power law spectrum of electrons of minimum energy 600 MeV and with indices 2.32 ± 0.03 below (6.1 ± 0.6) GeV and 3.39 ± 0.07 above. The figure has been adapted from [167]. The points from a previous analysis of the remnant are also shown as light-blue squares [168]. 88
- 3.4 Enlargement of the spectral energy distribution shown in Fig. 3.3 in the region below a few GeV. On the left panel the usual $E^2 \times \text{Flux}$ representation is used, while in the right panel the true differential flux is displayed, to emphasize the pion-bump feature. The figure has been adapted from [167]. 90
- 3.5 *Left side*: test statistic map of the two gamma-ray extended sources, NW-Source and SE-source. The white regions indicate the configuration of sources in the final model, the cyan regions indicate the sources that have been removed. The CO gas contours from the survey of Dame et al. (2000) [73] are plotted in yellow. *Right side*: the gas in the region of W44 as seen by the Nobeyama telescope [75] in four different velocity ranges, as indicated in the figure legend. The density has been normalized to the average value in each panel. The white regions indicate the two extended γ -ray sources, NW- and SE-source (solid) and the shell of the SNR (dashed). The figure has been adapted from [167] 93

- 3.6 Spectral energy distributions derived for the SE- (orange) and NW-source (blue). The colored areas indicate the 1-sigma confidence level derived from the fit with *naima*. The grey curve is the gamma-ray flux calculated from the local emissivity. The masses, M_{SE} and M_{NW} , have been calculated from the CO gas in these regions. In the rightmost panel the fluxes of the two sources are compared to the flux of the remnant. The figure has been adapted from [167]. 96
- 3.7 Spectral energy distribution derived for the whole gas complex is compared to the expected flux for a cloud of the same mass, M_{surr} , illuminated by the local CR flux. The green area is the *naima*-derived fitting curve assuming a pion-decay model. The area represents the 1- σ confidence level. The figure has been adapted from [167]. 97
- 4.1 Differential sensitivity of the most sensitive gamma-ray instruments available (top panel) or planned (low panel) for different energy ranges. The red areas represent the sensitivity of 10-yr Fermi-LAT accumulated data, in the outer Galaxy (dark red), and in the inner Galaxy (light red). The orange area indicates the sensitivity of 50-hr observations with the H.E.S.S.. The blue zone indicates LHAASO 1-year sensitivity, while the blue dashed line is the same curve for 10 years of observations, assuming a \sqrt{t} dependence; the magenta dashed line is the 5 years sensitivity level of HAWC. The green areas are the sensitivity of 50-h observations with the CTA North (light green) and the CTA South (dark green) array, in the baseline configuration. The dashed cyan line is the planned sensitivity for SWGO after 1 year of observations. The sensitivities are scaled to take into account the extension of the sources, spanning from 0.2° to 0.5° . The black curve indicates the gamma-ray flux expected from a molecular cloud with $A = 1$ illuminated by the local cosmic-ray spectrum, plotted in the inset panel. 107

- 4.2 Ratio between the sensitivity $S_0(E)$ of the above mention detectors and the flux of a gamma-ray emitting cloud illuminated by the local spectrum of cosmic rays. This represents the minimum A factor that a cloud should have in order to be detectable or equivalently the minimum improvement of the sensitivity obtained for example by increasing the observation time. An average size of 0.3° has been considered for the worsening factor ω . The curves correspond to: Fermi-LAT inner (light red) and outer (dark red) performances, H.E.S.S. (orange), CTA Northern (light green) and Southern (green) array, SWGO (cyan) and LHAASO (blue). The dashes blue curve represents the second branch of protons at high energies. 109
- 4.3 Distribution of the A parameters of the cloud of MD-catalog as a function of their galactic longitude. The detection threshold of the above described instruments is also shown for comparison respectively for 10 years Fermi-LAT observations (red), 50-hours with CTA (green) and H.E.S.S.(orange) and for LHAASO after 1 (blue solid) or 10 years (blue dashed). The threshold is an approximate value derived from the ratio between the sensitivity and the local flux. 110
- 4.4 The same sensitivities as in Fig 4.4 are plotted against the gamma-ray flux expected for a molecular cloud located at $R=10$ pc (grey curves) and $R=100$ pc (blue curves) from an impulsive accelerator, observed after a time $t = 10^3$ yr (solid), 10^4 yr (dashed) and 10^5 yr (dotted). An energy dependent diffusion coefficient of $D(E) = 10^{28}(E/10 \text{ GeV})^\delta \text{ cm}^2/\text{s}$ is assumed, as well as $W_p = 10^{50}$ erg and an injection spectrum of slope $\Gamma = 2.2$, see [48]. The experimental points of cloud R877 in the 4-6 kpc ring [151] and NW-source in the vicinity of W44 are also shown [167]. 112

-
- 4.5 The combined effect on the sensitivity due to an increase in the observation time τ and in the extension Λ of a Fermi-LAT-like detector. In the leftmost panel: the blue curve shows the effect of increasing only the time by a factor x , while the orange curve shows the effect due to an increase of only the size by a factor x . The other two curves show a combination of the two variables: for the green curve the time and size are increased by the same factor, while for the red curve the increase factor in time is $1/3$ of the increase factor in size. The middle panel instead shows how Λ and τ depends on each other for a fixed sensitivity improvement Σ . The rightmost panel instead shows the worsening, ω , of the sensitivity caused by different values of PSF as a function of the source extension. 113
- 4.6 The same as Fig. 4.3 but in the case of a $\Sigma = 2$ (orange) and of a $\Sigma = 4$ (blue) better sensitivity than Fermi-LAT. 115
- 4.7 Hystograms of the galacto-centric distances and galactic heights of the molecular clouds that are visible with the sensitivity of Fermi-LAT (dark red), with a $\Sigma = 2$ better sensitivity (orange) and a $\Sigma = 4$ times better one (blue). 115
- 4.8 Distribution on the (X_{gal}, Y_{gal}) plane (upper panels) and in the (R_{gal}, Z_{gal}) plane (lower panels) of Milky Way molecular clouds detectable with the current sensitivity of Fermi-LAT (dark red points) and with a sensitivity improved of a factor $\Sigma = 2$ (right panel, orange points) and $\Sigma = 4$ (right panel blue points). The Sun is indicated as a yellow star. 117

LIST OF TABLES

1.1	Typical physical parameters that characterize the different phases of the interstellar medium. Values are taken from ref. [72]	23
2.1	Physical properties of the sample of nearby molecular clouds chosen for the analysis. The position (l, b) of the center, the distances d from us, and the derived distances R_{gal} from the Galactic center, refer to [150], while the masses M and the A parameters have been calculated from the dust opacity map, using Eq. 1.2.11.	60
2.2	Parameters of the analyzed molecular clouds from the catalog of Rice et al. 2016 [86]. The numbers correspond to the catalog nomenclature. The mass and the A parameter have been calculated from the map of CO as explained in the text.	63
2.3	Emissivity (at 2 GeV) and spectral index for different galactocentric rings derived by fitting the measurements of Acero et al. (2016). The error relative to the fit is not reported as it is very small compared to the systematic error of these kind of investigations that is of the order of 30% due to the uncertainties on the gas column density.	72
2.4	Physical parameters of the chosen molecular clouds in the 1.5-4.5 kpc region from the MD-catalog. Both the distance reported in the catalog d and the one derived by the parallax based rotation curve d^{px} are reported. For the latter, the probability \mathcal{P} that the cloud is at that position is also reported. A_{tot}^{dust} and A_{tot}^{MC} are the A -parameters calculated for the entire column, both from the dust measurements [101] and as sum of clouds. Finally X is the fraction of gas that does not belong to the 1.5–4.5 kpc region, according to CO-line measurements.	73
2.5	The parameters for the cosmic-ray density derived for all the analyzed clouds with naima. The normalization $\rho_{0,CR}$ refers to the pivot value of 30 GeV.	80

3.1	Results from the modeling of W44. The maximum values of likelihood of the morphological and spectral models tested on the γ -ray observations are reported. Also the reduced AIC* values are reported. The best models have been highlighted in bold.	91
3.2	The different spectral models for proton and electrons tested with naima assuming a pion-decay emission mechanism and a bremsstrahlung radiation model, respectively. The BIC value is used to evaluate the best model and it is reported here for each spectral function. The best models have been highlighted in bold.	91
3.3	4FGL sources in the region of W44; the bolded sources are the ones for which we found a new morphology.	94
3.4	Results from the modeling of the sources that surrounds W44. The γ -ray spectrum has been derived starting from 60 MeV in the case of NW-source and SE-source, and starting from 1 GeV in the case of the surrounding gas. The highest values of likelihood and the lowest values of AIC* and BIC are highlighted in bold, as they indicate the best model.	98
4.1	Main parameters that characterize the performances of the current and planned γ -ray instruments. The effective area refers to on-axis observations. The sensitivity is given for different observation times, specifically: 10 years for space based instruments, 50 hours for IACT arrays and 1 year for WCs and LHAASO.	104

INTRODUCTION

Gamma-ray astronomy explores the highest energetic window of the electromagnetic spectrum of radiation. Photons that overcome 100 keV ($\sim 10^{10}$ GHz, ~ 0.1 Å) are classified, in astrophysics, as gamma (γ) rays. The gamma-ray band is the widest electromagnetic window, covering more than nine decades in energy. Radiation up to more than 100 teraelectronvolt (1 TeV = 10^{12} eV) has now been detected with the current instrumentation. A distinction is conventionally made between high-energy (HE) photons, which reach a few hundred GeV, very high energy (VHE) photons, that belong to the TeV energy range, and ultra-high-energy (UHE) photons, that overcome energies of 1 petaelectronvolt (1 PeV = 10^{15} eV). Different observational techniques are employed for each energy range: satellites like the Fermi Large Area Telescope (LAT) [1] or the *Astrorivelatore a Immagini Leggero* (AGILE) [2] are optimized for GeV photons, ground-based instruments, in form of Cherenkov telescopes (e.g. the Major Atmospheric Gamma-Ray Imaging Cherenkov Telescope (MAGIC) [3], the Very Energetic Radiation Imaging Telescope Array System (VERITAS) [4], the High Energetic Stereoscopic System (H.E.S.S.) [5] and the future Cherenkov Telescope Array (CTA) [6]) or water Cherenkov tanks (e.g. the High Altitude Water Cherenkov observatory, HAWC [7]) observe the VHE range, while the now-starting Large High Altitude Air Shower Observatory (LHAASO) [8] will open up the UHE window, thanks to a combination of particle and Cherenkov-light detectors.

Non-thermal processes regulate the production of such high energy photons. In particular, gamma-radiation is associated with the acceleration and interactions of high energy electrons (synchrotron, bremsstrahlung, and Inverse Compton) and nuclei (pion decay). For this reason, gamma-ray astronomy is strictly connected with the physics of the relativistic particles that populate the Galaxy, the Cosmic Rays, and serve as their primary tracer throughout the Galaxy (sec. 1.1.2). It is not a case in fact that the sky observed in gamma-rays directly corresponds to

the radio and infrared observations of diffuse gas, which constitutes the natural target for production of gamma-rays via interaction with high-energy particles (sec 1.2). Gamma-rays also share with radio-astronomy all those sources that emit primarily via non-thermal processes: from pulsar and supernova remnant to active galactic nuclei (sec. 1.1.3). A great synergy, therefore, exists between gamma and the other wavebands, especially with radio observations. Besides, gamma-ray astronomy serves as a link between the electromagnetic and the non-electromagnetic phenomena. Coalescence events that generate gravitational waves, for example, often produce detectable gamma radiation that helps to locate the progenitor of the waves. Also, signatures of dark matter are expected to be detected in gamma-rays, making it the main observational window for this phenomenon.

This work focuses on the physical properties of galactic cosmic rays, that can be measured via gamma-ray observations. Two main cases are considered: the case of cosmic rays mixed with the diffuse interstellar medium (Chapter 2) and the case of cosmic-rays freshly accelerated near sources (Chapter 3). The capabilities of gamma-ray instruments of providing a deep understanding of the galactic population of cosmic rays are then discussed in Chapter 4.

1.1 COSMIC RAYS

The term *cosmic rays* (CRs) indicates the ensemble of high-energy particles, mainly electrons, protons, and ions, that continuously bomb the Earth from any direction. The first hints of the existence of such radiation came in the early 1900s, by observing that electroscopes discharged even when kept away from radioactive sources. The *cosmic* origin of this radiation was then demonstrated by Victor Hess in 1912 [9], by showing that the ionization rate increased with altitude. Since then, many experiments were dedicated to measure cosmic rays either *directly* with calorimeters and magnetic spectrometers mounted on balloons (e.g. BESS [10, 11], CREAM [12, 13]), satellites (e.g. PAMELA [14, 15], Voyager [16], DAMPE [17]) and onboard of the International Space Station (AMS [18, 19], CALET [20, 21]) or *indirectly* by measuring their secondary products. Cosmic Rays, in fact, when impacting on the Earth's atmosphere produce a particle cascade that can then be detected by ground-based experiments such as Imaging Air Cherenkov Telescopes (e.g. H.E.S.S. [22]), Extensive Air Shower detectors (e.g. Pierre Auger Observatory [23, 24], KASCADE-GRANDE [25, 26], IceTop [27, 28]), and Radio-antenna networks (LOFAR [29, 30]).

These experiments, are capable to discern particle-initiated cascades from photon-initiated ones and therefore provide a valid method for measuring CRs, that extend to the highest energy end of the spectrum. Thanks to the synergy between these techniques, the measured spectral energy distribution extend from a few GeV to thousands of PeV. Moreover, we are able to determine the mass and the charge (with magnetic spectrometers) of the particle and thus to derive the CRs composition and ratios of different species. The information retrieved with the above-cited techniques concerns the so-called ‘local’ cosmic rays, namely the particles that reach Earth from an indefinite location. In the travel towards us, CRs get continuously deflected by the interstellar magnetic fields and mix, forming the so-called cosmic-ray ‘Sea’, thus losing information on their origin. However, while diffusing through the Galactic Disk, CRs produce secondary emission, by interacting with the interstellar medium. This emission, mainly in form of γ -rays, but also neutrinos, reaches Earth un-deflected and allows the derivation of the CR spectrum at the location of the interaction. Gamma-ray observations thus serve as unique tracers of the Galactic cosmic ray population.

In this chapter I will summarize the main observational properties of cosmic rays, from their composition to their propagation (sec. 1.1.2) and I will briefly present the current theory on acceleration and escape of these relativistic particles (sec. 1.1.3). In the second section (sec. 1.2) the properties of the interstellar medium as primary target for interaction with cosmic rays are presented followed by the description of the emission mechanism and the status of art of the observations of the radiation arising from the interactions of these high-energy particle with the interstellar matter (sec. 1.3).

1.1.1 Local Cosmic Rays

Cosmic Rays arriving at Earth consist for the 99% of nuclei of atoms, 90% of which are protons, 9% are helium nuclei and the remaining are heavier ions. Their chemical composition differs from the Solar one. In particular, in cosmic rays light elements (Li,Be,B), sub-iron atoms (Sc,Ti,V,Cr, and Mn) and metals are overabundant. This is the result of *spallation* reactions, namely of the fragmentation of heavier cosmic rays caused by the interaction with the interstellar matter. Electrons are 100 times less abundant than protons at GeV energies, with this fraction that decreases below 10^{-3} at 1 TeV [31]. Higher-energy electrons instead are not detected because they

cool down before reaching us. A small fraction of positrons is also detected. An over-abundance of these anti-particles above a few GeV with respect to the model predictions of secondary production in the interstellar medium, has been reported in [32] and it is still matter of debate as one of the possible explanations of this enhancement might be the annihilation of dark matter.

The all-particles energy distribution (spectrum) of local cosmic rays extends over 11 orders of magnitudes from 1 GeV (total energy) to 10^{11} GeV (see Fig. 1.1). The overall shape of the spectrum is approximately a Power Law:

$$J(E) = \frac{dN}{dE dA dt d\Omega} = J_0 \left(\frac{E}{E_0} \right)^{-\alpha} \quad (1.1.1)$$

of average index $\alpha = 2.7$. The spectral index is not constant over the different energy decades and several features emerge. At the lowest energy end, around a few GeV, the experimental fluxes are suppressed by solar modulation, namely by their interactions with the heliospheric magnetic field [33]. At the highest energy end, precisely at $10^{19.6}$ eV the spectrum exhibits a cutoff, the Greisen-Zatsepin-Kuzmin suppression, due to the interactions with the photons of the cosmic microwave background [34]. Moreover, the spectrum presents several breaks. The main ones are: a steepening to $E^{-3.1}$ at $10^{15.6}$ eV (~ 3 PeV), named *knee* [35] and a slight hardening at $10^{18.5}$ eV (~ 5 EeV), labeled *ankle* [36]. The knee is often interpreted as the boundary energy of cosmic rays of galactic origin. Particles of energy up to the knee are in fact believed to originate inside the Milky Way. Observations of γ -ray emission from the disk of our galaxy suggest that efficient acceleration is present at these energies [37]. Moreover, the Larmour radius for 1 PeV protons, following [38], is of the order of:

$$r_L = \left(\frac{E}{1 \text{ PeV}} \right) \left(\frac{B}{1 \mu\text{G}} \right)^{-1} \text{ pc} \quad (1.1.2)$$

much smaller than any length-scale of the Milky Way, suggesting that CRs of this energy, which originate in the Galaxy, can't leave it. An alternative explanation for the softening, in correspondence to the knee, is ascribed to the maximum-energy cutoff of protons, provided by the shock acceleration theory (see 1.1.3). In this framework, the contribution of heavier nuclei becomes more important than the proton one above a certain energy, as a consequence of the fact that the cutoff, expected to happen at the same rigidity for all species, falls earlier (in energy) for

protons than for heavier elements. The meaning of the ankle remains under debate, but is believed to be due to the rising contribution of extra-galactic sources.

Further sub-features arise, when observing the high quality data collected for protons. As revealed by PAMELA [15] and confirmed by AMS02 [18], the spectrum of CR protons hardens at $\sim 200\text{--}300$ GeV from a spectral index of 2.85 to 2.67. The spectrum of protons, including this hardening can be analytically described up to few TeV, following [18], as a function of rigidity, R ($R \equiv pc/Ze$, where p is the momentum, Z is the charge number e is the charge of the electron):

$$J_p(R) = 4.5 \times 10^{-5} \left(\frac{R}{45 \text{ GV}} \right)^{-2.85} \left[1 + \left(\frac{R}{336 \text{ GV}} \right)^{5.5} \right]^{0.024} \text{ GV}^{-1} \text{ cm}^{-2} \text{ sr}^{-1} \text{ s}^{-1} \quad (1.1.3)$$

Another break is then observed around 15 TeV in the data of CREAM [39], DAMPE [17] and CALET [40], with the spectral index that returns to be steep, ~ 2.9 , see Fig 1.2. Both features are also observed in the spectrum of Helium and heavier nuclei. A first explanation of the hardening could be found in the existence of two different classes of accelerators or in the modification of propagation properties according to the energy range. The addition of a further steepening however complicates the picture, making someone debate that the CR spectrum is the result of a universal acceleration mechanism at all [41]. Besides, an additional complication rises at higher energies ($> 10^5$ GeV), where different experiments provide incompatible results for protons. Two different branches can in fact been observed above few PeV (fig 1.2). To interpret that, one should take into consideration that the detection of cosmic rays above the knee is conducted exclusively by ground-based experiments which cannot distinguish between the different species that compose the cosmic radiation. The separation of different elements has to rely on Monte Carlo simulations of CR abundances and shower developments. Puzzling, the two proton spectra reported respectively by the Cascade [35] and the Ictop/Icecube [42] collaboration do not agree even when the same Monte Carlo code has been employed.

The spectra of cosmic-ray electrons and positrons also show different spectral features. A part from the steepening below 20 GeV due to solar modulation, a gradual hardening of both spectra is observed in the data of AMS02 [19] around 30 GeV. After that, the spectral indexes remain almost constant to $\gamma_{e^-} = 3.17$ $\gamma_{e^+} = 2.74$ up to ~ 1 TeV where an abrupt falloff is observed. Observations in the supra-TeV regime have been carried out both by DAMPE [44] and by H.E.S.S. [22] the latter

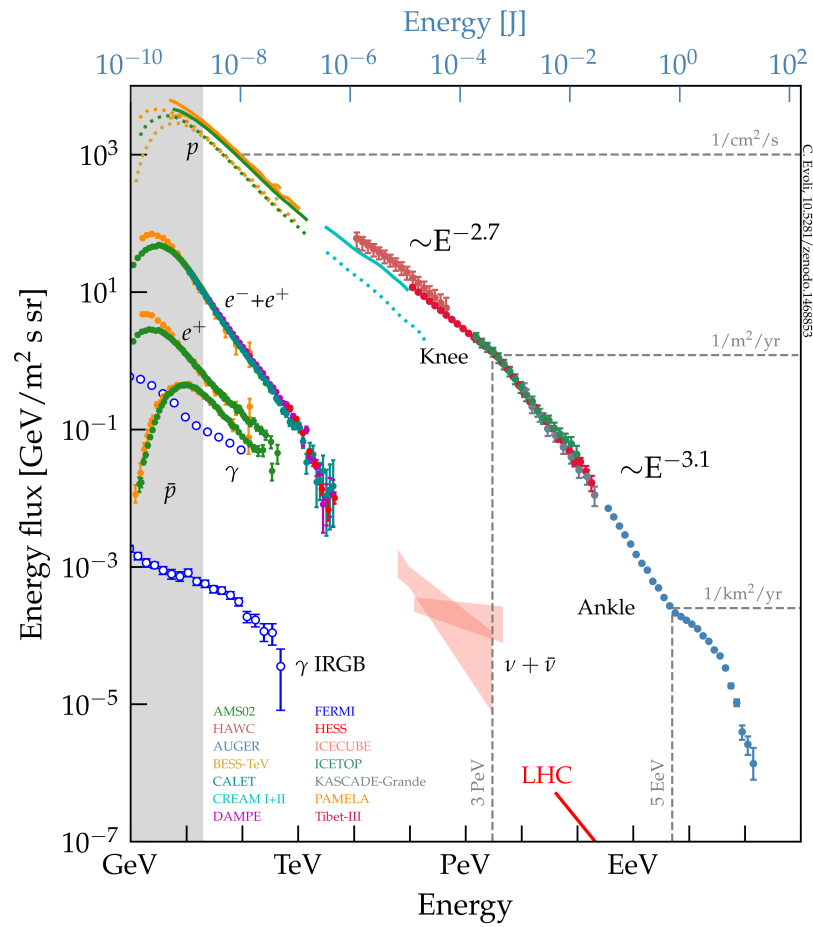


Fig. 1.1 Energy distribution, $J(E)$, of the local population of cosmic rays as measured by different experiments (see figure's legend). The points are multiplied by E^2 to emphasize the spectral features. The figure is from ref. [43].

showing preliminary data that extend up to 20 TeV [45]. These observations suggest a high energy slope of 3.92 and 3.78, respectively. In this case, the distinction between particles and antiparticles is no-longer possible but low energy extrapolations suggest that the spectrum must be dominated by electrons. The functional form of the electron spectrum above 30 GeV is well described as a broken power-law:

$$J_e(E) = K \left(\frac{E}{E_0} \right)^{-\gamma_1} \left[1 + \left(\frac{E}{E_b} \right)^{-(\gamma_2 - \gamma_1)/s} \right]^s. \quad (1.1.4)$$

The parameters are obtained by fitting the experimental points. For example, from DAMPE data [17] it results: $\gamma_1 = 3.09$, $\gamma_2 = 3.92$, and $E_b = 0.914$ TeV with s fixed to 0.1.

Another observational feature of cosmic rays is the high degree of *isotropy*. This means that the cosmic ray flux, at a given energy, is the same independently of the direction of observation. The degree of anisotropy, calculated as

$$\Delta = \frac{I_{max} - I_{min}}{I_{max} + I_{min}} \quad (1.1.5)$$

increases with energy from $\Delta \sim 0.06\%$ at 1 PeV, to $\Delta \sim 10\%$ at the highest energy end of the spectrum [46]. At lower energies the solar influence prevents to have reliable measurements. To guarantee such degree of isotropy, one has to assume that CRs propagate diffusively, otherwise strong anisotropy would be detected towards single sources, and in particular towards the central region of the Galaxy, where more spiral arms superimpose. CRs are repeatedly scattered by the turbulent interstellar magnetic fields and this results in a randomization of the path of the particles that mixes and isotropize them. It is then reasonable to assume that, on average, the same cosmic ray energy density characterizes the whole Galaxy. The latter can be calculated from the observed energy distribution, $J(E)$, as:

$$\rho_{CR} = \int_{E_{min}}^{\infty} n_{CR}(E) E dE = \frac{4\pi}{c} \int_{E_{min}}^{\infty} J(E) E dE \quad (1.1.6)$$

which in case of a power-law energy distribution becomes:

$$\rho_{CR}(\geq 1\text{GeV}) = \frac{4\pi}{c} \int_{1\text{ GeV}}^{\infty} J_0 \left(\frac{E}{E_0} \right)^{-\alpha} E dE = \frac{4\pi}{c} \frac{J_0}{E_0^{-\alpha}} \left[\frac{E^{-\alpha+2}}{\alpha-2} \right]_{1\text{ GeV}}^{\infty} \quad (1.1.7)$$

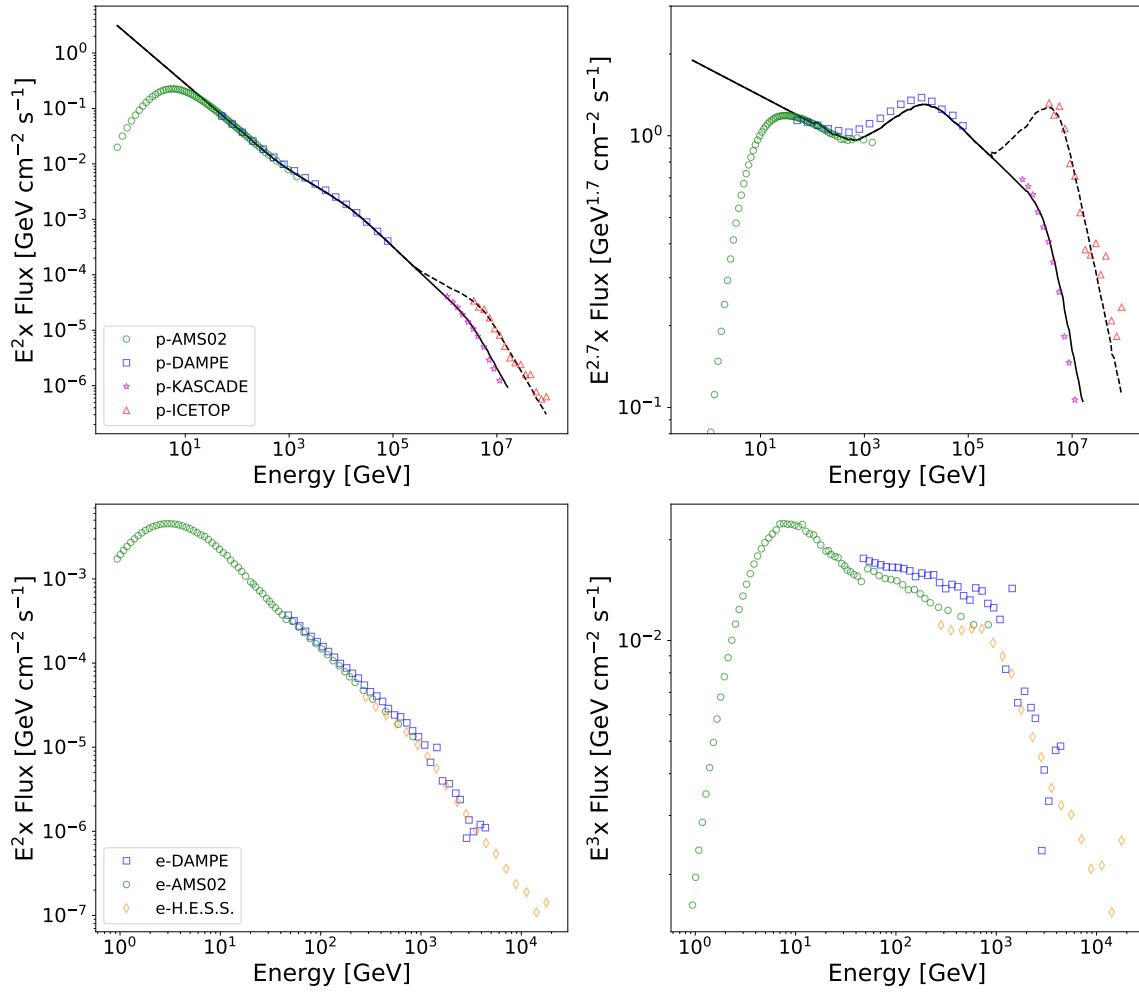


Fig. 1.2 Spectra of cosmic-ray protons (upper panels) and cosmic-ray electrons (lower panels) as a function of their kinetic energy. In the right panels the spectra have been multiplied to $E^{2.7}$ and E^3 respectively for protons and electrons, to emphasize the spectral features. The points are from refs. [17–19, 22, 26, 28, 44]

For the local environment taking $\alpha = 2.85$ and $J_0(E_0 = 1 \text{ GeV}) = 2.32 [\text{GeV cm}^2 \text{ s sr}]^{-1}$ (Eq. 1.1.3), it amounts to $\rho_{CR} = 1.1 \text{ eV cm}^{-3}$ at energies above 1 GeV. This is fortuitously of the same order of magnitude of the energy density of the interstellar magnetic field ($B^2/2\mu_0 \sim 0.6 \text{ eV cm}^{-3}$, with $B = 5 \mu\text{G}$) and of the Microwave Background Radiation ($\int En_{ph} dE \approx b T^3 \langle E \rangle = 0.3 \text{ eV cm}^{-3}$, with $b = 20.3 \text{ cm}^{-3} \text{ K}^{-3}$ and $\langle E \rangle = 6.6 \times 10^{-4} \text{ eV}$) [47], suggesting that cosmic rays contribute significantly to the energetic balance of the Galaxy.

1.1.2 Galactic Cosmic Rays

Local cosmic rays arrive at Earth after having lost memory of their origin, and their initial energy distribution. Any information on their starting point (the sources) and their path (propagation properties) need to be reconstructed from the situation observed at the arrival position (the Earth). Even though a uniform density for the CR-population is expected, as a consequence of diffusive motion over large timescales, such a scenario might not apply in different locations. Moreover, no one guarantees that the values that characterize the Earth's vicinity can be extended to further locations. Nevertheless, tests of the *Galactic* cosmic-ray populations can be performed by exploiting the secondary products that these particles produce in their travel through the Galaxy, giving further constraint on the dynamics and accelerations of these high-energy particles.

Confinement and propagation

As expressed in eq. 1.1.2, the gyro-radius of particles of sub-PeV energies is smaller than any galactic length-scale, suggesting that these particles are confined within the Galaxy. Observation of a significant fraction of secondary cosmic rays suggest that these high energy particle must have had enough time to interact via spallation with the interstellar medium. Hence, the measure of the grammage of these secondary particles provide a lower limit to the time, τ_{res} , cosmic rays reside in the Milky Way. In particular, the observed grammage of $\Lambda = 10 \text{ g cm}^{-2}$ is explained only assuming a minimum residence time of $\tau_{res} \sim 10^6 \text{ yr}$. The latter decreases with energy as $E^{-\delta}$, where $\delta = 0.3 - 0.6$. On the other hand an independent measure of this quantity is obtained by the observation of the ratio between abundances of unstable over stable isotopes. For example the ratio $^{10}\text{Be}/\text{Be}$, with a decay time of ^{10}Be of $\sim 1.4 \text{ Myr}$ tells us that the time spent in the Galaxy must be significantly longer than

what derived from the grammage of spallation product, about 10-20 Myr. This discrepancy implies that cosmic rays spend a big portion of the time in a area of lower density, where spallation is reduced, i.e. the Galactic halo. Besides, this is another indirect proof of the diffusion type of propagation in the Galaxy. If the propagation were rectilinear in fact, in such a long time the particles would quickly cross the galactic disk and exit it, confuting the observations.

The evolution of the CR energy ($\gamma = E/mc^2$) distribution $f(R, t, \gamma)$ in the diffusion through the interstellar medium is regulated by the presence of sources and by the energy losses that these high-energy particles undergo interacting with the interstellar matter and magnetic fields. The motion of cosmic rays is described by the conventional diffusion equation, that in case of spherical symmetry, reads: (e.g. [48]):

$$\frac{\partial f}{\partial t} = \frac{D}{R^2} \frac{\partial}{\partial R} R^2 \frac{\partial f}{\partial R} + \frac{\partial}{\partial \gamma} (Pf) + Q \quad (1.1.8)$$

where D is the diffusion coefficient, that generally depends on the energy, while the dependency on position can be neglected in the case of a homogeneous propagation medium. The other terms, P and Q denotes the energy loss rate and the injection rate respectively. An estimate of the diffusion coefficient D in the halo can also be computed from the observed grammage, Λ , on the scale-height H of the halo, knowing that $\Lambda = \rho \tau_{esc} c$ and substituting $\tau_{esc} \sim H^2/D_0$ one obtains:

$$D_0(E_0 = 1 \text{ GeV}) \sim 3 \times 10^{28} \left(\frac{H}{5 \text{ kpc}} \right) \left(\frac{\Lambda}{10 \text{ g/cm}^2} \right)^{-1} \frac{\text{cm}^2}{\text{s}} \quad (1.1.9)$$

that is valid for particles of energies ~ 1 GeV. Higher energy particles have a larger diffusion coefficient that scales as E^δ , opposite with respect to the residence time:

$$D(E) = D_0 \left(\frac{E}{E_0} \right)^\delta. \quad (1.1.10)$$

Secondaries as tracer of Galactic Cosmic Rays

A channel of observation of the cosmic rays in locations different from the Solar System is provided by the secondary neutral products of the interactions of charged cosmic rays with the interstellar matter. Cosmic-ray nuclei, for example, interact with the nuclei in the interstellar medium, giving birth to unstable mesons that

quickly decay in detectable γ -ray photons or neutrinos. The main channels of interactions are given by:

$$\begin{cases} p + p \rightarrow \pi^0 \rightarrow 2\gamma \\ p + p \rightarrow \pi^+ \rightarrow \mu^+ + \nu_\mu \\ p + p \rightarrow \pi^- \rightarrow \mu^- + \bar{\nu}_\mu \end{cases} \quad (1.1.11)$$

Photons and neutrinos produced in this way have the ability of reaching Earth without being deflected, carrying all the information on the energy of the parent particles.

The emissivity of secondaries j , per unit energy, i.e the amount of photons radiated per unit volume and time, is in a general form given by:

$$\varphi_j = \frac{dN_j}{dE_j dV dt} = \int dE_i \frac{d\sigma_{i \rightarrow j}(E_i, E_j)}{dE_j} \left(\frac{c\rho}{m}\right) \frac{4\pi}{c} J_i(E_i) \quad (1.1.12)$$

where $J(E_i) = \frac{dN_i}{dA dt d\Omega dE_i}$ is the energy spectrum of the parent particle, $d\sigma/dE$ is the differential cross section of the interaction and ρ and m are respectively the density and the average mass of the particles of the targeted medium.

From Eq. 1.1.12, the flux expected to reach Earth, can be calculated as

$$F_j = \frac{dN_j}{dE_j dA dt} = \int \frac{dV}{4\pi d^2} \int dE_i \frac{d\sigma_{i \rightarrow j}}{dE_j} \left(\frac{c\rho}{m}\right) \frac{4\pi}{c} J_i(E_i) = \quad (1.1.13)$$

$$= \frac{M}{m_p d^2} \int dE_i \frac{d\sigma_{i \rightarrow j}}{dE_j} J_i(E_i) = \frac{M}{m_p d^2} \varphi_j \quad (1.1.14)$$

$$= N \theta \varphi_j \quad (1.1.15)$$

where M is the total mass of the target under consideration and d is its distance from Earth. When observing an entire column of material is more convenient to use the expression in 1.1.15 where θ is the area of target under consideration and N its relative column density.

In the following, the channels producing neutrinos are ignored as the main methods of this research concern the observations of high-energy γ rays. For simplicity, it is common to assume that the projectile cosmic rays and the targeted interstellar material consist only of protons. In this case the differential cross section for $pp \rightarrow 2\gamma$ can be used. The latter has been measured in several accelerator

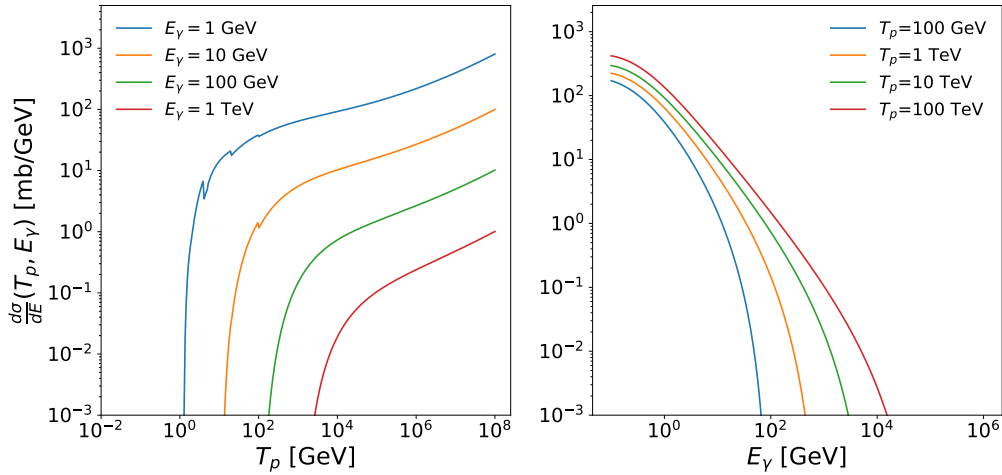


Fig. 1.3 The differential cross section of proton-proton interaction as derived by ref. [49] as a function of the proton kinetic energy with different fixed photon energies (left panel) and as a function of the photon energy with different fixed values for the proton energy (right panel).

experiments and its extension to higher energy has been recently parameterized by Kafexhiu et al. (2014) [49] up to energies of a few PeV by use of Monte Carlo simulations. The total proton-proton cross-section results of the order of 40 mb with a weak dependency on energy. The resulting gamma-ray spectrum is slightly harder than the proton one, with a difference in the spectral indexes of about 0.1. Approximately 10% of the proton kinetic energy is transferred to the photon, so for example a CR proton of energy of 10 GeV would produce gamma-ray photons of energy ~ 1 GeV, see Fig. 1.3.

The contribution of heavier nuclei both in the CRs and in the ISM however cannot be neglected. Even if these elements are sub-abundant, the numerous number of nucleons, which constitute them, significantly contribute to the interactions. The fraction of γ -ray flux contributed by metals, both in the projectile and in the target, is given by the so-called *nuclear enhancement factor*, ξ_N . The latter can be computed by knowing the relative abundances of each element in the interstellar medium and in the cosmic-ray population, together with their spectral shape. Mori (2009) [50] calculated ξ_N , after deriving with Monte Carlo simulations the factors m_{ip} and $m_{i\alpha}$, namely the ratio of cross sections and multiplicity (number of emitted γ photons

for interaction) of each element i , with respect to pp interactions, in the case when the target is H or He, respectively. Knowing these quantities, ξ_N is simply given by:

$$\xi_N = 1 + \sum_i m_{ip} \frac{J_i(E_i)}{J_p(E_p)} + \sum_i m_{i\alpha} \frac{J_i(E_i)}{J_p(E_p)} \frac{Y}{1-Y} \quad (1.1.16)$$

where Y is the abundance of He in the interstellar medium, that for solar abundance amounts to $Y=0.096$. Note that the spectrum of each element, $J_i(E_i)$ carries a dependence on energy and since the spectra of elements are not parallel (e.g. the spectrum of helium is harder) the nuclear enhancement factor depends, although slightly, on energy. The values found in ref. [50] ranges from 1.75 at a few GeV, to 2 at 1 TeV.

Once the parameters of interaction are fixed, the observed gamma-ray flux depends only on the CR flux, $J(E)$, and on the density of the target. It is straightforward then to derive $J(E)$, if the column density of the target is known. The derivation and the relative uncertainty that concerns the latter quantity are in depth discussed in sec. 1.2.

1.1.3 Cosmic-ray accelerators

Cosmic rays of energies up to 1 PeV, as discussed earlier, are confined within the Galactic disk. This means that their progenitors have to find themselves within the Milky Way. Detection of gamma-ray emission from discrete locations provides an indication of regions where powerful acceleration of particle occurs. High-energy radiation has been observed in correspondence of several supernova remnants both in the GeV and in the TeV energy range confirming the idea that these astrophysical objects are effective cosmic-ray accelerators. Other locations that provide a natural environment for particle acceleration are pulsars and their nebulae, binary systems like micro-quasars but also objects hosting young stellar activity e.g. star-forming regions or globular clusters. Nevertheless, both at GeV and at TeV energies a large fraction of sources is still of unknown nature, see the statistics in Fig. 1.4.

One caveat of γ -ray observations of the sources is that these cannot always tell if the accelerated particles are of hadronic or leptonic origin. Observations of consistent radio-synchrotron emission are often interpreted as an indication of a leptonic emission mechanism. A smoking-gun for hadronic interactions instead is the so-called *pion* bump, an accumulation of gamma-ray photons close to the

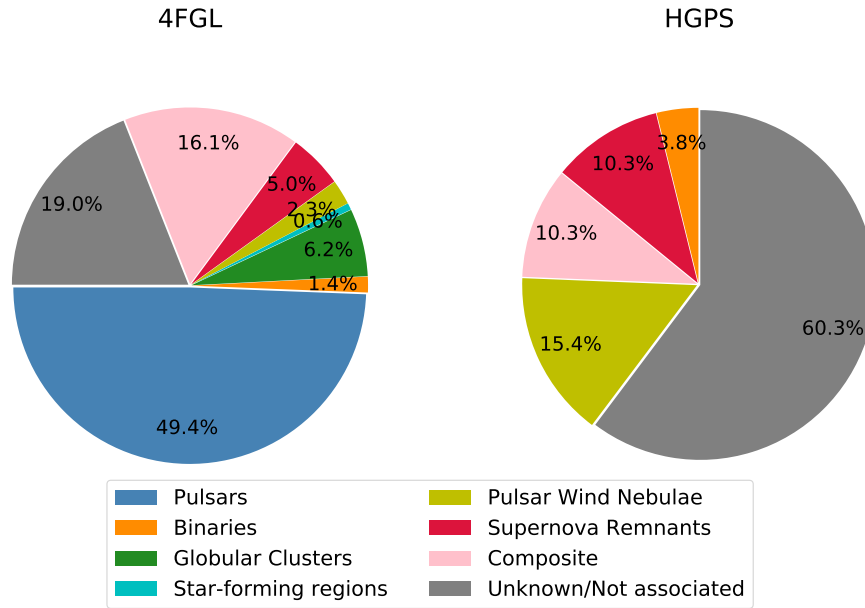


Fig. 1.4 Classes of galactic sources contained in the fourth Fermi-LAT (4FGL) catalog [51] and the H.E.S.S. galactic plane survey (HGPS) [52]

half-mass of pion $m_{\pi}/2 = 67.5$ MeV, as the process (Eq. 1.1.11) is symmetric around this energy (e.g.[53]). However, no instrument is currently sensitive to these low energies with the exception of Fermi-LAT that however suffer from large systematic uncertainties in this range. Therefore arguments based on the direct observation of this feature remain quite weak. A stronger smoking gun would be the detection of neutrinos in correspondence of the source, although the latter detection is much more difficult. Besides, also the detection of gamma rays of energy exceeding 100 TeV would be a strong indication of nuclei acceleration since the electrons are subject to severe losses at those high energies.

Supernova Remnants

Already in 1934, Baade and Zwicky [54] computed that Supernova explosions release a sufficient amount of energy to power the Galactic population of cosmic rays. Their calculation can be repeated straightforwardly. Assuming there is spatial homogeneity, namely the same cosmic-ray density everywhere, and no variation on the residence timescale in the disc, $\tau_{res} \sim 10^7$ yr, one can compute the power of

cosmic rays:

$$\mathcal{P}_{CR} = \frac{\mathcal{E}_{CR}}{t_{res}} = \frac{w_{CR} V_{disc}}{t_{res}} = \frac{1 \text{ eV/cm}^3 \cdot 1 \times 10^{67} \text{ cm}^3}{3 \times 10^{14} \text{ s}} \approx 10^{41} \text{ erg s}^{-1}. \quad (1.1.17)$$

This is easily provided in supernova explosions, which typically release $E_{SN} = 10^{51}$ erg. Accounting for the supernova explosion rate, R_{SN} (~ 3 per century), the power supplied by these objects amounts to:

$$\mathcal{P}_{SN} = E_{SN} \cdot R_{SN} = \frac{10^{51} \text{ erg}}{30 \text{ yr}} = 10^{42} \text{ erg s}^{-1} \quad (1.1.18)$$

therefore 10% of the energy released in supernova explosions is already sufficient to maintain the entire galactic CR density.

It later became clear that rather than the explosion itself, good conditions for particle acceleration are provided by the fast shocks that are generated in the hot plasma material in the remnant of the supernova explosions. A supernova remnant is in fact characterized by very hot ($\gtrsim 10^6$ K) and low-dense ($\sim 1 \text{ cm}^{-3}$) plasma, hence it provides perfect conditions for high-velocity ($\sim 0.1 c$) shock waves to propagate and exchange energy with charged particles. A supernova remnant undergoes different evolutionary stages: in a first phase, the *ejecta-dominated* phase, the expansion of the remnant proceeds almost freely, at a constant velocity, as the mass of the ejected material is much higher than the mass of the surrounding medium. As the expansion proceeds, the power of the blast wave decreases and the mass of the swept-up material increases until it equals the mass of the ejecta, giving start to the *Sedov-Taylor* phase, that typically lasts for 500-1000 yr. From that moment, the velocity of the shock starts decreasing and slowly the ejecta start to mix with the interstellar medium [55, 56].

The *diffusive shock acceleration* (DSA) [38] provides an efficient mechanism to exchange energy from the shock to charged particles. Cosmic rays are efficiently accelerated through a first order Fermi acceleration in the interaction with the shock wave. To gain a significant amount of energy, cosmic rays need to travel back and forth from the downstream to the upstream of the shock driven by the interactions between the magnetic field fluctuations in the plasma and the Alfvén waves generated by the cosmic ray themselves. In this *diffusive* motion the particles have the chance to cross the shock many times gradually increasing their energy. The maximum momentum is reached by particles in the ejecta-dominated phase,

after that as the velocity decreases also the amplitude of magnetic field fluctuations is reduced and cosmic rays do not scatter as efficiently. This implies that an upper limit to the maximum value of energy that can be reached with this mechanism exists. The latter depends on the characteristics of the plasma, namely the magnetic field B , the age of the remnant t and the shock velocity u but it in general is of the order of:

$$E_{max} \approx 10^2 \left(\frac{B}{1 \mu\text{G}} \right) \left(\frac{t}{10^3 \text{ yr}} \right) \left(\frac{u}{10^7 \text{ km/s}} \right)^2 \text{ TeV} \quad (1.1.19)$$

much below the energy of the knee, ~ 1 PeV, for typical parameters of supernova remnants. Observational data on supernova remnants confirm as well the existence of a cutoff in their spectrum (see Fig. 1.5), meaning that a different source class must be the responsible of PeV cosmic radiation. A more efficient acceleration could be obtained in the case of *magnetic field amplification*, where the cosmic rays themselves amplify the magnetic turbulence and consequently the gain in energy [57]. Evidences for this effect also come from the X-ray observations of hot-spots in SNR RX J1713.7-3946 [58]. In this case the predictions on the shape of the spectrum of accelerated particles change. The DSA theory in fact predicts a power-law shape $\propto E^{-q}$ for the spectrum of exiting particles with $q = 2$. When loosing the condition of cosmic rays as test particles, the spectrum becomes even harder, as the acceleration is more efficient. This however is in contrast with many observations of spectra of supernova remnants, which are as steep as $E^{-2.2} - E^{-2.4}$. The latter values are also necessary to explain the observed steep spectra of cosmic rays at Earth. Provided that the propagation modifies the spectra of a factor $\delta = 0.3 - 0.6$ a steeper than 2 injection spectrum is required to explained the data [59]. Thus, to explain all the observational features it remains to investigate whether another source class is involved or if different acceleration mechanism must be invoked.

If the acceleration power of supernova remnants slowly decreases as the shock slows down, other classes of accelerators, like pulsars and stellar clusters can become competitive as they keep accelerating particle with a continuous rate. A general distinction is made between sources according to the duration of the acceleration phase relative to their age, into *impulsive* and *continuous* sources. In the case of impulsive sources, the time in which particles are accelerated Δt is much shorter than the typical lifetime, T , of the source. Supernova remnants are usually treated

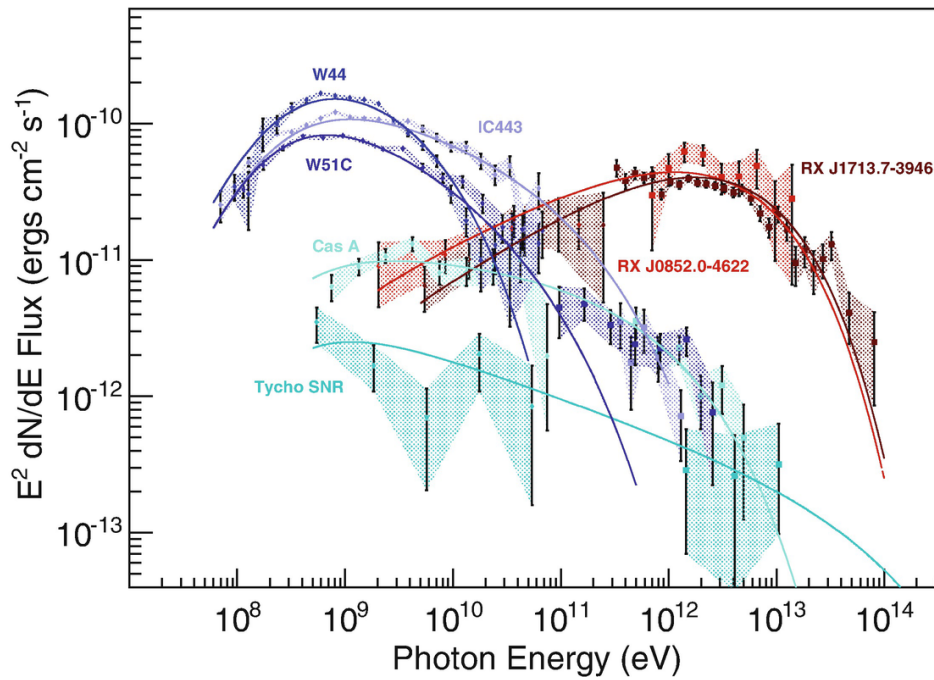


Fig. 1.5 Spectral energy distribution of several supernova remnants of the Galaxy. In particular the spectra of the youngest (< 1000 yr) SNRs (Tycho and Cas A) are plotted in cyan, slightly older (~ 2000) SNRs (RX J1713.7-3946 and RX J0852.0-4622) are plotted in red and middle-age (~ 10000 yr) remnants (W44, IC443 and W51C) are displayed in blue. The fluxes of the youngest ones reaches higher energy, however they all show a tendency to cut-off before 100 TeV. Figure is from ref. [60].

as impulsive sources, even though that is accurate only for long-lived, $\sim 10^3 - 10^4$ yr, remnants, as the acceleration phase lasts for thousands of years.

Other accelerators

The majority of the sources of GeV photons is composed of pulsars. These highly-magnetized fast-rotating neutron stars in fact have a magnetosphere able to accelerate particles, mostly leptons, along the field lines that emit then via curvature radiation. The typical power of pulsar extends up to 10 GeV, after that a cutoff in the spectrum is typically observed. Particles ejected from the pulsar form a relativistic wind that populates the surrounding region, forming a so-called Pulsar Wind nebula. The wind extends up to ~ 0.1 pc, until it encounters the residual shock from the supernova explosion that further accelerates particles up to TeV-PeV energies that then emit via synchrotron and inverse Compton radiation. A typical example of this source class is the Crab pulsar and its nebula which has been detected up to a few hundred TeV [61].

Other sources of cosmic rays, that could provide good conditions also for proton acceleration can be found in young stellar objects. In the collision region of winds of two co-rotating stars in a binary system, particles can be accelerated via diffusive shock acceleration [62–64]. Just recently, the hadronic origin of the emission has been proven for the η Carinae system [65]. On a larger scale, in the case of massive stellar clusters, the collection of multiple shocks can increase the power supply reaching also PeV energies [66], providing a valid alternative to supernova remnants.

The distribution of pulsars, supernova remnants, and HII regions, which trace young stellar activity, are shown in Fig. 1.6 as a function of the galacto-centric radius. It can be seen that potential accelerators can be found everywhere in the galaxy, but there is a higher concentration of sources in the inner galacto-centric regions, especially around 3–4 kpc.

Escape

Escape is another important effect to take into account when observing cosmic-ray accelerators is escape. Particles leave the region of acceleration in a timescale that depends on their energy, modifying the observed spectrum. Low-energy particles are expected to be confined for a longer time than more energetic ones, in agreement with the energy dependence of the diffusion coefficient. Thus, the highest energy

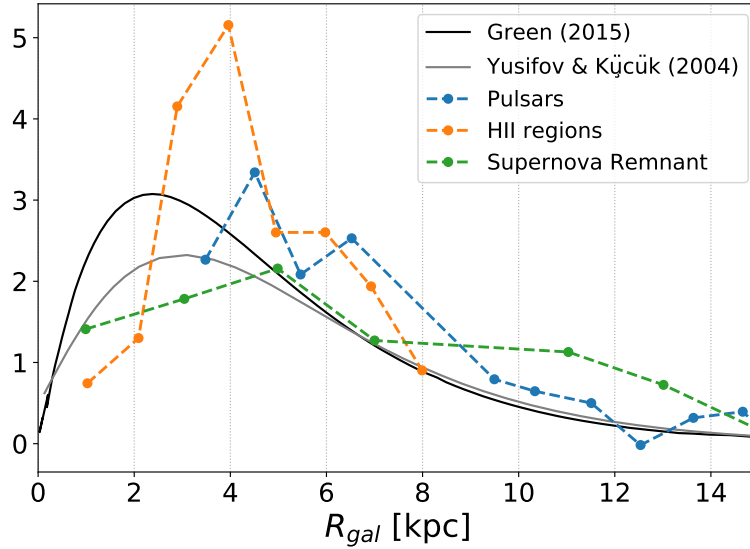


Fig. 1.6 Galacto-centric distribution of potential cosmic-ray accelerators (pulsars, supernova remnants and HII regions), from Stahler & Palla [67]. The distributions of pulsars from Yusifov & Küçük 2004 [68] and of supernova remnants from Green (2015) [69] are also plotted.

end of the spectrum might not be representative of the real acceleration capability of the source as the most energetic particles might have already left the source. For this reason, the observations of the surroundings of the accelerator are of great help. If a molecular cloud for example is located in the vicinity of an accelerator, it would be illuminated by the first escaping particles and therefore reflect the highest energy part of the distribution.

The energy distribution of the particles arriving at the cloud depends on many factors: the source injection spectrum, the type of acceleration (if impulsive or continuous), the energy losses of particles, and the diffusion properties in the interstellar medium. A unique prediction of the particle spectrum is therefore impossible. Some convenient assumptions however can be applied to Eq. 1.1.8 to have a general idea of the level of cosmic rays in the vicinity of an accelerator. A general solution of Eq. 1.1.8 is given by:

$$f(R, t, \gamma) = \frac{Q(\gamma_t)P(\gamma_t)}{\pi^{3/2}P(\gamma)R_{dif}^3} \exp\left(-\frac{R^2}{R_{dif}^2}\right) \quad (1.1.20)$$

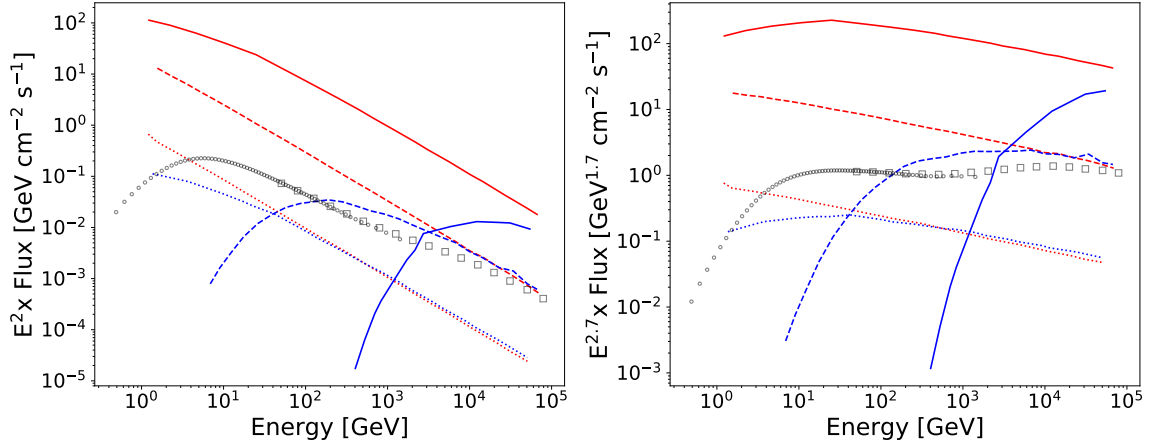


Fig. 1.7 Spectra of protons escaping from an impulsive accelerator, calculated at different distances $R=10$ pc (red), $R=100$ pc (blue) and for different times 10^3 yr (solid), 10^4 yr (dashed) 10^5 yr (dotted). The curves are from ref. [48]. For comparison the local spectrum of protons is plotted as grey points (as in Fig. 1.2).

and can be applied to the case of impulsive and continuous accelerators, as done in [48]. In the case of impulsive accelerator the injection spectrum assumes the form $Q(E, t) = Q_0 E^{-\Gamma} \delta(t)$ and, considering a diffusion coefficient of the form $D(E) \propto E^\delta$, and the main channel of energy loss due to nuclear interactions $P = E/\tau_{pp}$, Eq. 1.1.20 becomes:

$$f(E, R, t) \approx \frac{Q_0 E^{-\Gamma}}{\pi^{3/2} R_{dif}^3} \exp\left(-\frac{(\Gamma-1)t}{\tau_{pp}} - \frac{R^2}{R_{dif}^2}\right) \quad (1.1.21)$$

where

$$R_{dif} = 2\sqrt{D(E)t \frac{\exp(t\delta/\tau_{pp}) - 1}{t\delta/\tau_{pp}}} \approx 2\sqrt{D(E)t} \quad (1.1.22)$$

is the diffusion radius, namely the radial distance traveled by particle of energy E in a time t after their injection in the interstellar medium. The latter approximation is valid when $t \ll \tau_{pp}$. Particles of higher energies have larger diffusion coefficients and therefore travel further for the same time interval. The energy spectra obtained in the case of an impulsive accelerator that emit a total energy of $W_p = 10^{50}$ erg with a power-law injection spectrum of index $\Gamma = 2.2$ can be obtained from the general solution of Eq. 1.1.8 and are plotted in Fig. 1.7 for different time and distances [48].

In the case of continuous acceleration instead, the time dependence of the injection spectrum is a more general function: $Q(E, t) = Q_0 E^{-\Gamma} q(t)$. In this case, the particle distribution is given by:

$$f(E, R, t) = \frac{Q_0 E^{-\Gamma}}{4\pi D(E)R} \operatorname{erfc}\left(\frac{R}{R_{dif}(E, t)}\right) \quad (1.1.23)$$

As one can notice, the particle profile decreases as $1/R$, in case of a continuous source, meaning that a higher concentration of particles are expected in the vicinity of an accelerator. In case of a impulsive source instead, the particle density is constant at a given time within the diffusion radius (Eq. 1.1.22).

1.2 THE INTERSTELLAR MEDIUM

Space between stars in our Galaxy is filled by a diffuse medium, the Interstellar Medium (ISM), that accounts for 10–15 % of the total mass. The main part of the ISM consists of diffuse gas, in molecular, atomic, or ionized form, but a relevant fraction of dust ($\sim 1\%$) and a minor component in the form of plasma are also present. The most abundant element of the ISM is Hydrogen ($\sim 90\%$), followed by Helium ($\sim 9\%$) and by a small fraction of metals, usually embedded in dust grains. The matter of the ISM constitutes a natural target for cosmic rays during their diffusion through the Galaxy and therefore its understanding is directly connected to the understanding of the physics of cosmic rays. In the following, we describe the main components of the diffuse medium and their relevant properties, focusing on the primary detection methods and their uncertainties.

The gas component of the ISM coexists in different phases, depending on the balance between pressure and temperature. A distinction is made, as proposed by [70] between the *neutral medium*, distributed uniformly on large scales, and the *ionized medium*, that is distributed in-homogeneously and in smaller scales as it is heated up by Supernovae, Stellar Winds or OB young stars. The first is, in turn, divided into (e.g. [71]):

- Molecular Medium (MM), that is the densest and coolest phase, and hence provide ideal conditions for star formation;
- Cold Neutral Medium (CNM), which is the coolest part of the atomic medium, that typically populates and shields from radiation the outermost layers of Molecular Clouds and is detected primarily in absorption;
- Warm Neutral Medium (WNM), that is instead detected in emission and consists of the diffuse atomic gas component.

The ionized medium instead is usually divided into:

- Warm Ionized Medium (WIM), namely regions where the medium is ionized, generally due to shocks or recent star formation activity, and therefore emits via recombination lines (e.g. $H\alpha$);
- Hot Ionized Medium (HIM), the very hot phase of gas, ejected in SN explosions, that is characterized by thermal X-ray emission.

	MM	CNM	WNM	WIM	HIM
T [K]	10–20	50–100	6000–10000	~ 8000	$\geq 10^6$
n [cm^{-3}]	10^2 – 10^6	20–50	0.2–0.5	0.2–0.5	$< 10^{-2}$
h [pc]	70	100–300	300–400	900	> 1000
f_V	$< 1\%$	1–5%	10–20%	20–50%	50–70%
M [$10^9 M_\odot$]	1.2–2.5		≥ 6		≥ 1.6
Tracer	Radio/IR	21-cm absorption	21-cm emission	H α	X-rays

Table 1.1 Typical physical parameters that characterize the different phases of the interstellar medium. Values are taken from ref. [72]

Note that it is not a rigid distinction, as there is a continuous transition from the phases. The physical properties that characterize each of these phases are reported in Table 1.1. Going from MM to the HIM, the temperature increases and, at the same time, the medium expands lowering the density. Accordingly, the volume filling fraction increases. The high density of the MM and CNM medium makes them the main contributors to the total mass. Another thing to be noticed is that the scale height, h , changes for the different phases: while the molecular and cold neutral medium are concentrated in the galactic plane, the other phases expand further. It is clear, from the parameters in Table 1.1, that the neutral component, mostly constituted of H₂ and HI, is the most relevant in the galactic plane.

1.2.1 Molecular hydrogen

Molecules are in general detected via their rotational and vibrational transitions but molecular hydrogen, being composed of two identical atoms has no permanent dipole moment and consequently no related transition line. Other transition lines are either too weak (e.g. the rotational quadrupole emission) or require a much higher temperature than the average temperature of this medium to be excited (e.g. the para- and ortho-transitions, vibrational transitions). Mapping of this molecule must then rely on tracers, of which the most commonly used is the ¹²CO molecule and its isotopologues ¹³CO and ¹⁸CO. The link between CO and H₂ is due to the similar formation and destruction process the two molecules undergo inside dust grains, that protect them from UV-photodissociation. CO, although being 10^{-4} times less abundant than hydrogen, presents a high line intensity and its transitions are excited also in the cold medium. Excitation of CO is in fact caused by collision with H₂ and it occurs also at temperatures of 5–20 K, when the

density is high enough ($n_{crit} \gtrsim 10^3 \text{ cm}^{-3}$). The lowest and most commonly used level transition line, $^{12}\text{CO}(J=1 \rightarrow 0)$, falls in the millimeter waveband at 115 GHz (2.6 mm). The most comprehensive survey of this line was obtained by Dame, Hartmann and Thaddeus (DHT) [73] by combining the observations of two twin 1.2-m radio telescopes one located at the Harvard-Smithsonian Center for Astrophysics and the other in Cerro Tololo, in Chile. The survey covers the galactic plane at all longitudes with a sensitivity of 0.125° . Other surveys like NANTEN [74] reach a 2 times better resolution, but are limited to specific ranges of longitude. More recent surveys like the FOREST Unbiased Galactic plane Imaging survey with the Nobeyama 45-m telescope (FUGIN) [75], the Mopra telescope survey [76] and The Milky Way Imaging Scroll Painting (MWISP) [77], include also the contribution of ^{13}CO and ^{18}CO . The latter, being less abundant, produce generally optically thin emission, allowing for absorption correction in regions where ^{12}CO is optically thick. Besides, higher-level transition lines ($J=3 \rightarrow 2$) occur at higher densities (10^4 cm^{-3}) and hence trace the most compact regions of the MM. Surveys of this line include the CO High Resolution Survey (COHRS) [78] and the $^{13}\text{CO}/\text{C}^{18}\text{O}$ ($J=3-2$) Heterodyne Inner Milky Way Plane Survey (CHIMPS) [79]. The coverage (in galactic longitude) and the spatial resolution of these surveys are compared in figure 1.8 to the resolution of some γ -ray telescopes. It is clear that for Fermi-LAT data, the resolution of the DHT survey is more than sufficient, whereas next generation instruments like CTA will benefit from the higher resolution of the most recent surveys.

The obtained maps are 3-dimensional. The radial velocity of the gas, v_{LSR} , measured via Doppler spectroscopy methods, can be converted into a galactocentric distance, R_{gal} , provided that the motion of the gas is dominated by the rotation of the Galaxy, and that the Milky Way rotation curve, $V(R)$, is determined accurately:

$$v_{LSR} = R_{\odot} \left(\frac{V(R)}{R} - \frac{V_{\odot}}{R_{\odot}} \right) \sin(l) \cos(b), \quad (1.2.1)$$

here R_{\odot} and V_{\odot} are the radius and the rotation velocity of the Sun. For this reason, v_{LSR} is a measure of the distance along the line of sight and therefore to calculate the column density one performs an integration over v_{LSR} .

The $^{12}\text{CO}(J=1 \rightarrow 0)$ line (hereafter CO-line) is in general optically thick, however a correspondence between the velocity dispersion of the emission and the mass is guaranteed by the virial theorem (see e.g. [80]). Therefore, the column density of H_2 , with an opportune calibration, can be related to the brightness temperature of

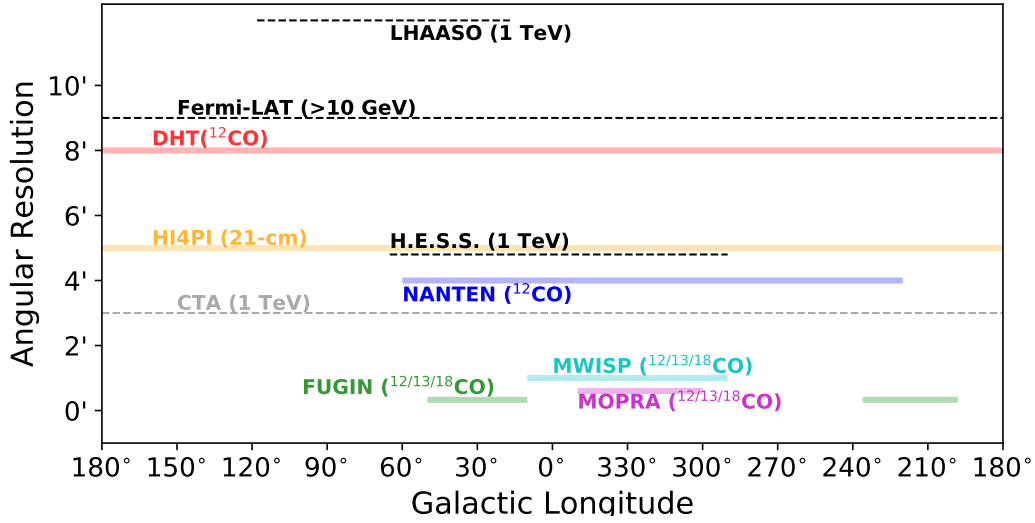


Fig. 1.8 Angular resolution of the main surveys of the molecular medium and their coverage of the galactic plane. The features of the HI4PI survey of galactic H α are also shown. For comparison, the resolution and coverage of several gamma-ray instruments are also plotted.

CO. That is an equivalent measure of brightness as it is defined as the temperature that characterizes a black body of a given brightness, according to Planck's law ($I_\nu = 2hc^{-2}\nu^3(e^{\frac{h\nu}{kT_b}} - 1)^{-1}$). The column density can then be calculated as:

$$N_{H_2}(l, b) = X_{CO} \int T_b(\nu, l, b) d\nu. \quad (1.2.2)$$

Here X_{CO} represents the conversion factor between the integrated brightness of CO and the column density of the H $_2$ molecule and amounts, on average, to $X_{CO} = 2 \times 10^{20} \text{ cm}^{-2} \text{ K}^{-1} \text{ km}^{-1} \text{ s}$ [80], with an uncertainty of 30%. Whether this factor can be applied uniformly in the Milky Way is still uncertain. In fact, while this factor may vary from site to site due to local conditions (e.g. composition, dissociation rate, density etc.), on the large scale several studies based on virial techniques [81], observations of other isotopologues [82], or extinction [83] agree with the value given above (see Table 1 in [80]), at least for the $1 \text{ kpc} < R_{gal} < 9 \text{ kpc}$ region. In the innermost part of the Galaxy ($\lesssim 500 \text{ pc}$) several pieces of evidence show a lowering of 3–10 times. Conversely, in the outer Galaxy, as a consequence of the decrease of metallicity the CO-to-H $_2$ factor is expected to increase. Furthermore CO fails to trace H $_2$ in certain regions, for example where there exists hydrogen in

molecular form, while carbon is not in CO molecules but rather atomic or ionized (C^+). Also, as the transition is excited by collisions, in regions where the gas density is too low, a significant excitation of CO is not granted. At the same time, a too high density can lead to saturation of the emission. What is not traced by CO or H α is generally known as *dark* gas and can be unveiled in dust extinction maps, as discussed later.

1.2.2 Molecular Clouds in the Milky Way

From the CO survey of Dame Hartmann and Thaddeus [73], several Molecular Clouds (MCs) catalogs have been produced, e.g. Nakanishi & Sofue (2006) [84], Pohl et al. (2008) [85], Rice et al. (2016) [86] and Miville Deschênes et al. (2016) [87]. Clouds are identified as peaks in the $l - b - v$ plane with different techniques. Of particular interest are the techniques employed by the two most recent catalogs, which have been used for the analyses described later: Rice et al. (2016) used a dendrogram technique that consists in finding coherent pixels in the CO map; Miville-Deschênes et al. (2016) used a Gaussian decomposition technique, that looks for Gaussian-like structures in the l - b - v space and clusters them together, if considered coherent. The firsts decomposed almost 40% of the surveyed CO data, while the seconds managed to include the 98%, and it is so far the most comprehensive catalog of MCs of the Milky Way. Clouds are then identified as bright clumps around a central location (l, b, v) . The center is determined by a weighted average of the CO integrated intensity, $W_{CO} = \int dv T_B(v)$ over the pixels:

$$l = \frac{\sum_i W_{CO}^i l_i}{W_{CO}^{tot}} \quad (1.2.3)$$

$$b = \frac{\sum_i W_{CO}^i b_i}{W_{CO}^{tot}} \quad (1.2.4)$$

and the radial extension is obtained in a similar way:

$$\sigma_l = \frac{\sum_i W_{CO}^i (l_i - l)}{W_{CO}^{tot}} \quad (1.2.5)$$

$$\sigma_b = \frac{\sum_i W_{CO}^i (b_i - b)}{W_{CO}^{tot}} \quad (1.2.6)$$

and from these the extension can be defined as $\theta = \sqrt{(\sigma_l \sigma_b)/\pi}$. The center in velocity and the relative dispersion function is determined as a emission-weighted average:

$$\langle v \rangle = \frac{\sum_i T_{B,i} v}{\sum_i T_{B,i}} \quad (1.2.7)$$

$$\sigma_v = \frac{\sum_i T_i (v_i - \langle v_i \rangle)^2}{\sum_i T_i} \quad (1.2.8)$$

where $T_B(v)$ is the cloud emission spectrum along the line of sight and result from the superposition of multiple gaussian peaks.

After having located the cloud position (l, b, v) , the distance, R , from the galactic center can be obtained by inverting equation 1.2.1:

$$R = R_\odot V(R) \sin(l) \cos(b) \frac{1}{V_\odot + \frac{v}{\sin(l) \cos(b)}} \quad (1.2.9)$$

However, besides the uncertainties related to the rotation curve, $V(R)$, in the inner Galaxy, this method suffers of an ambiguity, the so-called kinematic distance ambiguity (KDA), because two solutions exist, where $R < R_\odot$:

$$d = R_\odot \cos(l) \pm \sqrt{R^2 - R_\odot^2 \sin^2(l)} \quad (1.2.10)$$

The ambiguity can be resolved in the case of clouds by associating them with objects of known parallax (e.g HII regions or masers [88]), by evaluating the 21-cm line absorption against the clouds [89], or invoking physical relations as the dispersion-linear size $(\sigma_v - R_s)$ relation [81], a consequence of the virial theorem. In this case, the distance is chosen so that R_s better matches the $\sigma_v - R_s$ relation. Often, also the height on the galactic plane is used to discriminate between near and far distance: in fact if the result for the distance would locate a cloud too high in the plane ($|z| > 200$ pc), the other distance is selected, to conceal with the typical scale height of the molecular medium ($h_{MM} \sim 70$ pc; Table 1.1).

The mass of a molecular clouds is derived from the column density, once the distance is known:

$$M = m_p \sum_i N_{col,i}^H \Delta l \Delta b d^2 = m_p X_t W_t \Delta l \Delta b d^2 \quad (1.2.11)$$

It is useful to define a parameter $A = M_5/d_{kpc}^2$, where $M_5 = M/10^5 M_\odot$ and $d_{kpc} = d/1$ kpc to characterize the flux of a molecular cloud, see Equation 1.1.14. This parameter quantifies the portion of column density that is embedded in a molecular cloud (Equation 1.2.11). In the ratio A , the distance, d cancels out. As a consequence, this parameter is independent both of the uncertainty of the mass, and of the uncertainty on the distance, and therefore is not even subject to the KDA. The only uncertainty is determined by the gas tracer. In the case where CO is considered as tracer, the uncertainty is of the order of 30% [80], in case of dust it reduced to $\sim 20\%$.

The distribution of the main parameters: A , mass, angular size and velocity dispersion of the clouds catalogued in ref. [87], are plotted in Fig. 1.9, The total mass included in clouds amounts to $1.6 \times 10^9 M_\odot$. The mass distribution is dominated by small objects, with the peak that falls below $10^5 M_\odot$, for the outer Galaxy and below $10^6 M_\odot$ in the inner Galaxy, where the most massive objects are. Here the mass reaches also $10^7 M_\odot$ in a few cases. This is reflected in the A parameter that in some cases overcomes 1, in the inner Galaxy, although most of the objects have a relatively small A -factor $A < 0.2$. The smallest angular size of MCs coincides with the survey's angular resolution, 0.125° . The sizes of molecular clouds, approximated as circles, span from that threshold up to more than one degree for clouds close to the Earth, but the majority of clouds have a radius lower than 0.5° , that, for an average distance of 3 kpc corresponds to a physical radius of 80 pc. Naturally, the biggest clouds, in terms of angular size, are found in the outer Galaxy, as they are closer. A dichotomy is observed also in the velocity dispersion that tends to be higher in the inner Galaxy, probably as a combined effect of the presence of bigger clouds in the inner galaxy, especially around 4 kpc and of a selection bias in the detection.

1.2.3 Neutral atomic hydrogen

The neutral atomic hydrogen, HI, in typical conditions of the ISM, is hardly found to have excited electrons and its main transitions are uniquely observed in absorption towards UV-luminous stars [90]. Unfortunately, UV observations are limited by dust absorption and hence cannot trace the entire Milky Way. On the other hand, the spin-flip transition between the 2 hyperfine states, parallel to anti-parallel, although it has a rate of $2.5 \times 10^{-15} \text{ s}^{-1}$, is widely detected, thanks to the huge abundance of H in the Galaxy, and serves as the main tracer of atomic hydrogen. This line falls at $\lambda = 21.106 \text{ cm}$, that corresponds to $\nu = 1420 \text{ MHz}$, both in emission (CNM

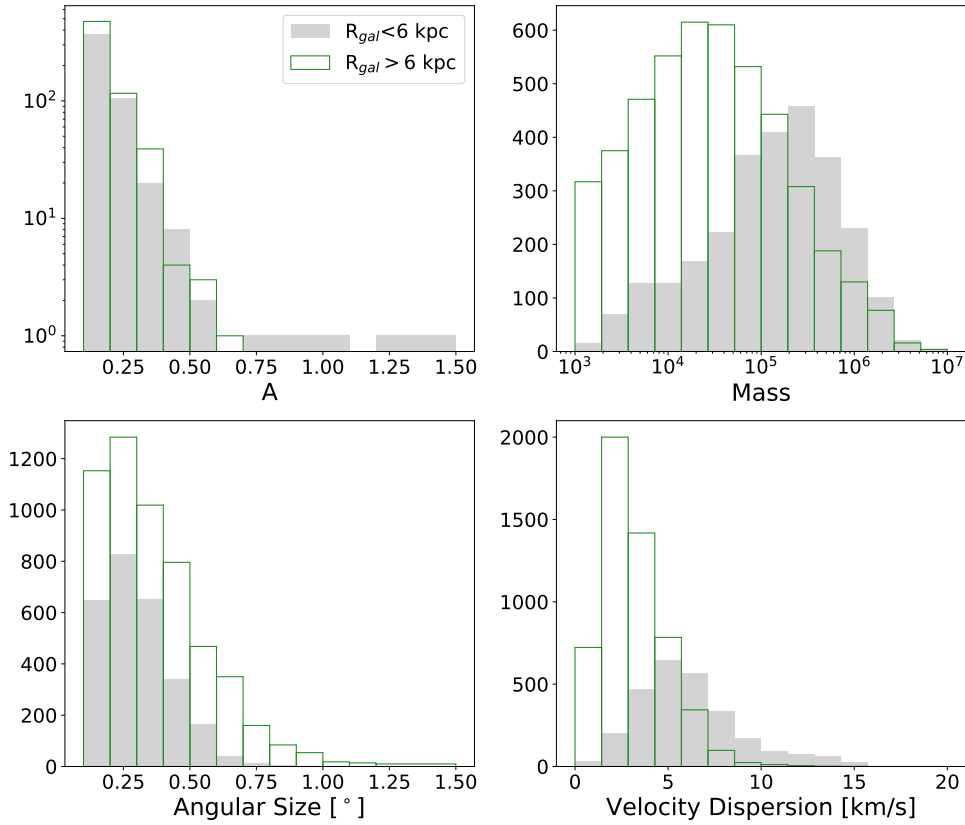


Fig. 1.9 Main physical properties of the clouds reported in [87]. From top left to bottom right: the A parameter, defined as the ratio between $M_5 \equiv M/10^5 M_{\odot}$ and $d_{kpc}^2 \equiv (d/1 \text{ kpc})^2$, which characterizes the γ -ray flux of a molecular cloud, the mass, the angular size and the velocity dispersion. In the plot, the clouds are divided into inner-galaxy clouds ($R_{gal} < 6$ kpc; grey bars) and outer-galaxy clouds ($R_{gal} > 6$ kpc; green-contoured bars).

and WNM) and in absorption (CNM). Observations of the 21-cm line have been carried out successfully by different observatories: the Parkes 64-m Radio Telescope (in Australia) produced the Galactic All-Sky Survey (GASS) [91], the Effelsberg 100-m telescope (in Germany) yielded to the Effelsberg-Bonn HI Survey (EBHIS) [92], later merged in the all-sky HI4PI survey [93] that achieves a resolution of 5 arcmin. Combined with the information on the radial velocity, these maps show that HI is distributed in the entire Galaxy up to a distance of ~ 30 kpc from the Galactic center, making this component fundamental to trace the outermost layers of the Galactic disk, where the molecular medium fades. Observations of the 21-cm line emission provide an all-sky map of HI brightness temperature, T_B , as a function of the radial velocity, v . This, equivalently to what was found for molecular hydrogen (see Eq. 1.2.2), is a proxy of the column density, which is then calculated as:

$$N_{col}(l, b) = X_{HI} \int T_b(v, l, b) dv \quad (1.2.12)$$

where $X_{HI} = 1.8 \times 10^{18} \text{cm}^{-2} \text{K}^{-1} \text{km}^{-1} \text{s}$ [94]. However, this equation holds as long as the emission can be considered optically thin. It can happen that along some lines of sights, some CNM interposes, absorbing part of the radiation. At the same time the emission of CNM could also be self-absorbed. In this way, the column density resulting from equation 1.2.12, would be an underestimation of the true density. Moreover, the continuum radio emission, raising from diffuse radio-synchrotron (with brightness temperature T_C) acts as background signal and it should be quantified correctly. In other words, the observed brightness temperature is not a good approximation of the line excitation temperature (or spin temperature), T_S , but rather $T_B = (T_S - T_C)(1 - \exp(-\tau))$, where τ is the optical thickness of the medium. The corrected expression for the column density results, by inverting the expression for T_B :

$$N_{HI} = X_{HI} \int \tau T_S dv = -X_{HI} T_S \int \ln\left(1 - \frac{T_B}{T_S - T_C}\right) dv \quad (1.2.13)$$

The spin temperature, T_S , can be determined using the *on-off* method, that compares the spectrum in emission of a gas cloud (off-emission), with the one in absorption against a bright continuum source (on-emission) [95–97]. However this method is limited to small specific regions and for the entire galaxy one has to rely on an average value.

1.2.4 *Interstellar dust*

Dust, being well mixed with the gas component, serves as an alternative tracer of the neutral medium. Dust is composed of grains of silicates (Mg/Fe-rich) or graphites (C) of different sizes up to a few micrometers. These grains absorb the radiation of hot stars and re-emit in the far-infrared waveband, hence offering two observational channels for this medium: extinction and thermal emission (e.g. [98]). The correlation of dust with CO and HI emerged from observations at 100 μm with the Diffuse Infrared Background Experiment (DIRBE onboard of COBE satellite [99]) and the Infrared Astronomy Satellite (IRAS [100]) and was later confirmed with the Planck mission also for dust opacity at different wavelength [101]. The relation between dust opacity, τ_D , and H column density is given by:

$$N_H = N_{HI} + 2X_{CO}W_{CO} = \left(\frac{\tau}{N_H}_{ref} \right)^{-1} \tau_D \quad (1.2.14)$$

where the conversion factor comes from the linear interpolation of the dust/gas relation and depends on the observed frequency, and for example it amounts to $8.5 \times 10^{25} \pm 20\%$ at 353 GHz [101]. Although in general dust appears proportional to the gas, significant variations from linearity appears, especially in the intermediate density range ($8 \times 10^{20} < N_H < 5 \times 10^{21}$). The latter has been interpreted as due to the contribution of dark gas. Validations of this hypothesis come from gamma-ray observations, that asses a similar level of enhancement over the expected gamma-ray emissivity from the gas component. However, this is valid only provided to know the density of the CRs at the interaction site, which is unknown a priori. Other arguments to explain the detected deviations of the dust/gas ratio are considered unlikely [101].

Taken into account that, dust is considered the most reliable tracer for the large-scale diffuse gas. However, missing the information on the radial velocity, it can only provide a bi-dimensional picture of the Galaxy and when a kinetic separation of the medium is needed, one needs to rely on the HI and CO data. Interestingly, the GAIA collaboration, exploiting the great precision on star parallax determination, has recently started a 3-dimensional mapping of the interstellar dust. They are able to constraint the location of dust by evaluating the extinction effects on stars at different distances [102]. This method is very promising, as it is able to distinguish structures as small as ~ 25 pc, [103]. Dust 3D maps obtained with Gaia, which is an optical instrument, are limited in depth and for now only the region within 3

kpc from the Sun has been mapped [103]. Complementary samplings have been obtained from infrared measurements, e.g. with APOGEE and managed to reach ~ 7 kpc, although with a lower resolution [104].

1.3 DIFFUSE GAMMA-RAY EMISSION

The first conjecture about the gamma-ray emissivity of the interstellar medium traces back to 1952, when Hayakawa [105] firstly noticed that cosmic rays confined in our Galaxy have sufficient time to interact and produce secondary radiation. Having a good understanding on the diffuse gamma-ray emission is fundamental not only as it constitutes the background in all sources analyses, and having it firmly constrained is necessary to have a good understanding of the observations, but also as it can provide itself unique information on the primary particles that produce the flux. The interstellar medium in fact, targeted by the galactic population of cosmic rays, produces high-energy radiation via the main gamma-ray mechanism: inverse Compton, bremsstrahlung, and pion decay.

From the pioneering experiments of SAS-2 [106], COS-B [107, 108], and EGRET [109] to the recent investigations with Fermi-LAT [110, 111] it appears a striking spatial correlation between the large-scale gamma-ray emission and the gas radio and infrared maps (see Fig. 1.10). The raising technologies, together with the improvements on the theoretical modeling allows us now to have a deep understanding of the single components and their relative contribution [112]. Nevertheless, uncertainties related to the density of the interstellar medium, to the interstellar magnetic fields and the propagation models of cosmic rays leave space for further investigations. In the following, the main emission process and their relative contribution at 1 GeV are described, then the state of art of the results of analyses of the diffuse γ -ray emission is presented and commented.

1.3.1 *Main radiation mechanism of the Interstellar Medium*

The main channels of production of diffuse gamma-ray emission above 1 GeV are the inverse Compton scattering, which happens when an energetic electron exchange energy with a photon (typically of lower energy), increasing its energy up to the γ -ray regime; Bremsstrahlung, the braking radiation produced by charged particles when deflected by the electric field of other charged particles, normally ions; the emission of pion decay, which happens as a consequence of nuclear collisions, mainly proton-proton that produce unstable mesons that quickly decay (see Eq. 1.1.11). Other non-thermal processes as synchrotron and annihilation of pairs are negligible

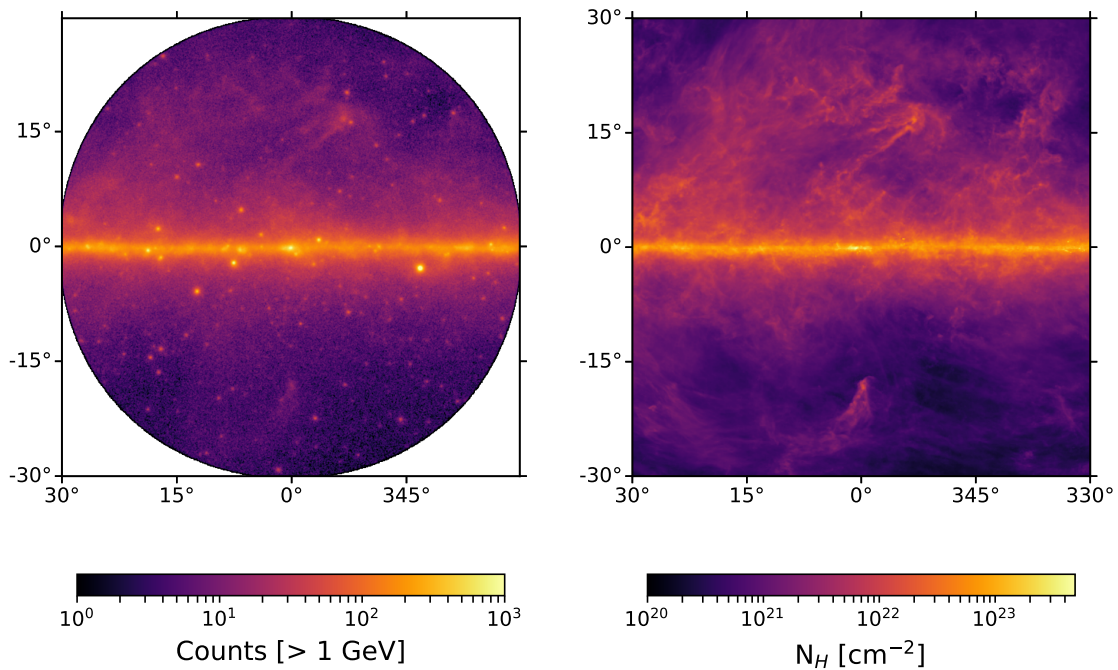


Fig. 1.10 Fermi-LAT counts map (left panel) collected above 1 GeV and the Planck 353 GHz dust opacity map (right panel) for the central 30° of the Milky Way ($|l| < 30^\circ$, $|b| < 30^\circ$). In both maps not only the galactic plane is well distinguishable, but also the regions of the molecular clouds ρ -Ophiuchi [$(l, b) = (353.7, 17.7)^\circ$] and RCrA [$(l, b) = (359.9, -17.8)^\circ$] are well visible. Fermi-LAT data have been retrieved from [113], Planck data from [114].

in comparison to the other emission mechanism at the considered energies (60 MeV–100 GeV).

The diffuse inverse Compton radiation originates when high-energy electrons scatter on the galactic radiation fields, primarily the 2.7 K-cosmic microwave background (CMB), that has a constant energy density of 0.25 eV/cm^3 , the starlight radiation that peaks in the near-infrared (NIR) at $1 \mu\text{m}$ and the thermal emission of dust grains around $100 \mu\text{m}$ in the far-infrared regime (FIR). To model this emission, a good knowledge of the distribution of the interstellar radiation fields (IRFs), which may vary significantly in different regions of the Galaxy, is needed but that is difficult to reconstruct, net of absorption. Stars and dust energy density can vary up to several orders of magnitudes from the center to the periphery of the Milky Way and along the direction perpendicular to the Galactic Disk (see the recent calculations of [115]). Furthermore, local variations, as for example due to star formation, are hard to predict and cannot be accounted in large-scale profiles. Besides, also the galactic electron spectrum is unknown. The spectrum measured at Earth (as in Eq. 1.1.4) can't be assumed to be representative of the whole Galaxy. Indeed, due to severe energy losses, high-energy electrons can't propagate further than a few hundred parsecs, so we expect different spectra from site to site. Moreover, the cosmic-ray electron spectrum below a few GeV is severely affected by solar modulation. Constraints on electrons far from Earth can be obtained in the energy range 100 MeV–1 GeV, from the radio synchrotron emission [116, 117]. This exploits the fact that the electron energy distribution in this range is parallel to the injection spectrum. Below 100 MeV, instead, the spectrum is deformed by ionization losses and above 1 GeV by synchrotron and inverse Compton losses. Recent investigations of this type, suggest a spectral index of $\Gamma_e = 2.1\text{--}2.2$, below a few GeV [118] and it get steeper, reasonably to $\Gamma_e \sim 3$ at higher energies. Knowing the spectral index, the inverse Compton flux can be calculated for each component i of the radiation field (CMB, NIR, FIR), if also the electron and photons energy density, w_e and w_i , are known:

$$F_{IC}^i \simeq 10^{-9} \frac{w_e}{0.1 \text{ eV/cm}^3} \frac{w_i}{1 \text{ eV/cm}^3} \frac{l_d}{10 \text{ kpc}} \left(\frac{\epsilon_0}{1 \text{ eV}} \right)^{\frac{\Gamma_e-3}{2}} \left(\frac{E}{1 \text{ GeV}} \right)^{\frac{3-\Gamma_e}{2}} \frac{\text{erg}}{\text{cm}^2 \text{ s sr}} \quad (1.3.1)$$

here ϵ_0 is the energy of photons, and is related to the energy of the out-coming gamma-ray photon, E as: $\epsilon_0 = (3/4)(E_e/m_e c^2)^{-2}/E$. The total flux in the galactic medium, provided by the sum of the different radiation components amounts on average to $10^{-8} \text{ erg cm}^{-2} \text{ s}^{-1} \text{ sr}^{-1}$ at 1 GeV. The peak of IC radiation is found around

100 GeV, and then decreases modulated by the cooling of HE electrons and by the steepening due to the onset of the Klein Nishina regime, where the cross section of IC rapidly decreases with energy.

Electrons interact as well with the interstellar gas, giving birth to bremsstrahlung radiation. In order to model this emission one needs to know the composition of the interstellar medium and the corresponding densities. Bremsstrahlung diffuse flux, computed for typical values of the ISM, following [112] results:

$$F_{brems} \simeq 10^{-8} \frac{w_e}{0.1 \text{ eV/cm}^3} \frac{N_H}{10^{22} \text{ cm}^{-2}} \left(\frac{E}{1 \text{ GeV}} \right)^{2-\Gamma_e} \frac{\text{erg}}{\text{cm}^2 \text{ s sr}} \quad (1.3.2)$$

This is comparable to the flux due to IC at 1 GeV. However at these energies, the bremsstrahlung spectrum has already started its fall-off. The shape of the emitted photon spectrum, in the case of bremsstrahlung follows the shape of electrons but with $E \sim E_e/2$. As a consequence, the steepening occurs at a lower energy in the case of photons, namely around few hundred MeV. At energies higher than 1 GeV the contribution of bremsstrahlung is always subdominant with respect to the other components, unless the hydrogen density is very high. Nevertheless, given the same N_H , the emission originating from the decay of neutral pion overcomes the bremsstrahlung in the GeV-TeV range.

The main channel considered in this work is the production of gamma-rays from the decay of neutral pions (Eq. 1.1.11), produced in the interaction between CRs and the matter in the ISM, as it serves as tracer for galactic CR protons. The flux in this case depends on the energy distribution of cosmic-ray protons, on the hydrogen column density and on the fraction of heavy nuclei. Assuming average values for column density and nuclear enhancement, it results:

$$F_{pion} \simeq 10^{-7} \frac{w_p}{1 \text{ eV/cm}^3} \frac{N_H}{10^{22} \text{ cm}^{-2}} \left(\frac{E}{1 \text{ GeV}} \right)^{2-\Gamma_p} \frac{\text{erg}}{\text{cm}^2 \text{ s sr}} \quad (1.3.3)$$

making the pion decay the dominant component at 1 GeV. A caveat that concerns this radiation component, is the penetration of CR protons in dense regions of the diffuse medium. This matter has been addressed, by considering the effects produced by the magnetic fields [119] and modification of the diffusion coefficient [120]. Both concluded that CRs of energy $E > 100$ MeV can freely penetrate the diffuse medium, in standard conditions. That is safely above the energy threshold for formation of pions that is ~ 300 MeV/nucleon. The characteristic cooling time

of pion-decay is estimated to be

$$\tau_{PP} = (n_p \sigma f c)^{-1} \approx 5 \times 10^7 \left(\frac{n}{1 \text{ cm}^{-3}} \right)^{-1} \text{ yr} \quad (1.3.4)$$

, assuming that per interaction the proton loses a fraction $f = 0.5$ of its energy. That can be compared to the average cooling time of bremsstrahlung $\tau_{brems} \approx 4 \times 10^7 (n/1 \text{ cm}^{-3})^{-1} \text{ yr}$ and of inverse Compton $\tau_{IC} \approx 3 \times 10^8 (w_i/eV/\text{cm}^3)(E/1 \text{ GeV})^{-1} \text{ yr}$ [31]. In regions with a high proton density, the pion-decay is expected to be the most efficient over bremsstrahlung although the ratio can change near regions rich in electrons. The same applies to inverse Compton, although in this case the cooling time depends on energy and the efficiency is much larger at higher energies.

The relative contribution of each component is displayed in Fig. 1.11 and it has been adjusted to fit the average spectrum measured on the Galactic disk between $|b| < 5^\circ$ by Fermi-LAT.

1.3.2 Observations of the gamma-ray diffuse component

If at energies $\geq 1 \text{ GeV}$ the contribution of pion-decay radiation is expected to dominate the γ -ray diffuse emission, observations of emission at that energy provide direct information on the galactic population of CR protons, since $F_{pion} \propto N_H \cdot J_{CR}$ (Eq. 1.1.15). Hence, knowing the density of the gas and measuring the gamma-ray flux, the energy distribution of cosmic rays can be easily derived.

The Earth atmosphere prevents high-energy ($\lambda \lesssim 100 \text{ nm}$) photons from reaching Earth as they collide with the atoms in the high layers of the atmosphere, producing cascades of secondary particles, the so-called *extensive air showers*. Ground-base observatories are aimed at detecting the products of these showers. Only photons of sufficient energy $\gtrsim 50 - 100 \text{ GeV}$ produce a long enough shower to be detected at Earth. Observations of MeV-GeV photons can be carried out only in the outer space, by means of satellites. The main technique used in this case is the pair-conversion: the incoming γ -ray photon enters the instruments and, traversing different layers of material, has the chance to decay into an electron-positron couple that is then revealed by a scintillator. Several instruments exploited this technique, from past experiments like the COS-B and the Energetic Gamma Ray Experiment Telescope (EGRET) to the ongoing AGILE and Fermi-LAT. The latter has the largest effective area (1 m^2) and is the best available instrument, in the GeV-energy range (60 MeV–

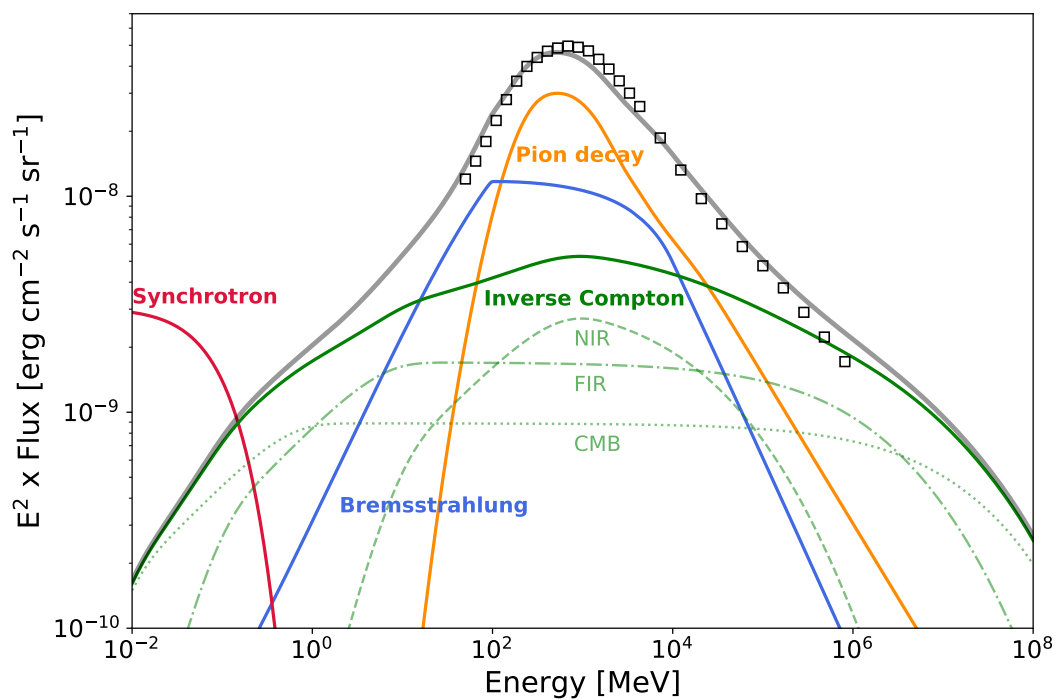


Fig. 1.11 Model of the gamma-ray energy spectrum of the Galactic Disk between latitudes -5° and 5° as measured by Fermi-LAT [110]. The relative contribution of the main radiation mechanism, namely synchrotron, inverse Compton, bremsstrahlung and pion decay are shown. They have been calculated with the *naima* python package [121] and have been adjusted to interpolate the gamma-ray data points.

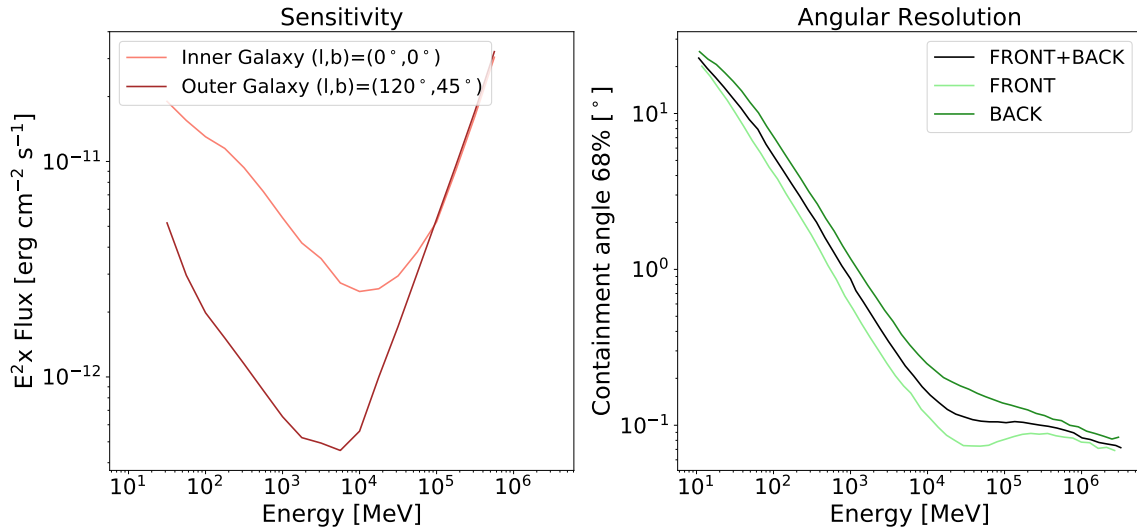


Fig. 1.12 Sensitivity and angular resolution of the Fermi-LAT. The values have been taken from the Fermi-LAT performance's web page [122]. The two sensitivity curves refer to the outer (dark red) and inner (light red) Galaxy. The angular resolution curves refer to photon converted at the front (light green) or at the back (dark green) of the instrument, while the average resolution when using photons converted both in the front and in the back of the detector is plotted in black.

300 GeV), both in terms of sensitivity (10^{-11} erg s $^{-1}$ cm $^{-2}$ at 1 GeV) and in terms of angular resolution (0.5° , at 10 GeV), see Fig. 1.12. More details on the functioning of the instrument can be found in Chapter 4. The use of satellites moreover, allows a full-sky coverage making an instrument like the Fermi-LAT the ideal detector of the diffuse pion-decay emission.

Study of the diffuse γ -ray emission have been carried out also in other energy bands. The INTErnational Gamma-Ray Astrophysics Laboratory (INTEGRAL) has studied the contribution between few keV and few MeV and managed to model the lowest energy part of the diffuse emission, despite the difficulties arising from the superposition of many different processes [123]. At the opposite extreme, at very high energy ($\gtrsim 1$ TeV) the contribution of the diffuse emission is fainter and fainter, and the galactic plane is totally dominated by sources, but it can be significant especially in the central galactic regions. The diffuse emission have been studied for example by H.E.S.S. [124] MILAGRO [125], and HAWC [126, 127], reporting a higher flux towards the inner galactocentric region, that can be at least partly accounted by a collection of unresolved sources, namely the source that have a flux lower than the sensitivity of the instruments.

On the radial profile of the Galactic diffuse emission as seen by Fermi-LAT

Several studies have analyzed these component of radiation by extracting the gamma-ray emissivity in several rings centered at the galactic center and delimited by different galactocentric distances. To do so, one has to create a template model for emission for each ring of gas, hence one needs to perform a kinematic separation of the interstellar medium. This can be done by assigning a distance to the gas via the kinematic distance method, using Eq. 1.2.1 [128]. Note that because of the dependency of this relation on $\sin(l)$ the separation becomes harder in the inner galaxy. Moreover in the innermost part of the Galaxy ($R \lesssim 3$ kpc) the rotation velocity is not well constrained [88].

First investigations of this kind were conducted by COS-B [129] and EGRET [109] that reported a shallow increase, of a factor $\sim 50\%$, of the gamma-ray emissivity towards inner Galactic radii, with a maximum somewhere around 4 kpc. More recent analyses with Fermi-LAT confirmed this tendency. The Fermi-LAT collaboration [111] and the independent analysis of Yang et al. (2016) [130] and Pothast et al. (2018) [131] observed an increase of the γ -ray emissivity with a peak of a factor ~ 4 , between 1.5 and 4.5 kpc in the first case and between 4 and 6 kpc in the second. The difference rises almost certainly from the different separation of the rings. On the other hand the emissivity gradient reported in [131] is much smoother, more similar to EGRET data. This is due to the assumptions made on the X_{CO} conversion factor as briefly discussed later. Besides, the authors measure a similar behavior also for the spectral index, that changes from 2.8 at the local (8–10 kpc) ring to 2.5 at a distance of ~ 4 kpc from the center, and drops again abruptly in the innermost part of the Galaxy, where it becomes close to 3.

As a first approximation one expects that the observed gradient in γ -rays matches the galactic distribution of CR sources. In a region with high density of accelerators, in fact, freshly injected particles may accumulate, giving birth to a higher emissivity and a harder spectrum, since the propagation has not spread the particles and softened the spectrum yet. However Strong et al. [117] pointed out how the degree of variation of γ -ray emissivity, as measured by EGRET, was much lower than the variation in the radial distribution of SNRs, considered the primary sources of cosmic rays. This discrepancy is resolved if the X_{CO} factor is allowed to vary as a function of the galactocentric distance. One of the caveats in the analysis based on CO templates resides in the accurate determination of N_H that depends, at least for the molecular component, on the aforementioned conversion factor. In fact it

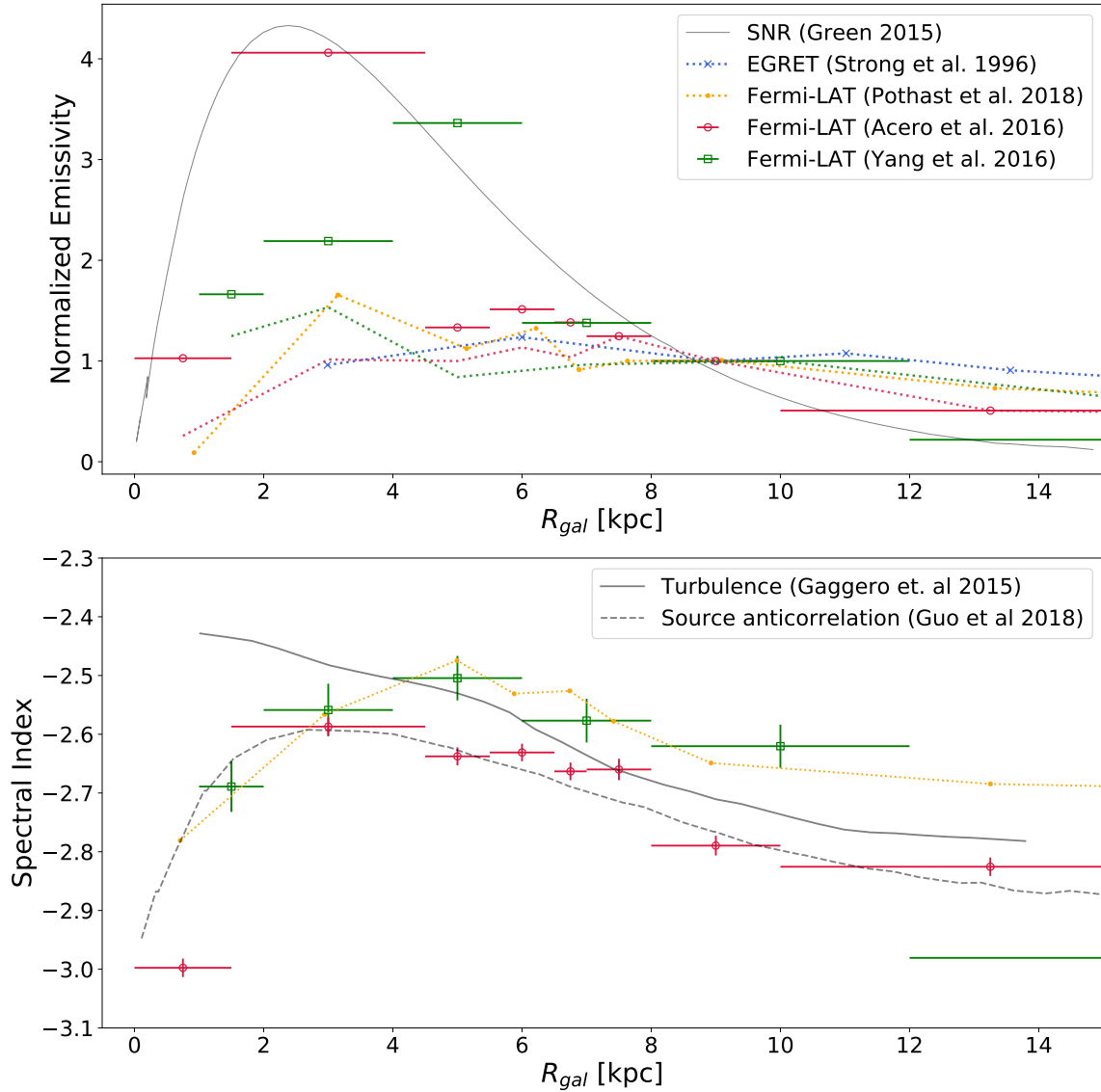


Fig. 1.13 Upper panel: radial distribution of the gamma-ray emissivity per H atom of the diffuse gas as measured by EGRET [109] and Fermi-LAT by different authors [111, 130, 131]. The values are normalized to the value observed in the local region (~ 8 kpc). For comparison, the radial distribution of supernova remnants from [69] is also plotted. Lower panel: radial distribution of the derived CR spectral indexes from the same works. Two model predictions for the radial distribution of the spectral index are also plotted: one takes into account the effect of turbulence [132], the other assumes anti-correlation between the sources and the diffusion coefficient [133], see the text for more details.

should be noticed that from observations of F_{pion} one does not derive directly F_{CR} but rather $Y \equiv X_{CO} \times F_{CR}$. The two values are strictly connected within each other and cannot be determined fully independently. Analyses of refs. [111, 130], that leave X_{CO} free to vary, are consistent with the galactic radial distribution of SNRs [69], as shown in figure 1.13. Arguments in favour of the radial dependency of X_{CO} are based on dust diffuse observations [134] and on the decrease in metallicity, towards the GC [135], even though the tests reported in [80] for the Milky Way tends to favor a constant value. Nevertheless, the emissivity derived in [130] from dust templates, that is independent of X_{CO} , show the same enhancement of ~ 3 in the inner Galaxy ($5^\circ < l < 15^\circ$).

There exist three main scenarios to explain such behavior of the CR distribution that consider: i) the contribution of ‘fresh’ accelerated particles, ii) the contribution of undetected sources or iii) the modification in the propagation parameters. In the first scenario, the contribution of recently accelerated particles is considered to vary in different regions of the Galaxy. Naturally, in regions close to an accelerator the injected particles will be more abundant and there will be an over-density of higher energy particles with respect to other regions, where there has been no acceleration and whereto particles have arrived only after diffusion. In a region with a higher number of accelerators, in the case of impulsive accelerators like SNRs, the rate of explosion is higher. This is analog to consider an ‘efficient’ age of the accelerator that is on average lower, and consequently, the particle spectrum results similar to the one derived for young SNRs (see Fig. 1.5), namely enhanced and harder [136]. This scenario conciliates with the fact that the highest and hardest spectra are measured at a galactocentric distance that hosts the highest density of supernova remnants. In the second scenario, the enhancement could be produced by the contribution of sources that, although not significant enough to be recognized and to be included in the source models, might still provide some photon counts to the overall diffuse emission. The effect of the so-called *unresolved* sources has been quantified in [131], where the authors pose an upper limit of 20% to their contribution. In the third case, modifications of the diffusion properties throughout the Galaxy are considered. This scenario is motivated by the fact that turbulence could significantly affect the propagation of particles. Objects as supernovae, pulsars, stars with strong winds, jets ect. can induce turbulence in the ISM. Because most of the galactic source populations peaks around 3–5 kpc from the GC, the maximum effect of turbulence is expected there. Guo et al. (2018) [133] propose a model where the diffusion

coefficient is anti-correlated with the distribution of sources. The model shows good agreement with the data. Moreover, this model accounts for several of the observed properties of local cosmic rays, such as the hardening of primaries and the electron/positrons ratio. On the other hand parametrizations like the one in [132], that assume a gradual decrease of the diffusion coefficient with the galactic radius, fails to reproduce the inner part of the Galaxy.

Interestingly a recent modeling [137] of the VHE emission, demonstrated that there is no need to have a continuation of the hard and enhanced spectrum measured at GeV-energies to explain TeV observations. In fact the pion emission as observed by Fermi, extrapolated at higher energies, together with the contribution of known sources saturates and sometimes exceed the measured TeV-flux, leaving no space for other components as unresolved sources, nor IC that is not negligible at TeV energies.

GIANT MOLECULAR CLOUDS AS PROBES OF GALACTIC COSMIC RAYS

Most of the molecular medium in our Galaxy is embedded in distinct structures, Molecular Clouds (MCs), that can be distinguished as over-dense clumps in the $l-b-v$ space. The mass of a MC, typically comprised between $10^3 M_{\odot}$ and $10^7 M_{\odot}$ is embedded in a radius of 10–100 pc, making them perfect targets for investigating the galactic population of CRs, not only for their enhanced density, but more importantly because they allow us to localize the origin of the emission within the radius of the cloud itself.

In this Chapter, I present the results obtained from the analysis of different regions of the Galaxy corresponding to the locations of several Giant Molecular Clouds from the nearby (~ 500 pc) Gould Belt complex up to a distance of ~ 10 kpc. Firstly, the parameters that determine the visibility of Molecular Clouds in γ -rays are discussed. Secondly, the employed analysis method is described and finally the results in terms of gamma-ray and proton are presented and commented.

2.1 COSMIC RAYS FROM MOLECULAR CLOUDS

In a similar way as for the diffuse medium, molecular clouds emits γ -ray radiation, when cosmic rays penetrate in their interiors. One can argue that the penetration of cosmic rays in high-density regions as molecular clouds are, is impeded or made more difficult by the turbulence that these particle induce on the outer layers of gas, altering the diffusion coefficient. The extent of this effect has been evaluated by several authors [119, 120, 138], that modeled the dynamics of CR-particles outside and inside the cloud and they all reached the common conclusion that, for typical conditions, only CRs of energy lower than 100 MeV can be effectively excluded from

MCs. This is safely below the threshold energy for pion production, granting that the originating γ -emission is a valid tracer of the ambient CR population.

Differently from diffuse analysis, where the contribution of the molecular medium is integrated over a large scale, in the case of MCs the considered target is embedded between a few tens to a few hundred parsec scale, therefore the derived cosmic ray parameters refer to that specific location of the Galaxy. This is the primary advantage of observing molecular clouds instead of diffuse gas, as they provide *differential* (site-to-site) information on the cosmic-ray density distribution, whereas from diffuse emission only *integrated* information, on a large scale, can be retrieved. This can be done, as the density in giant molecular clouds, in many cases, is large enough to overcome the detection threshold of the gamma-ray instruments alone. This is of fundamental importance to test the real distribution of the galactic cosmic-ray sea and to constrain the theories which concerns it (see Sec. 1.3.1). Furthermore, when the flux is extracted from a smaller region, the contribution of mis-modelled sources or unresolved gamma-ray sources has a smaller effect. For these reasons, γ -rays from *individual* GMCs offer a straightforward and unbiased channel for observation of galactic CRs and can operate as unique CR barometers throughout the Galaxy [139, 140]. In particular, *passive* GMCs, namely clouds located far from CR sources, provide a measurements of the level of the CR sea, that is free from any contamination of freshly injected particles. The measured spectrum of cosmic rays is then determined only by the propagation of the cosmic rays up to the cloud region. Even if it is hard to determine a priori whether a molecular cloud is truly passive, as it can be influenced by an undetected (*dark*) accelerator, or by a collection of relatively near accelerators, any deviations due to nearby injection would result in a enhancement of the CR density with respect to the value measured locally, providing that this can be identified as the average cosmic ray spectrum. If the spectrum instead matches the local level, not only it would guarantee that a truly passive cloud is observed, but it would also assure that similar propagation properties characterize regions of the Galactic Disk beyond the local environment. To test the uniform-sea hypothesis, as many objects as possible need to be analyzed. Unfortunately in some cases MCs overlap with other, generally brighter, γ -ray sources and therefore in these cases, the γ -ray flux cannot be safely extracted. It can also happen that other MCs fall on the same line of sight as the cloud of interest. Even if that is a quite remote case, as pointed out by [87] that noticed that most of the directions are characterized by 1 or 2 molecular clouds, it is important to evaluate the relative contribution of

the targeted cloud to its line of sight and understand if the contribution of the gas at different distances can be correctly modeled. Finally, the detectability of such emission with the given instrument sensitivity has to be considered. In the following, the performances of Fermi-LAT after 10-yr of data collection are discussed and compared with the expected flux level of MCs illuminated by the cosmic-ray sea, following Eq. 1.1.14. The expected flux from a MC can be factorized as the contribution due to the physical properties or the clouds, A , and the cosmic ray properties at the cloud location, $\phi(E)$, into: $F_\gamma = A \phi_\gamma(E)$, where ϕ includes also the nuclear enhancement parameter, ξ_N . One can predict the emission from a MC assuming a certain spectrum of protons. As the primary interest is to observe the sea of cosmic rays, one needs to assure that the emission produced by a spectrum of cosmic rays similar to the one measured locally is visible with a given instrument. For the same arguments presented for the diffuse emission, the Fermi-LAT is the most suitable instrument also for the studies of single molecular clouds. Its sensitivity [122], both for the inner ($|l| < 60^\circ$) and the outer galaxy ($|l| > 60^\circ$) is plotted in Fig. 2.1. For extended sources, such as molecular clouds, the sensitivity is worsened by a factor that depends on the instrument resolution (for Fermi-LAT: $\sigma_{PSF} < 0.15^\circ$ for $E > 10$ GeV ; $\sigma_{PSF} > 3.5^\circ$ for $E = 100$ MeV) and on the extension of the source, θ (e.g. [60]):

$$\omega = \frac{\sqrt{\sigma_{PSF}^2 + \theta^2}}{\sigma_{PSF}} \quad (2.1.1)$$

This factor is accounted for in the figure, by plotting the sensitivity in an area that spans from $\omega(\theta = 0.2^\circ)$ to $\omega(\theta = 1^\circ)$. The sensitivity has been compared to the flux calculated for molecular clouds of different $A=0.2,0.4,1$, assuming as proton spectrum the one reported by AMS02 [18] up to 100 GeV (solid line) and the one of Dampe [17] above (dashed line), which reported a small hardening at those energies.

It is clear from the plot that molecular clouds with an A parameter larger than 0.4 can be detected, considered the typical angular sizes of the clouds. This threshold can be lowered further when considering only the outer regions. To compensate for a loss in sensitivity due to a large area a large A factor is needed, as in the case of the near Gould Belt molecular clouds.

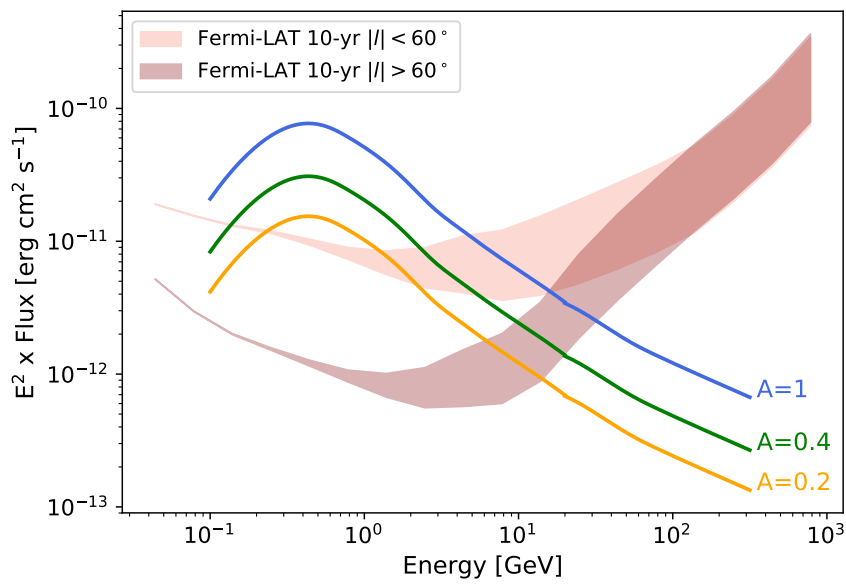


Fig. 2.1 Gamma-ray flux expected for molecular clouds of different A parameter (0.2, orange; 0.4, green; 1, blue) illuminated by cosmic rays of spectrum similar to the one measured by the local direct experiments. For comparison, the sensitivity of Fermi-LAT for the inner (light red) and outer (dark red) longitudes are plotted as areas, to account for the different worsening due to the observed source extension, θ , from a value relative to $\theta = 0.2^\circ$, to $\theta = 1^\circ$.

2.2 ANALYSIS TECHNIQUE

Analyses of gamma-ray data are based on Likelihood method, extensively described in [141]. In particular, the analysis of Fermi-LAT data performs a maximum likelihood fitting of the data on the 3-dimensional parameter space of coordinates and energy. The Likelihood, L , is defined as the probability of reproducing the observed data with a certain model. In other words, L measures to which extent the data resemble a given model. The input model, $M(E, \vec{p})$, to which the data are compared, includes the information on the position (\vec{p}) and on the energy spectrum of all the sources in a certain region of interest (ROI). To be commensurate to the data, the model is convoluted with the instruments response functions (IRFs), $R(E, \vec{p}|E', \vec{p}')$, that account for the modification of the data while passing through the detector. The IRFs include information on the point-spread function, on the energy dispersion and on the effective area. In this way, the expected number of counts would be given by:

$$\mathcal{M}_{exp}(E', \vec{p}') = \int dE d\vec{p} R(E, \vec{p}|E', \vec{p}') M(E, \vec{p}) \quad (2.2.1)$$

To construct the Likelihood function one can follow a *binned* or an *unbinned* approach. In the first case, the data are divided in bins in the $l - b - E$ space and for each bin the number of expected counts is derived, according to the given model. In the second case the methods are analogous to the first, but the dimension of the bins tends to zero. The unbinned approach is more precise but highly time-consuming, therefore is hardly employed and will not be treated. In the case of a Poissonian distribution of the events, for each bin the probability can be calculated as

$$\mathcal{P}(\lambda_i, n_i) = \frac{\lambda_i^{n_i}}{n_i!} e^{-\lambda_i} \quad (2.2.2)$$

where λ_i , the average number of events, is calculated from the model and n_i are the observed counts. Thus, the total Likelihood function results:

$$L = \prod_i \mathcal{P}(\lambda_i, n_i) = e^{-N_{exp}} \prod_i \frac{\lambda_i^{n_i}}{n_i!} \quad (2.2.3)$$

Most commonly, the Log-likelihood, \mathcal{L} , is used:

$$\mathcal{L} = -2\log(L) = 2N_{exp} - 2 \sum_i \left(\log \frac{\lambda_i^{n_i}}{n_i!} \right) \quad (2.2.4)$$

which, in the case of a large number of events this quantity is equivalent to the χ^2 distribution (Wilks theorem), so that maximizing L, is equivalent to minimize the χ^2 . The highest the log-likelihood of a model, the better it represents the data. In practical applications, this parameter is used both to test whether a model or another better describe the data, and to quantify the significance of a detection, by defining the Log-likelihood ratio between the maximum likelihood of the two models one containing the source and the other without (null-hypothesis):

$$TS = \sigma^2 = \frac{\mathcal{L}_{max,0}}{\mathcal{L}_{max,1}}. \quad (2.2.5)$$

When the two models only differ for the presence of one source, the TS value gives a measure of the significance, $\sigma = \sqrt{TS}$, of that source.

The analysis procedure of Fermi-LAT can be carried out with specific softwares. In the following fermipy [142] has been used, that allows us not only to select the data, create a model and fit the parameters in order to maximize the likelihood, but also to extract the source spectral energy distribution (SED) and analyze the residual maps. Fermi-LAT data for the specific sky region and energy range of interest can be downloaded from the online collaboration server [113]. The main steps of the analysis consist are the following:

- *Preparation of the model:* the starting model has to include all the known sources in a given region of interest (ROI), usually centered on the source of interest and several degrees wide. The information on the location and the spectrum of the sources can be retrieved in the Fermi catalogs of sources: the most recent are the 3FGL, released in 2015 [143], and the 4FGL, released in mid 2019 [51]. Besides discrete sources, the diffuse components need to be added. The Fermi-LAT collaboration provides templates for the galactic (galdiff) and extragalactic (isodiff) emission. The first embeds the contribution of pion emission, inverse Compton and bremsstrahlung, the second accounts for the isotropic emission observed at higher latitude that is believed to originate outside the Milky Way, e.g. from far active galactic nuclei. However, in the case of clouds analysis, the galactic diffuse template cannot be used, and a

customized template is needed, for the reason explained in the following section. The exposure time and the live-time spent on the specific ROI can be calculated from the information included in the spacecraft file, that can be retrieved with the data. The latter allows the production of a sourcemap, that includes the predicted parameters for each source, convoluted with the instrument response functions (Eq. 2.2.1).

- *Selection of the data:* I used the latest data release, Pass8 (evclass=128), which benefits from better IRFs: a better event reconstruction, a larger range in energy, an improved energy resolution and a significantly increased effective area [144]. The data have different point spread functions, depending if they originated on top of the instrument (FRONT) or at the bottom (BACK), as the traveled length, and therefore the scattering probability is different. The user can select to consider events that have originated in the front or in the back of the detector or both; in the analyses that follow, both FRONT and BACK events (evtype=3) have been considered, in order not to lower the number of detected photons, that would compromise the significance of the source detection. Other cuts are applied to guarantee the quality of the data: a maximum zenith angle of 90° assures to exclude the Earth limb luminosity, moreover a spacecraft file labels the events that have a valid pointing direction and time and the others are discarded. Finally, when a binned analysis procedure is followed, the data are binned in coordinates and energy. The width of the bin can be tuned. It is important that is not too low, as there is the risk to obtain pixels that don't contain a significant number of events, but it is also important that is not too large, in order to not affect the resolution. In the following I imposed a 0.1° -wide bin for the spatial coordinates and 8 logarithmically-spaced bins per each energy decade.
- *Optimization:* the first step, after having set up the data and the model, consists in a first optimization of the parameters. All sources are fitted one by one. This permit to update the parameters from the cataloged values. Usually the parameters of the large scale components of emission (galdiff and isodiff) are fixed during this procedure, as they could contaminate the sources. When using a customized background this is not ideal, as the uncertainty on the background could wrongly affect the sources parameters. In this case, it is

better to firstly fit the diffuse component alone, with fixed sources, to find the best values and then continue by optimizing the sources.

- *Fit*: after having tuned the initial parameters of the sources, a fit of the model is performed on the data. The optimizer used by fermipy can be chosen to be MINUIT or NEWMINUIT [145]. The fitting procedure gives the maximum \mathcal{L} value and the detection significance in terms of TS for each source. With this information, the model can be modified, by changing the source spatial or spectral model, until the best configuration is found.
- *Residual investigation*: to assess the quality of the fit, the residual maps are investigated. The latter are obtained by subtracting the data counts map to the final model map, resulting from the fit. Any significant excess need to be included in the model and re-fitted. The significance of the excess is computed for each pixel of the map as: $\sigma = (n - \lambda)/\sqrt{\lambda}$, where n is the number of counts in the data, and λ the counts in the model. Any excess with $\sigma > 3$ is considered as a significant source. Alternatively, fermipy permits to compute the Test Statistic (TS) map of the residuals for each pixel. This is particularly useful to identify new (non-cataloged) sources. As a criterion, any excess with $TS > 20$ is considered a new source and is added to the model.
- *Modeling of new sources*: The new source is usually modeled as a point source, centered at the center of the excess region and a Power Law energy spectrum ($dN/dE = N_0(E/E_0)^{-\alpha}$). In some cases, when the model results not sufficient to eliminate the residual, templates with a larger number of parameters are considered to model the source, for example a extended source hypothesis is tested against the point-source model, moreover the presence of a break or other features in the spectrum are also considered.
- *Extraction of the flux*: finally, when all the residuals have been optimized, the spectral energy distribution (SED) for the sources of interest can be computed. The SED method in fermipy consists in fitting, in each energy bin, the normalization of a Power Law function of fixed index. In this way, one obtains the flux level in each energy bin. An upper limit is set, when the counts in the bin does not overcome the significance threshold of 4, unless differently specified.

Diffuse background template

When analyzing Molecular Clouds, the standard template for the galactic background (galdiff) cannot be used, as it includes the emission from molecular clouds itself and that cannot be separated from the other components. Moreover, in some cases in the analysis of molecular clouds, a separation along the line of sight is needed, and that is not possible with the standard background, as it is 2-dimensional. I constructed, then, a new galactic background model, that includes the main emission component above 1 GeV:

- *Pion decay*. The template for pion decay emission is based on the maps of the Molecular and Neutral medium tracers:
 - CO+Hr; the advantage of using a template based on CO (e.g. [73]) and HI (e.g. [93]) is that both these tracers include the information on the radial velocity and hence the distribution of the gas along the line of sight is known. This allows us to extract the portion of gas that belongs to the cloud and analyze it as a separate component. In this way the model includes a background source constituted of the whole galactic gas datacube that falls into the ROI, except for the cube corresponding to the MC coordinates ($\Delta l \times \Delta b \times \Delta v$), and a source composed by the missing cube of gas at the location of the MC. The data-cubes so manipulated, integrated along v and normalized for the sum and the total solid angle, constitute the spatial templates for the cloud and the background gas (upper panels in Fig. 2.2). Two different spectral models are assigned to the background and to the cloud so that their parameters can be fitted independently. In this way, it is possible to isolate the flux contributed only by the cloud. The extracted spectrum, in fact, would refer only to the portion of space within $\Delta l \times \Delta b \times \Delta v$ that corresponds to a limited extent on the line of sight and hence allows the localization of the emission. However, large uncertainties raise from the CO conversion factor and the HI spin temperature, as discussed in the dedicated section of Chapter 1 (Sec. 1.2).
 - Dust opacity; templates based on dust opacity have lower uncertainties on the column density, however these do not include the information on the distance and can be used only when the cloud of interest is the only

or the absolute dominant object on the l.o.s., as in the case of Gould Belt Clouds, located at high latitudes. Otherwise, the contribution of each component along the column has to be considered meticulously.

- *Inverse Compton.* As a template for the inverse Compton emission, I used the output from the GALPROP code v.54 [146], which is a computational tool that solves the transport equation, assuming a given source distribution and certain boundary conditions. In the specifics, the model here employed, named $^{\text{S}}\text{Y}^{\text{Z}}6^{\text{R}}30^{\text{T}}150^{\text{C}}2$ assumes a distribution of the sources as the one reported in Yusifov & Krüçük (2004) [68] and boundary limits of 10 kpc to the galactic disk height and of 30 kpc to the galactic radius.
- *Bremsstrahlung* has been neglected as it is not expected to contribute significantly at GeV energies and in most cases can be easily confused with the pion emission.

Besides, a new model for the extra-galactic isotropic emission has been obtained. To do so, a portion of the sky at high latitude has been fitted, fixing the galactic components and sources. This guarantees that all components are balanced.

Proton parameters extraction

From the derived SED it is possible to derive the parameters of the parent proton population for example with the python package *naima* [121]. The latter performs a Markov Chain Monte Carlo (MCMC) fitting of the radiative models (Pion decay, IC, bremsstrahlung or synchrotron) to the high-energy observed data. *Naima* is particularly suitable for modelling pion decay emission, which dominates in MCs, as it implemented the latest parametrizations of the proton-proton cross section that accurately describes the interactions from the kinematic threshold to 1 PeV [49]. *Naima* exploits a modified version of Eq. 2.2.1, using the fact that $\rho_{\text{CR}} \equiv dN/(dE dV) = 4\pi c^{-1} J(E)$:

$$F_{\gamma} = \frac{c}{4\pi} \frac{\langle n \rangle}{d^2} \int dE_p \frac{d\sigma_{pp \rightarrow \gamma}}{dE_{\gamma}} \int dV \frac{dN_p}{dE dV} \quad (2.2.6)$$

$$= \frac{c}{4\pi} \frac{\langle n \rangle}{d^2} \int dE_p \frac{d\sigma_{pp \rightarrow \gamma}}{dE_{\gamma}} \frac{dN_p}{dE} \quad (2.2.7)$$

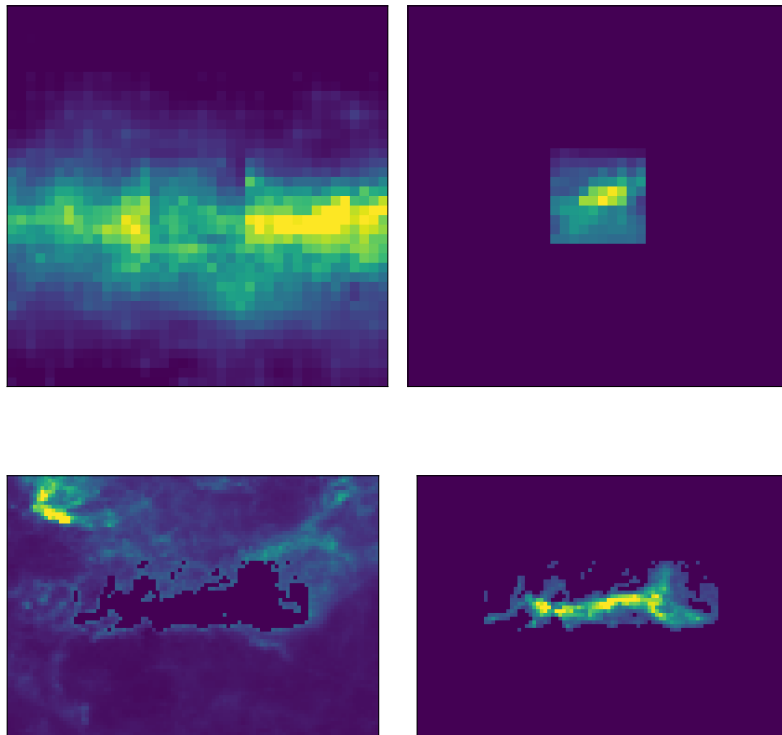


Fig. 2.2 The customized templates used in the analyses both for the background gas (left panels) and the clouds of interest (right panels). The top panel shows the template derived from CO and H_I for the cloud R877 from the catalog in [86]; the lower panel shows the template derived from dust opacity for the Gould Belt molecular cloud Orion A.

and returns the fitted parameters of the proton energy distribution, dN/dE , according to the chosen functional form (Power Law, LogParabola etc.). As input parameters the mean volume density, $\langle n \rangle$ and the distance, d , of the targeted material need to be provided, which are usually not known or uncertain. Nevertheless, the latter can be set to 1 cm^{-3} and 1 kpc , respectively, so that the resulting energy spectrum would be related to the true one as:

$$\frac{dN'}{dE} = \frac{\langle n \rangle}{d^2} \frac{dN}{dE} \quad (2.2.8)$$

and the CR density could be obtained from observable parameters of MCs or diffuse medium, as it is:

$$\rho_{CR} = \frac{dN}{dE dV} = \frac{d^2}{\langle n \rangle} \frac{dN'}{dE dV} \quad (2.2.9)$$

$$= \frac{m_p}{M} d^2 \frac{dN'}{dE} \quad \propto A^{-1} \frac{dN'}{dE} \quad (2.2.10)$$

$$\propto n_{col}^{-1} \frac{dN'}{dE}. \quad (2.2.11)$$

$$(2.2.12)$$

where M is the mass of the targeted gas and m_p is the mass of the proton. In this way, the uncertainty on the derived proton density is limited, as it would depend only on the uncertainty of the target column density, that is of the order of 20–30%.

2.3 RESULTS FROM MOLECULAR CLOUDS

In the following, the results obtained from different regions are presented. In each case, the most suitable background has been considered, as discussed below.

2.3.1 Gould Belt and nearby Molecular Clouds

The Gould belt complex is a ring-like region of young stars and gas clouds, located a few hundred parsecs from the Solar System. This region hosts some giant molecular clouds that are particularly interesting to be investigated since, due to their proximity, they have large A factors, often exceeding 1. Indeed, the first investigations of CR from molecular clouds were carried out on Gould Belt clouds [147–149]. My investigation started with 3 clouds of this complex, to cross check our results with

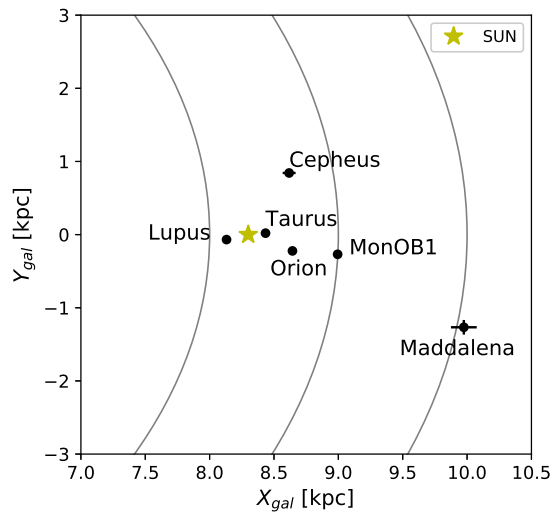


Fig. 2.3 Position on the (X_{gal}, Y_{gal}) plane of the analyzed nearby clouds. The position of the Sun is indicated as yellow star.

other authors. In particular, Taurus and Orion A were chosen, because they have the highest A factor. For completeness also Lupus have been analyzed, as it has not been investigated before. Furthermore, other nearby ($\lesssim 2$ kpc) clouds that do not belong to the belt have been considered. In particular, Cepheus, Monoceros OB1 and Maddalena located at ~ 800 pc, ~ 900 pc and ~ 2000 pc, respectively. The distance of these and the objects of the Gould Belt, have been recently reviewed exploiting the star reddening method and the precise distance determination of stars obtained with Gaia [150]. The values are reported in Table 2.1 together with the other relevant physical parameters of the selected clouds, e.g. position, mass, galactocentric distance and A parameter. The latter has been derived from Equation 1.2.11 for the specific region cut out for the analysis.

As one can notice, all the clouds lay several degrees off the plane, often in the outer wing of the Galaxy. This guarantees to have better performances of the instrument. Moreover, being in isolated locations, these clouds do not overlap with any other sources and in particular, they dominate the gas column density. In fact, almost all the gas of the column belongs to the corresponding clouds and hence a kinematic separation is not necessary. The spatial distribution of the gas both in the (l,b) and in the (l,v) plane is shown in Fig. 2.4 and Fig. 2.5.

Thanks to the favorable position of these clouds, it is possible to use the bi-dimensional dust opacity map to create the clouds spatial templates. After having

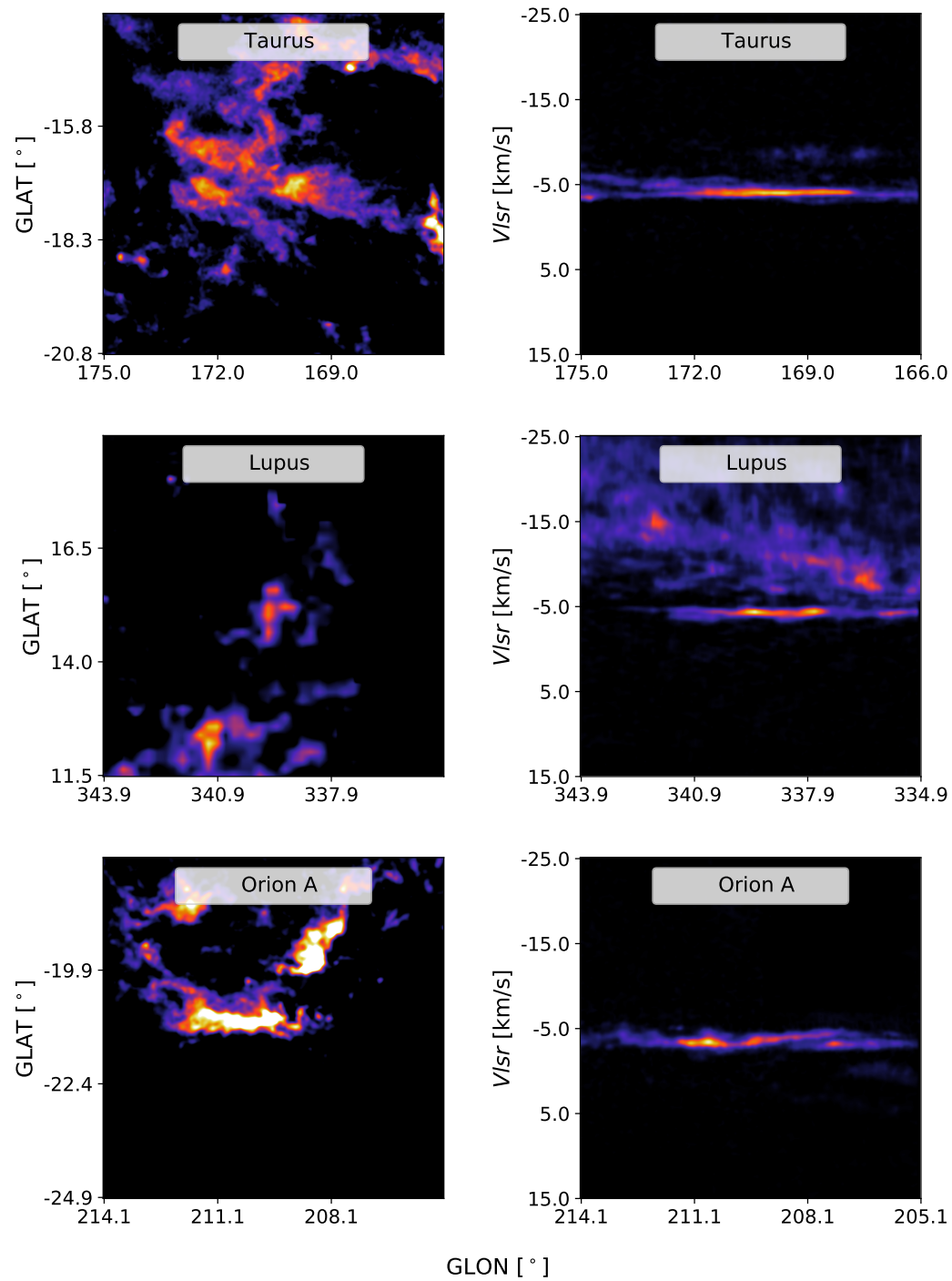


Fig. 2.4 (l, b) and (l, v) maps of the gas traced by CO [73] in the region of the considered Gould Belt clouds.

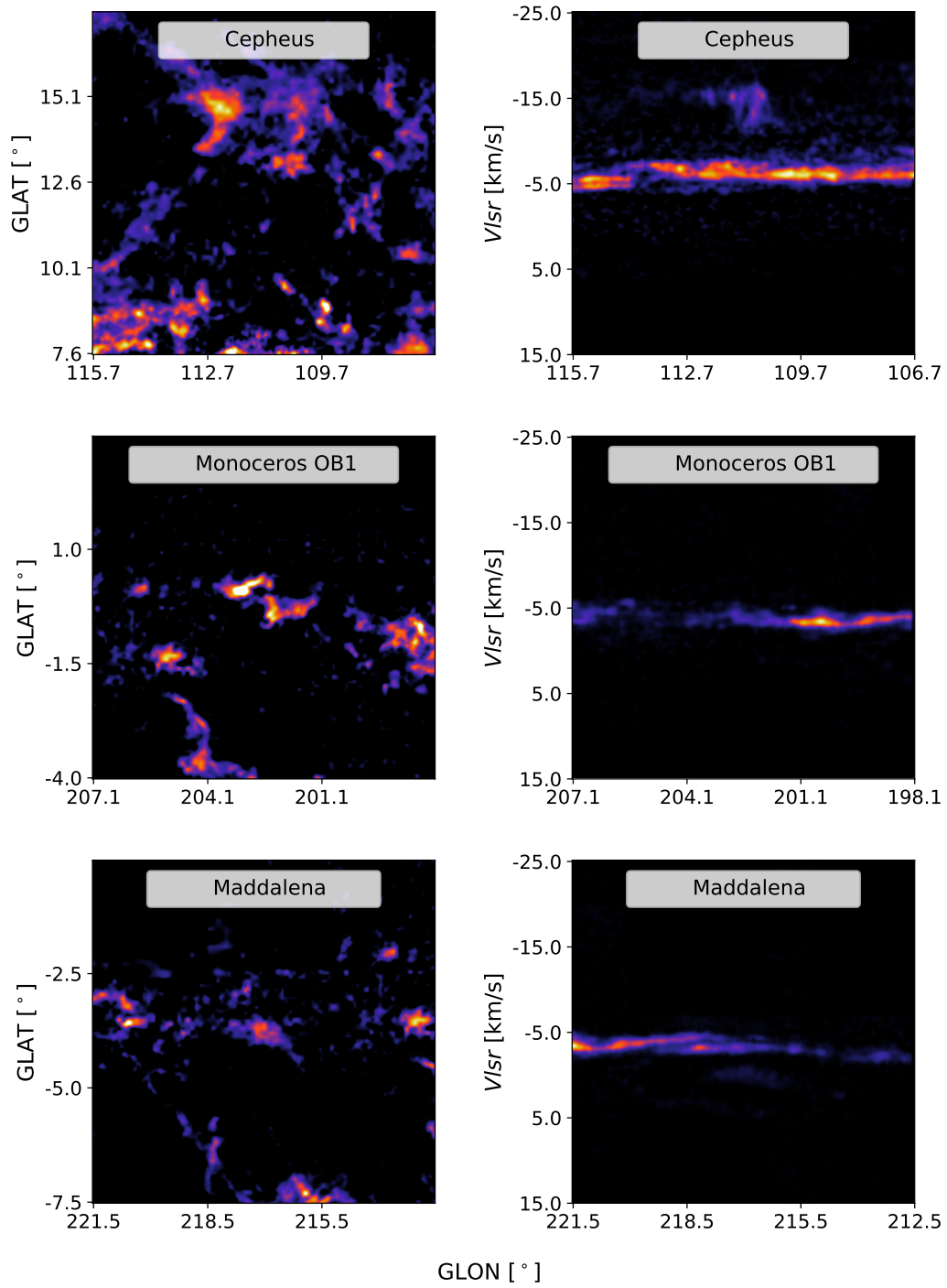


Fig. 2.5 Same as in Fig. 2.4, for the other nearby clouds.

	(l, b) [$^{\circ}$]	M [$10^5 M_{\odot}$]	d [pc]	R_{gal} [kpc]	A
Taurus	(171.6,-15.8)	0.11	141	8.4	5.6
Lupus	(338.9,16.5)	0.04	189	8.2	1.0
Orion A	(209.1,-19.9)	0.55	430	8.4	3.0
Cepheus	(110.7,12.6)	2.13	920	8.6	2.5
Monoceros OB1	(202.1,1.0)	1.33	750	9.1	2.4
Maddalena	(216.5,-2.5)	5.29	2100	10.2	1.2

Table 2.1 Physical properties of the sample of nearby molecular clouds chosen for the analysis. The position (l, b) of the center, the distances d from us, and the derived distances R_{gal} from the Galactic center, refer to [150], while the masses M and the A parameters have been calculated from the dust opacity map, using Eq. 1.2.11.

defined the model for the sources and the background, the analysis procedure followed the standard points described earlier. To assess the correctness of the source modeling, the residual maps have been investigated and they can be seen Fig. in 2.6. The residuals fluctuate around zero, confirming that there is no mismodeled emission. The extracted spectral energy distribution (SED) for each clouds is showed in Fig. 2.7, where it is compared to the flux derived for a molecular cloud with the same A factor, assuming a proton spectrum as the one measured at Earth by AMS02 [18] from 10 GeV up to ~ 1 TeV and by Dampe [17] beyond. For the region below 10 GeV, since the experimental points are severely affected by the modulation of the Sun, a power-law spectrum of index 2.8 has been considered, with normalization fixed at the level of the AMS02 measured points. The area in the plots accounts for the 20% uncertainty in the column density, due to the gas tracer. For the case of Taurus and Orion A also the spectra derived by Yang et al. (2013) [148], normalized to the same A , are shown for comparison. The results derived are in general compatible with the local spectrum. A slight tendency of hardening is observed around 50 GeV. That matches with the hardening of the CR spectrum already measured by Dampe [17]. Nevertheless higher-energy observations are needed to exclude a systematic effect in the analysis and confirm this change in slope.

2.3.2 Molecular Clouds in the Galactic Disk

The analysis was then extended to further molecular clouds, in order to probe the content of galactic cosmic rays in different regions, as far as possible from the Solar

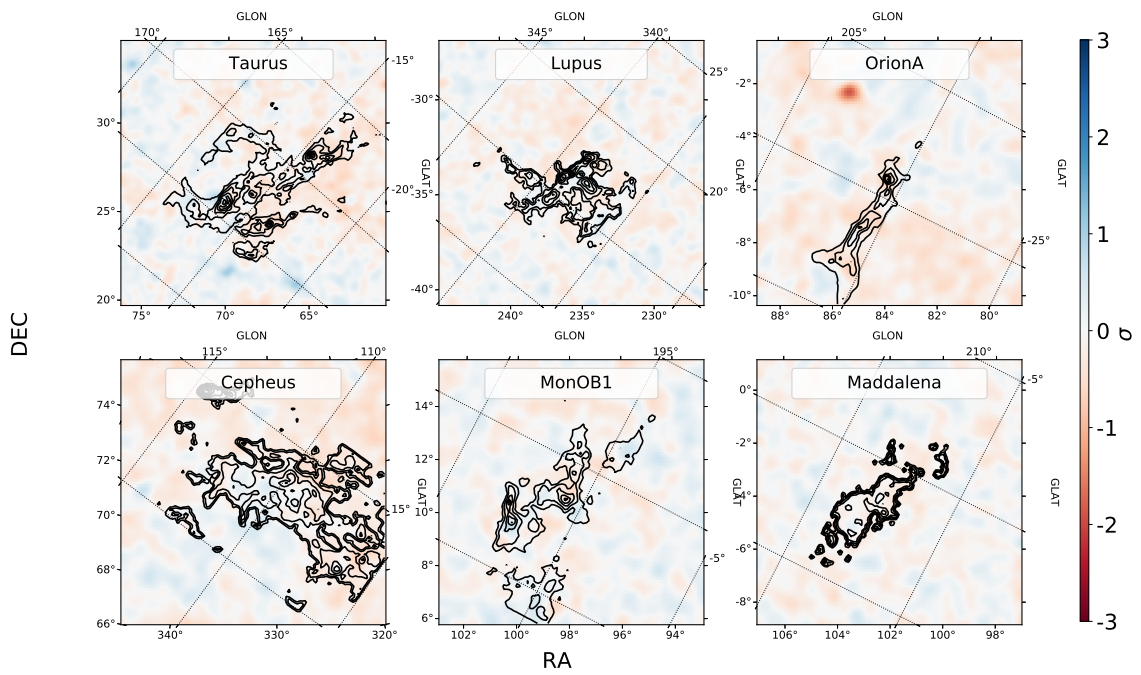


Fig. 2.6 Residual maps in terms of σ (see text) after the subtraction of all the sources in the region of interest. The black contours refer to dust opacity at 353 Hz traced by Planck [101]. The figure has been adapted from [151].

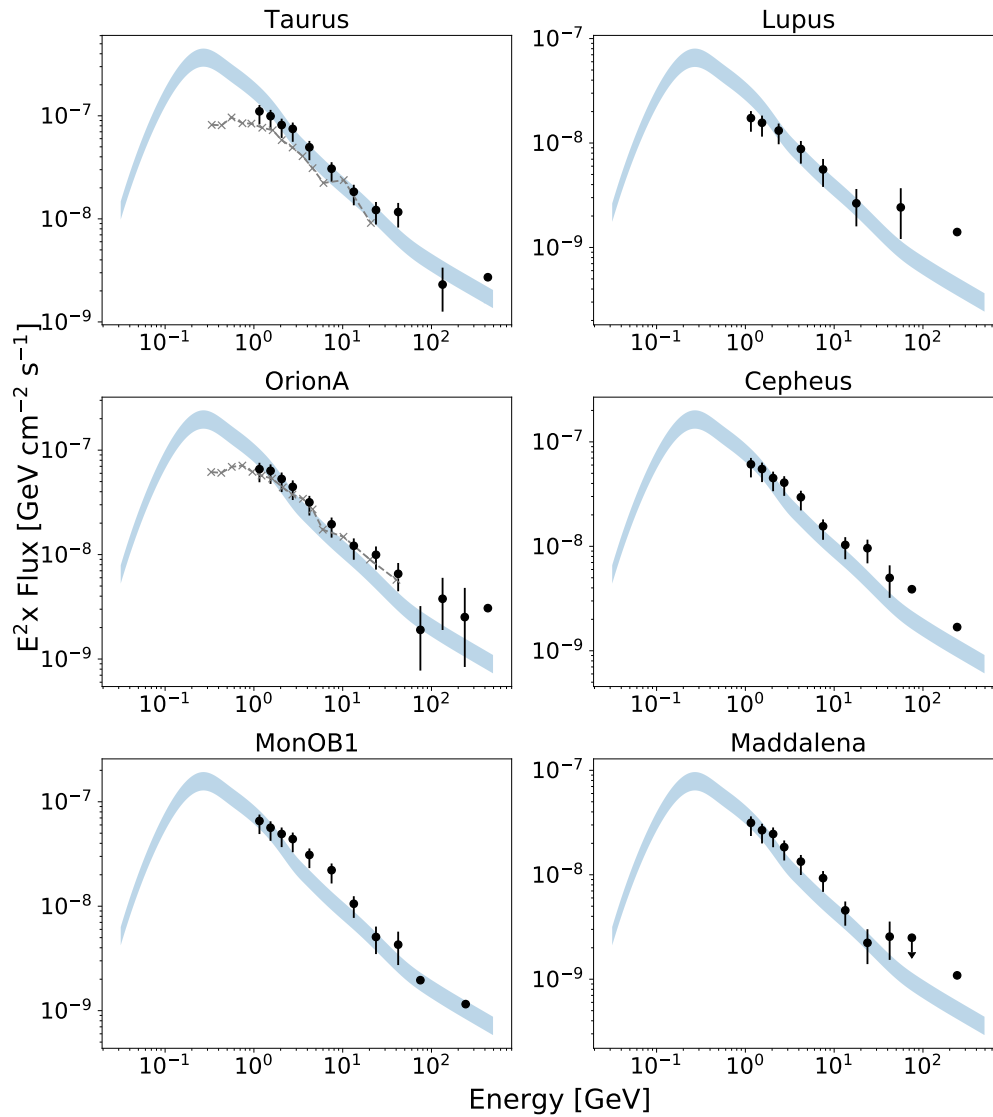


Fig. 2.7 Spectral energy distributions extracted from the six selected nearby molecular clouds. The blue regions show the expected flux for each cloud assuming the proton spectrum measured locally by AMS02 [18] up to 1 TeV and DAMPE [17] at higher energies. The area represents the 20% uncertainty on the flux normalization that derives from the uncertainty on the gas column density. In the case of Taurus and Orion A, the SED extracted by Yang et. al. 2013 [148] is also shown as grey crosses, renormalized in order to have the same value of A . The figure has been adapted from [151].

	(l, b) [°]	v [km/s]	θ [°]	M [$10^5 M_\odot$]	d [kpc]	R_{gal} [kpc]	A
R 243	(42.04, -0.36)	63.7	0.35	36	7.9 ± 0.6	5.85	0.58
R 418	(111.45, 0.79)	-52.9	0.32	5.2	4.1 ± 0.6	10.58	0.31
R 429	(109.84, -0.29)	-49.2	0.58	8.4	3.9 ± 0.6	10.35	0.55
R 610	(142.4, 1.38)	-12.6	0.54	0.21	0.7 ± 0.5	8.9	0.42
R 612	(126.87, -0.66)	-12.2	0.88	0.19	0.6 ± 0.5	8.72	0.53
R 804	(328.58, 0.4)	-91.9	0.41	36	5.7 ± 0.6	4.58	1.1
R 876	(323.61, 0.22)	-53.3	0.50	104	10.2 ± 0.4	6.05	1.0
R 877	(333.46, -0.31)	-49.5	0.33	12	3.4 ± 0.4	5.53	1.0
R 900	(318.07, -0.21)	-40.8	0.32	60	9.8 ± 0.4	6.65	0.62
R 902	(340.84, -0.3)	-43.2	0.31	125	12.5 ± 0.4	5.4	0.8
R 933	(305.49, 0.11)	-34.2	0.36	30	6.8 ± 0.9	7.07	0.66
R 964	(345.57, 0.79)	-13.9	0.41	2.9	1.9 ± 0.6	6.45	0.82

Table 2.2 Parameters of the analyzed molecular clouds from the catalog of Rice et al. 2016 [86]. The numbers correspond to the catalog nomenclature. The mass and the A parameter have been calculated from the map of CO as explained in the text.

System. The recently released catalogs of molecular clouds [86, 87] offer several objects of high enough mass to be detected with Fermi-LAT (see Fig. 2.1). I first considered the catalog provided by Rice et al. 2016 [86], which contains 1064 MCs distributed all over the galactic disk, within $|b| < 5^\circ$, except for the innermost galactic longitudes ($|l| < 13^\circ$). The coordinates (l, b, v) of the objects in this catalog have been cross-correlated to the coordinates of spiral arms or objects with parallax determined distances (e.g. masers) to obtain a stronger determination of the MC distance [152]. I selected from this catalog 12 MCs distributed up to 12 kpc from us at different galactocentric distances. The distribution of the selected cloud on the galactic plane is displayed in Fig. 2.8. The physical parameters of the selected clouds are reported in Table 2.2. A in this case, is calculated from the CO map of Dame [73] from equation 1.2.11, assuming a constant conversion factor $X_{CO} = 2 \times 10^{20} \text{ cm}^{-2} \text{ K}^{-1} \text{ km}^{-1} \text{ s}$ that has an uncertainty of 30% [80]. In the calculation, the mass of H I has not been included, as it will be considered as background in the analysis. It is in fact hard to cut precisely the edges of H I, as it is more extended than the molecular counterpart (see 1.2) and it is safer to consider it as background gas. The contribution of He or other metals has not been taken into account as well, when deriving the mass, as the fraction of nuclei of the interstellar medium is included already in the nuclear enhancement factor, ξ_N , when calculating the γ -ray flux.

The selection of the cloud to analyze was based on:

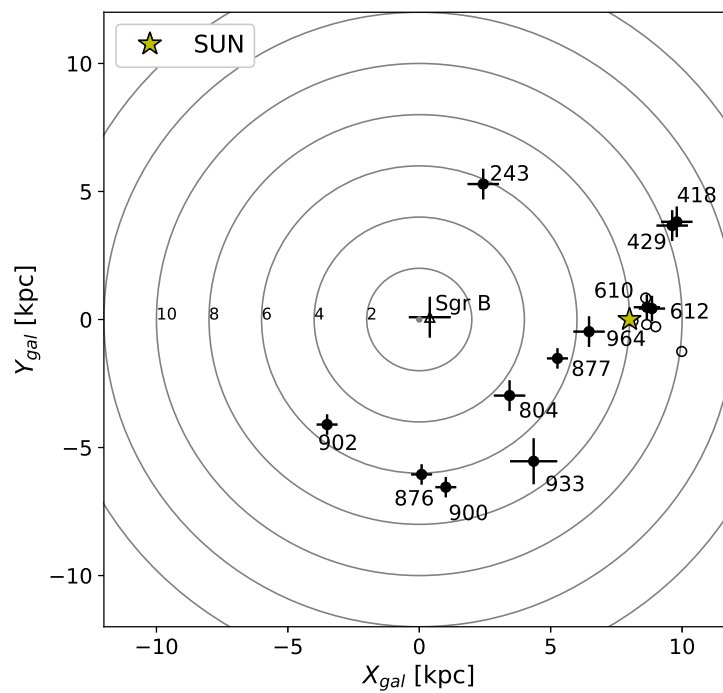


Fig. 2.8 Position on the (X_{gal}, Y_{gal}) plane of the analyzed clouds of the catalog of Rice et al. 2016 [86]. The position of nearby and Gould Belt clouds are indicated as open circles. The position of the Sagittarius B complex is also shown as a black triangle.

- *A* parameter. This is the main parameter that characterizes the flux of molecular clouds. I set the threshold to $A > 0.4$ that is a high enough value to have a detection of several spectral points both in the inner and in the outer Galaxy for a large range of clouds extensions (see Fig. 2.1) ;
- Gas on the line of sight. I evaluated the column density of the gas that falls on the same l.o.s. as the MC, and selected only the clouds that dominate the column in terms of density. All the chosen clouds contribute at least for the 40 % to the CO column density. The gas distribution in terms of H₂ and H I along the line of sight of the selected clouds is shown in Fig. 2.9. The density is summed over the pixels that constitute the cloud template, namely a box centered at the cloud coordinates (l, b, v) with sides determined by the cloud extension, θ , and cloud velocity dispersion, σ_v . This guarantees that the observed γ -ray emission actually originates in the region of the considered cloud.
- Superposition of gamma-ray sources. I discarded those clouds that overlapped with known γ -ray sources either from the Fermi catalog [51] or the H.E.S.S. survey of sources [52] as it would be difficult to avoid the contamination of bright sources and isolate the contribution of the MC alone. Besides, this allows us to avoid the influence of potential accelerators that can enhance the CR density in the clouds.

Even if the considered clouds are the dominant objects on the l.o.s., some residual gas is left in the foreground and in the background. For this reason, dust opacity maps, being bi-dimensional are not suitable to construct the spatial templates in this case. The gas has then been modeled starting from the CO and H I maps as described earlier. In this way, the portion of gas corresponding to the cloud can be analyzed separately. As earlier mentioned, only the CO line emission, which traces the molecular medium, has been considered in the template of the clouds, and the H I has been left in the background. The background gas in this way is constituted by the CO gas map, excluding the region of the MC and the H I together with the templates for the inverse Compton emission and the extra-galactic diffuse component. The analysis then proceeded following the points in 2.2. For this analysis the 3FGL catalog of sources has been employed, as the more recent 4FGL catalog was not available when starting this work. The sources not included in the catalog that showed significant residuals have been included in the model.

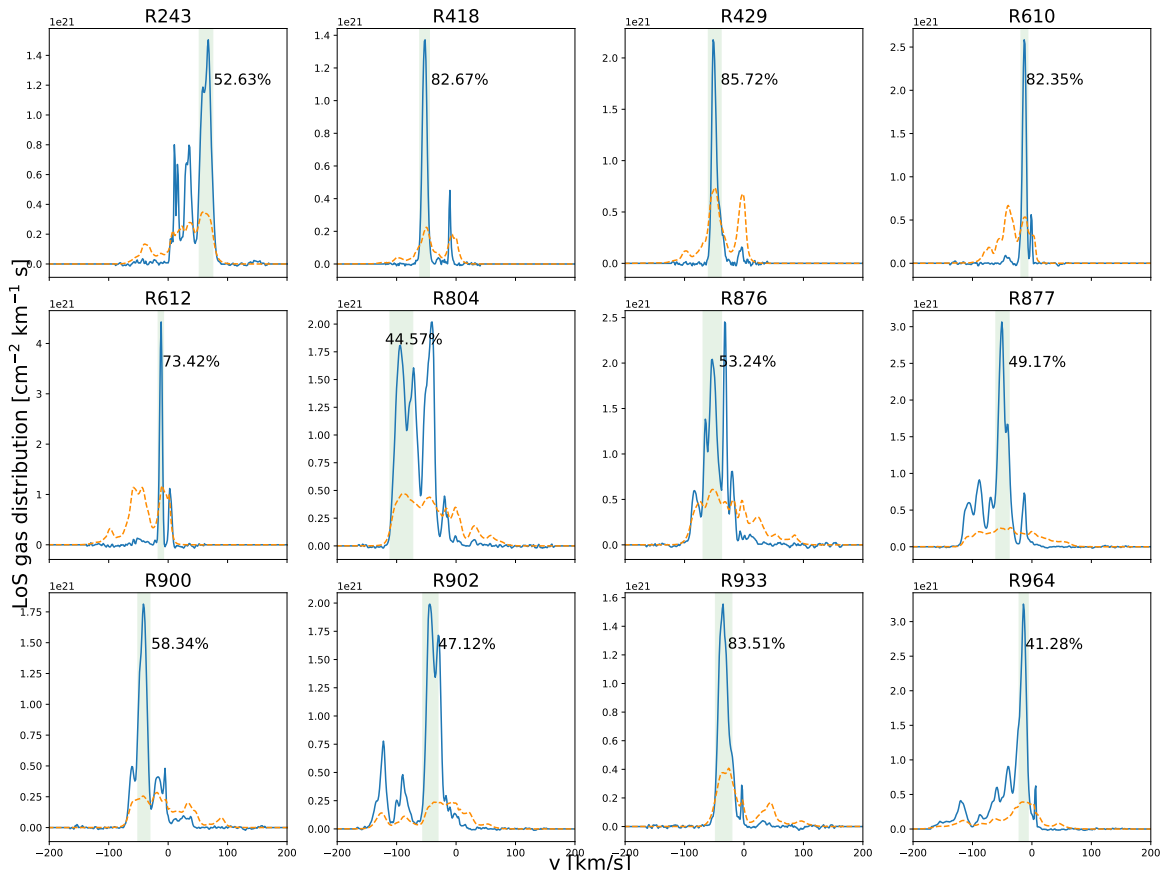


Fig. 2.9 Gas along the line of sight of the selected clouds. The gas densities have been summed over the area of the clouds. The blue curves show the contribution of molecular hydrogen and have been obtained from CO-datacubes. The orange ones show the abundance of the atomic hydrogen traced by the H I line. The position and extension on the line of sight of the cloud under analysis are indicated as a green area.

The map of residuals after the inclusion and fit of all sources are displayed in Fig. 2.10, and show that the residuals are contained between -3σ and 3σ , meaning that the model describes the data accurately.

The resulting SEDs are presented in Fig. 2.11, where the fluxes are normalized to $A=1$ and compared to the expected local flux. The systematic uncertainties accounts for the uncertainties related to the newly modeled sources and to the uncertainties on the background column density, in particular the one due to the HI spin temperature. The first has been evaluated simply by extracting the SEDs, before and after the inclusion of these sources and contributes for less than 10%. For the second, two different analyses have been conducted employing two different corrections to the HI column density (eq. 1.2.13), namely $T_s = 150$ K and $T_s = 500$ K. The latter is of the order of 30% and has been summed in quadrature to the other systematic errors.

The spectra derived in several locations, especially in the outer (> 8 kpc) galaxy show good agreement with the local spectrum. The clouds in the inner Galaxy instead show generally enhanced spectra, especially in the 4–6 kpc region where we observe the maximum values. At intermediate distances, in the 6–8 kpc region the values are more scattered, it is interesting to notice anyway that at least one cloud, R964, shows a flux as low as the local value although being located at the edges of the 4–6 kpc ring.

2.3.3 *Molecular Clouds in the inner (1.5–4.5 kpc) region*

The region embedded within ~ 1 kpc and ~ 5 kpc is particularly interesting as it was revealed to have the highest and hardest density of cosmic rays (see Sec. 1.3). Investigations of molecular clouds in this region are then crucial to understand if such enhancement is congenital, as due to a large scale modification of the CR dynamics, or if it is a result of averaging over several regions that are locally enhanced by CR accelerators. While in the first cases we would expect to find approximately the same value of CR density in all the considered clouds, in the second case fluctuations of the CR parameters from cloud to cloud are expected. This region is particularly complicated to analyze, because towards the inner Galaxy, multiple spiral arms intersect and it is difficult to isolate MCs from other gas components and from gamma-ray sources. Moreover, at low galactic longitudes ($|l| \lesssim 10^\circ$), an accurate kinetic separation of the components along the line of sight is not possible. As one

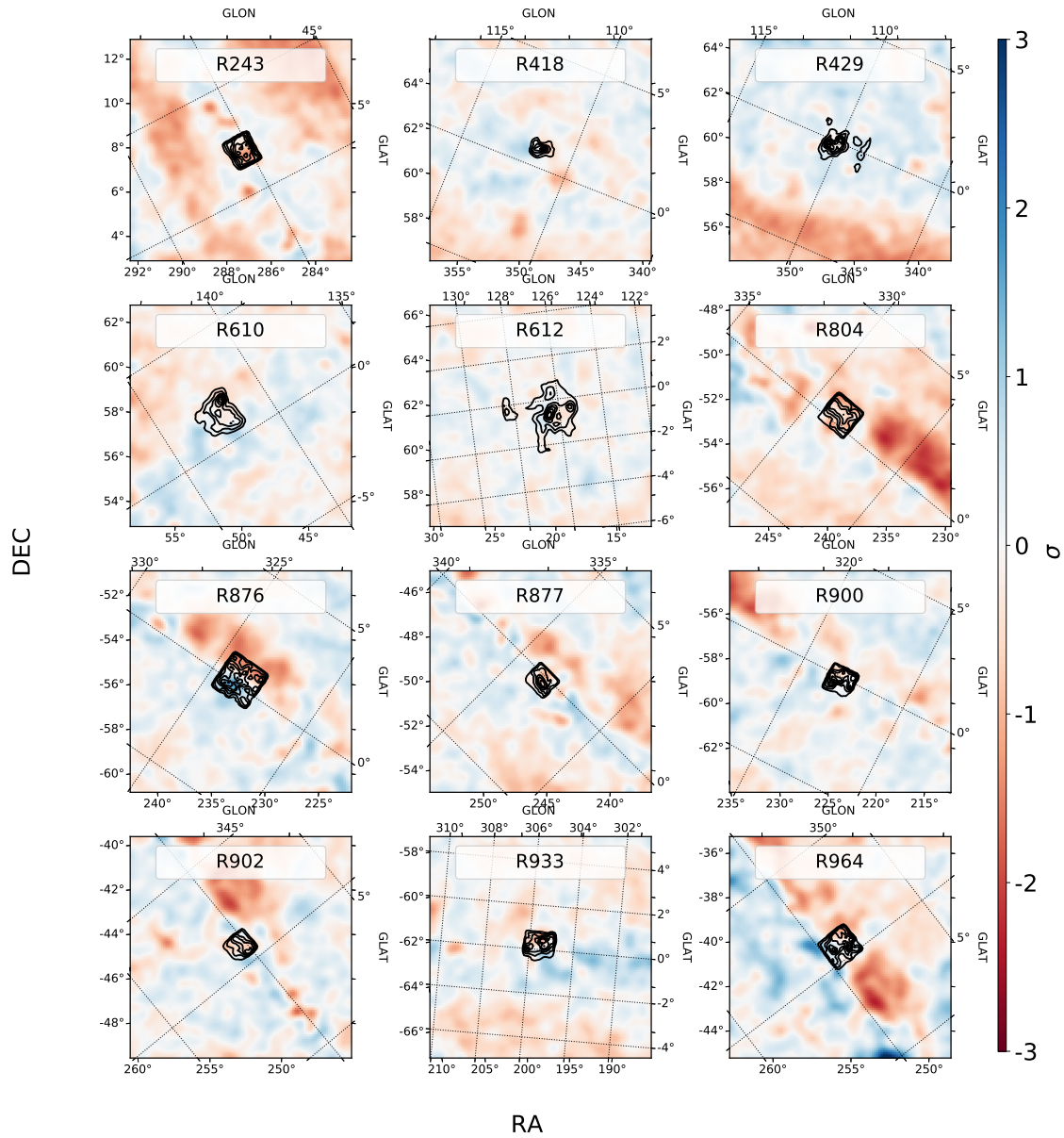


Fig. 2.10 Residual maps in terms of σ after the subtractions of all the sources in the region of interest. The black contours refer to the CO gas in the region ($\Delta l \times \Delta b \times \Delta v$) of the cloud. The figure has been adapted from [151].

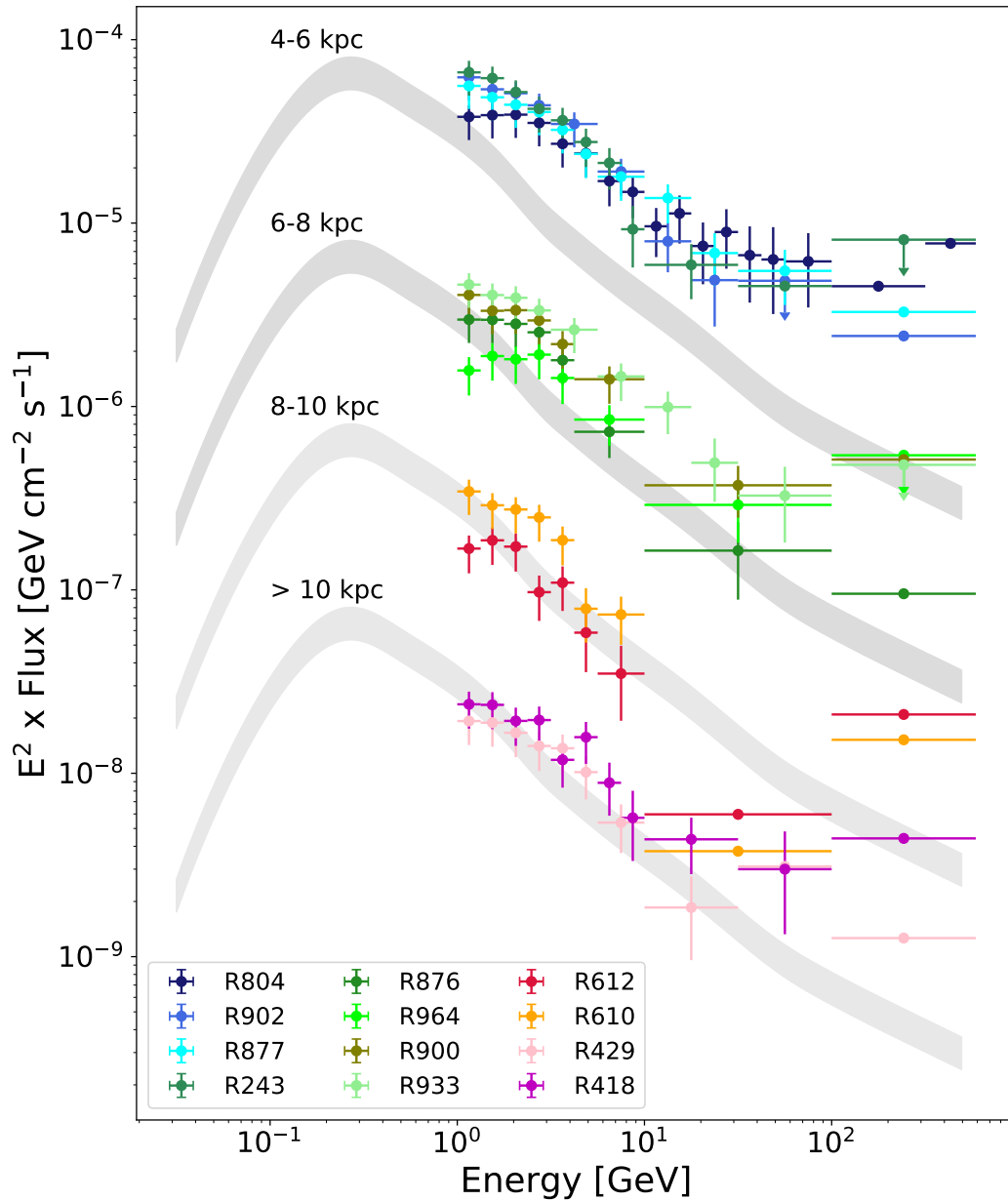


Fig. 2.11 The spectral energy distributions of the analyzed clouds are shown and compared to the expected gamma-ray flux derived from a local (as measured by AMS and Dampe) proton spectrum. The fluxes have been normalized to $A = 1$ and the curves have been multiplied by different factors (10,100,1000,10000) to separate the clouds belonging to different regions. The errorbars represent the systematic uncertainties derived as described in the text. The grey area represents the 30% uncertainty that affects the predicted flux, deriving from the uncertainty on the CO-to-H $_2$ conversion factor. The figure has been adapted from [151].

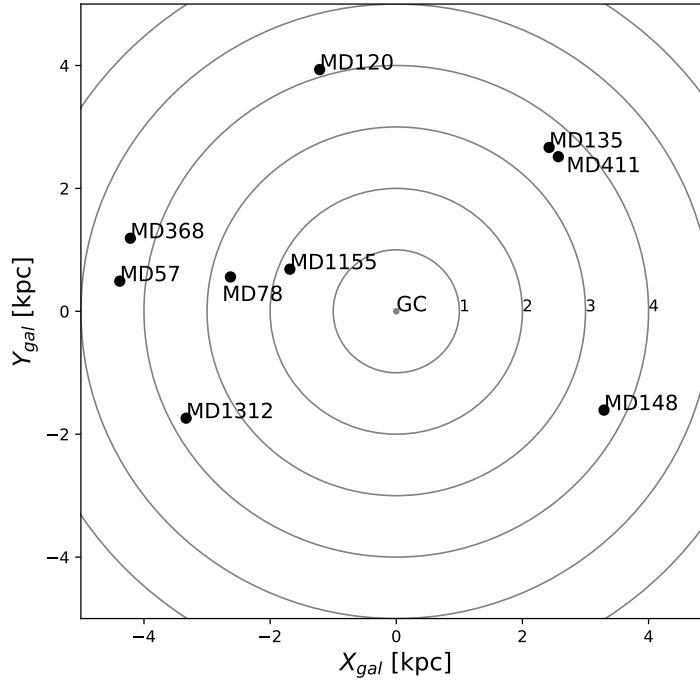


Fig. 2.12 Position on the (X_{gal}, Y_{gal}) plane of the analyzed molecular clouds of the 1.5–4.5 kpc region. The numeration corresponds to the indexes reported in the MD-catalog.

can see in eq. 1.2.1, the distance of the clouds depends on $\sin(l)$ that for low values of l tends to zero. Thus, also a small variation of v , of the order of the clouds velocity dispersion $\sigma_v \sim 10 - 20$ km/s, would correspond to huge ranges of distances. The catalog of Rice et al. (2016) [86] excluded this region from their decomposition. This region has been instead included in the catalog of Miville-Deschênes et al. (2016) [87]. As earlier stated, in their catalog clouds are identified as a combination of coherent gaussian peaks, in this way the uncertainty deriving from the velocity dispersion is limited.

As a kinematic separation is not possible in this region, there is no advantage in using CO and HI templates, so dust can be used as a tracer of gas. In this case, one needs to make sure that most of the observed emission arises from the zone of interest, like in the case of Gould Belt clouds. In the direction of the inner Galaxy, however, is rare to find isolated clouds, and an accurate selection of the target is needed to minimize the influence of the background gas. For clouds located within

1.5 kpc and 4.5 kpc from the Galactic Center the detection should be facilitated by the fact that the CR density in this region is expected to be higher. So clouds have been selected so that they are the dominant objects on the line of sight not only in terms of gas density but also of expected γ -ray flux. To investigate the detectability of such molecular clouds over the background, I assumed, at first, that the fraction of gas, X , that does not belong to the 1.5–4.5 kpc ring emits as the local 8–10 kpc ring, while the gas in the 1.5–4.5 kpc region has a ~ 3 times higher emissivity as reported by [111]. In this case, the maximum allowed X , to be able to detect the emission from the 1.5–4.5 kpc ring over the background is given by the condition:

$$(1 - X) \cdot N \cdot F_0 - X \cdot F_0 > 0.2[(1 - X) \cdot N \cdot F_0 + X \cdot F_0] \quad (2.3.1)$$

where F_0 is the flux in the local 8–10 kpc ring and N is the enhancement in CR density with respect to it. This allows us to distinguish an N -times enhanced flux from the local one, with a minimum separation of 20%, the typical uncertainty that characterizes the gas column density when using dust. For example, in the case of the 1.5–4.5 kpc ring $N = 3$ at 2 GeV and therefore the maximum fraction of column density that can fall in the background is $X = 66\%$. The fraction of background gas out of the 1.5–4.5 kpc ring have been determined by CO. The physical parameters for all the chosen clouds are reported in Table 2.4, including X . All clouds have a fraction of gas in the background, lower than 50%, except for the cloud MD78 that has a higher background, but still lower than the threshold of 66%.

That is a first approximation that allowed us to make a first screening. However the situation is more complicated. Firstly, the CO diffuse is not reliable for kinematic separation; secondly, the line of sight might include gas from different regions of the Galaxy with different emissivities, intermediate between the local and the 1.5–4.5 kpc one. For this purpose, for the selected clouds the expected flux from the entire line of sight has been estimated in two cases: a *uniform scenario*, where the gas along the line of sight emits with a constant emissivity, similar to the local value, φ_γ^{loc} , and a *radial dependent scenario*, where the emissivity depends on the galacto-centric location, r , of the gas, $\sum_i \varphi_\gamma^{r_i}$ and checked that they were distinguishable of an adequate level. For the latter case, I considered the gamma-ray fluxes of the rings derived by the Fermi-LAT collaboration (see Fig 1.13). The corresponding values for each ring are included in Table 2.3 and have been derived by fitting a power law $\varphi_\gamma = \varphi_{\gamma,0}(E/E_0)^{-\alpha_\gamma}$ to the points reported in Acero et al. (2016) [111]. To predict

Ring	$\varphi_{\gamma,0}(2 \text{ GeV})$ [GeV cm ⁻² s ⁻¹ sr ⁻¹]	α_{γ}
0.5–1.5 kpc	6.4×10^{-28}	2.77
1.5–4.5 kpc	1.3×10^{-27}	2.43
4.5–5.5 kpc	4.6×10^{-28}	2.47
5.5–6.5 kpc	5.2×10^{-28}	2.47
6.5–7 kpc	4.9×10^{-28}	2.50
7–8 kpc	4.5×10^{-28}	2.50
8–10 kpc	4.4×10^{-28}	2.60
10–16.5	2.4×10^{-28}	2.63
16.5–50 kpc	1.9×10^{-28}	2.67

Table 2.3 Emissivity (at 2 GeV) and spectral index for different galactocentric rings derived by fitting the measurements of Acero et al. (2016). The error relative to the fit is not reported as it is very small compared to the systematic error of these kind of investigations that is of the order of 30% due to the uncertainties on the gas column density.

the γ -ray flux contributed by each ring, one should know the fraction of gas that belongs to each of them. I evaluated the fraction of gas density that falls in each ring in terms of clouds, as they have a better determined distance with respect to the diffuse gas. To do so, I determined which clouds overlapped (also partially) with the area of interest. In the case of partial overlapping, I considered a fraction of mass, that corresponded to the fraction of pixels that fell in the considered area. For example, if only 5 of 25 pixels that belong to one cloud overlapped with the area of interest, only the 20% of the mass of the cloud has been considered. Then, knowing the galactocentric distance of the clouds from the catalog, the mass can be easily partitioned in the galactocentric rings. Because of the high degree of completeness of the catalog (98%), molecular clouds of the Miville-Deschênes-catalog trace completely the molecular medium. The correspondence between clouds and diffuse is also tested by the authors of the catalog [87] by comparing the values of surface density derived from clouds, to those derived with diffuse and assessed a good agreement between the two quantities. As a cross-check, for the selected regions, the A parameter derived from the dust column density has been compared to the one derived as a sum of the ratio M_5/d_{kpc}^2 of each cloud. The two estimations gave comparable results (see Table 2.4). Small difference can arise both because in the case of clouds the mass is considered to be uniformly divided among

#	(l, b) [$^{\circ}$]	v [km s^{-1}]	θ [$^{\circ}$]	d [kpc]	$d^{px} (\mathcal{P})$ [kpc]	R_{gal} [kpc]	A_{tot}^{dust}	A_{tot}^{MC}	X
57	(2.21, -0.21)	8.43	0.55	12.69	13.64(0.4)	4.21	2.59	2.68	0.47
78	(2.93, 0.27)	25.85	0.33	10.94	10.81(0.6)	2.49	1.07	1.83	0.63
120	(22.46, 0.16)	89.33	0.31	10.3	9.57(0.7)	4.06	0.77	0.78	0.34
135	(24.4, -0.09)	112.09	0.33	6.45	6.06(1.0)	3.74	0.91	1.06	0.46
148	(342.2, 0.26)	-79.0	0.46	5.26	5.27(0.9)	3.85	1.47	1.35	0.47
368	(5.43, -0.38)	20.87	0.28	12.57	12.38(0.75)	4.19	0.49	1.11	0.50
411	(23.71, 0.31)	108.99	0.35	6.26	6.03 (0.9)	3.74	1.04	0.60	0.28
1155	(3.93, -1.02)	59.32	0.47	10.01	8.92(0.7)	1.64	0.67	0.85	0.35
1312	(351.5, 0.22)	-43.21	0.46	11.76	11.47(0.6)	3.58	1.11	1.08	0.43

Table 2.4 Physical parameters of the chosen molecular clouds in the 1.5–4.5 kpc region from the MD-catalog. Both the distance reported in the catalog d and the one derived by the parallax based rotation curve d^{px} are reported. For the latter, the probability \mathcal{P} that the cloud is at that position is also reported. A_{tot}^{dust} and A_{tot}^{MC} are the A -parameters calculated for the entire column, both from the dust measurements [101] and as sum of clouds. Finally X is the fraction of gas that does not belong to the 1.5–4.5 kpc region, according to CO-line measurements.

all the pixels, and this is often not the case, and because the CO and dust template might differ in some locations.

The physical parameters of the analyzed regions, including the position (l, b, v) the angular extension (θ) and the distance from us (d) and from the galactic center (R_{gal}) , are reported in Table 2.4. To validate the cataloged distances, we compared them to the values derived with a parallax calibrated rotation curve [152], using the online available tool¹. The latter calculates a distance probability function, based also on the position of known spiral arms. The values derived in this way, d^{px} , are also presented in the Table (2.4), together with the probability, \mathcal{P} , that the cloud falls at the given location.

The resulting fluxes could then be compared with the flux expected in the case of a uniform (coincident with the one measured in the 8–10 kpc ring) or a radial-dependent emissivity, see Fig. 2.13. The local flux determined from the AMS02 and Dampe experiment, as in the previous section is also shown. The latter is softer than the value measured in the corresponding ring and therefore is worth to show it. The expected emissivity for each ring is also shown in the figure, to demonstrate that in each case the contribution of the 1.5–4.5 kpc ring is expected to be the dominant one. Nevertheless, none of the flux of the analyzed regions matches

¹<http://bessel.vlbi-astrometry.org/bayesian>

with the high values measured in the named ring. Conversely, in several cases the flux is consistent with the values measured in the local 8-10 kpc ring. Note that since the spectral points are derived for the entire column of gas, the spectrum needs to be low everywhere along the line of sight, to match with the low emissivity of the local environment. Any deviation from the local flux in fact, would produce an enhanced flux.

2.3.4 *The Central Molecular Zone*

The central part ($\lesssim 600$ pc) of the Milky Way contains a high concentration of molecular gas. The mass of this region amounts to $3 \times 10^7 M_{\odot}$ of which 20-30% is comprised within $0.4^{\circ} < l < 0.9^{\circ}$ and $-0.3^{\circ} < b < 0.2^{\circ}$, in the so-called Sagittarius B complex, that lies only 100 pc from the GC. The complex has a high enough mass, $\sim 10^7 M_{\odot}$, to be seen also at the huge distance of 8.5 kpc, having $A > 1$. The density in this central region reaches values of about 10^4 cm^{-3} , much higher than the average value that characterizes the Galactic disk. The turbulence in this zone is also higher, with values of velocity dispersion as high as ~ 50 km/s. The high velocity dispersion in this region do not allow an accurate kinematic decomposition for the motivations explained in the previous section. In addition, the high density of this region causes a high degree of saturation of CO, making it a non-reliable tracer of this part of the Galaxy. For this reason, when analyzing this complex, a template derived from dust is used. Observations of CH, HCN, CS and other molecules [153] show that the gas is for the most part concentrated in the galactic center zone, so that the bi-dimensional dust templates can be safely employed.

A dedicated analysis of the region of Sagittarius have been carried out by Yang et al. (2015) [154] and has been newly analyzed in Aharonian et al. (2020) with almost double amount of data. Both analyses agree on a spectrum very similar to the one measured at Earth. Similar values are also found in the analysis of the diffuse rings, in the innermost part of the galaxy [111, 130]. The analysis of the same region conducted at higher energies with H.E.S.S. [155] instead show a much flatter spectrum, as if the GeV and the TeV parts were uncorrelated, see Fig. 2.14.

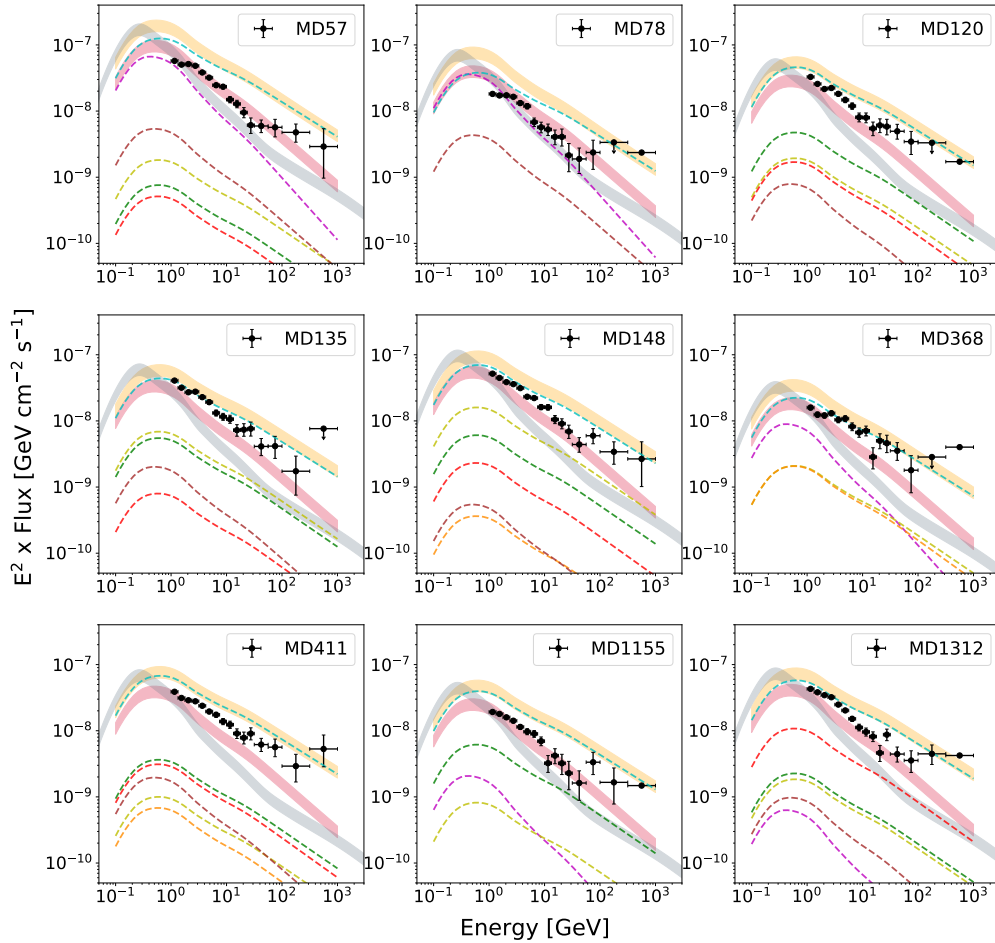


Fig. 2.13 Spectral energy distribution derived from the analyzed regions corresponding to the named clouds (black points). The expected γ -ray fluxes in case of a uniform and a radial emissivity are shown as yellow and red areas, respectively. The local γ -ray flux derived from direct CR measurements is also shown in blue. The area represents the 20% uncertainty that derives from the column density. The fluxes expected from each ring in the given direction are also plotted as dashed lines, respectively: 0–1.5 kpc (magenta), 1.5–4.5 kpc (cyan), 4.5–5.5 kpc (green), 5.5–6.5 kpc (yellow), 6.5–7 kpc (orange), 7–8 kpc (red), 8–10 kpc (brown), 10–16.5 kpc (violet), 16.5–50 kpc (blue).

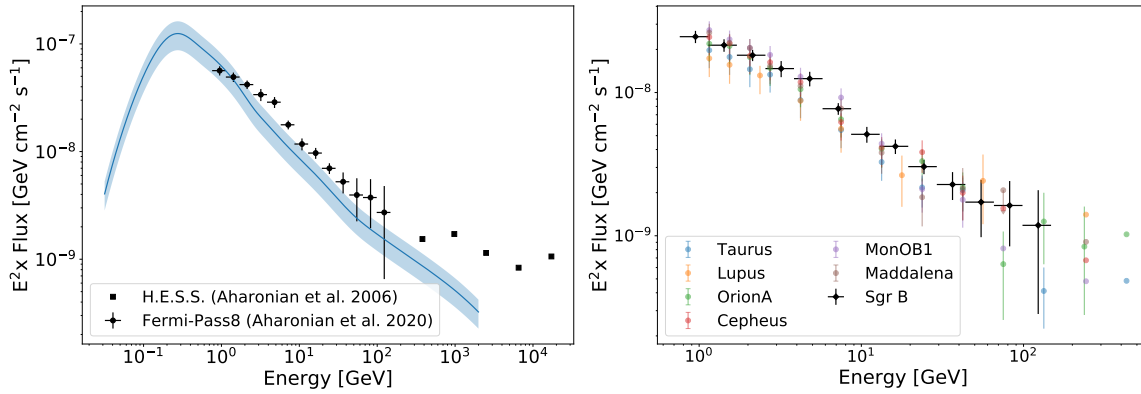


Fig. 2.14 Left panel: spectral energy distributions derived for the Sagittarius B complex by Fermi-LAT [151] (black bullets) and by H.E.S.S. [155] (black squares), compared to the flux expected from a local spectrum of cosmic rays (see previous sections). Right panel: spectral points of Sagittarius B compared to the one extracted in the clouds of the Gould Belt [151]. Fluxes have been normalized to $A = 1$.

2.4 DISCUSSION OF THE RESULTS

The results presented in the previous sections provide a very wide overview of the cosmic-ray galactic population through the emission of molecular clouds. The proton spectrum, embedded in each cloud, has been extracted with *naima* [121], with the procedure explained in section 2.2 and the results are reported in Table 2.5 and are displayed and compared to the values that characterize the rings in Fig. 2.15. In the Figure, the points relative to the clouds of the 1.5–4.5 kpc region are indicated as upper limits, because they are derived from the entire column of gas that comprises also parts that do not belong to this distance. A fiducial value of the γ -ray emissivity and of the cosmic-ray density is obtained subtracting the expected emissivity and CR density of the background fraction of gas, X , assuming that the latter is characterized by the local value of cosmic rays. Note that if the background were higher, the points (plotted in red) would be even lower.

A first conclusion can be drawn by looking at the values extracted from the clouds in the Gould Belt. The great similarities of the cosmic-ray spectrum to the value measured by direct experiments in the vicinity of Earth is striking. That means that the amount of cosmic rays measured in the Earth vicinity is not peculiar of the region that surrounds the Earth, but characterizes also other regions outside the Solar System. This allows us to exclude that the spectrum of local cosmic rays is determined by one or a collection of relatively nearby sources and suggests that is

rather contributed by the entire population of cosmic rays, that reached us and the Gould belt region after mixing in the propagation through the Galaxy. Nevertheless, due to the vicinity of the Gould Belt complex (~ 500 pc) one can not in principle exclude the possible influence of sources located within a few hundred parsec, or for example within the Gould Belt itself. The latter, in fact, hosts regions of star formation and several young stellar objects, which are potential cosmic-ray accelerators [63]. This hypothesis is ruled out by observing similar parameters also in the outermost part of the Galaxy, at galactic distances larger than 10 kpc. It is sufficient to see the example of Maddalena and of the clouds R418 and R429, located at 10.2 kpc, 10.58 kpc, and 10.35 kpc, respectively, that show a high degree of agreement with the local parameters. This rejects completely the possibility of a local bias determined by close sources, as the area of influence of single sources cannot extend over more than a few hundred parsec. Nevertheless, in order to prove that the cosmic ray sea is uniform, similar parameters need to be found in different parts of the Galaxy. In particular, to exclude or confirm the dependence of the cosmic-ray spectrum on the galacto-centric distance, clouds in different locations, but at a similar distance from the Galactic center need to be compared. Going towards inner galactocentric regions it appears that the cosmic-ray density increases, as observed also in the ring-based analyses, however, the values are not unique and a certain degree of fluctuations is observed. The best example is given by the values measured in the 6-8 kpc region. The clouds here show different values of the emissivity and correspondingly of CR densities, that are not compatible to one another even when considering the large systematic uncertainties. Remarkably a cloud in this region, R964, located around 6 kpc from the GC, shows compatible cosmic-ray normalization as the one measured locally. More closer to the center instead, the clouds in the region comprised within 4 and 6 kpc show a systematic enhancement with respect to the values measured in other locations. The maximum value of CR density measured from the ring analysis also falls around 4 kpc, (4–6 kpc for Yang et al. 2016 [130] and 1.5–4.5 kpc for Acero et al. 2016 [111]). This is natural, considering that the distributions of most of the potential CR sources, SNR [69], pulsars, young stellar objects peak in this location (see Fig. 1.6). A certain degree of scatter is also observed in the clouds of this ring, confirming the idea that such enhancement is related to the higher density of accelerators there. In fact, the other possible scenario, namely the modification of the propagation properties in different parts of the Galaxy, applies over larger areas, and does not

account for modifications of the diffusion parameters in such a small scale. A confirmation of this tendency comes from the observations of very low fluxes from regions corresponding to gamma-ray clouds in the 1.5-4.5 kpc ring. This area, that is supposed to have the highest density of cosmic rays, according to the observations of Fermi-LAT, hosts several objects where the CR flux is as low as the one measured in the local environment. This is a strong piece of evidence in favor of the idea of a uniform cosmic-ray sea, that is randomly enhanced in the proximity of sources. Due to the analysis methods, it is difficult to comment on the fluctuations in this region. However, the derived parameters, both for the total column and after the subtraction of a fiduciary background are indeed quite different, strengthening the argument in favor of a source-enhanced CR sea. The confirmation of a soft and low flux also in the extreme region of the Galactic center, corresponding to the location of the Sgr B complex, is the final confirmation that the value measured at Earth is indeed characteristic of many different environments of the Galaxy. More extensive mapping of the Galaxy is desirable, and necessary to have the final evidence for a uniform sea scenario. However the potential of Fermi-LAT is almost saturated, and a new GeV-instrument with 2-5 times improved sensitivity is needed to extend these studies, as motivated in Chapter 4.

The only limitation of this analysis arises from the uncertainty in the determination of the gas density. The value of cosmic-ray density is in fact strictly dependent on the value of the column density of the target. In the case of gas traced by CO, as discussed in section 1.2 the uncertainty is of the order of 30% and it derives from the conversion factor, X_{CO} , between CO and H₂. In addition, CO fails to trace the molecular medium, when its density is too low in comparison to H₂, making it possible to underestimate the mass of the gas. For this reason, when possible it is preferable to use dust as a tracer. The latter is more sensitive, although at some values of density the linear relation between gas and dust has a larger spread. In general, an uncertainty $\lesssim 20\%$ is assumed for this tracer. Unfortunately, being a measure of absorption when using dust is not possible to separate the gas along the line of sight and the entire column density has to be considered. In such cases, one has to assure that the molecular cloud of interest is not eclipsed by other more massive or closer clouds. Promising results for these purposes are now coming from the GAIA collaboration, that managed to create a three-dimensional map of the interstellar dust in the Milky Way by constraining it with the very precise determination of star distances [103]. Nevertheless, the results here presented on molecular

clouds confirm that the method works and can be extended, with some precautions, to different parts of the Galaxy.

		R_{gal} [kpc]	$\rho_{0,CR}$ (30 GeV) [$10^{-13} \text{ GeV}^{-1} \text{ cm}^{-3}$]	α
> 10 kpc	R418	10.6	0.91	2.69 ± 0.05
	R429	10.3	0.85	2.61 ± 0.05
	Maddalena	10.2	0.72	2.93 ± 0.07
Solar Ring (8–10 kpc)	Monoceros OB1	9.1	0.72	3.00 ± 0.07
	R610	8.9	1.14	2.77 ± 0.05
	R612	8.7	0.55	2.76 ± 0.16
	Cepheus	8.6	0.72	2.85 ± 0.05
	Taurus	8.4	0.58	2.89 ± 0.05
	Orion A	8.4	0.69	2.83 ± 0.07
	Lupus	8.2	0.56	2.73 ± 0.09
6-8 kpc	R933	7.1	1.72	2.69 ± 0.02
	R900	6.6	1.34	2.73 ± 0.04
	R964	6.4	0.78	2.58 ± 0.05
	R876	6.0	1.06	2.82 ± 0.05
4–6 kpc	R243	5.8	2.59	2.82 ± 0.02
	R877	5.5	2.06	2.69 ± 0.02
	R902	5.4	1.54	2.69 ± 0.03
	R804	4.6	1.53	2.58 ± 0.04
	MD57	4.2	0.88	2.66 ± 0.02
	MD368	4.2	1.34	2.52 ± 0.03
	MD120	4.1	1.45	2.68 ± 0.03
1.5-4 kpc	MD148	3.8	1.29	2.66 ± 0.02
	MD411	3.7	1.42	2.59 ± 0.02
	MD135	3.7	1.54	2.68 ± 0.03
	MD1312	3.6	1.40	2.71 ± 0.02
	MD78	2.5	0.71	2.66 ± 0.03
MD1155	1.6	1.09	2.68 ± 0.03	
CMZ (< 1 kpc)	Sagittarius B	0.1	0.78	2.80 ± 0.03

Table 2.5 The parameters for the cosmic-ray density derived for all the analyzed clouds with naima. The normalization $\rho_{0,CR}$ refers to the pivot value of 30 GeV.

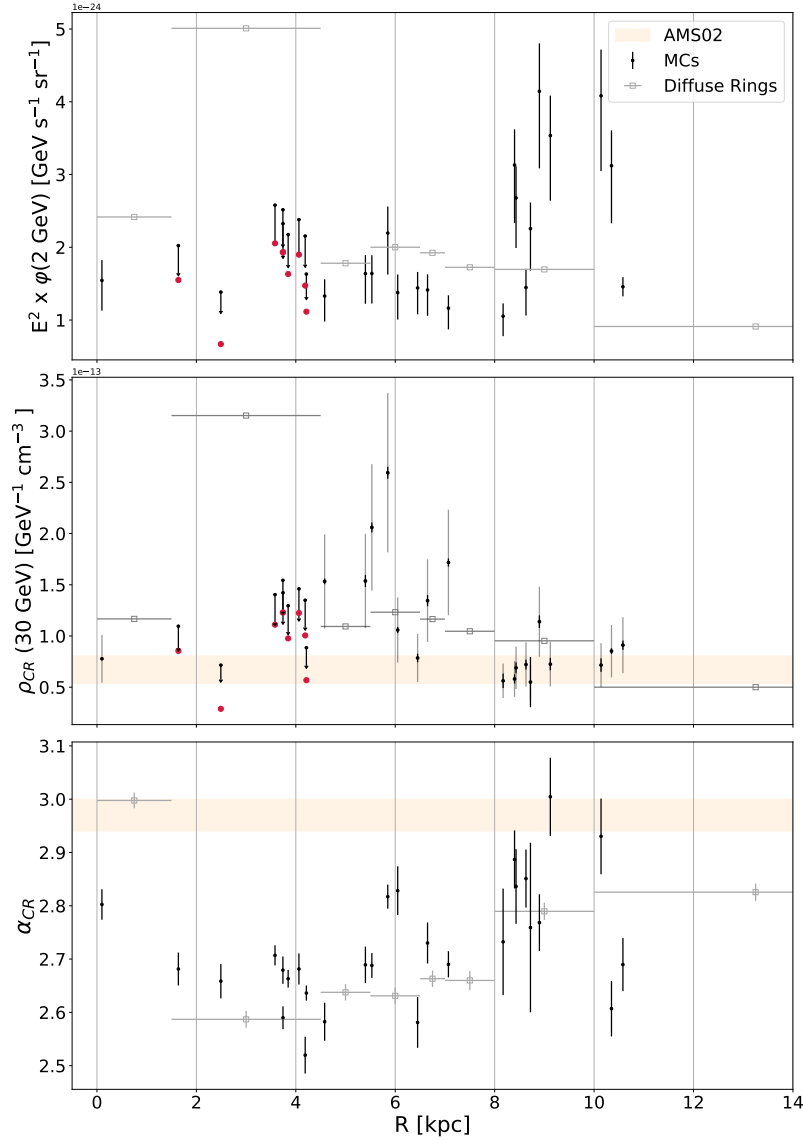


Fig. 2.15 The γ -ray and CR parameters are shown for each cloud against their distance from the Galactic Center. The top panel shows the gamma-ray emissivity at 2 GeV, the middle panel shows the cosmic-ray density at 30 GeV and the bottom panel shows the CR power law spectral index. The grey points indicate the corresponding values obtained from the ring analysis, in ref. [111]. The values for the clouds in the 1.5–4.5 kpc regions are indicated as upper limits, since they are characteristic of the entire column of gas. The red points instead indicate the derived value for these clouds after subtraction of the corresponding fraction of gas, assuming that it emits as the local (8–10 kpc) ring. The orange area highlights the local spectrum of cosmic rays, derived from the points of AMS02.

This chapter was based on the results published in:

- [151] Aharonian, F., Peron, G., Yang, R., Casanova, S., & Zanin, R. (2020). Probing the sea of galactic cosmic rays with Fermi-LAT. *Physical Review D*, 101(8), 083018.[151]

and discussed in the under-review letter:

Peron, G., Aharonian, F., Casanova, S., Yang, R., & Zanin, R. (2020) Probing the Cosmic-ray density in the inner Galaxy, *submitted to The Astrophysical Journal Letters*.

COSMIC-RAY ACCELERATORS AND THEIR SURROUNDINGS

Supernova remnants have been proven to be efficient accelerators of CR particles both at GeV and TeV energies, thanks to the effective diffusive shock acceleration mechanism discussed in sec 1.1.3. Nevertheless, high-energy observations of these objects always show a cutoff well before PeV energies, casting doubts on the ability of these sources to contribute to the CR spectrum up to the knee, at 10^{15} eV. The action of energy-dependent escape might play a role in shaping the energy spectrum of the remnant, especially in the case of middle-age (~ 10000 yr) supernova remnants, for which the shock has already started to slow down and particles have started to leave the remnant. In this case, to find high-energy particles, the observation of the surrounding is of great help, as it is expected to host the escaped particles. Only from the combined observations of the emission of the remnant and of the escaped particles one can reconstruct the acceleration history of the source. Moreover, the correlation with the gas distribution allows to further constrain the dynamics of the escape.

In the following, I present the latest analysis of Fermi-LAT data on W44 and its surrounding medium, that was shown to be populated by the particles escaped from the remnant. The emission of the supernova remnant is discussed, to determine whether it is most likely of leptonic or hadronic origin. Moreover, the configuration of the escaped particles is compared with the gas density to understand if they are related.

3.1 THE SUPERNOVA REMNANT W44

W44 is a supernova remnant located at $l, b = (34.6^\circ, -0.6^\circ)$. Its radial velocity has been estimated from OH masers observations to be $v = 46 \text{ km s}^{-1}$, which corresponds

to a distance of $d = 2.2$ kpc [156]. The interior of the remnant shows thermal X-ray emission, therefore W44 is classified as *mixed-morphology* supernova remnant. This class represents 8% of the entire population of supernova remnants and are of particular interest as, according to OH masers and infrared observations, they are often found to interact with molecular clouds of the surrounding medium [157]. Inside W44, a Pulsar, PSR B1853+01, and its nebula have been detected both in radio and in X rays, but they show no γ -ray counterparts [158]. The age of the supernova remnant has been estimated from its central pulsar characteristic age ($\tau_c \sim P/\dot{P}$, where P and \dot{P} are the pulsar period and its time derivative), to be approximately 2×10^4 years [159]. This agrees with the estimates deriving from the extension of the X-ray-emitting region (~ 15 pc), which suggests a minimum age of $\sim 1.7 \times 10^4$ yr, assuming an initial energy $\lesssim 10^{51}$ erg and an average density of the interstellar medium of 1 cm^{-3} [160]. The large age of W44 suggests that this supernova remnant is in the Sedov-Taylor phase, so the shock has already overcome its peak and it is slowing down. At this stage, it is expected that higher-energy particles have started to leave the remnant. The high-energy spectrum of the remnant is expected to reflect this behavior, namely to show a suppression in the highest energy part. At the same time, over-densities of relativistic particles are expected in the regions that surround the remnant. The shape of W44 is influenced by the interaction with the interstellar medium [161]. It shows in fact an elliptical shape, elongated along the Northwest-Southeast direction, as the maps in Fig. 3.1 show. The latter have been obtained in the radio (red), X-ray (green), and gamma-ray (blue) band. The magnetic field of W44 extends along its major axis, as determined by polarization measurements [162]

3.1.1 *Gamma-ray emission from the Remnant*

I analyzed Pass8 data that Fermi-LAT accumulated for 9.7 years in a 10° region of interest (ROI), centered on W44. I followed the standard procedure and applied the standard selection of the data, as described in section 2.2. After having optimized the model containing the sources from the 4FGL catalog [51] and the latest released diffuse galactic (gll_iem_v07.fits) and extragalactic (iso_P8R3_SOURCE_V2_v1.txt) backgrounds provided by the Fermi-LAT collaboration, I modeled the potential new sources. Once all the background sources have been fitted, the morphology of the remnant has been investigated. For this purpose, only data of energy higher than 1

GeV have been considered, to take advantage of the better point-spread function of the LAT. Nevertheless, the poor angular resolution of γ -ray instruments do not allow to evaluate the morphology by imaging (see Fig. 3.1), and a statistical investigation is needed. Morphological studies in these circumstances proceed by fitting different spatial templates (see Table 3.1), to find the one that better reproduces the data. For this purpose, the maximum log-likelihood values, \mathcal{L} , (Eq. 2.2.4) of the different tested models are compared: the model with the highest \mathcal{L} is considered the best in describing the data. A minimum difference of $\sqrt{\mathcal{L}} = \sigma = 3$ is considered necessary to prefer one model over another, otherwise the models are considered equivalent. The best morphology for W44 resulted to be an elliptic ring of axis $[0.18^\circ, 0.3^\circ]$ and $[0.13^\circ, 0.22^\circ]$, in accordance with the morphology reported in the 4FGL catalog. Interestingly, this is also similar to the shape revealed in radio continuum at different wavebands (e.g. 1.4 GHz [163]; 74 MHz and 324 MHz [164], see Fig. 3.1). This could be an indication, in case of leptonic origin of the radiation, that the same population of electrons is responsible both for the radio synchrotron and the γ -ray emission.

Once the morphology has been fixed, the spectral energy distribution (SED) of the remnant has been extracted in the whole energy range covered by Fermi, from 60 MeV to a few hundred GeV. The SED is presented in Fig. 3.3. The systematic uncertainties on the spectral points have been evaluated by performing the same analysis but with a different background template, namely the earliest release of the galactic background of the Fermi-LAT collaboration (gll_iem_v06.fits). The background model, in fact, is constructed based on the the large-scale galactic emission, that suffers from several different uncertainties (see Sec. 1.3.1) and for this reason, it is the main source of systematic uncertainties. Testing two different background models is a way to minimize this effect. The systematic difference between the two analysis results higher below a few hundred MeV where it reaches also 60%, whereas in the rest of the spectrum it is $\lesssim 10\%$.

The SED has a steep rise up to a few GeV and then decreases rapidly, with the last detected point at 200 GeV. To evaluate the best spectral model, the Akaike Information Criterion (AIC) [166] has been used. That allows us to compare models with different degrees of freedom. When the compared models are non-nested, meaning that they differ for more than one parameter, the likelihood method fails. In the AIC method, the parameter $AIC = 2k - 2\mathcal{L}$ is calculated for the different models and compared. k is the number of degrees of freedom and \mathcal{L} is the Log-likelihood, defined in Eq. 2.2.4. The model with the smallest AIC is the preferred

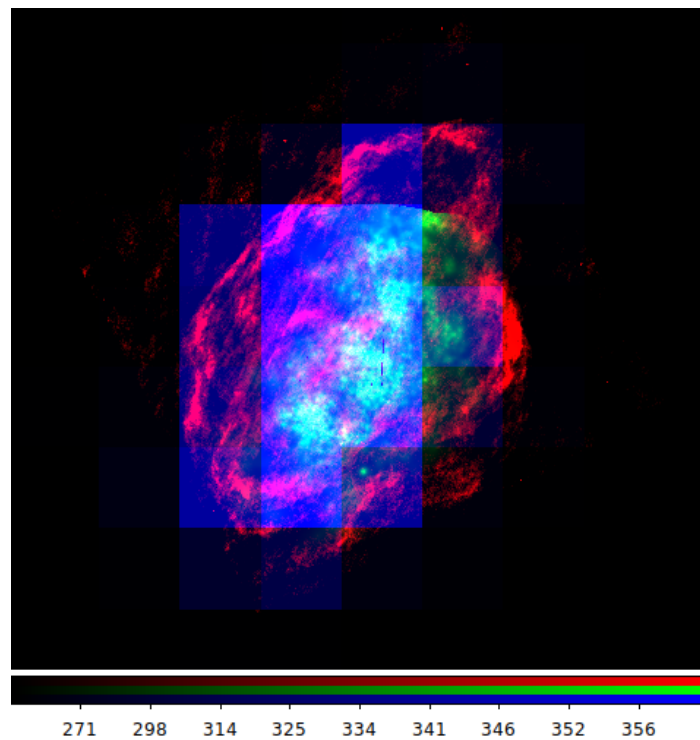


Fig. 3.1 RGB image of the supernova remnant W44 observed in radio at 324 GHz by the Very Large Array (red), in X-rays by CHANDRA between 0.3 and 2.1 keV (green) and in γ -rays in the energy range 1 GeV–1 TeV as seen by the Fermi-Large area telescope (blue). The radio and X-ray maps have been taken from the online-available catalog of supernova remnants from ref. [165].

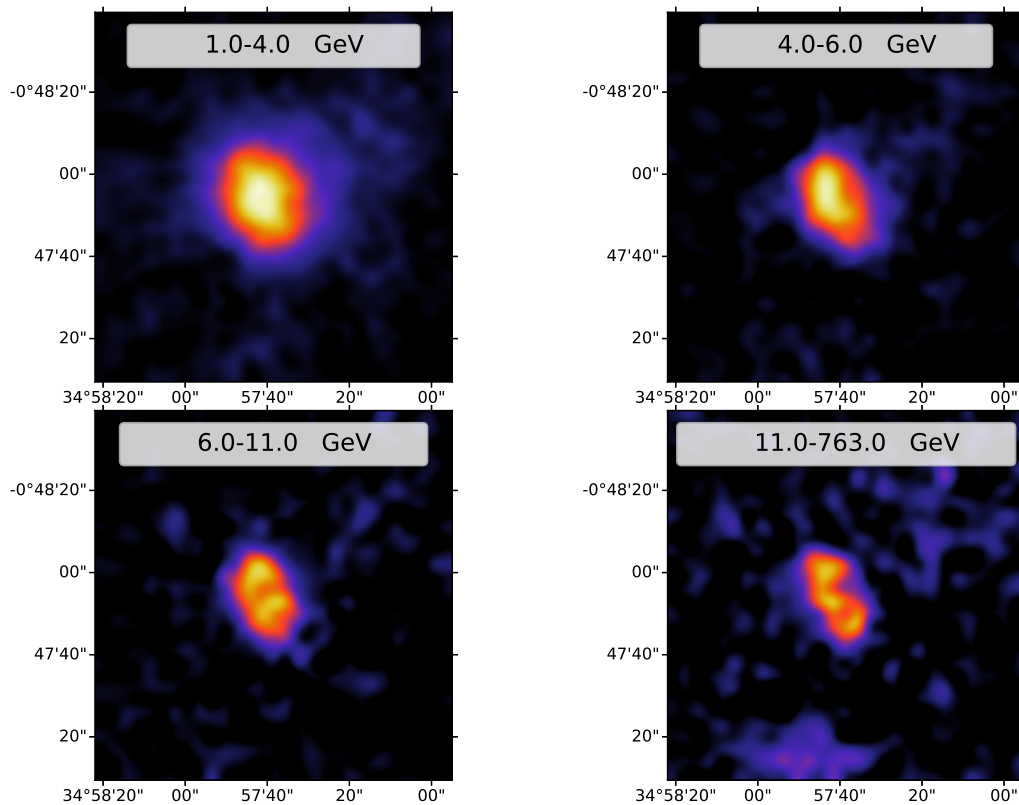


Fig. 3.2 Fermi-LAT count maps of the supernova remnant W44 for different energy ranges after the subtraction of all the background sources. The images have been smoothed, using a bicubic interpolation method included in the python library `matplotlib.pyplot`.

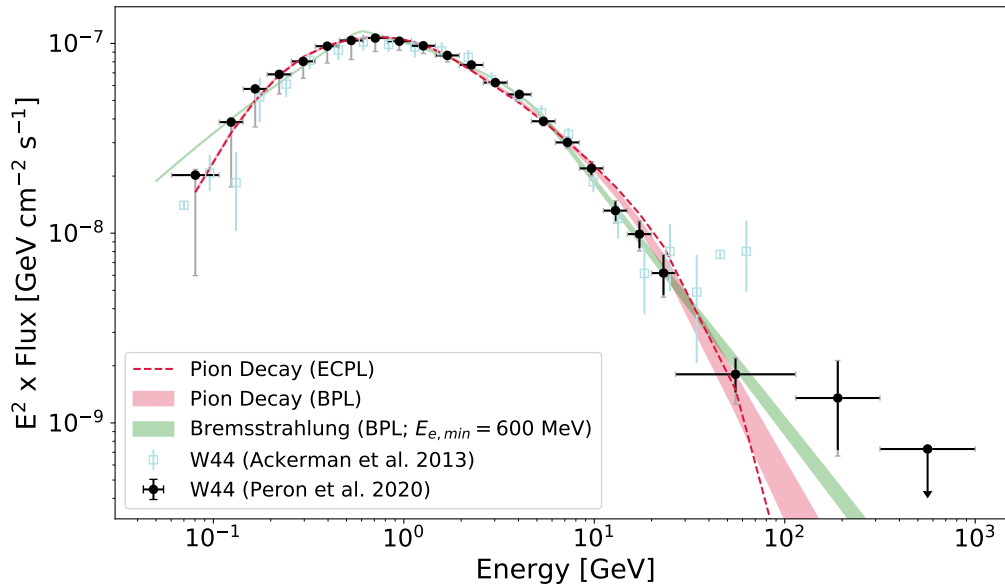


Fig. 3.3 Spectral energy distribution of the supernova remnant W44 as obtained from ~ 10 years of observation with the Fermi-LAT above 60 MeV. The red curves show the hadronic models that best represent the data, the area corresponds to a broken power law in total energy with indices 2.40 ± 0.02 and 3.87 ± 0.14 below and above 39 ± 3 GeV. The area corresponds to the 1σ confidence level of the model. A power law with an exponential cutoff at 71 ± 6 GeV and index of 2.30 ± 0.02 also fits the data and is plotted as red dashed line. The best leptonic model is displayed in green and it corresponds to bremsstrahlung radiation originating from a broken power law spectrum of electrons of minimum energy 600 MeV and with indices 2.32 ± 0.03 below (6.1 ± 0.6) GeV and 3.39 ± 0.07 above. The figure has been adapted from [167]. The points from a previous analysis of the remnant are also shown as light-blue squares [168].

one. For convenience one can calculate a modified parameter, $AIC^* = 2k^* - 2\mathcal{L}$ only considering the difference in numbers of parameters between the considered model and the null hypothesis.

The overall spectrum is well represented by a Log-Parabola function (see Table 3.1):

$$F(E) = F_0 \left(\frac{E}{E_b} \right)^{-(\alpha + \beta \log(E/E_b))} \quad (3.1.1)$$

with $F_0 = (9.5 \pm 0.1) \times 10^{-9}$ ($\text{GeV cm}^2 \text{s}^{-1}$), $\alpha = 2.57 \pm 0.01$, $\beta = 0.235 \pm 0.005$ and $E_b = 2.67$ GeV. Such a shape can be naturally explained by pion-emission [169, 168]. The pion-bump feature at 67.5 MeV (Sec. 1.1.2) has been claimed for

the very first time in the spectrum of W44 itself [168]. However, with Fermi-LAT, that have a low energy threshold of ~ 60 MeV only the second half of the peak is directly observable. This is clear when looking at the data in differential flux ($\propto dN/(dE dA dt)$) representation, as in the right panel of Fig. 3.4, and should not be confused with the spectrum turnover observed around a few GeV in the SED ($E^2 \times \text{Flux}$) representation (left panel of Fig. 3.4). The latter could also be reproduced by a leptonic scenario. A bremsstrahlung spectrum that reproduces the data, for example, could be realized if a sharp low energy cut is introduced in the electron spectrum [168]. Ambrogi et al. (2019) [170] found that, in the case of the supernova remnant HB21, an electron spectrum with a low energy threshold of 400 MeV satisfactorily reproduces the γ -ray data and that the obtained parameters for the electrons were very close to the values that characterize the electron spectrum at Earth. A similar behavior, with a break in the electron spectrum at $E_{e,min} = 600$ MeV could explain the sharp rise also in the case of W44 [168]. One should notice, however, that in this case the spectrum below $E_{e,min}$ assumes a fixed shape $\propto \omega^{-1} \propto E^{-1}$ [171, 172], characteristic of the bremsstrahlung emission of a single electron. The -1 slope (1, in SED representation) is the steepest spectrum obtainable with leptonic processes (IC is not efficient at these energies). Therefore any difference from this slope would be a clear indication of hadronic emission. The SED that I obtained below 1 GeV has a slope of 1.5, slightly higher than the expected value for bremsstrahlung. The systematic uncertainties suggest that the low energy points could be even lower and therefore the spectrum could be even steeper. That excludes even stronger the bremsstrahlung scenario.

The proton spectrum has been evaluated with *naima* (sec. 2.2). Different spectral functions have been tested (see Table 3.2) and a Broken Power Law:

$$F(E) = \begin{cases} F_0 \left(\frac{E}{E_0}\right)^{-\alpha_1} & \text{for } E < E_b \\ F_0 \left(\frac{E_b}{E_0}\right)^{\alpha_2 - \alpha_1} \left(\frac{E}{E_0}\right)^{-\alpha_2} & \text{for } E > E_b \end{cases} \quad (3.1.2)$$

of indices $\alpha_1 = 2.40 \pm 0.02$ and $\alpha_2 = 3.87 \pm 0.14$ before and after $E_b = (39 \pm 3)$ GeV resulted to be the best according to the Bayesian Information Criterion. The latter is implemented in *naima* and is an extension of the likelihood method. The BIC is calculated as: $\text{BIC} = k \ln(n) - 2\mathcal{L}$ where n is the number of data points, k is the number of free parameters and \mathcal{L} is the maximum Log-likelihood. The model with the lowest BIC is the best at describing the data. The method indicates the best model but not

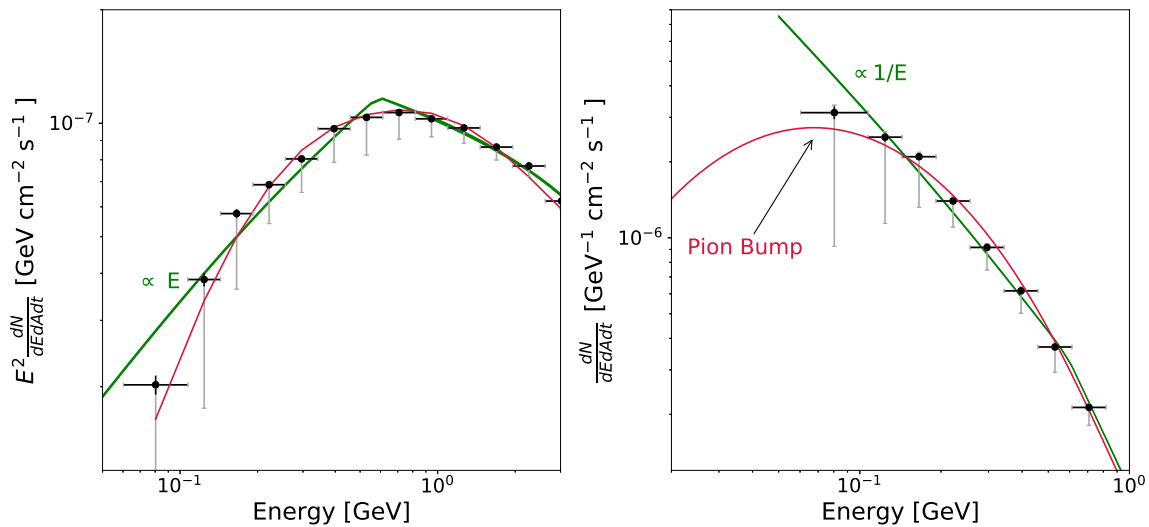


Fig. 3.4 Enlargement of the spectral energy distribution shown in Fig. 3.3 in the region below a few GeV. On the left panel the usual $E^2 \times \text{Flux}$ representation is used, while in the right panel the true differential flux is displayed, to emphasize the pion-bump feature. The figure has been adapted from [167].

the extent to which a model is preferred; I noticed in fact that a Power Law of index 2.3 ± 0.02 with an exponential cutoff at 71 ± 6 GeV equivalently fits the data points up to 100 GeV (dotted red curve in Fig. 3.3). In all the cases the spectrum is softer than expected from the first-order Fermi acceleration, which predicts a spectral index of 2 (see section 1.1.3). Non-linear theories of diffusive shock acceleration (NLDSA) predict an even harder spectrum and therefore cannot account for this behavior. One cause of the steepening could be the amplification of the magnetic field led by streaming instabilities. Although this needs further confirmation, it predicts spectra as steep as 2.3 [59]. An injection spectrum of 2.2–2.4 would allow us to assume a lower CR propagation index $\delta \sim 0.3$, which better agrees with the observations on anisotropy [173]. On the other hand, the very steep spectrum observed above the break ($\alpha_2 \sim 4$) is symptomatic of the effective escape of the highest energetic particles. This is to be expected, due to the age of the remnant. The cutoff predicted by the DSA theory is also a possibility, but the significant points detected above the cutoff energy would require an extra acceleration component as discussed in [174]. Moreover, indications of escaped particles have been revealed in the surroundings of the remnant as discussed in the following.

	Function	\mathcal{L}	AIC*
Morphology (> 1 GeV)	Null hypothesis	95 1065	–
	Radial Gaussian	956614	-1913226
	Ellipse	954330	-1908656
	Elliptic Ring	957958	-1915910
	Radio Template	956770	–
γ -ray Spectrum (>60 MeV)	Power Law	Failed	–
	Broken Power Law	9874900	-19749788
	Exp. Cutoff Power Law	Failed	–
	Log-Parabola	9875084	-19750160

Table 3.1 Results from the modeling of W44. The maximum values of likelihood of the morphological and spectral models tested on the γ -ray observations are reported. Also the reduced AIC* values are reported. The best models have been highlighted in bold.

	Function	BIC
Proton spectrum (Pion decay)	Power Law	894
	Broken Power Law	84
	Exp. Cutoff Power Law	105
Electron Spectrum (Brems.)	Power Law	10308
	Broken Power Law	153
	Exp. Cutoff Power Law	1419

Table 3.2 The different spectral models for proton and electrons tested with naima assuming a pion-decay emission mechanism and a bremsstrahlung radiation model, respectively. The BIC value is used to evaluate the best model and it is reported here for each spectral function. The best models have been highlighted in bold.

3.1.2 *Gamma-ray emission from the surrounding gas*

Supernova remnants are commonly found within giant molecular cloud complexes, as the latter host the formation of massive stars, which, having short lifetimes ($10^6 - 10^7$ yrs), end up in Supernova remnant explosion before having sufficient time to migrate from their place of birth. W44 itself resides in a massive, $M_{surr} \sim 1.5 \times 10^6 M_{\odot}$, molecular cloud complex, as already mentioned in Dame et al. (2000) [73]. This constitutes an optimal target where to look for escaped particles. The particles leaving the remnant are expected to interact with the surrounding medium producing detectable γ -ray emission. The high mass of the cloud around W44 would allow us to observe this complex with Fermi-LAT even if only illuminated by a low and steep spectrum of cosmic rays as the local one. At the distance of the remnant, $d = 2.2$ kpc, in fact, the corresponding A parameter is about 3, well above the detection threshold for MCs with Fermi-LAT (Fig. 2.1). Thus, any deviation from the local value, which we assume to be representative of the Sea, caused by freshly accelerated particles, would be easily detectable.

I analyzed this region after having fixed the model for the SNR, which is the brightest source in the ROI. I proceeded then in two steps: firstly I modeled all the sources located within 2-degrees from the remnant and secondly, I analyzed the emission of the gas complex. The 4FGL catalog contains several sources in this region, they are listed in Table 3.3 and their position is plotted in Fig. 3.5. Three unidentified point sources are detected in the northwestern side of the remnant, one of these (4FGL J1852.6+0203) has been indicated as possible young pulsar [175], while the others are still unknown. On the southwestern side, there appear other two unidentified point-sources very close to each other. Also in this case one has been suggested to be a young pulsar but the association is still uncertain. Other interesting sources in the area are the point source 4FGL J1857.6+0143, that was a confused source in the earlier 3FGL catalog and has now been confirmed to be a pulsar, and the extended sources 4FGL J1857.7+0246e and 4FGL J1857.7+0246e, that have been recently added to the Fermi catalog of sources and coincide with the pulsar wind nebula (PWN), HESS J1857+026 and with the supernova remnant Kes79, respectively. All the sources listed in table 3.3 have been removed from the model and re-modeled in accordance with the AIC method. For two couples of point-sources, respectively at the northwestern (4FGL J1854.7+0153 and 4FGL J1855.8+0150) and at the southeastern (4FGL J1857.4+0106 and 4FGL J1857.1+0056) edges of the

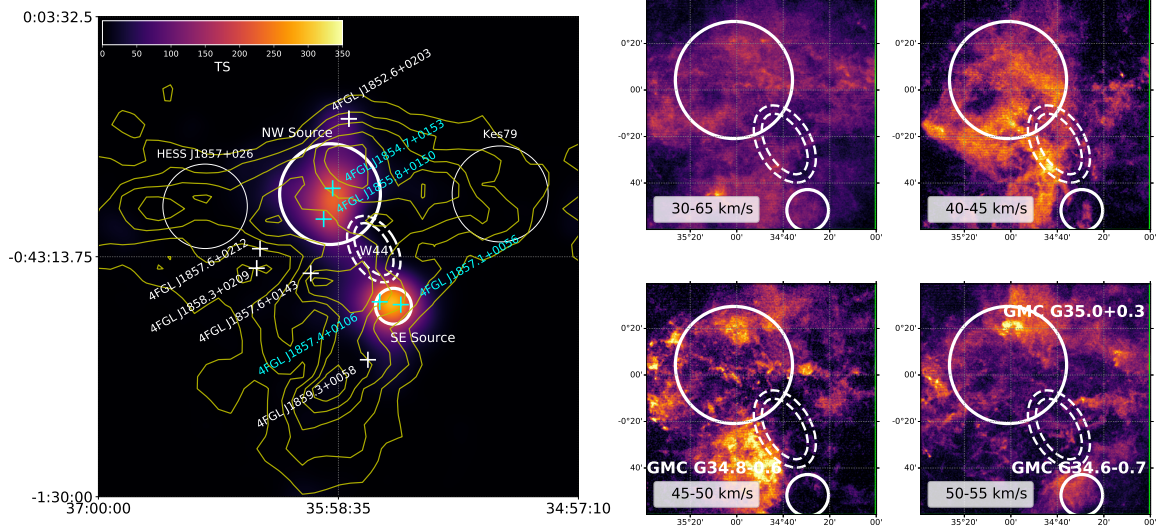


Fig. 3.5 *Left side*: test statistic map of the two gamma-ray extended sources, NW-Source and SE-source. The white regions indicate the configuration of sources in the final model, the cyan regions indicate the sources that have been removed. The CO gas contours from the survey of Dame et al. (2000) [73] are plotted in yellow. *Right side*: the gas in the region of W44 as seen by the Nobeyama telescope [75] in four different velocity ranges, as indicated in the figure legend. The density has been normalized to the average value in each panel. The white regions indicate the two extended γ -ray sources, NW- and SE-source (solid) and the shell of the SNR (dashed). The figure has been adapted from [167]

remnant, a single disk morphology is preferred. The latter have been evaluated with the AIC method in the same fashion as for the morphology of W44. The two new extended sources have been named NW-source and SE-source, to indicate that they are located North West and South East with respect to W44. The extension of the sources has been evaluated with the fermipy dedicated function, `GTAnalysis.extension()`, that tests different extended models and evaluates the best one by comparing the likelihood values. The test statistic value, which evaluates the likelihood of an extended-source hypothesis, against the point-source hypothesis is also returned and for both sources it was higher than 40, meaning that the extended model is preferred. An extension of $(0.42 \pm 0.03)^\circ$ and $(0.15 \pm 0.02)^\circ$ resulted for the NW- and the SE-source, respectively. Simultaneously, a fit on the position is also performed, the new centers are found at $(l, b)_{NW} = (35.00^\circ, 0.04^\circ)$ and $(l, b)_{SE} = (34.45^\circ, -0.86^\circ)$. Interesting to notice that the sources fall at two opposite edges of the SNR, along the major axis, which is the direction along which the magnetic field develops [162].

4FGL name	(l,b) ^o	3FGL name	Association	New Model
J1852.6+0203	(34.90,0.67)	J1852.8+0158	YNG PSR candidate ¹	Point Source
J1854.7+0153	(34.99,0.12)	–	–	0.4°-Disk (NW)
J1855.8+0150	(35.07,-0.14)	–	–	
J1857.4+0106	(34.605,0.026)	–	–	
J1857.1+0056	(34.43,-0.849)	J1857.2+0059	YNG PSR candidate ²	0.15°-Disk (SE)
J1857.6+0143	(35.18,-0.59)	J1857.8+0129c	PSR J1857+0143	–
1857.7+0246e	(36.12,-0.15)	–	PWN HESS 1857+026	0.3° Disk
J1858.3+0209	(35.63,-0.54)			–
J1857.6+0212	(35.60,-0.38)	J1857.9+0210	MC/SFR ³ HESS J1857.9+0210	–
J1852.4+0037e	(33.61,0.08)	–	SNR Kes79	0.4°-Disk

Table 3.3 4FGL sources in the region of W44; the bolded sources are the ones for which we found a new morphology.

Previously, at these locations, two gamma-ray emitting sources have been unveiled and were associated with the emission of cosmic rays penetrating the dense molecular cloud complex [176]. However, the extension of the gas complex is much larger than the scale of the gamma-ray emitting sources and there is no significant enhancement of the gas density at the location of the sources, as the right panel of Fig. 3.5 displays. The CO data of the high-resolution Nobeyama telescope indicate that the big gas complex can be decomposed into several smaller molecular clouds of masses $(0.3-3.0)\times 10^5 M_{\odot}$ [177]. However, there is no direct correspondence between the newly identified γ -ray sources and these clouds. NW-source partially overlaps with the cloud GMC G35.0+0.3(V=50), as it can be seen in the corresponding velocity panel in figure 3.5. SE-source, in turn, is located in the proximity of GMC G34.6-0.7(V=53), a small cloud southern of the remnant. The latter has been shown to have some indication of interaction with the remnant, even if it was not confirmed. Otherwise, the gas density in these location is close to the average $n_{NW} \sim n_{SE} \sim 10 \text{ cm}^{-3}$. The mass of these clouds is also quite small: it has been calculated to be $M_{NW} = 2 \times 10^5 M_{\odot}$ and $M_{SE} = 0.4 \times 10^5 M_{\odot}$, from CO, with an uncertainty of 30%. Interesting to notice that other bigger or closer clouds in the region, like G34.8-0.6 (V=48 km/s), show no γ -ray emission, even if the latter is dynamically interacting with the remnant.

The SEDs of NW- and SE-source have been derived and are shown in figure 3.6, where they are compared to the SED calculated for clouds of the same mass, illuminated by the local flux of CRs. The latter have been derived from the experimental points measured by the AMS02 and DAMPE experiments, as described in previous sections, from Eq. 1.1.14. The spectra of both clouds are very different from the

local one, and it is enhanced several times especially above a few GeV. According to the AIC method (see Table 3.4), both spectra can be described by a Log-Parabola function (Eq. 3.1.1) as they both have a steep rise before a few GeV and then fall off quickly. The fit has been performed keeping fixed $E_b = 1$ GeV. The spectral parameters resulted in the two cases read: $\alpha_{NW} = 2.14 \pm 0.03$, $\beta_{NW} = 0.18 \pm 0.02$ and $\alpha_{SE} = 1.62 \pm 0.17$, $\beta_{SE} = 0.25 \pm 0.06$. The NW-source spectrum shows a peak around ~ 1 GeV that can be identified as the pion-bump feature. Assuming a hadronic origin for the emission, the spectrum of protons has been derived with *naima* and it resulted a power law of index $\alpha = 2.61 \pm 0.03$. The latter is harder than the flux measured in the vicinity of Earth ($\sim E^{-2.85}$) and it is also harder than the spectrum of the supernova remnant, as clearly visible in the rightmost panel of Fig. 3.6. In particular, while the spectrum of W44 drops above few tens of GeV, the spectrum of NW-source continues showing no sign of attenuation. It is possible that particles of > 100 GeV may have left the remnant and are populating the region of NW-source, while lower energy protons are still confined within the shell. The flux of the SE-source in turn, shows a bump feature at several GeV, that cannot be identified as the pion bump, because it occurs at higher energies. The flux after that bump drops quickly as $E^{-3.4}$ (in photons). This shape could be obtained from a pion-decay mechanism if the parent proton spectrum is suppressed both at low and high energy. This behavior is reflected into the proton spectrum derived with *naima*, that resulted a Broken Power Law (Eq. 3.1.2) with indexes $\alpha_1 = 1.2 \pm 0.2$ and $\alpha_2 = 5.4 \pm 0.8$ before and after $E_b = 51 \pm 7$ GeV. This would mean that lower energy particles haven't reached the region of SE yet and, at the same time, higher energy particles have already left the region. Another possibility is that the highest energetic particles are instead escaping only in the direction of NW. It is anyway interesting to note that the two sources have different spectra from each other, even if the projected distances from the remnant and the gas densities are similar. In case of an impulsive accelerator, in fact, the escaping particles are expected to populate the surrounding medium homogeneously, and therefore the spatial distribution of γ -rays should follow the pattern of the gas.

In order to understand the large scale distribution of escaped particles, the entire GMC complex, included in the region $(l, b, v) \in [(33 : 37)^\circ, (-2.5 : 1.5)^\circ, (30 : 60) \text{ km s}^{-1}]$ has been analyzed as separate component. To do so, the same analysis technique, used for molecular clouds, as described in sec. 2.2, has been applied. The background templates have been constructed based on the CO and H_I maps, in order

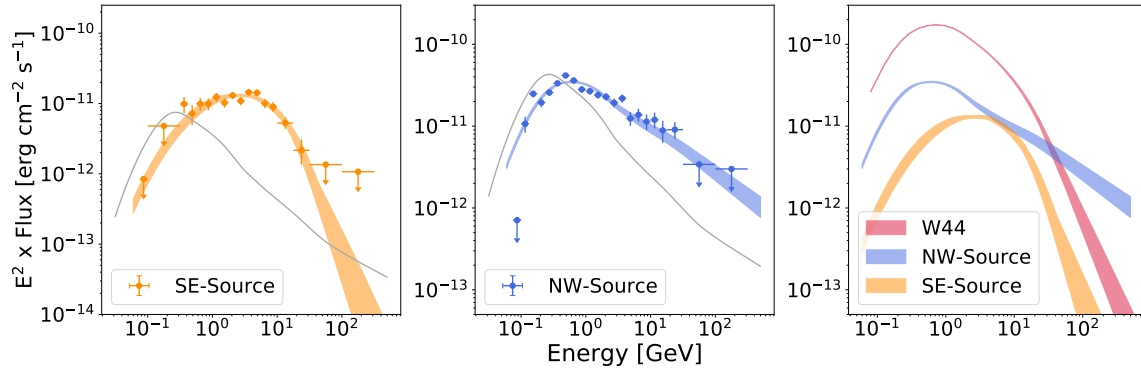


Fig. 3.6 Spectral energy distributions derived for the SE- (orange) and NW-source (blue). The colored areas indicate the 1-sigma confidence level derived from the fit with *naima*. The grey curve is the gamma-ray flux calculated from the local emissivity. The masses, M_{SE} and M_{NW} , have been calculated from the CO gas in these regions. In the rightmost panel the fluxes of the two sources are compared to the flux of the remnant. The figure has been adapted from [167].

to be able to perform a kinematic separation along the line of sight. The atomic component has been considered only in the background and not in the template of the source, but it is small compared to the molecular component ($\lesssim 30\% M_{surr}$). The same IC and isotropic diffuse as previously described have been used; no template for diffuse bremsstrahlung has been included, instead. The latter is non-trivial to model, both as it suffers of the uncertainties in the electrons distribution and because it is not easily decoupled from the pion-emission, where the gas density is high. For this reason, the analysis of this component has been conducted considering only photons of energy higher than 1 GeV, where the bremsstrahlung contribution is negligible. The resulting SED has a similar shape to the SED of the CR sea, calculated for the corresponding mass (Fig. 3.7). The small deviation ($\lesssim 50\%$), is compatible with the uncertainty of the cloud mass. The enhancement can also arise from the shallow increase of the CR density in the inner Galaxy. This effect should be of the order of 25% at the galactocentric distance of W44 ~ 6.5 kpc [111, 130]. The parameters derived with *naima*, confirms the similarity observed in gamma-rays also for protons. The derived proton spectrum, in fact, has a slope of 2.87 at the observed energies. This confirms that the enhancement of CRs is found only in correspondence of the two extended sources *NW* and *SE*. The SEDs of the two sources, normalized by A , are compared to the SED of the surrounding gas complex in the right panel of Fig. 3.7. The spectrum of *NW*-source is higher of a factor ~ 2

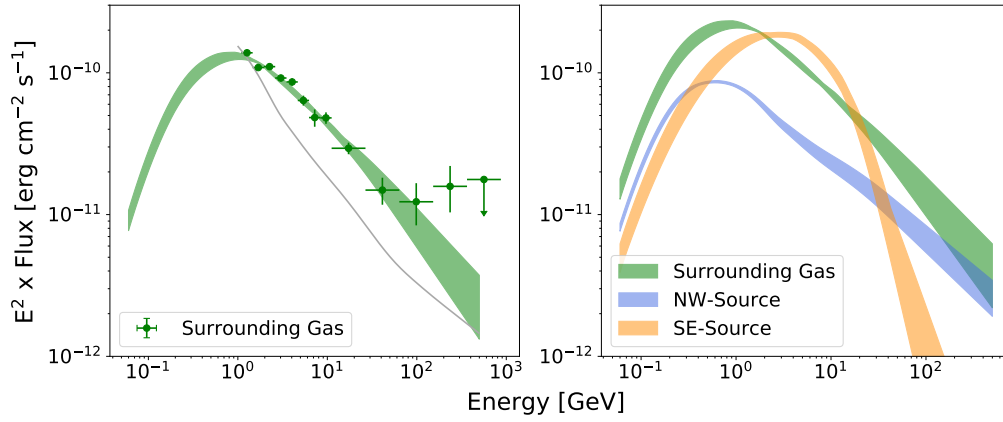


Fig. 3.7 Spectral energy distribution derived for the whole gas complex is compared to the expected flux for a cloud of the same mass, M_{surr} , illuminated by the local CR flux. The green area is the naima-derived fitting curve assuming a pion-decay model. The area represents the $1-\sigma$ confidence level. The figure has been adapted from [167].

than the one of the surrounding gas and it is also slightly harder. The SE-source has a completely different spectral shape and overcomes the spectrum of the whole complex up to a factor >5 in certain points.

3.2 DISCUSSION

The supernova remnant W44 has proven itself to be a perfect laboratory to test both the emission mechanism and the escape dynamics of accelerated particles. My analysis shows that the spectrum of the remnant is compatible with a pion-decay emission mechanism. A leptonic origin of the radiation instead has to be excluded due to the steep rise at low energy, that does not conceal with the E^{-1} predictions for bremsstrahlung below a threshold energy of 600 MeV. This argument can be applied in future observations also to other objects, for which efficient acceleration of protons is debated.

Furthermore, an enhanced concentration of high-energy particles is found at the edges of the SNR W44 in locations where there are no detected MCs, and the gas density is similar or below the average. Previous analyses identified this emission with the giant molecular cloud complex that embeds W44, however the analysis of that specific portion of gas unveils that the CR concentration in that region is quite low, almost at the level of the local CR density. The enhancement and the

	Model		NW-region	SE-region	Surr. Gas
Morphology (> 1 GeV)	Null	\mathcal{L}	956793	956847	–
	1 Point-Source	\mathcal{L}	956611	–	–
		AIC*	-1913218	–	–
	1 Disk	\mathcal{L}	956649	957064	–
		AIC*	-1913292	-1914122	–
	2 Point-sources	\mathcal{L}	957059	957059	–
		AIC*	-1914110	-1914110	–
	1 Disk + 1 P.S.	\mathcal{L}	957081	–	–
AIC*		-1914152	–	–	
2 Disks		failed	–	–	
γ -ray spectrum	Power Law	\mathcal{L}	9875887	9875954	952919
		AIC*	-19751774	-19751908	
	Broken PL	\mathcal{L}	9875954	9875979	952932
		AIC*	-19751904	-19751954	
	Log Parabola	\mathcal{L}	9875965	9876007	952938
		AIC*	-19751926	-19752010	
Proton spectrum	Power Law	BIC	56	86	44
	Broken PL	BIC	59	22	31
	Exp. Cutoff PL	BIC	58	23	39

Table 3.4 Results from the modeling of the sources that surrounds W44. The γ -ray spectrum has been derived starting from 60 MeV in the case of NW-source and SE-source, and starting from 1 GeV in the case of the surrounding gas. The highest values of likelihood and the lowest values of AIC* and BIC are highlighted in bold, as they indicate the best model.

spectral shape of the SEDs of the two clouds prove that these regions are exceptional objects. If these are really related to the supernova remnant and not to foreground sources, they most likely must be related to particles escaped from the shell. The fact that the emissivity is enhanced only in two regions, implies that these particles are escaping collectively, forming two *CR clouds*. This phenomenon had been predicted by Malkov et al. (2013), that calculated that, for a stopped accelerators, particles escape collectively in clumps, driven by self generated waves. Deeper investigations are needed to constrain the nature of these two cosmic-ray cloud and in particular to clarify their differences. In fact although they are located at a similar distance from the remnant ($\sim 20\text{-}30$ pc), their spectra are very different. That could be due to an intrinsic asymmetry in the shock, for example due to a non-constant Mach number. An alternative cause may be found in propagation: either because the real distances of the two clouds are not similar, regardless of what the projected distances suggest or because of interaction of the particles with the diffuse medium that alters the propagation. Finally, irregularities in the interstellar magnetic fields can also shape the clouds of escaping particles in non trivial ways, for example forming escaping filaments as calculated in [178].

The results presented in this chapter have been published in:

- [167] Peron, G., Aharonian, F., Casanova, S., Zanin, R., & Romoli, C. (2020). On the gamma-ray emission of W44 and its surroundings. *The Astrophysical Journal Letters*, 896(2), L23

A NEW INSTRUMENT FOR COSMIC-RAY ASTROPHYSICS

In the previous chapters, results obtained with the Fermi-LAT were presented and discussed. The performances of this instrument allowed us to obtain strong constraints concerning both the diffuse galactic γ -ray emission, detected in Giant Molecular Clouds (see Chapter 2), and the emission in accelerators and in their surroundings (see Chapter 3), providing further information on the properties of acceleration and escape of these high-energy particles. The Fermi-LAT has been operating now (2020) for more than 12 years and it is difficult to foresee that the operation will go on for much longer. Its potential in detecting the faint γ -ray emission arising from clouds is almost saturated, and limited to the exploration of few locations, corresponding to exceptionally massive ($\gtrsim 10^6 M_{\odot}$) or near ($\lesssim 1$ kpc) Molecular Clouds [151], which represent only a small percentage of the total. Next-generation γ -ray instruments are oriented to the observations of the very-high-energy regime ($\gtrsim 1$ TeV). At these energies, the spectrum of passive clouds is reduced by a few orders of magnitudes, and therefore VHE observations are not suitable for studying the global distribution of cosmic rays. However, these instruments could play a role in constraining the highest-energy part of the spectrum, at least for the most massive clouds, and in observations of clouds where the flux is enhanced, e.g. due to the vicinity of a strong accelerator.

In this chapter, I review the potential, in studying both passive and active molecular clouds, of the available and planned γ -ray instruments. Furthermore, I discuss the necessary features of a new instrument, optimized for the investigation of Galactic cosmic rays, that could overcome the Fermi-LAT. I also discuss some science cases, that could be addressed with such instrument.

4.1 SENSITIVITY

The sensitivity of an instrument is defined as the minimum flux that can be detected with significant excess over the background. The significance \mathcal{S} , is estimated as the ratio between the number of excess events over the background, N_s , and its variance $\sigma(N_s)$, that is a combination of the fluctuations of the source counts, N_{on} , and of the background counts N_{off} :

$$\mathcal{S} = \frac{N_s}{\sigma(N_s)} = \frac{N_{on} - \alpha N_{off}}{\sqrt{\alpha(N_{on} + N_{off})}}. \quad (4.1.1)$$

The latter is obtained in the hypothesis of Poissonian statistic; $\alpha = t_{on}/t_{off}$ is the ratio between the observation time *on* the source and *off* the source (i.e. on the background) and it is often 1. In the case of Fermi-LAT the sensitivity is calculated imposing $\mathcal{S}_{min} = 5$ and the further condition of a minimum number of detected photons $N_{on} > 5$. The significance calculated in this way is equivalent to the expression in terms of Log-likelihood presented in Eq. 2.2.5, as demonstrated in [179].

To improve the sensitivity, one needs to increase the significance of the measurements, for example enlarging the number of detected excess photons, namely $N_s = N_{on}(E, A, t_{on}) - N_{off}(E, A, t_{off})$. The latter depends on the emission properties of the source and of the background, but also on the collection area, A , of the detector and on the observation time $t_{on/off}$. Fixing the energy spectrum, for a given source and a given background it results: $N_{on/off} \propto A \cdot t_{on/off}$, assuming $t_{on} = t_{off}$ one obtains:

$$\mathcal{S} \propto \sqrt{A \cdot t_{on}}. \quad (4.1.2)$$

It is possible to increase the significance of the observations by i) reducing the background, N_{off} ; ii) increasing the observation time; or iii) enlarging the collection area.

The sensitivity curves are usually calculated for point-like sources, considered the instrument point-spread function, σ_{PSF} . When observing extended sources, the number of counts belonging to the background is larger, because a larger area is considered. In this case, the sensitivity scales as a factor $\omega(\sigma_{PSF}, \theta)$, defined in Eq. 2.1.1, which depends on the extension of the source.

4.2 CURRENT AND NEXT-FUTURE GAMMA-RAY INSTRUMENTS

Gamma-ray instruments are usually divided into *space-based* and *ground-based* experiments. Exhaustive reviews of gamma-ray observational techniques can be found for example in refs. [31, 180–182], here I summarize the basics of the detection methods and the parameters that influence the instruments' sensitivity (see Table 4.1).

Space-based instruments directly collect gamma-rays but are limited in the effective area ($\lesssim 1 \text{ m}^2$) and consequently also in the observable energy range, that is normally between few tens of MeV up to almost 1 TeV. The detection principle is based on pair-conversion: photons of sufficiently high energy enter the detector, decay in e^+e^- couples, and are then revealed in calorimeters. The arrival direction of the incoming photon, which determines the instrument angular resolution, is determined using position-sensitive detectors. The angular resolution in this way can be as low as 0.15° at high energy, but it is gravely affected by scattering inside the detector at lower energies, where it can be several degrees large. The background signal induced by cosmic rays is controlled by an anti-coincidence detector, which surrounds the entire instrument and provides a veto signal when a cosmic-ray particle passes through it. Currently operating space-based instruments are the Fermi-LAT [1] and AGILE [2], which have a similar design, although the latter has reduced performances due to its smaller effective area.

Ground-based γ -ray instruments can extend over larger areas and thus can measure higher-energy ($> 100 \text{ GeV}$) photons. The detection principle consists in measuring the cascade of particles, the so-called *Extensive Air Showers* (EAS), that γ -rays initiate when impacting on the Earth atmosphere. Showers extend on average for 10 km and can be detected either at high-altitude with EAS detectors (ED), usually with scintillators or in water tanks, where the particles produce Cherenkov light (Water Cherenkov technique, WCT) or at lower altitude by imaging their Cherenkov light with the Imaging Air Cherenkov Technique (IACTs). The lower energy threshold of the firsts is about $\sim 300 \text{ GeV}$ –1 TeV, depending on their altitude while the seconds can observe also events of 50–100 GeV. Both photons and particles can initiate a shower and the ability to separate between the type of parent particle directly influences the sensitivity of these instruments at different energies. CR-initiated showers can be rejected based on their composition (detecting secondary products of hadron-decays, mainly muons), on their shape (hadronic

		Energy Range	A_{eff} [m ²]	σ_{PSF}	Sensitivity [erg cm ⁻² s ⁻¹]
Space-based	AGILE	30 MeV–50 GeV	0.5	0.2°–4.7°	$\gtrsim 5 \times 10^{-12}$
	Fermi-LAT	20 MeV–1 TeV	0.95	0.15°–3.5°	$\gtrsim 2 \times 10^{-13}$
Current Ground-based	VERITAS	85 GeV–30 TeV			
	MAGIC	50 GeV–10 TeV	$\lesssim 10^5$	0.08°–0.15°	$\gtrsim 5 \times 10^{-13}$
	H.E.S.S.	50 GeV–100 TeV			
	HAWC	300 GeV–100 TeV	$\lesssim 10^4$	0.3°–2°	$\gtrsim 2 \times 10^{-12}$
	LHAASO	200 GeV–1 PeV	$\lesssim 10^6$	0.2°–2°	$\gtrsim 10^{-14}$
Planned Ground-based	SWGO	400 GeV–200 TeV	3.5×10^4	0.15°–1°	$\gtrsim 10^{-13}$
	CTA-South	20 GeV–200 TeV	$\lesssim 4 \times 10^6$	0.03°–0.25°	$\gtrsim 5 \times 10^{-14}$
	CTA-North		$\lesssim 10^6$		$\gtrsim 10^{-13}$

Table 4.1 Main parameters that characterize the performances of the current and planned γ -ray instruments. The effective area refers to on-axis observations. The sensitivity is given for different observation times, specifically: 10 years for space based instruments, 50 hours for IACT arrays and 1 year for WCs and LHAASO.

initiated particles are thicker, due to the higher momentum transfer) or the arrival direction (CRs arrive from random directions).

The current operating IACT instruments are VERITAS [4, 183], that is a system of 4 telescopes located in Arizona, U.S.A., MAGIC [3, 184] in La Palma, Spain that consists of 2 telescopes and the H.E.S.S. [185, 186], in the Khomas highland, in Namibia, now operating with five telescopes. The usage of an array of telescopes has turned out to be very efficient for lowering the detection threshold, improving the angular resolution, and suppressing the CR-background. The above-cited instruments have similar performances, reaching a sensitivity of $\sim 10^{-13}$ erg s⁻¹ cm⁻² and an angular resolution of $\sim 0.1^\circ$. The next-generation plans for the IACT point towards a larger array of Cherenkov telescopes, the Cherenkov Telescope Array (CTA) [6, 187], that will have 2 sites one in the Canary Islands, and one in Chile, with 35 and 39 telescopes respectively, reaching a ~ 2 times better sensitivity than the northern array. Since the configuration is still uncertain the performance of this observatory cannot be correctly estimated. However CTA promised to reach a ~ 10 times better sensitivity and a ~ 5 times better angular resolution than the current generation of IACTs. For the category of WC, we find now in operation the HAWC observatory [7, 188], in Puebla, Mexico. A new project is now starting, in the

Southern hemisphere, the so called Southern Wide Field Gamma-ray Observatory (SWGGO) [189, 190], that will have the same detection principle as HAWC, but with a larger number of tanks. The latter will reach the same level of sensitivity of H.E.S.S. after only 1 year of operation. Finally, the LHAASO observatory [8, 191] started the observations in October 2019 with half of the array already active. The completion of the instruments is planned for the end of 2021. This observatory combines different techniques, electromagnetic particle detectors (ED), water Cherenkov, and air Cherenkov telescopes. This configuration permits to reach unprecedented levels of sensitivity in the widest energy range from a few hundreds GeV to 1 PeV. The strength of this observatory resides in its unbeatable rejection power at a level of 10^{-5} above 100 TeV, where it is basically background free.

4.2.1 *The sea of Galactic Cosmic Rays with current gamma-ray instruments*

The potential of the above-mentioned instruments in detecting the γ -ray flux from molecular clouds have been investigated by comparing their sensitivity to the flux induced by different CR spectra. Of particular interest is the ability of detecting the so-called Sea-level of galactic cosmic rays, namely the nominal baseline flux that characterizes the entire Galaxy, see Sec. 1.1.2. Here we assume that the CR-sea level coincides with the value measured at Earth. Analysis of MCs in different locations confirms this statement, and no location showed a flux lower than that (see discussion in Chapter 2), meaning that this can be safely assumed as the lowest CR-level at least for the considerations regarding the visibility of molecular clouds. I assumed then as proton spectrum the interpolation of locally measured data from different experiments spanning several energy ranges: AMS02 below 1 TeV, DAMPE up to 100 TeV, and the two different branches derived by KASCADE and by Ice-top, at higher energies (see Fig. 1.1) [17, 18, 26, 28]. The parent CR proton spectrum so defined is plotted as a black line in the inset panel of Fig. 4.4. The expected flux of a molecular cloud has been calculated for such spectrum, from Eq. 1.1.14. A reference value of $A = 1$ has been considered as well as the standard value for $\xi_N = 1.8$, although the latter value slightly increases of $\sim 10\%$ at higher energies. The sensitivities of the currently operating instruments, Fermi-LAT, H.E.S.S., HAWC and LHAASO (top panel of Fig 4.4) and of the next-future instruments, CTA and SWGO (bottom panel) are compared to the given cloud spectrum. To take into account the extension of the sources, the sensitivities have been worsened by the

factor $\omega(\theta, \sigma_{PSF})$ (Eq. 2.1.1) appropriate for each instrument. The areas in the plot span from $\omega(\theta = 0.2^\circ)$ to $\omega(\theta = 0.5^\circ)$.

It is clear that Fermi-LAT is by far the most suitable instrument for detection of MC emission, as most of the energy is concentrated in the GeV energy band. At higher energy, the spectrum, being quite soft, falls rapidly and becomes more difficult to detect.

In order to increase the chances of clouds detection, larger clouds ($A > 1$) could be targeted or longer observation times, t , might be employed, as the sensitivity decreases as $t^{-1/2}$ (Eq. 4.1.2). The minimum detectable gamma-ray flux at a given energy, $F_\gamma(E)$, is the one that matches the sensitivity $S(E)$. So in general one should have:

$$F_\gamma(E) \geq S(E) \quad (4.2.1)$$

that translates into:

$$A\phi_\gamma(E) \geq S_0(E)\sqrt{\frac{t_0}{t}} \quad (4.2.2)$$

where $S_0(E)$ is the sensitivity corresponding to an observation time t_0 , A is the M_5/d_{kpc}^2 parameter, that characterizes molecular clouds emission and ϕ_γ is the γ -ray emissivity, that depends on the cosmic-ray content and on the nuclear enhancement factor (see Eq. 1.1.14). For simplicity the slight energy dependence of the nuclear enhancement factor have been ignored and a uniform value of 1.8 has been assumed for the following discussion. It is practical to define the ratio, $\mathcal{R}(E)$:

$$\mathcal{R}(E) \equiv \frac{S_0(E)}{\phi_\gamma(E)} = A\sqrt{\frac{t}{t_0}} \quad (4.2.3)$$

to characterize the minimum requirement for a molecular cloud to be visible with a certain instrument at a given energy, considering its A parameter and an observation time t . The curves for $\mathcal{R}(E)$ for the instruments discussed above are plotted in Fig. 4.2 as a function of energy. This value is quite high for IACTs, being of the order of units or higher. For H.E.S.S. is always $\mathcal{R}_{HESS}(E) \gtrsim 10$ that means that with the current sensitivity and with an exposure $t_0 = 50$ hr H.E.S.S. could detect only clouds with $A > 10$. However, no clouds with such a high value of A are known and to compensate this with observation time one should increase it, by a factor $t/t_0 \sim \mathcal{R}_{HESS}^2 = 100$, which is far too long. On the other hand, CTA is very close to the detection of such objects having $\mathcal{R}_{CTA} \sim 1$ below a few TeV. In this

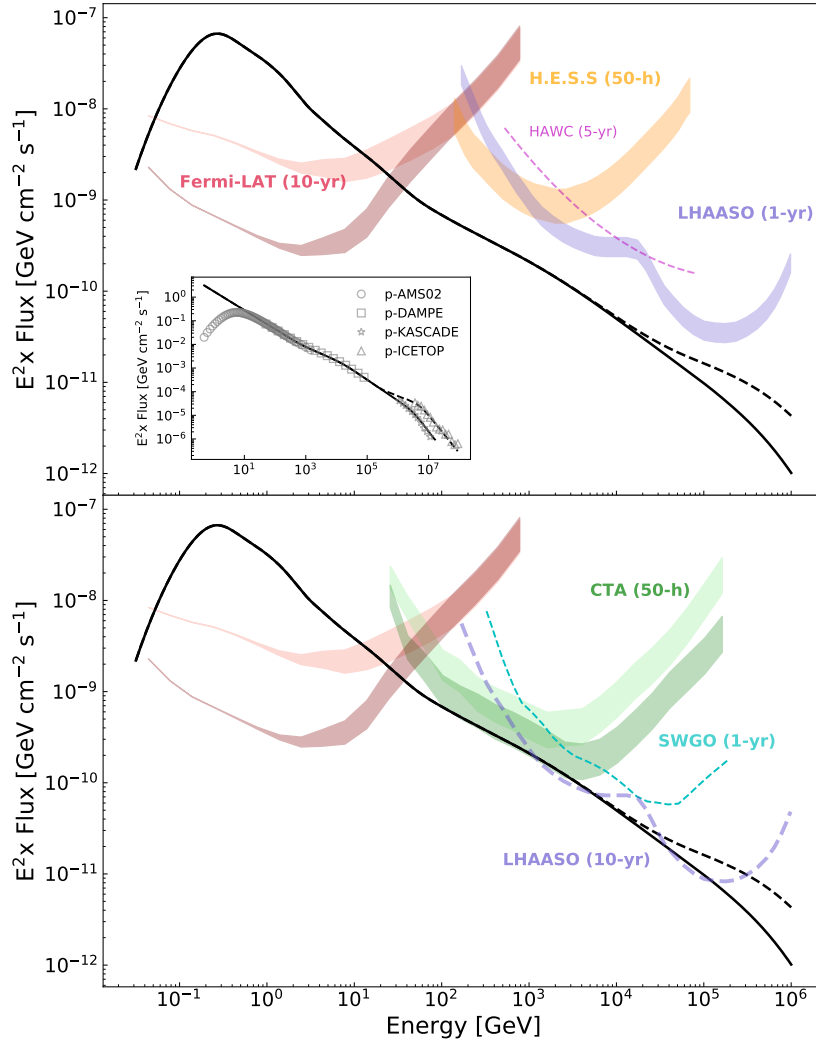


Fig. 4.1 Differential sensitivity of the most sensitive gamma-ray instruments available (top panel) or planned (low panel) for different energy ranges. The red areas represent the sensitivity of 10-yr Fermi-LAT accumulated data, in the outer Galaxy (dark red), and in the inner Galaxy (light red). The orange area indicates the sensitivity of 50-hr observations with the H.E.S.S.. The blue zone indicates LHAASO 1-year sensitivity, while the blue dashed line is the same curve for 10 years of observations, assuming a \sqrt{t} dependence; the magenta dashed line is the 5 years sensitivity level of HAWC. The green areas are the sensitivity of 50-h observations with the CTA North (light green) and the CTA South (dark green) array, in the baseline configuration. The dashed cyan line is the planned sensitivity for SWGO after 1 year of observations. The sensitivities are scaled to take into account the extension of the sources, spanning from 0.2° to 0.5° . The black curve indicates the gamma-ray flux expected from a molecular cloud with $A = 1$ illuminated by the local cosmic-ray spectrum, plotted in the inset panel.

case, few molecular clouds having a large enough A can be detected, provided that a sufficient observation time is granted. A factor of 2 better sensitivity could be gained for example by accumulating data for 200 hours on a single object, even if it is not very convenient. LHAASO presents a $\mathcal{R}_{LHAASO} \sim 4$ at 100 TeV, that is reduced to 2 when considering the higher branch of protons. Since LHAASO observes the outer edge of the Galaxy, not many massive molecular clouds fall in its field of view, nevertheless the close Gould Belt clouds could serve as interesting targets, having often A exceeding 1. In the latter case though, a good compromise with the angular extension needs to be found, as the latter exceeds 1 degree in several cases. On the other hand, the improvement induced by the time increase could be significant. In the case of LHAASO in fact, the background rejection is so efficient, that in some energy-ranges the observations can be considered background-free. In such a case, the sensitivity does not scale with \sqrt{t} but with t , making it possible to improve the sensitivity of a factor 4 only in a few years. Interesting to see that \mathcal{R}_{SWG0} is of same order of magnitude, being ~ 3 around 10 TeV. If the performances of this instrument will be confirmed, the SWGO will be a valid counterpart of LHAASO in the Southern hemisphere.

The distribution of molecular clouds' A parameter from the MD-catalog [87] are displayed in Fig. 4.3 as a function of the clouds galactic longitudes. The minimum value of A required from each instruments for detection is also shown. The latter is close to the minimum of $\mathcal{R}_i(E)$ for fixed times t_0 . This value is derived to guarantee the detection in some energy bands, but do not assure that a spectrum in the entire energy range can be obtained.

4.2.2 *Accelerators and their surroundings with current gamma-ray instruments*

While the VHE and UHE instrument cannot tell much about the nominal sea of cosmic rays in molecular clouds, a different scenario is expected in the vicinity of an accelerator. In the surrounding of a source, in fact, the cosmic ray density is enhanced also of orders of magnitude. Moreover, the energy dependence of the diffusion coefficient makes the spectrum of the escaping particles harder than the accelerator itself [120]. This effect is observed for example in the surrounding medium of the supernova remnant W44 (Chapter 3), for which a condensation of cosmic-rays with a much harder spectrum than the remnant is found at a few tens of parsec at the location of what we named NW-source. On the other hand,

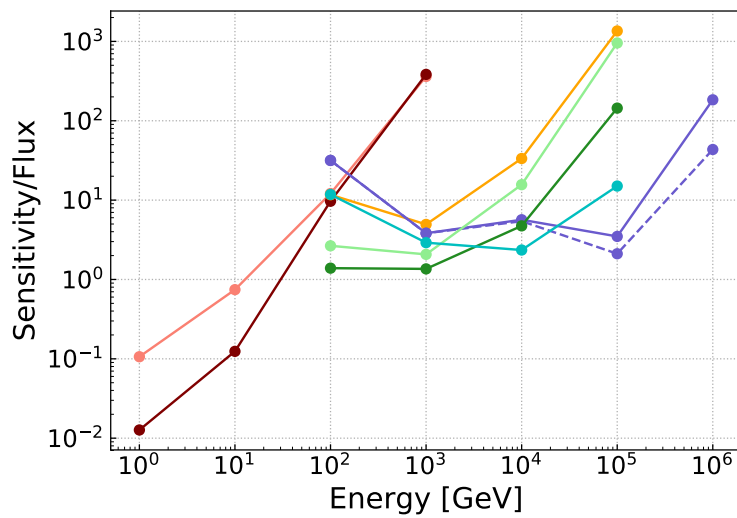


Fig. 4.2 Ratio between the sensitivity $S_0(E)$ of the above mentioned detectors and the flux of a gamma-ray emitting cloud illuminated by the local spectrum of cosmic rays. This represents the minimum A factor that a cloud should have in order to be detectable or equivalently the minimum improvement of the sensitivity obtained for example by increasing the observation time. An average size of 0.3° has been considered for the worsening factor ω . The curves correspond to: Fermi-LAT inner (light red) and outer (dark red) performances, H.E.S.S. (orange), CTA Northern (light green) and Southern (green) array, SWGO (cyan) and LHAASO (blue). The dashed blue curve represents the second branch of protons at high energies.

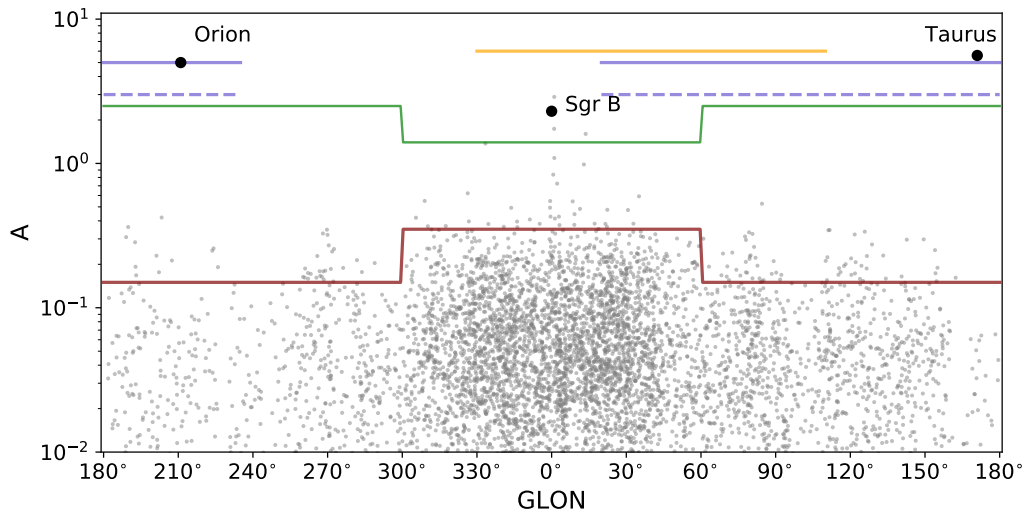


Fig. 4.3 Distribution of the A parameters of the cloud of MD-catalog as a function of their galactic longitude. The detection threshold of the above described instruments is also shown for comparison respectively for 10 years Fermi-LAT observations (red), 50-hours with CTA (green) and H.E.S.S.(orange) and for LHAASO after 1 (blue solid) or 10 years (blue dashed). The threshold is an approximate value derived from the ratio between the sensitivity and the local flux.

enhanced fluxes are observed also in location of clouds that are not associated with any identified accelerator, as in the case of the clouds in the inner galactic region, that were presented in Chapter 2. These clouds presented fluxes 3-4 times higher than the one measured in the vicinity of Earth, therefore their visibility is much improved. The SED of both NW-source and R877, as a representative of the inner-galactic clouds are plotted in Fig. 4.4 against the sensitivity of the current and next-future generation instruments. An extrapolation of the spectrum of these objects at high energies seem feasible and desirable. For example, in the case of molecular clouds in the vicinity of an accelerator observations of very-high and ultra-high energy are fundamental to understand the source acceleration power and specifically their maximum energy, to understand if they can serve as PeVatrons, (i.e. accelerators of PeV particles). It is clear in fact that PeV particles hardly can be confined within the source itself and they are rather populating the surrounding medium. Similar arguments can be brought up in the case of molecular clouds not correlated with a specific accelerator. The enhancement can be due to a collection of accelerators that are more abundant in a particular regions of the Galaxy or

rather be due to a 'dark', undetected accelerator. In the latter case, the high angular resolution of IACTs might play a role in constraining the location of the source itself, by determining the direction from which the CRs are illuminating the cloud.

The spectrum of an accelerator-illuminated cloud is however difficult to foresee as it depends on the age and on the distance of the accelerator, as well as on the diffusion coefficient of the ambient medium. Some example of CR spectra have been calculated in ref. [48] and are shown in Fig. 1.7. The gamma-ray fluxes derived from these CR fluxes, illuminating a MC of $A = 1$ are compared to the instruments' sensitivities in Fig. 4.4. The case of very young accelerators (10^3 yr; solid lines) is the most advantageous to be observed at high energy, nevertheless, when the distance from the accelerator is too high (100 pc; blue lines) the GeV counterpart is suppressed and the detection with Fermi-LAT might be missed.

4.3 BEYOND THE FERMI-LAT

With the use of the current and next-future generation of instruments is possible to measure the γ -ray spectrum of only a limited number of molecular clouds and consequently the cosmic-ray density can be mapped only in a few locations. On the other hand, massive molecular clouds are found in the entire Galaxy potentially providing the target to sample the galactic population of cosmic rays all over the Milky Way. To probe comprehensively the sea of galactic cosmic rays the sensitivity of GeV-instruments needs to be significantly improved. While ground based gamma-ray instruments are making huge progresses and several experiments are planned for the next future, the same cannot be said for what concerns space based missions. The GeV window, to which the the bulk of energy deriving from the CR sea belongs, is left to explore to the already 12-years-old Fermi-LAT. Also assuming that the LAT continue its operation for another 10 years, the improvement in the sensitivity would be of only $\sqrt{2} \sim 1.4$. Taking the Fermi-LAT instrument as prototype, we evaluated the factors that can improve the sensitivity to a necessary level to allow the detection of γ -ray fluxes in giant molecular clouds from many different locations.

The rejection power of Fermi-LAT already reached the unprecedented level of efficiency of 0.99997 [192] leaving no much space for further improvement in this direction. According to Eq. 4.1.2, extending the observation time of a factor τ would improve the significance only of a factor $\Sigma = \sqrt{\tau}$ so to obtain a considerable improvement, a long time is required. One solution could be the implementation

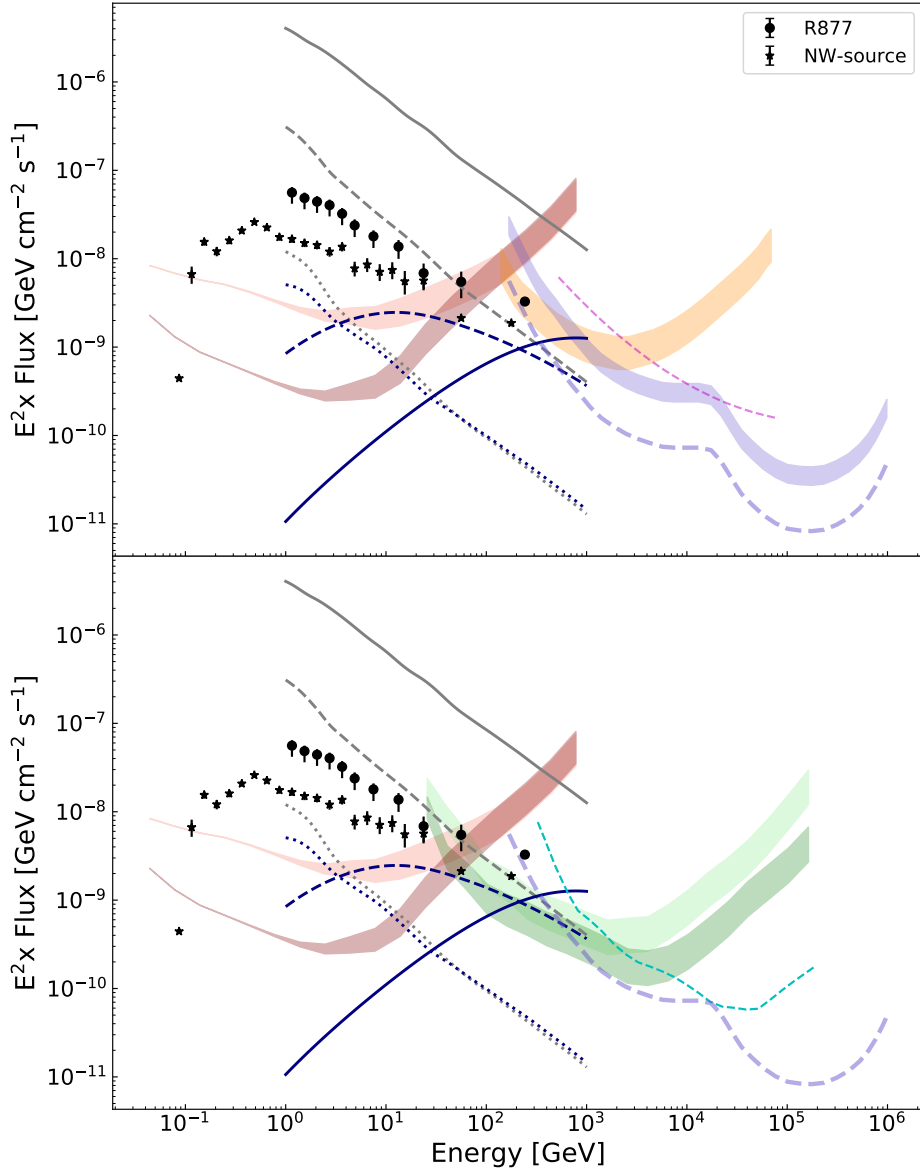


Fig. 4.4 The same sensitivities as in Fig 4.4 are plotted against the gamma-ray flux expected for a molecular cloud located at $R=10$ pc (grey curves) and $R=100$ pc (blue curves) from an impulsive accelerator, observed after a time $t = 10^3$ yr (solid), 10^4 yr (dashed) and 10^5 yr (dotted). An energy dependent diffusion coefficient of $D(E) = 10^{28}(E/10 \text{ GeV})^\delta \text{ cm}^2/\text{s}$ is assumed, as well as $W_p = 10^{50}$ erg and an injection spectrum of slope $\Gamma = 2.2$, see [48]. The experimental points of cloud R877 in the 4-6 kpc ring [151] and NW-source in the vicinity of W44 are also shown [167].

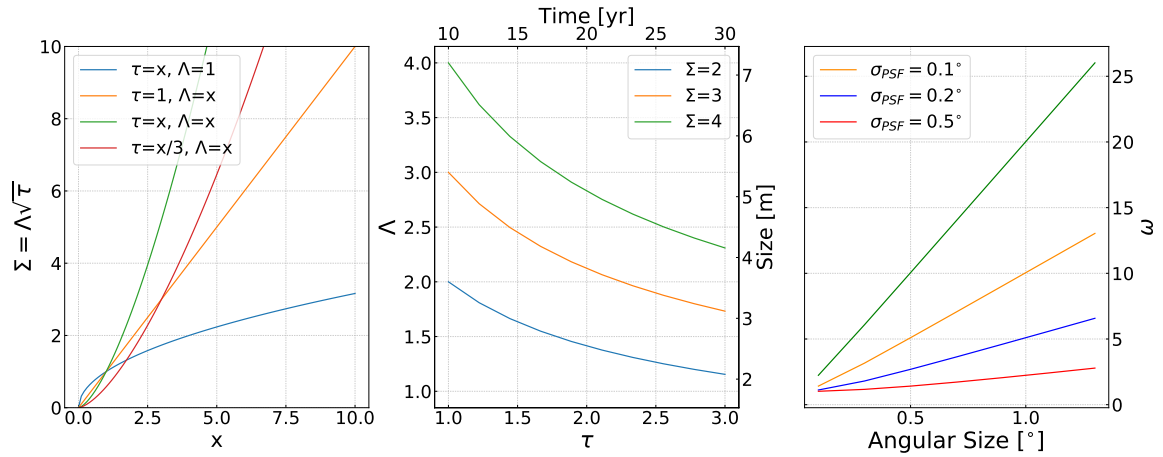


Fig. 4.5 The combined effect on the sensitivity due to an increase in the observation time τ and in the extension Λ of a Fermi-LAT-like detector. In the leftmost panel: the blue curve shows the effect of increasing only the time by a factor x , while the orange curve shows the effect due to an increase of only the size by a factor x . The other two curves show a combination of the two variables: for the green curve the time and size are increased by the same factor, while for the red curve the increase factor in time is 1/3 of the increase factor in size. The middle panel instead shows how Λ and τ depends on each other for a fixed sensitivity improvement Σ . The rightmost panel instead shows the worsening, ω , of the sensitivity caused by different values of PSF as a function of the source extension.

of a pointing system to focus only on specific regions (e.g. the Galactic plane) for a longer time, but that would mean sacrifice time on other areas. Enlarging the collection area is the most efficient way to achieve a significant improvement of the instrument sensitivity. The improvement in sensitivity, is linearly proportional to the increase in size, Λ , so it is sufficient to have a 2 times larger ($\Lambda = 2$) detector to have a 2 times more sensitive instrument. A combination between τ and Λ can yield to great improvement of the sensitivity, $\Sigma = \Lambda\sqrt{\tau}$, as Fig. 4.5 shows. An improvement of the sensitivity of a factor ~ 3 can be achieved for example observing for 12.5 years with a Fermi-like instrument of size $5 \text{ m} \times 5 \text{ m}$. Furthermore, one can also think of stacking the data obtained with such instrument to the data collected by the Fermi-LAT to increase even more the significance of the source [193].

The angular resolutions σ_{PSF} of the order of the size of the cloud is desirable as a narrower point-spread function would decrease the flux and consequently the significance of the source of a several units (see Eq. 2.1.1). The influence of this parameter is also plotted in Fig 4.5. The current resolution of Fermi-LAT ($0.2^\circ - 0.5^\circ$)

is in fact ideal for the observation of galactic extended sources that have areas of $\sim 0.2^\circ$ or larger.

4.3.1 *Expected results from improved sensitivity*

In the following, the potential of an instrument with a $\Sigma = 2$ or $\Sigma = 4$ better sensitivity with respect to Fermi-LAT is investigated. Firstly, the case of molecular clouds illuminated by the local cosmic ray flux is considered. As it can be observed in Fig. 4.6, the number of detectable objects is significantly increased in this case. Only with an increase of the sensitivity by a factor 2 the fraction of detectable clouds raises from $\sim 3\%$ to 10%. This fraction reaches almost the 20% by improving it by a factor 4. Furthermore, the gain is much larger when focusing on single location of the Milky Way. While most of the MCs detectable by Fermi-LAT concentrate in the vicinity of the Solar System, and only few objects are detectable at further distances, an improved sensitivity would allow us to deeply sample also further locations. The number of detectable clouds for each range of galacto-centric radius, R_{gal} , and galactic height Z_{gal} are reported in Fig. 4.7. It emerges that already with an improvement of $\Sigma = 2$ tens of molecular clouds become visible in each galacto-centric ring. Of special interest is the 2–4 kpc ring, where only few clouds are accessible with the current Fermi-LAT sensitivity. At the same time, while Fermi-LAT is limited to the observation of molecular clouds relatively close to the galactic plane, an improved sensitivity would allow to access several locations up to 400 parsecs from the plane. The combined knowledge of the cosmic-ray density at different distances from the Galactic center and at different height from the Galactic plane would improve the knowledge regarding the propagation properties of these high-energy particles in the radial and in the perpendicular direction. A map of the Milky Way locations that can be probed with the above mentioned level of sensitivity is displayed in Fig. 4.8, showing that a comprehensive mapping, of most of the Galaxy, can be obtained.

The above considerations are valid in the case of a cosmic-ray spectrum similar to the local one. In the case of enhanced flux, as in the vicinity of a source, the visibility is further improved. Moreover, in the case of a very hard spectrum, the low-energy part of the spectrum is suppressed and can be missed by Fermi-LAT. An instrument with a much improved sensitivity could instead be sensitive to such low fluxes and tell more about the GeV counterpart of sources with hard spectra (see

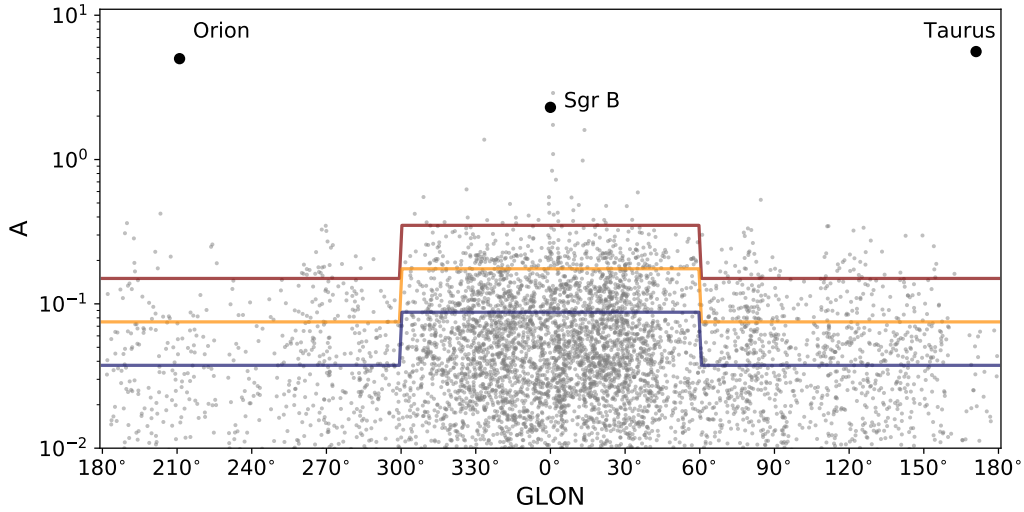


Fig. 4.6 The same as Fig. 4.3 but in the case of a $\Sigma = 2$ (orange) and of a $\Sigma = 4$ (blue) better sensitivity than Fermi-LAT.

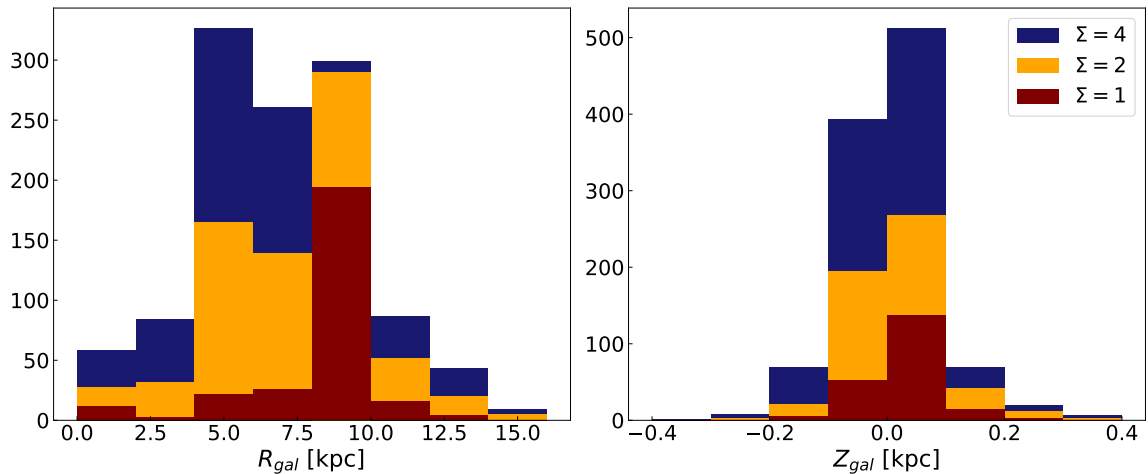


Fig. 4.7 Histograms of the galacto-centric distances and galactic heights of the molecular clouds that are visible with the sensitivity of Fermi-LAT (dark red), with a $\Sigma = 2$ better sensitivity (orange) and a $\Sigma = 4$ times better one (blue).

solid blue line in Fig. 4.4). Although a precise emission model needs to be calculated with known injection and diffusion properties and it is difficult to predict the exact emission of this kind, intuitively it is foreseeable that several counterparts of very hard sources will pop-up observing with a more sensitive instrument.

Even if it is not in the main interest of this research, it should be mentioned that the enlargement of the sensitivity would also have great benefits in the search of dark matter signatures. One of the hypothesis on the nature of dark matter involves in fact weakly interacting massive particles (WIMPs), which are expected to annihilate producing gamma-ray photons. Signatures of dark matter are expected to be found in gamma-rays surveys especially towards region of enhanced matter density, like in the Galactic Center, or in regions where a dynamical anomaly is usually observed and attributed to dark matter, like in the case of galactic halos. A special case is constituted by dwarf galaxies, as they are expected to be dominated in mass by dark matter. The monitoring of these objects with the current generation instruments has produced constraining upper limits to the cross-section of dark matter annihilation. Observation of Fermi-LAT suggests an upper limit of $\langle\sigma v\rangle < 10^{26} \text{ cm}^3 \text{ s}^{-1}$. A 2 or 4 times better sensitivity would decrease this limit even more (see [194] for a recent review).

At the same time, a new instruments monitoring the gamma-ray sky with a larger collection area will increase the chances for detection of transient phenomena, including the gamma-ray bursts originating in the coalescence of compact objects. The detection of an electromagnetic counterpart of gravitational waves signals is particularly important for determining the origin of the waves, but also to constrain the model parameters [195].

4.4 DISCUSSION

The sea of galactic cosmic rays, as defined in the previous chapter can be effectively traced in the locations of giant molecular clouds. However, most of the molecular clouds in the Milky Way are either too small or too far to be detected with Fermi-LAT, which can reach only the $\sim 3\%$ for the most part located in the vicinity of the Earth. This number is further decreased when considering possible overlapping with other gamma-ray sources, especially in the inner Galaxy, where the spiral arms overlap along a single line of sight. A deep investigation of the galactic cosmic-ray distribution can be carried out with a Fermi-LAT type instrument if the sensitivity is

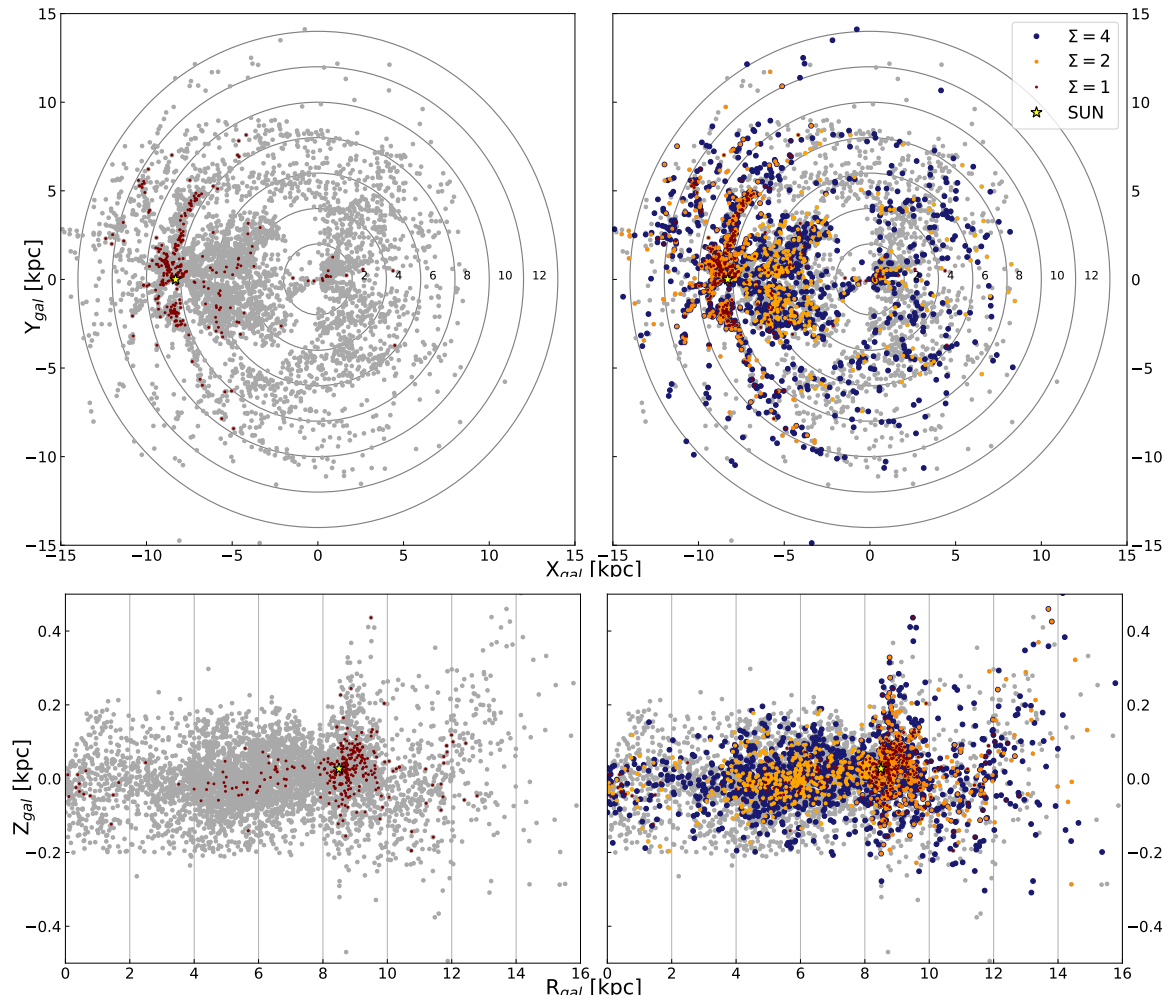


Fig. 4.8 Distribution on the (X_{gal}, Y_{gal}) plane (upper panels) and in the (R_{gal}, Z_{gal}) plane (lower panels) of Milky Way molecular clouds detectable with the current sensitivity of Fermi-LAT (dark red points) and with a sensitivity improved of a factor $\Sigma = 2$ (right panel, orange points) and $\Sigma = 4$ (right panel blue points). The Sun is indicated as a yellow star.

improved of factor 2 or more. Extending the sampling of cosmic-ray density to many different locations both along the radial and the perpendicular direction allows us to further constrain the propagation properties of these high energy particles. The radial modification of the propagation properties has been discussed in depth in the previous chapters and having many further locations to investigate would definitely be beneficial for understanding more the diffusion in the disk. In addition, the possibility of observing molecular clouds off the plane would allow us to test the extent of the cosmic rays in the galactic halo. Moreover, being the CR density a result of magnetic fields and turbulence, these measurements can serve as indirect tracers of these properties of the interstellar medium. Cosmic rays also have a deep influence on the interstellar gas as they are one of the main sources of heating and thus influence the star formation rate.

Higher energy investigations seem also promising for the starting of operations of LHAASO. The latter when operating at full regime will be able to detect, in only a few years, the flux of the biggest molecular clouds. This will be a great opportunity to test the cosmic-ray spectrum at the ultra-high energies at locations different than Earth, gaining unprecedented knowledge on the distribution of multi-TeV sources. Water Cherenkov detectors, in a sufficient amount of time, might become competitive with LHAASO, especially the future SWGO. The latter will be located in the southern hemisphere and therefore will be complementary to LHAASO. Covering the inner part of the Galaxy, it will have the advantage of observing the most massive molecular clouds. IACTs are in general limited by their small angular resolution, typically of few arcmin. But at least CTA, with the considered configuration, seems able to detect the biggest molecular clouds if sufficient time is provided. In such a case, its small angular resolution could allow us to resolve smaller structures and tell about the spatial distribution of cosmic rays inside molecular clouds themselves.

Regions in the vicinity of accelerators will be of particular interest for the TeV-PeV detectors as the flux is expected to be enhanced and harder allowing to reconstruct the acceleration history of the source or to identify the location of still unknown sources. In this context, the realization of a more sensitive instrument for the GeV-energy band with an improved sensitivity would allow us to test the low-energy counterpart of these objects.

The results of this chapter have been presented in:

Peron, G. Ultra High Energy γ -ray emission from Giant Molecular Clouds, *invited talk* at "Multimessenger high energy astrophysics in the era of LHAASO", online conference, July 2020

and are included in the work in preparation:

Peron, G., & Aharonian, F., The galactic cosmic ray density with current and future γ -ray instrument, *prepared for the submission* in *Astronomy & Astrophysics*

SUMMARY AND CONCLUSIONS

The results of my Ph.D. study demonstrate the potential of high-energy gamma-ray observations for investigating the spectral and spatial distribution of cosmic rays in the Milky Way.

In Chapter 2, I reported the results from the Fermi-LAT analysis of the γ -ray flux from 28 passive molecular clouds, distributed all-over the Milky Way ranging from distances of 100 pc to more than 12 kpc away from us. Earlier analyses were dedicated to the investigation of the large-scale diffuse emission, and studies on single clouds were limited to the clouds of the nearby Gould Belt region or to the exceptionally massive Sagittarius B complex. Thanks to the recognition of the presence of several massive molecular clouds at a close enough distance, it was possible, for the first time, to extend the investigation of the galactic cosmic-ray distribution to a significant number of locations, farther than the Gould Belt region. The cosmic-ray flux derived in several different locations coincides with the measurements obtained in the vicinity of Earth by direct experiments, therefore suggesting the idea that this level is a fair representation of the "cosmic-ray sea". Significant deviations from this level are detected only in the region within the galactocentric distances ~ 4 kpc and ~ 6 kpc, where the large-scale diffuse emission is also higher and harder than the local one. Nevertheless, the cosmic-ray fluxes derived from different clouds show noticeable fluctuations and do not always match the average value reported in previous publications. This is an indication of the presence of active or recent cosmic-ray accelerators in proximity of the analyzed clouds. Also in the innermost part of the Galaxy ($\lesssim 4$ kpc) the results show significantly lower fluxes than the values claimed by the Fermi-LAT collaboration based on their analysis of the diffuse γ -ray background. The results on molecular clouds illustrate the feasibility of the method and, in addition, demonstrate the advantages of the suggested method for deriving information on Galactic Cosmic Rays. Studies on molecular clouds provide

more objective and unbiased information about the Galactic cosmic rays compared to the method based on the analysis of the large-scale diffuse emission, since the latter could be biased by the inclusion of regions of larger cosmic ray density. The impact of this effect is especially significant for the regions where the diffuse gas is not smoothly distributed but rather tends to agglomerate in patchy clumps.

In Chapter 3, the results of the analysis of the supernova remnant W44 have been presented. Because of its age (20 kyr), this object is an ideal source for probing cosmic rays both inside the accelerator (the shell) and in the regions surrounding the remnant, which are filled by relativistic particles that have already left the shell. The high quality of the spectral points derived from this remnant allow us to determine the hadronic origin of the radiation, based on the recognition of the characteristic pion-bump turnover below 1 GeV. The analysis of the surrounding medium unveiled two extended γ -ray sources at the edges of the remnant, along the direction of the remnant magnetic field. The analysis of the high-resolution gas data for the region demonstrates that these sources do not correlate to any region of gas over-density and are then identified as *cosmic-ray clouds*. The configuration and orientation of these clouds indicate that these conglomerates of relativistic particles propagate anisotropically after they escape the shell of the supernova remnant.

In Chapter 4 the capabilities of current and future γ -ray instruments in detecting “passive” and “active” molecular clouds were investigated. The new generation of gamma-ray telescopes will strengthen the detection power at TeV (CTA, SWGO) and PeV (LHAASO) energies. Yet, they will be limited to the observation of *active* molecular clouds, which present an enhanced and/or harder flux. This will allow us to better investigate the acceleration power of the sources and the escape phenomena. This will further permit in-depth studies of the physics of particle acceleration, their escape, and propagation close to the accelerators. Concerning passive clouds, namely those regions far from any accelerator, a new GeV instrument with improved sensitivity compared to Fermi-LAT would be beneficial. According to my calculations, an improvement of only a factor 2, could enable most of the regions of the Galaxy to be mapped. That would guarantee a deeper understanding of the propagation properties of these high-energy particles, but also to constrain the distribution of sources. Furthermore, cosmic rays hold an important component of the energy density of the Galaxy, being comparable with the energy density of the cosmic microwave background, and of the interstellar magnetic field and they also regulate the dynamic of star formation. Having their spectral and spatial distri-

bution firmly constrained is undoubtedly of paramount importance for a variety of astrophysical aspects.

ACKNOWLEDGMENTS

I would like to greatly thank all the people whose assistance and support was a huge help in completing this project, as well as all the people that supported me professionally, emotionally or both.

First of all, I wish to express my deepest gratitude to my supervisor Prof. Dr. Felix Aharonian, who welcomed me in his research group as his last Ph.D. student, giving me the chance to always work on stimulating topics and continually motivating me also during the toughest times.

I would like to thank Prof. Dr. James (Jim) Hinton for the support and hospitality in the High-energy astrophysics group at MPIK and also for the willingness of being part of my thesis advisor committee. In this regard, my gratitude goes also to Prof. Dr. Eva Grebel, for her guidance as a member of my thesis committee. A special thanks to Prof. Dr. Quirrenbach that kindly agreed to review this dissertation.

I would like to thank Dr. Christian Fendt for his kind advice at the beginning of my Ph.D. career and the International Max Planck Research School (IMPRS) and the Heidelberg Graduate School for Physics (HGSFP) for creating a stimulating and friendly environment to carry out a doctoral degree.

A special thanks goes to all the colleagues and former colleagues in particular Dr. Roberta Zanin, Dr. Sabrina Casanova, and Dr. Ruizhi Yang with whom I worked closely and who have always been patient when I needed help or advice. Thanks in particular to Sabrina for proof-reading this whole thesis and patiently marking every single time I forgot "us" in the instance "allow us". To Roberta that was always willing to help also outside of work and to Ruizhi, that during these hard times remembered about us also from a long distance. I am particularly grateful for the assistance given by Dr. Carlo Romoli in going through the modeling codes and to Mischa, who helped me with the German translation. To Silvia and Lucia, that when visiting were always bringing good vibes at the institute. To Francesco and Carlo (again) for delighting the lunch and coffee breaks and for always waiting for me to go to the cafeteria, when I was busy in a meeting, even if they were starving.

I wish to thank my family and friends here, back-home, or in random parts of the world for their support and encouragement throughout these three years. Starting with my oldest friends Cecilia, Francesca, Irene, Serena, and Sofia, that have always pushed me and supported even from afar. My special thanks to Alex, who is one of the main people responsible for my decision to stay in Heidelberg. Of course I can't forget all the amazing people I had the opportunity to meet in this city including Chiara, Elena, Valentina, Miriam, Giulia, Federica, Ginevra, Riccardo and all the others that shared the best moments with me. Thanks to my IMPRS fellows for the great times together, in particular to Diana and Ben, who were always there along my side for every step of the Ph.D., both for the serious matters and for the fun times.

Lastly, my deepest gratitude goes to Carlo, who always stood by my side and gave me incommensurable help.

PERSONAL BIBLIOGRAPHY

PUBLICATIONS

- AI. Aharonian, F., **Peron, G.**, Yang, R., Casanova, S., & Zanin, R. (2020). Probing the sea of galactic cosmic rays with Fermi-LAT. *Physical Review D*, 101(8), 083018.
- AII. **Peron, G.**, Aharonian, F., Casanova, S., Zanin, R., & Romoli, C. (2020). On the gamma-ray emission of W44 and its surroundings. *The Astrophysical Journal Letters*, 896(2), L23.
- AIII. Ambrogi, L., Zanin, R., Casanova, S., Wilhelmi, E. D. O., **Peron, G.**, & Aharonian, F. (2019). Spectral and morphological study of the gamma radiation of the middle-aged supernova remnant HB 21. *Astronomy & Astrophysics*, 623, A86.
- AIV. Baghmany, V., **Peron, G.**, Casanova, S., Aharonian, F., & Zanin, R., (2020) Evidence of Cosmic-Ray Excess from Local Giant Molecular Clouds, *The Astrophysical Journal Letters*, 901(1)

In preparation:

- AV. **Peron, G.**, Aharonian, F., Casanova, S., Yang, R., & Zanin, R. (2020) Probing the Cosmic-ray density in the inner Galaxy, *submitted to The Astrophysical Journal Letters*.
- AVI. **Peron, G.** & Aharonian, F., The galactic cosmic ray density with current and future γ -ray instrument, *prepared for the submission in Astronomy & Astrophysics*.

CONFERENCE PROCEEDINGS

- PI. **Peron, G.**, Aharonian, F., Casanova, S., Yang, R., & Zanin, R. (2019). Giant Molecular Clouds as probes of Galactic Cosmic Rays with Fermi-LAT. In EPJ Web of Conferences (Vol. 209, p. 01016). EDP Sciences.

CONFERENCE CONTRIBUTION

- TI. **Peron, G.** Giant Molecular Clouds as probes of Galactic Cosmic Rays with Fermi-LAT, *contributed talk* at "7th Roma International Conference on AstroParticle Physics", Rome, Italy, September 2018
- TII. **Peron, G.** Giant Molecular Clouds as probes of Galactic Cosmic Rays with Fermi-LAT, *seminar* at "MPIK Kaffeepalaver", Heidelberg, Germany, November 2018
- TIII. **Peron, G.** Giant Molecular Clouds as probes of Galactic Cosmic Rays with Fermi-LAT, *invited talk* at "Very High Energy Phenomena Around Supermassive Black Holes", Yerevan, Armenia, April 2019
- TIV. **Peron, G.** Giant Molecular Clouds as probes of Galactic Cosmic Rays with Fermi-LAT, *contributed talk* at "Multimessenger Data Analysis in the Era of CTA", Sexten, Italy, June 2019
- TV. **Peron, G.** Ultra High Energy γ -ray emission from Giant Molecular Clouds, *invited talk* at "Multimessenger high energy astrophysics in the era of LHAASO", online conference, July 2020

REFERENCES

- [1] W B Atwood, A A Abdo, M Ackermann, W Althouse, B Anderson, M Axelsson, L Baldini, J Ballet, D L Band, G Barbiellini, J Bartelt, D Bastieri, B M Baughman, K Bechtol, D Bédérède, F Bellardi, R Bellazzini, B Berenji, G F Bignami, D Bisello, E Bissaldi, R D Blandford, E D Bloom, J R Bogart, E Bonamente, J Bonnell, A W Borgland, A Bouvier, J Bregeon, A Brez, M Brigida, P Bruel, T H Burnett, G Busetto, G A Caliendo, R A Cameron, P A Caraveo, S Carius, P Carlson, J M Casandjian, E Cavazzuti, M Ceccanti, C Cecchi, E Charles, A Chekhtman, C C Cheung, J Chiang, R Chipaux, A N Cillis, S Ciprini, R Claus, J Cohen-Tanugi, S Condamoor, J Conrad, R Corbet, L Corucci, L Costamante, S Cutini, D S Davis, D Decotigny, M DeKlotz, C D Dermer, A de Angelis, S W Digel, E do Couto Silva, P S Drell, R Dubois, D Dumora, Y Edmonds, D Fabiani, C Farnier, C Favuzzi, D L Flath, P Fleury, W B Focke, S Funk, P Fusco, T Glanzman, G Godfrey, I A Grenier, M-h Grondin, J E Grove, L Guillemot, S Guiriec, G Haller, A K Harding, P A Hart, E Hays, S E Healey, M Hirayama, L Hjalmarsdotter, R Horn, R E Hughes, G Jóhannesson, G Johansson, A S Johnson, R P Johnson, T J Johnson, W N Johnson, T Kamae, H Katagiri, J Kataoka, A Kavelaars, N Kawai, H Kelly, M Kerr, W Klamra, J Knödseder, M L Kocian, N Komin, F Kuehn, M Kuss, D Landriu, L Latronico, B Lee, S-h Lee, M Lemoine, M E Monzani, E Moretti, A Morselli, I V Moskalenko, S Murgia, T Nakamori, S Nishino, P L Nolan, J P Norris, E Nuss, M Ohno, T Ohsugi, N Omodei, E Orlando, J F Ormes, A Paccagnella, D Paneque, J H Panetta, D Parent, E Rapposelli, M Razzano, A Reimer, O Reimer, T Reposeur, L C Reyes, S Ritz, L S Rochester, A Y Rodriguez, R W Romani, M Roth, J J Russell, F Ryde, S Sabatini, H F-W Sadrozinski, D Sanchez, A Sander, L Sapozhnikov, P M Saz Parkinson, J D Scargle, T L Schalk, G Scolieri, C SgròSgr, G H Share, M Shaw, T Shimokawabe, C Shrader, A Sierpowska-Bartosik, E J Siskind, D A Smith, P D Smith, G Spandre, P Spinelli, J-l Starck, T E Stephens, M S Strickman, A W Strong, D J Suson, H Tajima, H Takahashi, T Takahashi, T Tanaka, A Tenze, S Tether, J B Thayer, J G Thayer, D J Thompson, L Tibaldo, O Tibolla, D F Torres, G Tosti, A Tramacere, M Turri, T L Usher, N Vilchez, V Vitale, P Wang, K Watters, B L Winer, K S Wood, T Ylinen, and M Ziegler. THE LARGE AREA TELESCOPE ON THE FERMI GAMMA-RAY SPACE TELESCOPE MISSION. *The Astrophysical Journal*, 697:12, 2009.
- [2] M. Tavani, G. Barbiellini, A. Argan, A. Bulgarelli, P. Caraveo, A. Chen, V. Cocco, E. Costa, G. De Paris, E. Del Monte, G. Di Cocco, I. Donnarumma, M. Feroci, M. Fiorini, T. Froyland, F. Fuschino, M. Galli, F. Gianotti, A. Giuliani, Y. Evangelista, C. Labanti, I. Lapshov, F. Lazzarotto, P. Lipari, F. Longo, M. Marisaldi, M. Mastropietro, F. Mauri, S. Mereghetti, E. Morelli, A. Morselli, L. Pacciani, A. Pellizzoni, F. Perotti, P. Picozza, C. Pontoni, G. Porrovecchio, M. Prest, G. Pucella, M. Rapisarda, E. Rossi, A. Rubini, P. Soffitta, M. Trifoglio, A. Trois, E. Vallazza, S. Vercellone, A. Zambra, D. Zanello, P. Giommi, A. An-

- tonelli, and C. Pittori. The AGILE space mission. *Nuclear Instruments and Methods in Physics Research, Section A: Accelerators, Spectrometers, Detectors and Associated Equipment*, 588(1-2):52–62, apr 2008.
- [3] Daniel Ferenc. The MAGIC gamma-ray observatory. In *Nuclear Instruments and Methods in Physics Research, Section A: Accelerators, Spectrometers, Detectors and Associated Equipment*, volume 553, pages 274–281, nov 2005.
- [4] F. Krennrich, I. H. Bond, P. J. Boyle, S. M. Bradbury, J. H. Buckley, D. Carter-Lewis, O. Celik, W. Cui, M. Daniel, M. D’Vali, I. de la Calle Perez, C. Duke, A. Falcone, D. J. Fegan, S. J. Fegan, J. P. Finley, L. F. Fortson, J. Gaidos, S. Gammell, K. Gibbs, G. H. Gillanders, J. Grube, J. Hall, T. A. Hall, D. Hanna, A. M. Hillas, J. Holder, D. Horan, A. Jarvis, M. Jordan, G. E. Kenny, M. Kertzman, D. Kieda, J. Kildea, J. Knapp, K. Kosack, H. Krawczynski, M. J. Lang, S. LeBohec, E. Linton, J. Lloyd-Evans, A. Milovanovic, P. Moriarty, D. Müller, T. Nagai, S. Nolan, R. A. Ong, R. Pallassini, D. Petry, B. Power-Mooney, J. Quinn, M. Quinn, K. Ragan, P. Rebillot, P. T. Reynolds, H. J. Rose, M. Schroedter, G. Sembroski, S. P. Swordy, A. Syson, V. V. Vassiliev, G. Walker, S. P. Wakely, T. C. Weekes, and J. Zweerink. VERITAS: The Very Energetic Radiation Imaging Telescope Array System. *New Astronomy Reviews*, 48(5-6):345–349, apr 2004.
- [5] W Hofmann. Status of the High Energy Stereoscopic System (H.E.S.S.) Project. In *Proceedings of ICRC 2001:*, 2001.
- [6] R M Wagner, E Lindfors, A Sillanpää, and S Wagner. The CTA Observatory. In *Fermi Symposium*, 2009.
- [7] Tyce Deyoung. The HAWC observatory. In *Nuclear Instruments and Methods in Physics Research, Section A: Accelerators, Spectrometers, Detectors and Associated Equipment*, volume 692, pages 72–76. North-Holland, nov 2012.
- [8] G. Di Sciascio. The LHAASO experiment: From Gamma-Ray Astronomy to Cosmic Rays. *Nuclear and Particle Physics Proceedings*, 279-281:166–173, oct 2016.
- [9] Victor F. Hess. Über Beobachtungen der durchdringenden Strahlung bei sieben Freiballonfahrten. *Physik Zeitschr.*, 13:1084–1091, 1912.
- [10] T. Yoshida, A. Yamamoto, J. Mitchell, K. Abe, H. Fuke, S. Haino, T. Hams, N. Ikeda, A. Itazaki, K. Izumi, M. H. Lee, T. Maeno, Y. Makida, S. Matsuda, H. Matsumoto, A. Moiseev, J. Nishimura, M. Nozaki, H. Omiya, J. F. Ormes, M. Sasaki, E. S. Seo, Y. Shikaze, A. Stephens, R. Streitmatter, J. Suzuki, Y. Takasugi, K. Tanaka, K. Tanizaki, T. Yamagami, Y. Yamamoto, K. Yamato, and K. Yoshimura. BESS-polar experiment. *Advances in Space Research*, 33(10):1755–1762, jan 2004.
- [11] Y. Shikaze, S. Haino, K. Abe, H. Fuke, T. Hams, K. C. Kim, Y. Makida, S. Matsuda, J. W. Mitchell, A. A. Moiseev, J. Nishimura, M. Nozaki, S. Orito, J. F. Ormes, T. Sanuki, M. Sasaki, E. S. Seo, R. E. Streitmatter, J. Suzuki, K. Tanaka, T. Yamagami, A. Yamamoto, T. Yoshida, and K. Yoshimura. Measurements of

- 0.2-20 GeV/n cosmic-ray proton and helium spectra from 1997 through 2002 with the BESS spectrometer. *Astroparticle Physics*, 28(1):154–167, sep 2007.
- [12] E. S. Seo, H. S. Ahn, S. Beach, J. J. Beatty, S. Coutu, M. A. DuVernois, O. Ganel, Y. J. Han, H. J. Kim, S. K. Kim, M. H. Lee, L. Lutz, S. Nutter, S. Swordy, and J. Z. Wang. Cosmic-Ray energetics and mass (CREAM) balloon experiment. *Advances in Space Research*, 30(5):1263–1272, jan 2002.
- [13] O. Adriani, G. C. Barbarino, G. A. Bazilevskaya, R. Bellotti, M. Boezio, E. A. Bogomolov, L. Bonechi, M. Bongi, V. Bonvicini, S. Bottai, A. Bruno, F. Cafagna, D. Campana, P. Carlson, M. Casolino, G. Castellini, M. P. De Pascale, G. De Rosa, D. Fedele, A. M. Galper, L. Grishantseva, P. Hofverberg, A. Leonov, S. V. Koldashov, S. Y. Krutkov, A. N. Kvashnin, V. Malvezzi, L. Marcelli, W. Menn, V. V. Mikhailov, M. Minori, E. Mocchiutti, M. Nagni, S. Orsi, G. Osteria, P. Papini, M. Pearce, P. Picozza, M. Ricci, S. B. Ricciarini, M. Simon, R. Sparvoli, P. Spillantini, Y. I. Stozhkov, E. Taddei, A. Vacchi, E. Vannuccini, G. Vasilyev, S. A. Voronov, Y. T. Yurkin, G. Zampa, N. Zampa, and V. G. Zverev. New measurement of the antiproton-to-proton flux ratio up to 100 GeV in the cosmic radiation. *Physical Review Letters*, 102(5), feb 2009.
- [14] V. Bonvicini, G. Barbiellini, M. Boezio, E. Mocchiutti, P. Schiavon, G. Scian, A. Vacchi, G. Zampa, N. Zampa, D. Bergström, P. Carlson, T. Francke, J. Lund, M. Pearce, M. Hof, W. Menn, M. Simon, S. A. Stephens, M. Ambriola, R. Bellotti, F. Cafagna, F. Ciaccio, M. Circella, C. De Marzo, N. Giglietto, B. Marangelli, N. Mirizzi, P. Spinelli, O. Adriani, M. Boscherini, R. D’Alessandro, N. Finetti, M. Grandi, P. Papini, A. Perego, S. Piccardi, P. Spillantini, E. Vannuccini, S. Bartalucci, L. Marino, M. Ricci, B. Spataro, V. Bidoli, M. Casolino, M. P. De Pascale, G. Furano, A. Morselli, P. Picozza, R. Sparvoli, L. M. Barbier, E. R. Christian, J. F. Krizmanic, J. W. Mitchell, J. F. Ormes, R. E. Streitmatter, U. Bravar, S. J. Stochaj, S. Bertazzoni, A. Salsano, G. Bazilevskaja, A. Grigorjeva, R. Mukhametshin, Y. Stozhokov, E. Bogomolov, S. Krutkov, G. Vasiljev, A. M. Galper, S. V. Koldashov, M. G. Korotkov, V. V. Mikhailov, A. A. Moissev, J. V. Ozerov, S. A. Voronov, Y. Yurkin, G. Castellini, A. Gabbanini, F. Taccetti, M. Tesi, and V. Vignoli. The PAMELA experiment in space. *Nuclear Instruments and Methods in Physics Research, Section A: Accelerators, Spectrometers, Detectors and Associated Equipment*, 461(1-3):262–268, apr 2001.
- [15] O. Adriani, G. C. Barbarino, G. A. Bazilevskaya, R. Bellotti, M. Boezio, E. A. Bogomolov, M. Bongi, V. Bonvicini, S. Borisov, S. Bottai, A. Bruno, F. Cafagna, D. Campana, R. Carbone, P. Carlson, M. Casolino, G. Castellini, L. Consiglio, M. P. De Pascale, C. De Santis, N. De Simone, V. Di Felice, A. M. Galper, W. Gillard, L. Grishantseva, G. Jerse, A. V. Karelin, S. V. Koldashov, S. Y. Krutkov, A. N. Kvashnin, A. Leonov, V. Malakhov, V. Malvezzi, L. Marcelli, A. G. Mayorov, W. Menn, V. V. Mikhailov, E. Mocchiutti, A. Monaco, N. Mori, N. Nikonov, G. Osteria, F. Palma, P. Papini, M. Pearce, P. Picozza, C. Pizzolotto, M. Ricci, S. B. Ricciarini, L. Rossetto, R. Sarkar, M. Simon, R. Sparvoli, P. Spillantini, S. J. Stochaj, J. C. Stockton, Y. I. Stozhkov, A. Vacchi, E. Vannuccini, G. Vasilyev, S. A. Voronov, J. Wu, Y. T. Yurkin, G. Zampa, N. Zampa, and

- V. G. Zverev. Cosmic-ray electron flux measured by the PAMELA experiment between 1 and 625 GeV. *Physical Review Letters*, 106(20):201101, may 2011.
- [16] D. E. Stilwell, W. D. Davis, R. M. Joyce, F. B. McDonald, J. H. Trainor, W. E. Althouse, A. C. Cummings, T. L. Garrard, E. C. Stone, and R. E. Vogt. The voyager cosmic ray experiment. *IEEE Transactions on Nuclear Science*, 26(1):513–520, 1979.
- [17] Q. An, R. Asfandiyarov, P. Azzarello, P. Bernardini, X. J. Bi, M. S. Cai, J. Chang, D. Y. Chen, H. F. Chen, J. L. Chen, W. Chen, M. Y. Cui, T. S. Cui, H. T. Dai, A. D’Amone, A. De Benedittis, I. De Mitri, M. Di Santo, M. Ding, T. K. Dong, Y. F. Dong, Z. X. Dong, G. Donvito, D. Droz, J. L. Duan, K. K. Duan, D. D’Urso, R. R. Fan, Y. Z. Fan, F. Fang, C. Q. Feng, L. Feng, P. Fusco, V. Gallo, F. J. Gan, M. Gao, F. Gargano, K. Gong, Y. Z. Gong, D. Y. Guo, J. H. Guo, X. L. Guo, S. X. Han, Y. M. Hu, G. S. Huang, X. Y. Huang, Y. Y. Huang, M. Ionica, W. Jiang, X. Jin, J. Kong, S. J. Lei, S. Li, W. L. Li, X. Li, X. Q. Li, Y. Li, Y. F. Liang, Y. M. Liang, N. H. Liao, C. M. Liu, H. Liu, J. Liu, S. B. Liu, W. Q. Liu, Y. Liu, F. Loparco, C. N. Luo, M. Ma, P. X. Ma, S. Y. Ma, T. Ma, X. Y. Ma, G. Marsella, M. N. Mazziotta, D. Mo, X. Y. Niu, X. Pan, W. X. Peng, X. Y. Peng, R. Qiao, J. N. Rao, M. M. Salinas, G. Z. Shang, W. H. Shen, Z. Q. Shen, Z. T. Shen, J. X. Song, H. Su, M. Su, Z. Y. Sun, A. Surdo, X. J. Teng, A. Tykhonov, S. Vitillo, C. Wang, H. Wang, H. Y. Wang, J. Z. Wang, L. G. Wang, Q. Wang, S. Wang, X. H. Wang, X. L. Wang, Y. F. Wang, Y. P. Wang, Y. Z. Wang, Z. M. Wang, D. M. Wei, J. J. Wei, Y. F. Wei, S. C. Wen, D. Wu, J. Wu, L. B. Wu, S. S. Wu, X. Wu, K. Xi, Z. Q. Xia, H. T. Xu, Z. H. Xu, Z. L. Xu, Z. Z. Xu, G. F. Xue, H. B. Yang, P. Yang, Y. Q. Yang, Z. L. Yang, H. J. Yao, Y. H. Yu, Q. Yuan, C. Yue, J. J. Zang, F. Zhang, J. Y. Zhang, J. Z. Zhang, P. F. Zhang, S. X. Zhang, W. Z. Zhang, Y. Zhang, Y. J. Zhang, Y. L. Zhang, Y. P. Zhang, Y. Q. Zhang, Z. Zhang, Z. Y. Zhang, H. Zhao, H. Y. Zhao, X. F. Zhao, C. Y. Zhou, Y. Zhou, X. Zhu, Y. Zhu, and S. Zimmer. Measurement of the cosmic ray proton spectrum from 40 GeV to 100 TeV with the DAMPE satellite. *Science Advances*, 5(9), sep 2019.
- [18] M. Aguilar, D. Aisa, B. Alpat, A. Alvino, G. Ambrosi, K. Andeen, L. Arruda, N. Attig, P. Azzarello, A. Bachlechner, F. Barao, A. Barrau, L. Barrin, A. Bartoloni, L. Basara, M. Battarbee, R. Battiston, J. Bazo, U. Becker, M. Behlmann, B. Beischer, J. Berdugo, B. Bertucci, G. Bigongiari, V. Bindi, S. Bizzaglia, M. Bizzarri, G. Boella, W. De Boer, K. Bollweg, V. Bonnivard, B. Borgia, S. Borsini, M. J. Boschini, M. Bourquin, J. Burger, F. Cadoux, X. D. Cai, M. Capell, S. Caroff, J. Casaus, V. Cascioli, G. Castellini, I. Cernuda, D. Cerreta, F. Cervelli, M. J. Chae, Y. H. Chang, A. I. Chen, H. Chen, G. M. Cheng, H. S. Chen, L. Cheng, H. Y. Chou, E. Choumilov, V. Choutko, C. H. Chung, C. Clark, R. Clavero, G. Coignet, C. Consolandi, A. Contin, C. Corti, E. Cortina Gil, B. Coste, W. Creus, M. Crispoltoni, Z. Cui, Y. M. Dai, C. Delgado, S. Della Torre, M. B. Demirköz, L. Derome, S. Di Falco, L. Di Masso, F. Dimiccoli, C. Díaz, P. Von Doetinchem, F. Donnini, W. J. Du, M. Duranti, D. D’Urso, A. Eline, F. J. Eppling, T. Eronen, Y. Y. Fan, L. Farnesini, J. Feng, E. Fiandrini, A. Fiasson, E. Finch, P. Fisher, Y. Galaktionov, G. Gallucci, B. García, R. García-López, C. Gargiulo, H. Gast, I. Gebauer, M. Gervasi, A. Ghelfi, W. Gillard, F. Giovacchini, P. Goglov, J. Gong, C. Goy, V. Grabski, D. Grandi, M. Graziani,

- C. Guandalini, I. Guerri, K. H. Guo, D. Haas, M. Habiby, S. Haino, K. C. Han, Z. H. He, M. Heil, J. Hoffman, T. H. Hsieh, Z. C. Huang, C. Huh, M. Incagli, M. Ionica, W. Y. Jang, H. Jinchi, K. Kanishev, G. N. Kim, K. S. Kim, Th Kirn, R. Kossakowski, O. Kounina, A. Kounine, V. Koutsenko, M. S. Krafczyk, G. La Vacca, E. Laudi, G. Laurenti, I. Lazzizzera, A. Lebedev, H. T. Lee, S. C. Lee, C. Leluc, G. Levi, H. L. Li, J. Q. Li, Q. Li, Q. Li, T. X. Li, W. Li, Y. Li, Z. H. Li, Z. Y. Li, S. Lim, C. H. Lin, P. Lipari, T. Lippert, D. Liu, H. Liu, M. Lolli, T. Lomtadze, M. J. Lu, S. Q. Lu, Y. S. Lu, K. Luebelsmeyer, J. Z. Luo, S. S. Lv, R. Majka, C. Mañá, J. Marín, T. Martin, G. Martínez, N. Masi, D. Maurin, A. Menchaca-Rocha, Q. Meng, D. C. Mo, L. Morescalchi, P. Mott, M. Müller, J. Q. Ni, N. Nikonov, F. Nozzoli, P. Nunes, A. Obermeier, A. Oliva, M. Orcinha, F. Palmonari, C. Palomares, M. Paniccia, A. Papi, M. Pauluzzi, E. Pedreschi, S. Pensotti, R. Pereira, N. Picot-Clemente, F. Pilo, A. Piluso, C. Pizzolotto, V. Plyaskin, M. Pohl, V. Poireau, E. Postaci, A. Putze, L. Quadrani, X. M. Qi, X. Qin, Z. Y. Qu, T. Rähä, P. G. Rancoita, D. Rapin, J. S. Ricol, I. Rodríguez, S. Rosier-Lees, A. Rozhkov, D. Rozza, R. Sagdeev, J. Sandweiss, P. Saouter, C. Sbarra, S. Schael, S. M. Schmidt, A. Schulz Von Dratzig, G. Schwing, G. Scolieri, E. S. Seo, B. S. Shan, Y. H. Shan, J. Y. Shi, X. Y. Shi, Y. M. Shi, T. Siedenburger, D. Son, F. Spada, F. Spinella, W. Sun, W. H. Sun, M. Tacconi, C. P. Tang, X. W. Tang, Z. C. Tang, L. Tao, D. Tescaro, Samuel C.C. Ting, S. M. Ting, N. Tomassetti, J. Torsti, C. Türkolü, T. Urban, V. Vagelli, E. Valente, C. Vannini, E. Valtonen, S. Vaurynovich, M. Vecchi, M. Velasco, J. P. Vialle, V. Vitale, S. Vitillo, L. Q. Wang, N. H. Wang, Q. L. Wang, R. S. Wang, X. Wang, Z. X. Wang, Z. L. Weng, K. Whitman, J. Wienkenhöver, H. Wu, X. Wu, X. Xia, M. Xie, S. Xie, R. Q. Xiong, G. M. Xin, N. S. Xu, W. Xu, Q. Yan, J. Yang, M. Yang, Q. H. Ye, H. Yi, Y. J. Yu, Z. Q. Yu, S. Zeissler, J. H. Zhang, M. T. Zhang, X. B. Zhang, Z. Zhang, Z. M. Zheng, H. L. Zhuang, V. Zhukov, A. Zichichi, N. Zimmermann, P. Zuccon, and C. Zurbach. Precision Measurement of the Proton Flux in Primary Cosmic Rays from Rigidity 1 GV to 1.8 TV with the Alpha Magnetic Spectrometer on the International Space Station. *Physical Review Letters*, 114(17), apr 2015.
- [19] M. Aguilar, D. Aisa, A. Alvino, G. Ambrosi, K. Andeen, L. Arruda, N. Atig, P. Azzarello, A. Bachlechner, F. Barao, A. Barrau, L. Barrin, A. Bartoloni, L. Basara, M. Battarbee, R. Battiston, J. Bazo, U. Becker, M. Behlmann, B. Beischer, J. Berdugo, B. Bertucci, G. Bigongiari, V. Bindi, S. Bizzaglia, M. Bizzarri, G. Boella, W. De Boer, K. Bollweg, V. Bonnivard, B. Borgia, S. Borsini, M. J. Boschini, M. Bourquin, J. Burger, F. Cadoux, X. D. Cai, M. Capell, S. Caroff, J. Casaus, V. Cascioli, G. Castellini, I. Cernuda, F. Cervelli, M. J. Chae, Y. H. Chang, A. I. Chen, H. Chen, G. M. Cheng, H. S. Chen, L. Cheng, A. Chikanian, H. Y. Chou, E. Choumilov, V. Choutko, C. H. Chung, C. Clark, R. Clavero, G. Coignet, C. Consolandi, A. Contin, C. Corti, B. Coste, Z. Cui, M. Dai, C. Delgado, S. Della Torre, M. B. Demirköz, L. Derome, S. Di Falco, L. Di Masso, F. Dimiccoli, C. Díaz, P. Von Doetinchem, W. J. Du, M. Duranti, D. D'Urso, A. Eline, F. J. Eppling, T. Eronen, Y. Y. Fan, L. Farnesini, J. Feng, E. Fiandrini, A. Fiasson, E. Finch, P. Fisher, Y. Galaktionov, G. Gallucci, B. García, R. García-López, H. Gast, I. Gebauer, M. Gervasi, A. Ghelfi, W. Gillard, F. Giovacchini, P. Goglov, J. Gong, C. Goy, V. Grabski, D. Grandi, M. Graziani, C. Guandalini, I. Guerri, K. H. Guo, M. Habiby, S. Haino, K. C. Han, Z. H. He,

- M. Heil, J. Hoffman, T. H. Hsieh, Z. C. Huang, C. Huh, M. Incagli, M. Ionica, W. Y. Jang, H. Jinchi, K. Kanishev, G. N. Kim, K. S. Kim, Th Kirn, R. Kosakowski, O. Kounina, A. Kounine, V. Koutsenko, M. S. Krafczyk, S. Kunz, G. La Vacca, E. Laudi, G. Laurenti, I. Lazzizzera, A. Lebedev, H. T. Lee, S. C. Lee, C. Leluc, H. L. Li, J. Q. Li, Q. Li, Q. Li, T. X. Li, W. Li, Y. Li, Z. H. Li, Z. Y. Li, S. Lim, C. H. Lin, P. Lipari, T. Lippert, D. Liu, H. Liu, T. Lomtadze, M. J. Lu, Y. S. Lu, K. Luebelsmeyer, F. Luo, J. Z. Luo, S. S. Lv, R. Majka, A. Malinin, C. Mañá, J. Marín, T. Martin, G. Martínez, N. Masi, D. Maurin, A. Menchaca-Rocha, Q. Meng, D. C. Mo, L. Morescalchi, P. Mott, M. Müller, J. Q. Ni, N. Nikonov, F. Nozzoli, P. Nunes, A. Obermeier, A. Oliva, M. Orcinha, F. Palmonari, C. Palomares, M. Paniccia, A. Papi, E. Pedreschi, S. Pensotti, R. Pereira, F. Pilo, A. Piluso, C. Pizzolotto, V. Plyaskin, M. Pohl, V. Poireau, E. Postaci, A. Putze, L. Quadrani, X. M. Qi, P. G. Rancoita, D. Rapin, J. S. Ricol, I. Rodríguez, S. Rosier-Lees, A. Rozhkov, D. Rozza, R. Sagdeev, J. Sandweiss, P. Saouter, C. Sbarra, S. Schael, S. M. Schmidt, D. Schuckardt, A. Schulz Von Dratzig, G. Schwering, G. Scolieri, E. S. Seo, B. S. Shan, Y. H. Shan, J. Y. Shi, X. Y. Shi, Y. M. Shi, T. Siedenburger, D. Son, F. Spada, F. Spinella, W. Sun, W. H. Sun, M. Tacconi, C. P. Tang, X. W. Tang, Z. C. Tang, L. Tao, D. Tescaro, Samuel C.C. Ting, S. M. Ting, N. Tomassetti, J. Torsti, C. Türkolu, T. Urban, V. Vagelli, E. Valente, C. Vannini, E. Valtonen, S. Vaurynovich, M. Vecchi, M. Velasco, J. P. Vialle, L. Q. Wang, Q. L. Wang, R. S. Wang, X. Wang, Z. X. Wang, Z. L. Weng, K. Whitman, J. Wienkenhöver, H. Wu, X. Xia, M. Xie, S. Xie, R. Q. Xiong, G. M. Xin, N. S. Xu, W. Xu, Q. Yan, J. Yang, M. Yang, Q. H. Ye, H. Yi, Y. J. Yu, Z. Q. Yu, S. Zeissler, J. H. Zhang, M. T. Zhang, X. B. Zhang, Z. Zhang, Z. M. Zheng, H. L. Zhuang, V. Zhukov, A. Zichichi, N. Zimmermann, P. Zuccon, and C. Zurbach. Electron and positron fluxes in primary cosmic rays measured with the alpha magnetic spectrometer on the international space station. *Physical Review Letters*, 113(12):121102, sep 2014.
- [20] The CALET collaboration. The CALET experiment on ISS. *Nuclear Physics B - Proceedings Supplements*, 166:43–49, apr 2007.
- [21] O. Adriani, Y. Akaike, K. Asano, Y. Asaoka, M. G. Bagliesi, E. Berti, G. Bigongiari, W. R. Binns, S. Bonechi, M. Bongi, P. Brogi, J. H. Buckley, N. Cannady, G. Castellini, C. Checchia, M. L. Cherry, G. Collazuol, V. Di Felice, K. Ebisawa, H. Fuke, T. G. Guzik, T. Hams, M. Hareyama, N. Hasebe, K. Hibino, M. Ichimura, K. Ioka, W. Ishizaki, M. H. Israel, K. Kasahara, J. Kataoka, R. Kataoka, Y. Katayose, C. Kato, N. Kawanaka, Y. Kawakubo, K. Kohri, H. S. Krawczynski, J. F. Krizmanic, T. Lomtadze, P. Maestro, P. S. Marrocchesi, A. M. Messineo, J. W. Mitchell, S. Miyake, A. A. Moiseev, K. Mori, M. Mori, N. Mori, H. M. Motz, K. Munakata, H. Murakami, S. Nakahira, J. Nishimura, G. A. De Nolfo, S. Okuno, J. F. Ormes, S. Ozawa, L. Pacini, F. Palma, P. Papini, A. V. Penacchioni, B. F. Rauch, S. B. Ricciarini, K. Sakai, T. Sakamoto, M. Sasaki, Y. Shimizu, A. Shiomi, R. Sparvoli, P. Spillantini, F. Stolzi, J. E. Suh, A. Sulaj, I. Takahashi, M. Takayanagi, M. Takita, T. Tamura, N. Tateyama, T. Terasawa, H. Tomida, S. Torii, Y. Tsunesada, Y. Uchihori, S. Ueno, E. Vannuccini, J. P. Wefel, K. Yamaoka, S. Yanagita, A. Yoshida, and K. Yoshida. Extended Measurement of the Cosmic-Ray Electron and Positron Spectrum from 11 GeV to

- 4.8 TeV with the Calorimetric Electron Telescope on the International Space Station. *Physical Review Letters*, 120(26):261102, jun 2018.
- [22] F. Aharonian, A. G. Akhperjanian, U. Barres De Almeida, A. R. Bazer-Bachi, Y. Becherini, B. Behera, W. Benbow, K. Bernlöhr, C. Boisson, A. Bochow, V. Borrel, I. Braun, E. Brion, J. Brucker, P. Brun, R. Bühler, T. Bulik, I. Büsching, T. Boutelier, S. Carrigan, P. M. Chadwick, A. Charbonnier, R. C.G. Chaves, A. Cheesebrough, L. M. Chounet, A. C. Clapson, G. Coignet, L. Costamante, M. Dalton, B. Degrange, C. Deil, H. J. Dickinson, A. Djannati-Ataï, W. Domainko, L. O.C. Drury, F. Dubois, G. Dubus, J. Dyks, M. Dyrda, K. Egberts, D. Emmanoulopoulos, P. Espigat, C. Farnier, F. Feinstein, A. Fiasson, A. Förster, G. Fontaine, M. Füßling, S. Gabici, Y. A. Gallant, L. Gérard, B. Giebels, J. F. Glicenstein, B. Glück, P. Goret, C. Hadjichristidis, D. Hauser, M. Hauser, S. Heinz, G. Heinzlmann, G. Henri, G. Hermann, J. A. Hinton, A. Hoffmann, W. Hofmann, M. Holleran, S. Hoppe, D. Horns, A. Jacholkowska, O. C. De Jager, I. Jung, K. Katarzyński, S. Kaufmann, E. Kendziorra, M. Kerschhaggl, D. Khangulyan, B. Khélifi, D. Keogh, Nu Komin, K. Kosack, G. Lamanna, J. P. Lenain, T. Lohse, V. Marandon, J. M. Martin, O. Martineau-Huynh, A. Marcowith, D. Maurin, T. J.L. McComb, C. Medina, R. Moderski, E. Moulin, M. Naumann-Godo, M. De Naurois, D. Nedbal, D. Nekrassov, J. Niemiec, S. J. Nolan, S. Ohm, J. F. Olive, E. De Oña Wilhelmi, K. J. Orford, J. L. Osborne, M. Ostrowski, M. Panter, G. Pedalletti, G. Pelletier, P. O. Petrucci, S. Pita, G. Pühlhofer, M. Punch, A. Quirrenbach, B. C. Raubenheimer, M. Raue, S. M. Rayner, M. Renaud, F. Rieger, J. Ripken, L. Rob, S. Rosier-Lees, G. Rowell, B. Rudak, C. B. Rulten, J. Ruppel, V. Sahakian, A. Santangelo, R. Schlickeiser, F. M. Schöck, R. Schröder, U. Schwanke, S. Schwarzburg, S. Schwemmer, A. Shalchi, J. L. Skilton, H. Sol, D. Spangler, Stawarz, R. Steenkamp, C. Stegmann, G. Superina, P. H. Tam, J. P. Tavernet, R. Terrier, O. Tibolla, C. Van Eldik, G. Vasileiadis, C. Venter, J. P. Vialle, P. Vincent, M. Vivier, H. J. Völk, F. Volpe, S. J. Wagner, M. Ward, A. A. Zdziarski, and A. Zech. Energy spectrum of cosmic-ray electrons at TeV energies. *Physical Review Letters*, 101(26):261104, dec 2008.
- [23] J. Abraham, M. Aglietta, I. C. Aguirre, M. Albrow, D. Allard, I. Allekotte, P. Allison, J. Alvarez Muñoz, M. G. Do Amaral, M. Ambrosio, L. Anchordoqui, R. Andrews, M. Anguiano, J. C. Dos Anjos, C. Aramo, S. Argiro, K. Arisaka, J. C. Arteaga, S. Atulugama, M. Ave, G. Avila, R. Baggio, X. Bai, A. F. Barbosa, H. M.J. Barbosa, D. Barnhill, S. L.C. Barroso, P. Bauleo, J. Beatty, T. Beau, K. H. Becker, J. A. Bellido, P. Bello, T. Bergmann, E. Berman, X. Bertou, P. Biermann, P. Billoir, R. Biral, H. Bluemer, M. Bohacova, E. Bollmann, C. Bonifazi, M. Boratav, A. Boselli, J. Brack, J. M. Brunet, H. Bui-Duc, V. Cabrera, D. V. Camin, J. N. Capdevielle, A. Carreño, N. Cartiglia, R. Caruso, L. A. De Carvalho, S. Casanova, E. Casimiro, A. Castellina, J. Castro, P. W. Cattaneo, L. Cazon, R. Cester, N. Chávez, D. Cheam, A. Chiavassa, J. A. Chinellato, M. Chiosso, A. Chou, J. Chye, A. Cillis, B. Civit, D. Claes, P. D.J. Clark, R. W. Clay, F. Cohen, A. Cordero, A. Cordier, E. Cormier, J. Cotzomi, U. Cotti, S. Coutu, C. E. Covault, A. Creusot, J. W. Cronin, M. Cuautle, S. Dagoret-Campagne, T. Dang-Quang, P. Da Silva, J. Darling, P. Darriulat, K. Daumiller, B. R. Dawson, L. De Bruijn, A. De Capoa, M. A.L. De Oliveira, V. De Souza, A. Della Selva,

O. Deligny, J. C. Diaz, C. Dobrigkeit, J. C. D'Olivo, A. Dorofeev, M. T. Dova, A. Dye, M. A. Duvernois, R. Engel, L. N. Epele, P. Eschstruth, C. O. Escobar, A. Etchegoyen, P. Facal San Luis, A. C. Fauth, N. Fazzini, A. Fernández, A. M.J. Ferrero, B. Fick, A. Filevich, A. Filipčivč, R. Fonte, W. Fulgione, E. Gámez, B. Garcia, C. A. Garcia, H. Geenen, H. Gemmeke, C. Germain-Renaud, P. L. Ghia, K. Gibbs, M. Giller, J. Gitto, H. Glass, M. Gómez Berisso, P. F. Gomez Vitale, J. González, J. González, D. Gora, A. Goodwin, P. Gouffon, V. Grassi, A. F. Grillo, C. Grunfeld, J. Grygar, F. Guarino, G. Guedes, C. Guerard, R. Gumbshaimer, J. L. Harton, F. Hasenbalg, D. Heck, J. M. Hernández, D. Hoffer, C. Hojvat, P. Homola, M. Horvat, M. Hrabovsky, A. Insolia, S. Jaminion, Y. Jerónimo, L. Jiang, M. Kaducak, K. H. Kampert, B. Keilhauer, E. Kemp, H. Klages, M. Kleifges, J. Kleinfeller, J. Knapp, A. Kopmann, N. Kunka, M. Kutschera, C. Lachaud, M. Lapolla, A. Letessier-Selvon, I. Lhenry-Yvon, J. Lloyd-Evans, R. López, A. Lopez Aguera, M. Lucano, R. Luna, Y. Ma, M. E. Manceñido, P. F. Manfredi, L. Manhaes, P. Mantsch, A. G. Mariazzi, M. J. Markus, G. Martin, O. Martineau, J. Martinez, N. Martinez, O. Martínez, H. J. Mathes, J. A.J. Matthews, J. Matthews, G. Matthiae, E. Marques, P. Matussek, G. Maurin, D. Maurizio, P. Mazur, T. McCauley, M. McEwen, R. R. McNeil, C. Medina, M. C. Medina, G. Medina-Tanco, D. Melo, M. Melocchi, E. Menichetti, A. Menshikov, F. Meyer, R. Meyhandan, J. C. Meza, G. Miele, W. Miller, M. Mohammed, D. Monnier-Ragaigne, C. Morello, E. Moreno, M. Mostafa, R. Mussa, H. Nassini, G. Navarra, L. Nellen, F. Nerling, C. Newman-Holmes, D. Nicotra, S. Nigro, D. Nitz, H. Nogima, D. Nosek, M. Nuñez, T. Ohnuki, A. Olinto, S. Ostapchenko, M. Palatka, G. Parente, E. Parizot, E. H. Pasaye, N. Pastrone, M. Patel, T. Paul, I. Pedraza, J. Pekala, R. Pelayo, I. M. Pepe, A. Pérez-Lorenzana, L. Perrone, N. Peshman, S. Petrera, P. Petrinca, D. Pham-Ngoc, P. Pham-Trung, T. Pierog, O. Pisanti, N. Playez, E. Ponce, T. A. Porter, L. Prado Junior, P. Privitera, M. Prouza, C. L. Pryke, J. B. Rafert, G. Raia, S. Ranchon, L. Ratti, D. Ravignani, V. Re, H. C. Reis, S. Reucroft, B. Revenue, M. Richten, J. Ridky, A. Risi, M. Risse, V. Rizi, M. D. Roberts, C. Robledo, G. Rodriguez, J. Rodriguez, J. Rodriguez Martino, S. Román, L. Rosa, M. Roth, A. C. Rovero, H. Salazar, G. Salina, F. Sanchez, M. Santander, L. G. Dos Santos, R. Sato, P. Schovanek, V. Scherini, S. J. Sciutto, G. Sequeiros-Haddad, R. C. Shellard, E. Shibuya, F. V. Siguas, W. Slater, N. Smetniansky-De Grande, K. Smith, G. R. Snow, P. Sommers, C. Song, H. Spinka, F. Suarez, T. Suomijärvi, D. Supanitsky, J. Swain, Z. Szadkowski, A. Tamashiro, G. J. Thornton, T. Thouw, R. Ticona, W. Tkaczyk, C. J. Todero Peixoto, A. Tripathi, G. Tristram, M. Trombley, D. Tscherniakhovski, P. Tuckey, V. Tunnicliffe, M. Urban, C. Uribe Estrada, J. F. Valdés, A. Vargas, C. Vargas, R. Vazquez, D. Veberič, A. Veiga, A. Velarde, F. Vernet, V. Verzi, M. Videla, C. Vigorito, L. M. Villaseñor, M. Vlcek, L. Voyvodic, T. Vo-Van, T. Waldenmaier, P. Walker, D. Warner, A. A. Watson, Ch Wiebusch, G. Wiczorek, B. Wilczynska, H. Wilczynski, N. R. Wild, T. Yamamoto, E. Zas, D. Zavrtnik, M. Zavrtnik, A. Zepeda, C. Zhang, and Q. Zhu. Properties and performance of the prototype instrument for the Pierre Auger Observatory. *Nuclear Instruments and Methods in Physics Research, Section A: Accelerators, Spectrometers, Detectors and Associated Equipment*, 523(1-2):50–95, may 2004.

- [24] Francesco Fenu. The cosmic ray energy spectrum measured using the Pierre Auger Observatory. In *Proceedings of Science*, volume 2017, page 486. Sissa Medialab Srl, jul 2017.
- [25] H. O. Klages, W. D. Apel, K. Bekk, E. Bollmann, H. Bozdog, I. M. Brancus, M. Brendle, A. Chilingarian, K. Daumiller, P. Doll, J. Engler, M. Föller, P. Gabriel, H. J. Gils, R. Glasstetter, A. Haungs, D. Heck, J. Hörandel, K. H. Kampert, H. Keim, J. Kempa, J. Knapp, H. J. Mathes, H. J. Mayer, H. H. Mielke, D. Mühlberg, J. Oehlschläger, M. Petcu, U. Raidt, H. Rebel, M. Roth, G. Schatz, H. Schieler, G. Schmalz, H. J. Simonis, T. Thouw, J. Unger, G. Völker, B. Vulpescu, G. J. Wagner, J. Wdowczyk, J. Weber, J. Wentz, Y. Wetzel, T. Wibig, T. Wiegert, D. Wochele, J. Wochele, J. Zabierowski, S. Zagromski, and B. Zeitnitz. The KASCADE Experiment. *Nuclear Physics B - Proceedings Supplements*, 52(3):92–102, feb 1997.
- [26] W. D. Apel, J. C. Arteaga-Velázquez, K. Bekk, M. Bertaina, J. Blümer, H. Bozdog, I. M. Brancus, E. Cantoni, A. Chiavassa, F. Cossavella, K. Daumiller, V. De Souza, F. Di Pierro, P. Doll, R. Engel, J. Engler, M. Finger, B. Fuchs, D. Fuhrmann, H. J. Gils, R. Glasstetter, C. Grupen, A. Haungs, D. Heck, J. R. Hörandel, D. Huber, T. Huege, K. H. Kampert, D. Kang, H. O. Klages, K. Link, P. Łuczak, M. Ludwig, H. J. Mathes, H. J. Mayer, M. Melissas, J. Milke, B. Mitrica, C. Morello, J. Oehlschläger, S. Ostapchenko, N. Palmieri, M. Petcu, T. Pierog, H. Rebel, M. Roth, H. Schieler, S. Schoo, F. G. Schröder, O. Sima, G. Toma, G. C. Trinchero, H. Ulrich, A. Weindl, J. Wochele, M. Wommer, and J. Zabierowski. KASCADE-Grande measurements of energy spectra for elemental groups of cosmic rays. *Astroparticle Physics*, 47:54–66, jun 2013.
- [27] X. Bai. The IceCube/IceTop air shower experiment. In *Nuclear Physics B - Proceedings Supplements*, volume 175-176, pages 415–420, jan 2008.
- [28] R. Abbasi, Y. Abdou, T. Abu-Zayyad, M. Ackermann, J. Adams, J. A. Aguilar, M. Ahlers, D. Altmann, K. Andeen, J. Auffenberg, X. Bai, M. Baker, S. W. Barwick, V. Baum, R. Bay, J. L. Bazo Alba, K. Beattie, J. J. Beatty, S. Bechet, J. K. Becker, K. H. Becker, M. Bell, M. L. Benabderrahmane, S. Benzvi, J. Berdermann, P. Berghaus, D. Berley, E. Bernardini, D. Bertrand, D. Z. Besson, D. Bindig, M. Bissok, E. Blaufuss, J. Blumenthal, D. J. Boersma, C. Boehm, D. Bose, S. Böser, O. Botner, L. Brayeur, A. M. Brown, S. Buitink, K. S. Caballero-Mora, M. Carson, M. Casier, D. Chirkin, B. Christy, F. Clevermann, S. Cohen, D. F. Cowen, A. H. Cruz Silva, M. V. D’Agostino, M. Danninger, J. Daughhetee, J. C. Davis, C. De Clercq, T. Degner, F. Descamps, P. Desiati, G. De Vries-Uiterweerd, T. Deyoung, J. C. Díaz-Vélez, J. Dreyer, J. P. Dumm, M. Dunkman, J. Eisch, R. W. Ellsworth, O. Engdegård, S. Euler, P. A. Evenson, O. Fadiran, A. R. Fazely, A. Fedynitch, J. Feintzeig, T. Feusels, K. Filimonov, C. Finley, T. Fischer-Wasels, S. Flis, A. Franckowiak, R. Franke, T. K. Gaisser, J. Gallagher, L. Gerhardt, L. Gladstone, T. Glüsenskamp, A. Goldschmidt, J. A. Goodman, D. Góra, D. Grant, A. Groß, S. Grullon, M. Gurtner, C. Ha, A. Haj Ismail, A. Hallgren, F. Halzen, K. Han, K. Hanson, D. Heereman, P. Heimann, D. Heinen, K. Helbing, R. Hellauer, S. Hickford, G. C. Hill, K. D. Hoffman, B. Hoffmann, A. Homeier, K. Hoshina, W. Huelsnitz, P. O. Hulth, K. Hultqvist,

- S. Hussain, A. Ishihara, E. Jacobi, J. Jacobsen, G. S. Japaridze, H. Johansson, A. Kappes, T. Karg, A. Karle, J. Kiryluk, F. Kislak, S. R. Klein, S. Klepser, J. H. Köhne, G. Köhnen, H. Kolanoski, L. Köpke, S. Kopper, D. J. Koskinen, M. Kowalski, M. Krasberg, G. Kroll, J. Kunnen, N. Kurahashi, T. Kuwabara, M. Labare, K. Laihem, H. Landsman, M. J. Larson, R. Lauer, J. Lünemann, J. Madsen, R. Maruyama, K. Mase, H. S. Matis, K. Meagher, M. Merck, P. Mészáros, T. Meures, S. Miarecki, E. Middell, N. Milke, J. Miller, T. Montaruli, R. Morse, S. M. Movit, R. Nahnauer, J. W. Nam, U. Naumann, S. C. Nowicki, D. R. Nygren, S. Odrowski, A. Olivas, M. Olivo, A. O'Murchadha, S. Panknin, L. Paul, C. Pérez De Los Heros, D. Pieloth, J. Posselt, P. B. Price, G. T. Przybylski, K. Rawlins, P. Redl, E. Resconi, W. Rhode, M. Ribordy, M. Richman, B. Riedel, J. P. Rodrigues, F. Rothmaier, C. Rott, T. Ruhe, D. Rutledge, B. Ruzybayev, D. Ryckbosch, H. G. Sander, M. Santander, S. Sarkar, K. Schatto, M. Scheel, T. Schmidt, S. Schöneberg, A. Schönwald, A. Schukraft, L. Schulte, A. Schultes, O. Schulz, M. Schunck, D. Seckel, B. Semburg, S. H. Seo, Y. Sestayo, S. Seunarine, A. Silvestri, M. W.E. Smith, G. M. Spiczak, C. Spiering, M. Stamatikos, T. Stanev, T. Stezelberger, R. G. Stokstad, A. Stöbl, E. A. Strahler, R. Ström, M. Stür, G. W. Sullivan, H. Taavola, I. Taboada, A. Tamburro, S. Ter-Antonyan, S. Tilav, P. A. Toale, S. Toscano, D. Tosi, N. Van Eijndhoven, A. Van Overloop, J. Van Santen, M. Vehring, M. Voge, C. Walck, T. Waldenmaier, M. Wallraff, M. Walter, R. Wasserman, Ch Weaver, C. Wendt, S. Westerhoff, N. Whitehorn, K. Wiebe, C. H. Wiebusch, D. R. Williams, R. Wischniewski, H. Wissing, M. Wolf, T. R. Wood, K. Woschnagg, C. Xu, D. L. Xu, X. W. Xu, J. P. Yanez, G. Yodh, S. Yoshida, P. Zarzhitsky, and M. Zoll. All-particle cosmic ray energy spectrum measured with 26 IceTop stations. *Astroparticle Physics*, 44:40–58, 2013.
- [29] P. Schellart, A. Nelles, S. Buitink, A. Corstanje, J. E. Enriquez, H. Falcke, W. Frieswijk, J. R. Horandel, A. Horneffer, C. W. James, M. Krause, M. Mevius, O. Scholten, S. Ter Veen, S. Thoudam, M. Van Den Akker, A. Alexov, J. Anderson, I. M. Avruch, L. Bahren, R. Beck, M. E. Bell, P. Bennema, M. J. Bentum, G. Bernardi, P. Best, J. Bregman, F. Breitling, M. Brentjens, J. Broderick, M. Bruggen, B. Ciardi, A. Coolen, F. De Gasperin, E. De Geus, A. De Jong, M. De Vos, S. Duscha, J. Eisloffel, R. A. Fallows, C. Ferrari, M. A. Garrett, J. Griesmeier, T. Grit, J. P. Hamaker, T. E. Hassall, G. Heald, J. W.T. Hessels, M. Hoeft, H. A. Holties, M. Iacobelli, E. Juette, A. Karastergiou, W. Klijn, J. Kohler, V. I. Kondratiev, M. Kramer, M. Kuniyoshi, G. Kuper, P. Maat, G. Macario, G. Mann, S. Markoff, D. McKay-Bukowski, J. P. McKean, J. C.A. Miller-Jones, J. D. Mol, D. D. Mulcahy, H. Munk, R. Nijboer, M. J. Norden, E. Orru, R. Overeem, H. Paas, M. Pandey-Pommier, R. Pizzo, A. G. Polatidis, A. Renting, J. W. Romein, H. Rottgering, A. Schoenmakers, D. Schwarz, J. Sluman, O. Smirnov, C. Sobey, B. W. Stappers, M. Steinmetz, J. Swinbank, Y. Tang, C. Tasse, C. Toribio, J. Van Leeuwen, R. Van Nieuwpoort, R. J. Van Weeren, N. Vermaas, R. Vermeulen, C. Vocks, C. Vogt, R. A.M.J. Wijers, S. J. Wijnholds, M. W. Wise, O. Wucknitz, S. Yatawatta, P. Zarka, and A. Zensus. Detecting cosmic rays with the LOFAR radio telescope. *Astronomy and Astrophysics*, 560:98, dec 2013.

- [30] S. Thoudam, S. Buitink, A. Corstanje, J. E. Enriquez, H. Falcke, J. R. Hörandel, A. Nelles, J. P. Rachen, L. Rossetto, P. Schellart, O. Scholten, S. Ter Veen, T. N.G. Trinh, and L. Van Kessel. Measurement of the cosmic-ray energy spectrum above 1016 eV with the LOFAR Radboud Air Shower Array. *Astroparticle Physics*, 73:34–43, jan 2016.
- [31] F. A. Aharonian. *Very High Energy Cosmic Gamma Radiation - A Crucial Window on the Extreme Universe*. World Scientific Publishing Co. Pte. Ltd., 2004.
- [32] O. Adriani, G. C. Barbarino, G. A. Bazilevskaia, R. Bellotti, M. Boezio, E. A. Bogomolov, L. Bonechi, M. Bonghi, V. Bonvicini, S. Bottai, A. Bruno, F. Cafagna, D. Campana, P. Carlson, M. Casolino, G. Castellini, M. P. De Pascale, G. De Rosa, N. De Simone, V. Di Felice, A. M. Galper, L. Grishantseva, P. Hofverberg, S. V. Koldashov, S. Y. Krutkov, A. N. Kvashnin, A. Leonov, V. Malvezzi, L. Marcelli, W. Menn, V. V. Mikhailov, E. Mocchiutti, S. Orsi, G. Osteria, P. Papini, M. Pearce, P. Picozza, M. Ricci, S. B. Ricciarini, M. Simon, R. Sparvoli, P. Spillantini, Y. I. Stozhkov, A. Vacchi, E. Vannuccini, G. Vasilyev, S. A. Voronov, Y. T. Yurkin, G. Zampa, N. Zampa, and V. G. Zverev. An anomalous positron abundance in cosmic rays with energies 1.5-100 GeV. *Nature*, 458(7238):607–609, apr 2009.
- [33] M. S. Potgieter and R. R. Nndanganeni. A local interstellar spectrum for galactic electrons. *Astroparticle Physics*, 48:25–29, feb 2013.
- [34] R. U. Abbasi, T. Abu-Zayyad, M. Allen, J. F. Amman, G. Archbold, K. Belov, J. W. Belz, S. Y. Ben Zvi, D. R. Bergman, S. A. Blake, O. A. Brusova, G. W. Burt, C. Cannon, Z. Cao, B. C. Connolly, W. Deng, Y. Fedorova, C. B. Finley, R. C. Gray, W. F. Hanlon, C. M. Hoffman, M. H. Holzschneider, G. Hughes, P. Hütemeyer, B. F. Jones, C. C.H. Jui, K. Kim, M. A. Kirn, E. C. Loh, M. M. Maestas, N. Manago, L. J. Marek, K. Martens, J. A.J. Matthews, J. N. Matthews, S. A. Moore, A. O’Neill, C. A. Painter, L. Perera, K. Reil, R. Riehle, M. Roberts, D. Rodriguez, N. Sasaki, S. R. Schnetzer, L. M. Scott, G. Sinnis, J. D. Smith, P. Sokolsky, C. Song, R. W. Springer, B. T. Stokes, S. B. Thomas, J. R. Thomas, G. B. Thomson, D. Tupa, S. Westerhoff, L. R. Wiencke, X. Zhang, and A. Zech. First observation of the Greisen-Zatsepin-Kuzmin suppression. *Physical Review Letters*, 100(10):101101, mar 2008.
- [35] T. Antoni, W. D. Apel, A. F. Badea, K. Bekk, A. Bercuci, J. Blümer, H. Bozdog, I. M. Brancus, A. Chilingarian, K. Daumiller, P. Doll, R. Engel, J. Engler, F. Feßler, H. J. Gils, R. Glasstetter, A. Haungs, D. Heck, J. R. Hörandel, K. H. Kampert, H. O. Klages, G. Maier, H. J. Mathes, H. J. Mayer, J. Milke, M. Müller, R. Obenland, J. Oehlschläger, S. Ostapchenko, M. Petcu, H. Rebel, A. Risse, M. Risse, M. Roth, G. Schatz, H. Schieler, J. Scholz, T. Thouw, Holger Ulrich, J. van Buren, A. Vardanyan, A. Weindl, J. Wochele, and J. Zabierowski. KASCADE measurements of energy spectra for elemental groups of cosmic rays: Results and open problems. *Astroparticle Physics*, 24(1-2):1–25, 2005.
- [36] D. J. Bird, S. C. Corbata, H. Y. Dai, B. R. Dawson, J. W. Elbert, T. K. Gaisser, K. D. Green, M. A. Huang, D. B. Kieda, S. Ko, C. G. Larsen, E. C. Loh, M. Luo, M. H. Salamon, D. Smith, P. Sokolsky, P. Sommers, T. Stanev, J. K.K. Tang, S. B.

- Thomas, and S. Tilav. Evidence for correlated changes in the spectrum and composition of cosmic rays at extremely high energies. *Physical Review Letters*, 71(21):3401–3404, nov 1993.
- [37] V. L. Ginzburg and V. S. Ptuskin. On the origin of cosmic rays: Some problems in high-energy astrophysics. *Reviews of Modern Physics*, 48(2):161–189, apr 1976.
- [38] A. R. Bell. Cosmic ray acceleration. *Astroparticle Physics*, 43:56–70, mar 2013.
- [39] Y. S. Yoon, T. Anderson, A. Barrau, N. B. Conklin, S. Coutu, L. Derome, J. H. Han, J. A. Jeon, K. C. Kim, M. H. Kim, H. Y. Lee, J. Lee, M. H. Lee, S. E. Lee, J. T. Link, A. Menchaca-Rocha, J. W. Mitchell, S. I. Mognet, S. Nutter, I. H. Park, N. Picot-Clemente, A. Putze, E. S. Seo, J. Smith, and J. Wu. Proton and Helium Spectra from the CREAM-III Flight. *The Astrophysical Journal*, 839(1):5, apr 2017.
- [40] O. Adriani, Y. Akaike, K. Asano, Y. Asaoka, M. G. Bagliesi, E. Berti, G. Bigongiari, W. R. Binns, S. Bonechi, M. Bongi, P. Brogi, A. Bruno, J. H. Buckley, N. Cannady, G. Castellini, C. Checchia, M. L. Cherry, G. Collazuol, V. Di Felice, K. Ebisawa, H. Fuke, T. G. Guzik, T. Hams, N. Hasebe, K. Hibino, M. Ichimura, K. Ioka, W. Ishizaki, M. H. Israel, K. Kasahara, J. Kataoka, R. Kataoka, Y. Katayose, C. Kato, N. Kawanaka, Y. Kawakubo, K. Kohri, H. S. Krawczynski, J. F. Krizmanic, T. Lomtadze, P. Maestro, P. S. Marrocchesi, A. M. Messineo, J. W. Mitchell, S. Miyake, A. A. Moiseev, K. Mori, M. Mori, N. Mori, H. M. Motz, K. Munakata, H. Murakami, S. Nakahira, J. Nishimura, G. A. De Nolfo, S. Okuno, J. F. Ormes, S. Ozawa, L. Pacini, F. Palma, P. Papini, A. V. Penacchioni, B. F. Rauch, S. B. Ricciarini, K. Sakai, T. Sakamoto, M. Sasaki, Y. Shimizu, A. Shiomi, R. Sparvoli, P. Spillantini, F. Stolzi, J. E. Suh, A. Sulaj, I. Takahashi, M. Takayanagi, M. Takita, T. Tamura, T. Terasawa, H. Tomida, S. Torii, Y. Tsunesada, Y. Uchihori, S. Ueno, E. Vannuccini, J. P. Wefel, K. Yamaoka, S. Yanagita, A. Yoshida, and K. Yoshida. Direct Measurement of the Cosmic-Ray Proton Spectrum from 50 GeV to 10 TeV with the Calorimetric Electron Telescope on the International Space Station. *Physical Review Letters*, 122(18):28, may 2019.
- [41] Paolo Lipari and Silvia Vernetto. The shape of the cosmic ray proton spectrum. *Astroparticle Physics*, 120:102441, jul 2020.
- [42] M. G. Aartsen, M. Ackermann, J. Adams, J. A. Aguilar, M. Ahlers, M. Ahrens, C. Alispach, K. Andeen, T. Anderson, I. Anseau, G. Anton, C. Argüelles, J. Auffenberg, S. Axani, P. Backes, H. Bagherpour, X. Bai, A. Barbano, S. W. Barwick, V. Baum, S. Baur, R. Bay, J. J. Beatty, K. H. Becker, J. Becker Tjus, S. Benzvi, D. Berley, E. Bernardini, D. Z. Besson, G. Binder, D. Bindig, E. Blaufuss, S. Blot, C. Boehm, M. Börner, S. Böser, O. Botner, J. Böttcher, E. Bourbeau, J. Bourbeau, F. Bradascio, J. Braun, H. P. Bretz, S. Bron, J. Brostean-Kaiser, A. Burgman, J. Buscher, R. S. Busse, T. Carver, C. Chen, E. Cheung, D. Chirkin, K. Clark, L. Classen, G. H. Collin, J. M. Conrad, P. Coppin, P. Correa, D. F. Cowen, R. Cross, P. Dave, J. P.A.M. De André, C. De Clercq, J. J. Delaunay, H. Dembinski, K. Deoskar, S. De Ridder, P. Desiati, K. D. De Vries, G. De

Wasseige, M. De With, T. Deyoung, A. Diaz, J. C. Díaz-Vélez, H. Dujmovic, M. Dunkman, E. Dvorak, B. Eberhardt, T. Ehrhardt, P. Eller, P. A. Evenson, S. Fahey, A. R. Fazely, J. Felde, T. Feusels, K. Filimonov, C. Finley, A. Franckowiak, E. Friedman, A. Fritz, T. K. Gaisser, J. Gallagher, E. Ganster, S. Garrappa, L. Gerhardt, K. Ghorbani, T. Glauch, T. Glüsenkamp, A. Goldschmidt, J. G. Gonzalez, D. Grant, Z. Griffith, M. Günder, M. Gündüz, C. Haack, A. Hallgren, L. Halve, F. Halzen, K. Hanson, D. Hebecker, D. Heereman, P. Heix, K. Helbing, R. Hellauer, F. Henningsen, S. Hickford, J. Hignight, G. C. Hill, K. D. Hoffman, R. Hoffmann, T. Hoinka, B. Hokanson-Fasig, K. Hoshina, F. Huang, M. Huber, K. Hultqvist, M. Hünnefeld, R. Hussain, S. In, N. Iovine, A. Ishihara, E. Jacobi, G. S. Japaridze, M. Jeong, K. Jero, B. J.P. Jones, F. Jonske, R. Joppe, W. Kang, A. Kappes, D. Kappesser, T. Karg, M. Karl, A. Karle, U. Katz, M. Kauer, J. L. Kelley, A. Kheirandish, J. Kim, T. Kintscher, J. Kiryluk, T. Kittler, S. R. Klein, R. Koirala, H. Kolanoski, L. Köpke, C. Kopper, S. Kopper, D. J. Koskinen, M. Kowalski, K. Krings, G. Krückl, N. Kulacz, S. Kunwar, N. Kurahashi, A. Kyriacou, M. Labare, J. L. Lanfranchi, M. J. Larson, F. Lauber, J. P. Lazar, K. Leonard, M. Leuermann, Q. R. Liu, E. Lohfink, C. J. Lozano Mariscal, L. Lu, F. Lucarelli, J. Lünemann, W. Luszczak, J. Madsen, G. Maggi, K. B.M. Mahn, Y. Makino, P. Mallik, K. Mallot, S. Mancina, I. C. Mariş, R. Maruyama, K. Mase, R. Maunu, K. Meagher, M. Medici, A. Medina, M. Meier, S. Meighen-Berger, T. Menne, G. Merino, T. Meures, S. Miarecki, J. Micallef, G. Momenté, T. Montaruli, R. W. Moore, R. Morse, M. Moulai, P. Muth, R. Nagai, R. Nahnauer, P. Nakarmi, U. Naumann, G. Neer, H. Niederhausen, S. C. Nowicki, D. R. Nygren, A. Obertacke Pollmann, A. Olivas, A. O'Murchadha, E. O'Sullivan, T. Palczewski, H. Pandya, D. V. Pankova, N. Park, P. Peiffer, C. Pérez De Los Heros, S. Philippen, D. Pieloth, E. Pinat, A. Pizzuto, M. Plum, A. Porcelli, P. B. Price, G. T. Przybylski, C. Raab, A. Raissi, M. Rameez, L. Rauch, K. Rawlins, I. C. Rea, R. Reimann, B. Relethford, G. Renzi, E. Resconi, W. Rhode, M. Richman, S. Robertson, M. Rongen, C. Rott, T. Ruhe, D. Ryckbosch, D. Rysewyk, I. Safa, S. E. Sanchez Herrera, A. Sandrock, J. Sandroos, M. Santander, S. Sarkar, S. Sarkar, K. Satalecka, M. Schaufel, P. Schlunder, T. Schmidt, A. Schneider, J. Schneider, L. Schumacher, S. Sclafani, D. Seckel, S. Seunarine, S. Shafali, M. Silva, R. Snihur, J. Soedingrekso, D. Soldin, M. Song, G. M. Spiczak, C. Spiering, J. Stachurska, M. Stamatikos, T. Stanev, A. Stasik, R. Stein, J. Stettner, A. Steuer, T. Stezelberger, R. G. Stokstad, A. Stößl, N. L. Strotjohann, T. Stürwald, T. Stuttard, G. W. Sullivan, M. Sutherland, I. Taboada, F. Tenholt, S. Ter-Antonyan, A. Terliuk, S. Tilav, L. Tomankova, C. Tönnis, S. Toscano, D. Tosi, M. Tselengidou, C. F. Tung, A. Turcati, R. Turcotte, C. F. Turley, B. Ty, E. Unger, M. A. Unland Elorrieta, M. Usner, J. Vandenbroucke, W. Van Driessche, D. Van Eijk, N. Van Eijndhoven, S. Vanheule, J. Van Santen, M. Vraeghe, C. Walck, A. Wallace, M. Wallraff, N. Wandkowsky, T. B. Watson, C. Weaver, M. J. Weiss, J. Weldert, C. Wendt, J. Werthebach, S. Westerhoff, B. J. Whelan, N. Whitehorn, K. Wiebe, C. H. Wiebusch, L. Wille, D. R. Williams, L. Wills, M. Wolf, J. Wood, T. R. Wood, K. Woschnagg, G. Wrede, D. L. Xu, X. W. Xu, Y. Xu, J. P. Yanez, G. Yodh, S. Yoshida, T. Yuan, and M. Zöcklein. Cosmic ray spectrum and composition from PeV to EeV using 3 years of data from IceTop and IceCube. *Physical Review D*, 100(8):46, oct 2019.

- [43] Carmelo Evoli. The Cosmic-Ray Energy Spectrum <<http://doi.org/10.5281/zenodo.2360277>>, visited on 03.09.2020, oct 2018.
- [44] G. Ambrosi, Q. An, R. Asfandiyarov, P. Azzarello, P. Bernardini, B. Bertucci, M. S. Cai, J. Chang, D. Y. Chen, H. F. Chen, J. L. Chen, W. Chen, M. Y. Cui, T. S. Cui, A. D'Amone, A. De Benedittis, I. De Mitri, M. Di Santo, J. N. Dong, T. K. Dong, Y. F. Dong, Z. X. Dong, G. Donvito, D. Droz, K. K. Duan, J. L. Duan, M. Duranti, D. D'Urso, R. R. Fan, Y. Z. Fan, F. Fang, C. Q. Feng, L. Feng, P. Fusco, V. Gallo, F. J. Gan, M. Gao, S. S. Gao, F. Gargano, S. Garrappa, K. Gong, Y. Z. Gong, D. Y. Guo, J. H. Guo, Y. M. Hu, G. S. Huang, Y. Y. Huang, M. Ionica, D. Jiang, W. Jiang, X. Jin, J. Kong, S. J. Lei, S. Li, X. Li, W. L. Li, Y. Li, Y. F. Liang, Y. M. Liang, N. H. Liao, H. Liu, J. Liu, S. B. Liu, W. Q. Liu, Y. Liu, F. Loparco, M. Ma, P. X. Ma, S. Y. Ma, T. Ma, X. Q. Ma, X. Y. Ma, G. Marsella, M. N. Mazziotta, D. Mo, X. Y. Niu, X. Y. Peng, W. X. Peng, R. Qiao, J. N. Rao, M. M. Salinas, G. Z. Shang, W. H. Shen, Z. Q. Shen, Z. T. Shen, J. X. Song, H. Su, M. Su, Z. Y. Sun, A. Surdo, X. J. Teng, X. B. Tian, A. Tykhonov, V. Vagelli, S. Vitillo, C. Wang, H. Wang, H. Y. Wang, J. Z. Wang, L. G. Wang, Q. Wang, S. Wang, X. H. Wang, X. L. Wang, Y. F. Wang, Y. P. Wang, Y. Z. Wang, S. C. Wen, Z. M. Wang, D. M. Wei, J. J. Wei, Y. F. Wei, D. Wu, J. Wu, L. B. Wu, S. S. Wu, X. Wu, K. Xi, Z. Q. Xia, Y. L. Xin, H. T. Xu, Z. L. Xu, Z. Z. Xu, G. F. Xue, H. B. Yang, P. Yang, Y. Q. Yang, Z. L. Yang, H. J. Yao, Y. H. Yu, Q. Yuan, C. Yue, J. J. Zang, C. Zhang, D. L. Zhang, F. Zhang, J. B. Zhang, J. Y. Zhang, J. Z. Zhang, L. Zhang, P. F. Zhang, S. X. Zhang, W. Z. Zhang, Y. Zhang, Y. J. Zhang, Y. Q. Zhang, Y. L. Zhang, Y. P. Zhang, Z. Zhang, Z. Y. Zhang, H. Zhao, H. Y. Zhao, X. F. Zhao, C. Y. Zhou, Y. Zhou, X. Zhu, Y. Zhu, and S. Zimmer. Direct detection of a break in the teraelectronvolt cosmic-ray spectrum of electrons and positrons. *Nature*, 552(7683):63–66, 2017.
- [45] The H.E.S.S. collaboration. Probing Local Sources with High Energy Cosmic Ray Electrons <<https://www.mpi-hd.mpg.de/hfm/HESS/pages/home/som/2017/09/>> visited on 03.09.2020, 2017.
- [46] Markus Ahlers and Philipp Mertsch. Origin of Small-Scale Anisotropies in Galactic Cosmic Rays. *Progress in Particle and Nuclear Physics*, 94:184–216, 2017.
- [47] Malcolm Longair. *High Energy Astrophysics*. Cambridge University Press, 2011.
- [48] F. A. Aharonian and A. M. Atoyan. On the emissivity of π^0 -decay gamma radiation in the vicinity of accelerators of galactic cosmic rays. *Astronomy & Astrophysics*, 309:917–928, 1996.
- [49] Ervin Kafexhiu, Felix Aharonian, Andrew M Taylor, and Gabriela S Vila. Parametrization of gamma-ray production cross-sections for pp interactions in a broad proton energy range from the kinematic threshold to PeV energies. *Physical Review D*, 90(12):123014, 2014.

- [50] Masaki Mori. Nuclear enhancement factor in calculation of Galactic diffuse gamma-rays: A new estimate with DPMJET-3. *Astroparticle Physics*, 31(5):341–343, jun 2009.
- [51] The Fermi-LAT collaboration. Fermi Large Area Telescope Fourth Source Catalog. *The Astrophysical Journal Supplement Series*, 242(1), feb 2019.
- [52] H. Abdalla, A. Abramowski, F. Aharonian, F. Ait Benkhali, E. O. Angüner, M. Arakawa, M. Arrieta, P. Aubert, M. Backes, A. Balzer, M. Barnard, Y. Becherini, J. Becker Tjus, D. Berge, S. Bernhard, K. Bernlöhr, R. Blackwell, M. Böttcher, C. Boisson, J. Bolmont, S. Bonnetfoy, P. Bordas, J. Bregeon, F. Brun, P. Brun, M. Bryan, M. Büchele, T. Bulik, M. Capasso, S. Carrigan, S. Caroff, A. Carosi, S. Casanova, M. Cerruti, N. Chakraborty, R. C.G. Chaves, A. Chen, J. Chevalier, S. Colafrancesco, B. Condon, J. Conrad, I. D. Davids, J. Decock, C. Deil, J. Devin, P. De Wilt, L. Dirson, A. Djannati-Ataï, W. Domainko, A. Donath, L. O.C. Drury, K. Dutson, J. Dyks, T. Edwards, K. Egberts, P. Eger, G. Emery, J. P. Ernenwein, S. Eschbach, C. Farnier, S. Fegan, M. V. Fernandes, A. Fiasson, G. Fontaine, A. Förster, S. Funk, M. Füßling, S. Gabici, Y. A. Gallant, T. Garrigoux, H. Gast, F. Gaté, G. Giavitto, B. Giebels, D. Glawion, J. F. Glicenstein, D. Gottschall, M. H. Grondin, J. Hahn, M. Haupt, J. Hawkes, G. Heinzlmann, G. Henri, G. Hermann, J. A. Hinton, W. Hofmann, C. Hoischen, T. L. Holch, M. Holler, D. Horns, A. Ivascenko, H. Iwasaki, A. Jacholkowska, M. Jamroz, D. Jankowsky, F. Jankowsky, M. Jingo, L. Jouvin, I. Jung-Richardt, M. A. Kastendieck, K. Katarzyński, M. Katsuragawa, U. Katz, D. Kerszberg, D. Khangulyan, B. Khélifi, J. King, S. Klepser, D. Klochkov, W. Kluzniak, Nu Komin, K. Kosack, S. Krakau, M. Kraus, P. P. Krüger, H. Laffon, G. Lamanna, J. Lau, J. P. Lees, J. Lefaucheur, A. Lemièrre, M. Lemoine-Goumard, J. P. Lenain, E. Leser, T. Lohse, M. Lorentz, R. Liu, R. López-Coto, I. Lytova, V. Marandon, D. Malyshev, A. Marcowith, C. Mariaud, R. Marx, G. Maurin, N. Maxted, M. Mayer, P. J. Meintjes, M. Meyer, A. M.W. Mitchell, R. Moderski, M. Mohamed, L. Mohrmann, K. Morå, E. Moulin, T. Murach, S. Nakashima, M. De Naurois, H. Ndiyavala, F. Niederwanger, J. Niemiec, L. Oakes, P. O’Brien, H. Odaka, S. Ohm, M. Ostrowski, I. Oya, M. Padovani, M. Panter, R. D. Parsons, M. Paz Arribas, N. W. Pekeur, G. Pelletier, C. Perennes, P. O. Petrucci, B. Peyaud, Q. Piel, S. Pita, V. Poireau, H. Poon, D. Prokhorov, H. Prokoph, G. Pühlhofer, M. Punch, A. Quirrenbach, S. Raab, R. Rauth, A. Reimer, O. Reimer, M. Renaud, R. De Los Reyes, F. Rieger, L. Rinchuso, C. Romoli, G. Rowell, B. Rudak, C. B. Rulten, S. Safi-Harb, V. Sahakian, S. Saito, D. A. Sanchez, A. Santangelo, M. Sasaki, M. Schandri, R. Schlickeiser, F. Schüssler, A. Schulz, U. Schwanke, S. Schwemmer, M. Seglar-Arroyo, M. Settimo, A. S. Seyffert, N. Shafi, I. Shilon, K. Shiningayamwe, R. Simoni, H. Sol, F. Spanier, M. Spir-Jacob, Stawarz, R. Steenkamp, C. Stegmann, C. Steppa, I. Sushch, T. Takahashi, J. P. Tavernet, T. Tavernier, A. M. Taylor, R. Terrier, L. Tibaldo, D. Tiziani, M. Tluczykont, C. Trichard, M. Tsirou, N. Tsuji, R. Tuffs, Y. Uchiyama, D. J. Van Der Walt, C. Van Eldik, C. Van Rensburg, B. Van Soelen, G. Vasileiadis, J. Veh, C. Venter, A. Viana, P. Vincent, J. Vink, F. Voisin, H. J. Völk, T. Vuillaume, Z. Wadiasingh, S. J. Wagner, P. Wagner, R. M. Wagner, R. White, A. Wiercholska, P. Willmann, A. Wörnlein, D. Wouters, R. Yang, D. Zaborov, M. Zacharias, R. Zanin, A. A. Zdziarski,

- A. Zech, F. Zefi, A. Ziegler, J. Zorn, and N. Zywucka. The H.E.S.S. Galactic plane survey. *Astronomy and Astrophysics*, 612:A1, apr 2018.
- [53] F. W. Stecker. *Cosmic Gamma Rays*. Scientific and Technical Information Office, National Aeronautics and Space Administration, 1971., 1971.
- [54] W. Baade and F. Zwicky. Cosmic Rays from Super-Novae. *Proceedings of the National Academy of Sciences*, 20(5):259–263, may 1934.
- [55] Stephen P. Reynolds. Supernova Remnants at High Energy. *Annual Review of Astronomy and Astrophysics*, 46(1):89–126, sep 2008.
- [56] Jacco Vink. Supernova remnants: the X-ray perspective. *Astronomy & Astrophysics Review*, 20:49, 2012.
- [57] S. G. Lucek and A. R. Bell. Non-linear amplification of a magnetic field driven by cosmic ray streaming. *Monthly Notices of the Royal Astronomical Society*, 314(1):65–74, may 2000.
- [58] Yasunobu Uchiyama, Felix A. Aharonian, Takaaki Tanaka, Tadayuki Takahashi, and Yoshitomo Maeda. Extremely fast acceleration of cosmic rays in a supernova remnant. *Nature*, 449(7162):576–578, oct 2007.
- [59] Damiano Caprioli. Cosmic-ray acceleration in supernova remnants: Non-linear theory revised. *Journal of Cosmology and Astroparticle Physics*, 2012(7):038, jul 2012.
- [60] Stefan Funk. Space-and Ground-Based Gamma-Ray Astrophysics Dark Matter Cosmic rays Gamma-ray Astronomy Fermi-LAT Imaging atmospheric Cherenkov Telescopes Galactic Center. 2015.
- [61] R. Bühler and R. Blandford. The surprising Crab pulsar and its nebula: A review, jun 2014.
- [62] M. Casse and J. A. Paul. Local gamma rays and cosmic-ray acceleration by supersonic stellar winds. *The Astrophysical Journal*, 237:236, apr 1980.
- [63] Catherine J. Cesarsky and Thierry Montmerle. Gamma rays from active regions in the galaxy: The possible contribution of stellar winds. *Space Science Reviews*, 36(2):173–193, oct 1983.
- [64] M. De Becker and F. Raucq. Catalogue of particle-accelerating colliding-wind binaries. *Astronomy & Astrophysics*, 558:A28, oct 2013.
- [65] R. White, M. Breuhaus, R. Konno, S. Ohm, B. Reville, and J. A. Hinton. Gamma-ray and X-ray constraints on non-Thermal processes in eta Carinae. *Astronomy and Astrophysics*, 635:A144, mar 2020.
- [66] Felix Aharonian, Ruizhi Yang, and Emma de Oña Wilhelmi. Massive stars as major factories of Galactic cosmic rays. *Nature Astronomy*, 3(6):561–567, jun 2019.

- [67] Steven W Stahler and Francesco Palla. *The Formation of Stars*. 2008.
- [68] I. Yusifov and I. Kucuk. Revisiting the radial distribution of pulsars in the Galaxy. *Astronomy and Astrophysics*, 422(2):545–553, may 2004.
- [69] D A Green. Constraints on the distribution of supernova remnants with Galactocentric radius. *MNRAS*, 454(2):p.1517–1524, 2015.
- [70] CF McKee and JP Ostriker. A theory of the interstellar medium-Three components regulated by supernova explosions in an inhomogeneous substrate. *The Astrophysical Journal*, 218:148–169, 1977.
- [71] Michael A Dopita and Ralph S. Sutherland. *Astrophysics of the Diffuse Universe* - . Springer, Berlin, Heidelberg, 2nd edition, 2003.
- [72] Katia M. Ferrière. The interstellar environment of our galaxy. *Reviews of Modern Physics*, 73(4):1031–1066, oct 2001.
- [73] T. M. Dame, Dap Hartmann, and P. Thaddeus. The Milky Way in Molecular Clouds: A New Complete CO Survey. *The Astrophysical Journal*, 547(2):792–813, sep 2000.
- [74] A Mizuno and Y Y Fukui. Physical properties of molecular clouds as revealed by NANTEN CO survey: from the galactic center to the galactic warp. In *Milky Milky Way Surveys: The Structure and Evolution of our Galaxy*, 2004.
- [75] T Umemoto, T Minamidani, and N Kuno. FOREST unbiased Galactic plane imaging survey with the Nobeyama 45 m telescope (FUGIN). I. Project overview and initial results. *Publications of the Astronomical Society of Japan*, 69, 2017.
- [76] Michael G Burton, C Braiding, C Glueck, P Goldsmith, J Hawkes, D J Hollenbach, C Kulesa, C L Martin, J L Pineda, G Rowell, R Simon, A A Stark, J Stutzki B, N J H Tothill, J S Urquhart, C Walker, A J Walsh, and M Wolfire. The Mopra Southern Galactic Plane CO Survey. *Publications of the Astronomical Society of Australia*, 30, 2013.
- [77] Yang Su, Ji Yang, Shaobo Zhang, Yan Gong, Hongchi Wang, Xin Zhou, Min Wang, Zhiwei Chen, Yan Sun, Xuepeng Chen, Ye Xu, and Zhibo Jiang. The Milky Way Imaging Scroll Painting (MWISP): Project Details and Initial Results from the Galactic Longitudes of 25°.8-49°.7. *he Astrophysical Journal Supplement Series*, 240(9), 2019.
- [78] J. T. Dempsey, H. S. Thomas, and M. J. Currie. CO (3 – 2) HIGH-RESOLUTION SURVEY OF THE GALACTIC PLANE: R1. *The Astrophysical Journal Supplement Series*, 209(1):8, oct 2013.
- [79] A. J. Rigby, T. J.T. Moore, R. Plume, D. J. Eden, J. S. Urquhart, M. A. Thompson, J. C. Mottram, C. M. Brunt, H. M. Butner, J. T. Dempsey, S. J. Gibson, J. Hatchell, T. Jenness, N. Kuno, S. N. Longmore, L. K. Morgan, D. Polychroni, H. Thomas, G. J. White, and M. Zhu. CHIMPS: The 13CO/C18O (J = 3 →

- 2) Heterodyne Inner Milky Way Plane Survey. *Monthly Notices of the Royal Astronomical Society*, 456(3):2885–2899, mar 2016.
- [80] Alberto D. Bolatto, Mark Wolfire, and Adam K. Leroy. The CO-to-H₂ Conversion Factor. *Annual Review of Astronomy and Astrophysics*, 51(1):207–268, aug 2013.
- [81] P. M. Solomon, A. R. Rivolo, J. Barrett, and A. Yahil. Mass, luminosity, and line width relations of Galactic molecular clouds. *The Astrophysical Journal*, 319:730, aug 1987.
- [82] Paul F. Goldsmith, Mark Heyer, Gopal Narayanan, Ronald Snell, Di Li, and Chris Brunt. Large-Scale Structure of the Molecular Gas in Taurus Revealed by High Linear Dynamic Range Spectral Line Mapping. *The Astrophysical Journal*, 680(1):428–445, jun 2008.
- [83] M. A. Frerking, W. D. Langer, and R. W. Wilson. The relationship between carbon monoxide abundance and visual extinction in interstellar clouds. *The Astrophysical Journal*, 262:590, nov 1982.
- [84] Hiroyuki Nakanishi and Yoshiaki Sofue. Three-dimensional distribution of the ISM in the Milky Way galaxy: II. The molecular gas disk. *Publications of the Astronomical Society of Japan*, 58(5):847–860, 2006.
- [85] Martin Pohl, Peter Englmaier, and Nicolai Bissantz. 3D Distribution of Molecular Gas in the Barred Milky Way. *The Astrophysical Journal*, 677(1):283–291, dec 2008.
- [86] Thomas S Rice, Alyssa A Goodman, Edwin A Bergin, Christopher Beaumont, and T M Dame. A Uniform Catalog of Molecular Clouds in the Milky Way. *The Astrophysical Journal*, 822, 2016.
- [87] Marc-Antoine Miville-Deschênes, Norman Murray, and Eve J. Lee. Physical properties of molecular clouds for the entire Milky Way disk. *The Astrophysical Journal*, 834(1):57, oct 2016.
- [88] M J Reid, K M Menten, A Brunthaler, X W Zheng, T M Dame, Y Xu, Y Wu, B Zhang, A Sanna, M Sato, K Hachisuka, Y K Choi, K Immer, L Moscadelli, K L J Rygl, and A Bartkiewicz. TRIGONOMETRIC PARALLAXES OF HIGH MASS STAR FORMING REGIONS: THE STRUCTURE AND KINEMATICS OF THE MILKY WAY. *The Astrophysical Journal*, 783(14pp):130, 2014.
- [89] Michal A. Kolpak, James M. Jackson, T. M. Bania, D. P. Clemens, and John M. Dickey. Resolving the Kinematic Distance Ambiguity toward Galactic H_{ii} Regions. *The Astrophysical Journal*, 582(2):756–769, jan 2003.
- [90] Blair D Savage and Edward B Jenkins. A Survey of Local Interstellar Hydrogen from OAO-2 Observations of Lyman Alpha Absorption. *Astrophysical Journal*, 172:492, 1972.

- [91] N M McClure-Griffiths, D J Pisano, M R Calabretta, H Alyson Ford, Felix J Lockman, L Staveley-Smith, P M W Kalberla, J Bailin, L Dedes, S Janowiecki, B K Gibson, T Murphy, H Nakanishi, and K Newton-Mcgee. GASS: the Parkes Galactic all-sky survey I. Survey description, goals and initial data release. *The Astrophysical Journal Supplement Series*, 181:398–412, 2009.
- [92] J. Kerp, B. Winkel, N. Ben Bekhti, L. Flöer, and P.M.W. Kalberla. The Effelsberg Bonn HI Survey (EBHIS). *Astronomische Nachrichten*, 332(6):637–648, jul 2011.
- [93] N. Ben Bekhti, L. Flöer, R. Keller, J. Kerp, D. Lenz, B. Winkel, J. Bailin, M. R. Calabretta, L. Dedes, H. A. Ford, B. K. Gibson, U. Haud, S. Janowiecki, P. M.W. Kalberla, F. J. Lockman, N. M. McClure-Griffiths, T. Murphy, H. Nakanishi, D. J. Pisano, and L. Staveley-Smith. HI4PI: A full-sky HI survey based on EBHIS and GASS. *Astronomy and Astrophysics*, 594, oct 2016.
- [94] T. L. Wilson, K. Rohlfs, and S. Hüttemeister. *Tools of radio astronomy*, volume 5. Berlin:Springer, 2009.
- [95] John M Dickey, Simon Strasser, B M Gaensler, Marijke Haverkorn, Dain Kavars, N M McClure-Griffiths, Jeroen Stil, and A R Taylor. THE OUTER DISK OF THE MILKY WAY SEEN IN $\lambda 21$ cm ABSORPTION. *The Astrophysical Journal*, 693:1250–1260, 2009.
- [96] S. Bühr, H. Beuther, J. Ott, K. G. Johnston, A. Brunthaler, L. D. Anderson, F. Bigiel, P. Carlhoff, E. Churchwell, S. C.O. Glover, P. F. Goldsmith, F. Heitsch, T. Henning, M. H. Heyer, T. Hill, A. Hughes, R. S. Klessen, H. Linz, S. N. Longmore, N. M. McClure-Griffiths, K. M. Menten, F. Motte, Q. Nguyen-Luong, R. Plume, S. E. Ragan, N. Roy, P. Schilke, N. Schneider, R. J. Smith, J. M. Stil, J. S. Urquhart, A. J. Walsh, and F. Walter. THOR: The HI, OH, Recombination line survey of the Milky Way: The pilot study: HI observations of the giant molecular cloud W43. *Astronomy and Astrophysics*, 580, aug 2015.
- [97] Yoshiaki Sofue. Optical Thickness, Spin Temperature, and Correction Factor for Density of the Galactic HI Gas. *Mon. Not. R. Astron. Soc.*, 468(4):4030–4038, 2017.
- [98] B. T. Draine. Interstellar Dust Grains. *Annual Review of Astronomy and Astrophysics*, 41:241–289, nov 2003.
- [99] M. G. Hauser, R. G. Arendt, T. Kelsall, E. Dwek, N. Odegard, J. L. Weiland, H. T. Freudenreich, W. T. Reach, R. F. Silverberg, S. H. Moseley, Y. C. Pei, P. Lubin, J. C. Mather, R. A. Shafer, G. F. Smoot, R. Weiss, D. T. Wilkinson, and E. L. Wright. The COBE Diffuse Infrared Background Experiment Search for the Cosmic Infrared Background: I. Limits and Detections. *The Astrophysical Journal*, 508(1):25–43, jun 1998.
- [100] David J. Schlegel, Douglas P. Finkbeiner, and Marc Davis. Maps of Dust Infrared Emission for Use in Estimation of Reddening and Cosmic Microwave Background Radiation Foregrounds. *The Astrophysical Journal*, 500(2):525–553, jun 1998.

- [101] P.A.R Ade, N. Aghanim, M. Arnaud, and M. Ashdown. Planck early results. XIX. All-sky temperature and dust optical depth from Planck and IRAS. Constraints on the “dark gas” in our Galaxy. *Astronomy & Astrophysics*, 536:16, 2011.
- [102] S. Rezaei Kh, C. A.L. Bailer-Jones, R. J. Hanson, and M. Fouesneau. Inferring the three-dimensional distribution of dust in the Galaxy with a non-parametric method: Preparing for Gaia. *Astronomy and Astrophysics*, 598, feb 2017.
- [103] R Lallement, C Babusiaux, J L Vergely, D Katz, F Arenou, B Valette, C Hottier, and L Capitanio. Astronomy Gaia-2MASS 3D maps of Galactic interstellar dust within 3 kpc. *Astronomy & Astrophysics*, 625:16, 2019.
- [104] Sara Rezaei Kh, Coryn A.L. Bailer-Jones, David W. Hogg, and Mathias Schultheis. Detection of the Milky Way spiral arms in dust from 3D mapping. *Astronomy and Astrophysics*, 618:168, oct 2018.
- [105] S. Hayakawa. Propagation of the Cosmic Radiation through Interstellar Space. *Progress of Theoretical Physics*, 8(5):571–572, nov 1952.
- [106] Francois Lebrun and Jacques Paul. Gamma-ray astronomy and structure and content of the local interstellar medium. In *International Cosmic Ray Conference, 16th, Kyoto, Japan, August 6-18*, volume 12, 1979.
- [107] H. A. Mayer-Hasselwander, G. F. Bennett, K., Bignami, R. Buccheri, P. A. Caraveo, W. Hermsen, and J. A Paul. Large-scale distribution of galactic gamma radiation observed by COS-B. *Astronomy and Astrophysics*, 105:164–175, 1982.
- [108] F. Lebrun, J. A. Paul, G. F. Bignami, P. A. Caraveo, R. Buccheri, W. Hermsen, and R. D. Wills. COS-B gamma-ray measurements, cosmic rays and the local interstellar medium. *Astronomy and Astrophysics*, 107:390–396, 1982.
- [109] A. W. Strong and J. R. Mattox. Gradient model analysis of EGRET diffuse Galactic gamma-ray emission. *Astronomy and Astrophysics*, 308:L21–L24, 1996.
- [110] M. Ackermann, M. Ajello, W. B. Atwood, L. Baldini, J. Ballet, G. Barbiellini, D. Bastieri, K. Bechtol, R. Bellazzini, B. Berenji, R. D. Blandford, E. D. Bloom, E. Bonamente, A. W. Borgland, T. J. Brandt, J. Bregeon, M. Brigida, P. Bruel, R. Buehler, S. Buson, G. A. Caliandro, R. A. Cameron, P. A. Caraveo, E. Cavazzuti, C. Cecchi, E. Charles, A. Chekhtman, J. Chiang, S. Ciprini, R. Claus, J. Cohen-Tanugi, J. Conrad, S. Cutini, A. de Angelis, F. de Palma, C. D. Dermer, S. W. Digel, E. do Couto e Silva, P. S. Drell, A. Drlica-Wagner, L. Falletti, C. Favuzzi, S. J. Fegan, E. C. Ferrara, W. B. Focke, P. Fortin, Y. Fukazawa, S. Funk, P. Fusco, D. Gaggero, F. Gargano, S. Germani, N. Giglietto, F. Giordano, M. Giroletti, T. Glanzman, G. Godfrey, J. E. Grove, S. Guiriec, M. Gustafsson, D. Hadasch, Y. Hanabata, A. K. Harding, M. Hayashida, E. Hays, D. Horan, X. Hou, R. E. Hughes, G. Jóhannesson, A. S. Johnson, R. P. Johnson, T. Kamae, H. Katagiri, J. Kataoka, J. Knödseder, M. Kuss, J. Lande, L. Latronico, S.-H.

- Lee, M. Lemoine-Goumard, F. Longo, F. Loparco, B. Lott, M. N. Lovellette, P. Lubrano, M. N. Mazziotta, J. E. McEnery, P. F. Michelson, W. Mitthumsiri, T. Mizuno, C. Monte, M. E. Monzani, A. Morselli, I. V. Moskalenko, S. Murgia, M. Naumann-Godo, J. P. Norris, E. Nuss, T. Ohsugi, A. Okumura, N. Omodei, E. Orlando, J. F. Ormes, D. Paneque, J. H. Panetta, D. Parent, M. Pesce-Rollins, M. Pierbattista, F. Piron, G. Pivato, T. A. Porter, S. Rainò, R. Rando, M. Razzano, S. Razzaque, A. Reimer, O. Reimer, H. F.-W. Sadrozinski, C. Sgrò, E. J. Siskind, G. Spandre, P. Spinelli, A. W. Strong, D. J. Suson, H. Takahashi, T. Tanaka, J. G. Thayer, J. B. Thayer, D. J. Thompson, L. Tibaldo, M. Tinivella, D. F. Torres, G. Tosti, E. Troja, T. L. Usher, J. Vandenbroucke, V. Vasileiou, G. Vianello, V. Vitale, A. P. Waite, P. Wang, B. L. Winer, K. S. Wood, M. Wood, Z. Yang, M. Ziegler, and S. Zimmer. FERMI-LAT OBSERVATIONS OF THE DIFFUSE γ -RAY EMISSION: IMPLICATIONS FOR COSMIC RAYS AND THE INTERSTELLAR MEDIUM. *The Astrophysical Journal*, 750(1):3, 2012.
- [111] F. Acero, M. Ackermann, M. Ajello, A. Albert, L. Baldini, J. Ballet, G. Barbiellini, D. Bastieri, R. Bellazzini, E. Bissaldi, E. D. Bloom, R. Bonino, E. Bottacini, T. J. Brandt, J. Bregeon, P. Bruel, R. Buehler, S. Buson, G. A. Calianandro, R. A. Cameron, M. Caragiulo, P. A. Caraveo, J. M. Casandjian, E. Cavazzuti, C. Cecchi, E. Charles, A. Chekhtman, J. Chiang, G. Chiaro, S. Ciprini, R. Claus, J. Cohen-Tanugi, J. Conrad, A. Cuoco, S. Cutini, F. D'Ammando, A. de Angelis, F. de Palma, R. Desiante, S. W. Digel, L. Di Venere, P. S. Drell, C. Favuzzi, S. J. Fegan, E. C. Ferrara, W. B. Focke, A. Franckowiak, S. Funk, P. Fusco, F. Gargano, D. Gasparrini, N. Giglietto, F. Giordano, M. Giroletti, T. Glanzman, G. Godfrey, I. A. Grenier, S. Guiriec, D. Hadasch, A. K. Harding, K. Hayashi, E. Hays, J. W. Hewitt, A. B. Hill, D. Horan, X. Hou, T. Jogler, G. Jóhannesson, T. Kamae, M. Kuss, D. Landriu, S. Larsson, L. Latronico, J. Li, L. Li, F. Longo, F. Loparco, M. N. Lovellette, P. Lubrano, S. Maldera, D. Malyshev, A. Manfreda, P. Martin, M. Mayer, M. N. Mazziotta, J. E. McEnery, P. F. Michelson, N. Mirabal, T. Mizuno, M. E. Monzani, A. Morselli, E. Nuss, T. Ohsugi, N. Omodei, M. Orienti, E. Orlando, J. F. Ormes, D. Paneque, M. Pesce-Rollins, F. Piron, G. Pivato, S. Rainò, R. Rando, M. Razzano, S. Razzaque, A. Reimer, O. Reimer, Q. Remy, N. Renault, M. Sánchez-Conde, M. Schaal, A. Schulz, C. Sgrò, E. J. Siskind, F. Spada, G. Spandre, P. Spinelli, A. W. Strong, D. J. Suson, H. Tajima, H. Takahashi, J. B. Thayer, D. J. Thompson, L. Tibaldo, M. Tinivella, D. F. Torres, G. Tosti, E. Troja, G. Vianello, M. Werner, K. S. Wood, M. Wood, G. Zaharijas, and S. Zimmer. Development of the Model of Galactic Interstellar Emission for Standard Point-Source Analysis of Fermi Large Area Telescope Data. *The Astrophysical Journal Supplement Series*, 223(2), feb 2016.
- [112] F A Aharonian and A M Atoyan. Broad-band diffuse gamma ray emission of the Galactic Disk. *Astronomy & Astrophysics*, 362, 2000.
- [113] Fermi SSC. LAT Photon, Event and Spacecraft Data <<https://fermi.gsfc.nasa.gov/cgi-bin/ssc/LAT/LATDataQuery.cgi>> visited on 25.09.2020.
- [114] Planck Legacy Archive. Planck - Cosmos <<https://www.cosmos.esa.int/web/planck/pla>> visited on 25.09.2020.

- [115] C C Popescu, R Yang, R J Tuffs, G Natale, M Rushton, and F Aharonian. A radiation transfer model for the Milky-Way: I. Radiation fields and application to High Energy Astrophysics. *MNRAS*, 470(3), 2017.
- [116] W.R. Webber, G.A. Simpson, and Cane H. V. Radio emission, cosmic ray electrons, and the production of gamma-rays in the Galaxy. *The Astrophysical Journal*, 236:448–459, 1980.
- [117] A. W. Strong, I. V. Moskalenko, O. Reimer, S. Digel, and R. Diehl. The distribution of cosmic-ray sources in the Galaxy, gamma-rays, and the gradient in the CO-to-H₂ relation. *Astronomy and Astrophysics*, 422(3):L47–L50, may 2004.
- [118] A. W. Strong, E. Orlando, and T. R. Jaffe. The interstellar cosmic-ray electron spectrum from synchrotron radiation and direct measurements. *Astronomy and Astrophysics*, 534, 2011.
- [119] Cesarsky C. J. and H.J Voelk. Cosmic Ray Penetration into Molecular Clouds - NASA/ADS. *Astronomy and Astrophysics*, 70:367, nov 1978.
- [120] Stefano Gabici, Felix A. Aharonian, and Pasquale Blasi. Gamma rays from molecular clouds. *Astrophysics and Space Science*, 309(1-4):365–371, jun 2007.
- [121] V. Zabalza. Naima: A Python package for inference of relativistic particle energy distributions from observed nonthermal spectra. In *Proceedings of Science*, volume 30-July-20. Proceedings of Science (PoS), 2015.
- [122] S. Maldera, M. Wood, R. Caputo, R. Rando, E. Charles, S. Digel, and L. Baldini. Fermi-LAT Performance <https://www.slac.stanford.edu/exp/glast/groups/canda/lat_Performance.htm> visited on 08.09.2020, oct 2019.
- [123] Laurent Bouchet, Andrew W Strong, Troy A Porter, Igor V Moskalenko, Elisabeth Jourdain, and Jean-Pierre Roques. Diffuse Emission Measurement with the Spectrometer on INTEGRAL as an Indirect Probe of Cosmic-ray Electrons and Positrons. *The Astrophysical Journal*, 739(15pp):29, 2011.
- [124] A. Abramowski, F. Aharonian, F. Ait Benkhali, A. G. Akhperjanian, E. O. Angüner, M. Backes, S. Balenderan, A. Balzer, A. Barnacka, Y. Becherini, J. Becker Tjus, D. Berge, S. Bernhard, K. Bernlöhr, E. Birsin, J. Biteau, M. Böttcher, C. Boisson, J. Bolmont, P. Bordas, J. Bregeon, F. Brun, P. Brun, M. Bryan, T. Bulik, S. Carrigan, S. Casanova, P. M. Chadwick, N. Chakraborty, R. Chalme-Calvet, R. C.G. Chaves, M. Chrétiens, S. Colafrancesco, G. Cologna, J. Conrad, C. Couturier, Y. Cui, I. D. Davids, B. Degrange, C. Deil, P. Dewilt, A. Djannati-Ataï, W. Domainko, A. Donath, L. O.C. Drury, G. Dubus, K. Dutton, J. Dyks, M. Dyrda, T. Edwards, K. Egberts, P. Eger, P. Espigat, C. Farnier, S. Fegan, F. Feinstein, M. V. Fernandes, D. Fernandez, A. Fiasson, G. Fontaine, A. Förster, M. Füßling, S. Gabici, M. Gajdus, Y. A. Gallant, T. Garrigoux, G. Giavitto, B. Giebels, J. F. Glicenstein, D. Gottschall, M. H. Grondin, M. Grudzińska, D. Hadasch, S. Häffner, J. Hahn, J. Harris, G. Heinzlmann, G. Henri, G. Hermann, O. Hervet, A. Hillert, J. A. Hinton, W. Hofmann, P. Hofverberg,

- M. Holler, D. Horns, A. Ivascenko, A. Jacholkowska, C. Jahn, M. Jamrozy, M. Janiak, F. Jankowsky, I. Jung-Richardt, M. A. Kastendieck, K. Katarzyński, U. Katz, S. Kaufmann, B. Khélifi, M. Kieffer, S. Klepser, D. Klochkov, W. Kluzniak, D. Kolitzus, Nu Komin, K. Kosack, S. Krakau, F. Krayzel, P. P. Krüger, H. Laffon, G. Lamanna, J. Lefaucheur, V. Lefranc, A. Lemièrre, M. Lemoine-Goumard, J. P. Lenain, T. Lohse, A. Lopatin, C. C. Lu, V. Marandon, A. Marcowith, R. Marx, G. Maurin, N. Maxted, M. Mayer, T. J.L. McComb, J. Méhault, P. J. Meintjes, U. Menzler, M. Meyer, A. M.W. Mitchell, R. Moderski, M. Mohamed, K. Morå, E. Moulin, T. Murach, M. De Naurois, J. Niemiec, S. J. Nolan, L. Oakes, H. Odaka, S. Ohm, B. Opitz, M. Ostrowski, I. Oya, M. Panter, R. D. Parsons, M. Paz Arribas, N. W. Pekeur, G. Pelletier, P. O. Petrucci, B. Peyaud, S. Pita, H. Poon, G. Pühlhofer, M. Punch, A. Quirrenbach, S. Raab, I. Reichardt, A. Reimer, O. Reimer, M. Renaud, R. De Los Reyes, F. Rieger, C. Romoli, S. Rosier-Lees, G. Rowell, B. Rudak, C. B. Rulten, V. Sahakian, D. Salek, D. A. Sanchez, A. Santangelo, R. Schlickeiser, F. Schüssler, A. Schulz, U. Schwanke, S. Schwarzburg, S. Schwemmer, H. Sol, F. Spanier, G. Spengler, F. Spies, A. L. Stawarz, R. Steenkamp, C. Stegmann, F. Stinzing, K. Stycz, I. Sushch, J. P. Tavernet, T. Tavernier, A. M. Taylor, R. Terrier, M. Tluczykont, C. Trichard, K. Valerius, C. Van Eldik, B. Van Soelen, G. Vasileiadis, J. Veh, C. Venter, A. Viana, P. Vincent, J. Vink, H. J. Völk, F. Volpe, M. Vorster, T. Vuillaume, S. J. Wagner, P. Wagner, R. M. Wagner, M. Ward, M. Weidinger, Q. Weitzel, R. White, A. Wiercholska, P. Willmann, A. Wörnlein, D. Wouters, R. Yang, V. Zabalza, D. Zaborov, M. Zacharias, A. A. Zdziarski, A. Zech, H. S. Zechlin, and Y. Fukui. Diffuse Galactic gamma-ray emission with H.E.S.S. *Physical Review D - Particles, Fields, Gravitation and Cosmology*, 90(12):122007, dec 2014.
- [125] A. A. Abdo, B. Allen, T. Aune, D. Berley, E. Blaufuss, S. Casanova, C. Chen, B. L. Dingus, R. W. Ellsworth, L. Fleysler, R. Fleysler, M. M. Gonzalez, J. A. Goodman, C. M. Hoffman, P. H. H"untemeyer, B. E. Kolterman, C. P. Lansdell, J. T. Linnemann, J. E. McEnery, A. I. Mincer, I. V. Moskalenko, P. Nemethy, D. Noyes, T. A. Porter, J. Pretz, J. M. Ryan, P. M. Saz Parkinson, A. Shoup, G. Sinnis, A. J. Smith, A. W. Strong, G. W. Sullivan, V. Vasileiou, G. P. Walker, D. A. Williams, and G. B. Yodh. A Measurement of the Spatial Distribution of Diffuse TeV Gamma Ray Emission from the Galactic Plane with Milagro. *The Astrophysical Journal*, 688(2):1078–1083, may 2008.
- [126] Hao Zhou, Chang Dong Rho, and Giacomo Vianello. Probing galactic diffuse TeV gamma-ray emission with the HAWC observatory. In *Proceedings of Science*. Sissa Medialab Srl, 2017.
- [127] Amid Nayerhoda, Francisco Salesa Greus, Sabrina Casanova, and for the HAWC collaboration. TeV Diffuse Emission From the Inner Galaxy. *Frontiers in Astronomy and Space Sciences*, 5:8, apr 2018.
- [128] Julia Roman-Duval, James M. Jackson, Mark Heyer, Alexis Johnson, Jill Rathborne, Ronak Shah, and Robert Simon. Kinematic Distances to Molecular Clouds identified in the Galactic Ring Survey. *The Astrophysical Journal*, 699(2), may 2009.

- [129] A. W. Strong, J. B. G. M. Bloemen, T. M. Dame, I. A. Grenier, W. Hermsen, F. Lebrun, and P. Thaddeus. The radial distribution of galactic cosmic rays. *Astronomy and Astrophysics*, 207, 1988.
- [130] Ruizhi Yang, Felix Aharonian, and Carmelo Evoli. Radial distribution of the diffuse γ -ray emissivity in the Galactic disk. *Physical Review D*, 93(12), jun 2016.
- [131] Mart Pothast, Daniele Gaggero, Emma Storm, and Christoph Weniger. On the progressive hardening of the cosmic-ray proton spectrum in the inner Galaxy. *Journal of Cosmology and Astroparticle Physics*, 2018(10):45, 2018.
- [132] Daniele Gaggero, Alfredo Urbano, Mauro Valli, and Piero Ullio. Gamma-ray sky points to radial gradients in cosmic-ray transport. *Physical Review D*, 91(8):083012, apr 2015.
- [133] Yi-Qing Guo and Qiang Yuan. Understanding the spectral hardenings and radial distribution of Galactic cosmic rays and Fermi diffuse gamma-rays with spatially-dependent propagation. *Physical Review D*, 97(6), jan 2018.
- [134] TJ Sodroski and N Odegard. The Ratio of H₂ Column Density to 12CO Intensity in the Vicinity of the Galactic Center. *The Astrophysical Journal*, 452, 1995.
- [135] S. M. Andrievsky, D. Bersier, V. V. Kovtyukh, R. E. Luck, W. J. Maciel, J. R. D. Lépine, and Yu. V. Beletsky. Using Cepheids to determine the galactic abundance gradient. *Astronomy & Astrophysics*, 384(1):140–144, mar 2002.
- [136] A. D. Erlykin and A. W. Wolfendale. Cosmic rays in the inner galaxy and the diffusion properties of the interstellar medium. *Astroparticle Physics*, 42:70–75, 2013.
- [137] M. Cataldo, G. Pagliaroli, V. Vecchiotti, and F. L. Villante. Probing galactic cosmic ray distribution with TeV gamma-ray sky. *Journal of Cosmology and Astroparticle Physics*, (12), 2019.
- [138] G. Morlino and S. Gabici. Cosmic ray penetration in diffuse clouds. *Monthly Notices of the Royal Astronomical Society: Letters*, 451(1):L100–L104, may 2015.
- [139] F. A. Aharonian. Gamma rays from molecular clouds. *Space Science Reviews*, 99(1-4):187–196, 2001.
- [140] Sabrina Casanova, Felix A. Aharonian, Yasuo Fukui, Stefano Gabici, David I. Jones, Akiko Kawamura, Toshikazu Onishi, Gavin Rowell, Hidetoshi Sano, Kazufumi Torii, and Hiroaki Yamamoto. Molecular clouds as Cosmic-Ray Barometers. *Publications of the Astronomical Society of Japan*, 62(3):769–777, jun 2010.
- [141] J. R. Mattox, D. L. Bertsch, J. Chiang, B. L. Dingus, S. W. Digel, J. A. Eposito, J. M. Fierro, R. C. Hartman, S. D. Hunter, G. Kanbach, D. A. Kniffen, Y. C. Lin, D. J. Macomb, H. A. Mayer-Hasselwander, P. F. Michelson, C. von Montigny,

- R. Mukherjee, P. L. Nolan, P. V. Ramanamurthy, E. Schneid, P. Sreekumar, D. J. Thompson, and T. D. Willis. The Likelihood Analysis of EGRET Data. *The Astrophysical Journal*, 461:396, apr 1996.
- [142] Matthew Wood, Regina Caputo, Eric Charles, Mattia Di Mauro, Jeffrey Magill, and Jeremy Perkins. Fermipy: An open-source Python package for analysis of Fermi-LAT Data. In *Proceedings of Science*. Sissa Medialab Srl, 2017.
- [143] F. Acero, M. Ackermann, M. Ajello, A. Albert, W. B. Atwood, M. Axelsson, L. Baldini, J. Ballet, G. Barbiellini, D. Bastieri, A. Belfiore, R. Bellazzini, E. Bissaldi, R. D. Blandford, E. D. Bloom, J. R. Bogart, R. Bonino, E. Bottacini, J. Bregeon, R. J. Britto, P. Bruel, R. Buehler, T. H. Burnett, S. Buson, G. A. Caliandro, R. A. Cameron, R. Caputo, M. Caragiulo, P. A. Caraveo, J. M. Casandjian, E. Cavazzuti, E. Charles, R. C.G. Chaves, A. Chekhtman, C. C. Cheung, J. Chiang, G. Chiaro, S. Ciprini, R. Claus, J. Cohen-Tanugi, L. R. Cominsky, J. Conrad, S. Cutini, F. D'Ammando, A. De Angelis, M. Deklotz, F. De Palma, R. Desiante, S. W. Digel, L. Di Venere, P. S. Drell, R. Dubois, D. Dumora, C. Favuzzi, S. J. Fegan, E. C. Ferrara, J. Finke, A. Franckowiak, Y. Fukazawa, S. Funk, P. Fusco, F. Gargano, D. Gasparrini, B. Giebels, N. Giglietto, P. Giommi, F. Giordano, M. Giroletti, T. Glanzman, G. Godfrey, I. A. Grenier, M. H. Grondin, J. E. Grove, L. Guillemot, S. Guiriec, D. Hadasch, A. K. Harding, E. Hays, J. W. Hewitt, A. B. Hill, D. Horan, G. Iafate, T. Jogler, G. Jóhannesson, R. P. Johnson, A. S. Johnson, T. J. Johnson, W. N. Johnson, T. Kamae, J. Kataoka, J. Katsuta, M. Kuss, G. La Mura, D. Landriu, S. Larsson, L. Latronico, M. Lemoine-Goumard, J. Li, L. Li, F. Longo, F. Loparco, B. Lott, M. N. Lovellette, P. Lubrano, G. M. Madejski, F. Massaro, M. Mayer, M. N. Mazziotta, J. E. McEnery, P. F. Michelson, N. Mirabal, T. Mizuno, A. A. Moiseev, M. Mongelli, M. E. Monzani, A. Morselli, I. V. Moskalenko, S. Murgia, E. Nuss, M. Ohno, T. Ohsugi, N. Omodei, M. Orienti, E. Orlando, J. F. Ormes, D. Paneque, J. H. Panetta, J. S. Perkins, M. Pesce-Rollins, F. Piron, G. Pivato, T. A. Porter, J. L. Racusin, R. Rando, M. Razzano, S. Razzaque, A. Reimer, O. Reimer, T. Reposeur, L. S. Rochester, R. W. Romani, D. Salvetti, M. Sánchez-Conde, P. M. Saz Parkinson, A. Schulz, E. J. Siskind, D. A. Smith, F. Spada, G. Spandre, P. Spinelli, T. E. Stephens, A. W. Strong, D. J. Suson, H. Takahashi, T. Takahashi, Y. Tanaka, J. G. Thayer, J. B. Thayer, D. J. Thompson, L. Tibaldo, O. Tibolla, D. F. Torres, E. Torresi, G. Tosti, E. Troja, B. Van Klavere, G. Vianello, B. L. Winer, K. S. Wood, M. Wood, and S. Zimmer. Fermi Large Area Telescope Third Source Catalog. *Astrophysical Journal, Supplement Series*, 218(2), jun 2015.
- [144] W. Atwood, A. Albert, L. Baldini, M. Tinivella, J. Bregeon, M. Pesce-Rollins, C. Sgrò, P. Bruel, E. Charles, A. Drlica-Wagner, A. Franckowiak, T. Jogler, L. Rochester, T. Usher, M. Wood, J. Cohen-Tanugi, and S. Zimmer. Pass 8: Toward the Full Realization of the Fermi-LAT Scientific Potential. In *Fermi Symposium proceedings*, mar 2013.
- [145] F James. CERN Program Library Long Writeup D506 Function Minimization and Error Analysis Reference Manual Version 94.1, 1998.

- [146] A. E. Vladimirov, S. W. Digel, G. Jóhannesson, P. F. Michelson, I. V. Moskalenko, P. L. Nolan, E. Orlando, T. A. Porter, and A. W. Strong. GALPROP WebRun: An internet-based service for calculating galactic cosmic ray propagation and associated photon emissions. *Computer Physics Communications*, 182(5):1156–1161, may 2011.
- [147] S. W. Digel, S. D. Hunter, and R. Mukherjee. EGRET observations of gamma-ray emission from the interstellar gas in Orion. *The Astrophysical Journal*, 441:270, mar 1995.
- [148] Rui-zhi Yang, Emma de Oña Wilhelmi, and Felix Aharonian. Probing Cosmic Rays in Nearby Giant Molecular Clouds with the Fermi Large Area Telescope. *Astronomy and Astrophysics*, 566:142, mar 2013.
- [149] Andrii Neronov, Denys Malyshev, and Dmitri V. Semikoz. Cosmic-ray spectrum in the local Galaxy. *Astronomy and Astrophysics*, 606, oct 2017.
- [150] Catherine Zucker, Joshua S. Speagle, Edward F. Schlafly, Gregory M. Green, Douglas P. Finkbeiner, Alyssa A. Goodman, and João Alves. A Large Catalog of Accurate Distances to Local Molecular Clouds: The Gaia DR2 Edition. *The Astrophysical Journal*, 879(2):125, jul 2019.
- [151] F. Aharonian, G. Peron, R. Yang, S. Casanova, and R. Zanin. Probing the sea of galactic cosmic rays with Fermi-LAT. *Physical Review D*, 101(8), 2020.
- [152] M. J. Reid, T. M. Dame, K. M. Menten, and A. Brunthaler. A Parallax-based Distance Estimator for Spiral Arm Sources. *The Astrophysical Journal*, 823(2):77, apr 2016.
- [153] P A Jones, M G Burton, M R Cunningham, M A Requena-Torres, K M Menten, P Schilke, A Belloche, S Leurini, J Martín-Pintado, J Ott, and A J Walsh. Spectral imaging of the Central Molecular Zone in multiple 3-mm molecular lines. *Mon. Not. R. Astron. Soc*, 419:2961–2986, 2012.
- [154] Rui-Zhi Yang, David I Jones, and Felix Aharonian. Fermi-LAT observations of the Sagittarius B complex. *Astronomy and Astrophysics*, 580:90, 2015.
- [155] F. Aharonian, A. G. Akhperjanian, A. R. Bazer-Bachi, M. Beilicke, W. Benbow, D. Berge, K. Bernlöhr, C. Boisson, O. Bolz, V. Borrel, I. Braun, F. Breitling, A. M. Brown, P. M. Chadwick, L. M. Chounet, R. Cornils, L. Costamante, B. Degrange, H. J. Dickinson, A. Djannati-Ataï, L. O.C. Drury, G. Dubus, D. Emmanoulopoulos, P. Espigat, F. Feinstein, G. Fontaine, Y. Fuchs, S. Funk, Y. A. Gallant, B. Giebels, S. Gillessen, J. F. Glicenstein, P. Goret, C. Hadjichristidis, D. Hauser, M. Hauser, G. Heinzlmann, G. Henri, G. Hermann, J. A. Hinton, W. Hofmann, M. Holleran, D. Horns, A. Jacholkowska, O. C. De Jager, B. Khélifi, S. Klages, Nu Komin, A. Konopelko, I. J. Latham, R. Le Gallou, A. Lemiére, M. Lemoine-Goumard, N. Leroy, T. Lohse, A. Marcowith, J. M. Martin, O. Martineau-Huynh, C. Masterson, T. J.L. McComb, M. De Naurois, S. J. Nolan, A. Noutsos, K. J. Orford, J. L. Osborne, M. Ouchrif, M. Panter, G. Pelletier, S. Pita, G. Pühlhofer, M. Punch, B. C. Raubenheimer, M. Raue, J. Raux, S. M. Rayner, A. Reimer, O. Reimer, J. Ripken, L. Rob, L. Rolland,

- G. Rowell, V. Sahakian, L. Saugé, S. Schlenker, R. Schlickeiser, C. Schuster, U. Schwanke, M. Siewert, H. Sol, D. Spangler, R. Steenkamp, C. Stegmann, J. P. Tavernet, R. Terrier, C. G. Théoret, M. Tluczykont, C. Van Eldik, G. Vasileiadis, C. Venter, P. Vincent, H. J. Völk, and S. J. Wagner. Discovery of very-high-energy γ -rays from the Galactic Centre ridge. *Nature*, 439(7077):695–698, feb 2006.
- [156] Ian M. Hoffman, W. M. Goss, C. L. Brogan, and M. J. Claussen. The OH (1720 MHz) Supernova Remnant Masers in W44: MERLIN and VLBA Polarization Observations. *The Astrophysical Journal*, 627(2):803–812, jul 2005.
- [157] Jeonghee Rho and R. Petre. Mixed-Morphology Supernova Remnants. *The Astrophysical Journal*, 503(2):L167–L170, aug 1998.
- [158] A. A. Abdo, M. Ackermann, M. Ajello, L. Baldini, J. Ballet, G. Barbiellini, M. G. Baring, D. Bastieri, B. M. Baughman, K. Bechtol, R. Bellazzini, B. Berenji, R. D. Blandford, E. D. Bloom, E. Bonamente, A. W. Borgland, J. Bregeon, A. Brez, M. Brigida, P. Bruel, T. H. Burnett, S. Buson, G. A. Caliandro, R. A. Cameron, P. A. Caraveo, J. M. Casandjian, C. Cecchi, Ö Çelik, A. Chekhtman, C. C. Cheung, J. Chiang, S. Ciprini, R. Claus, I. Cognard, J. Cohen-Tanugi, L. R. Cominsky, J. Conrad, S. Cutini, C. D. Dermer, A. De Angelis, F. De Palma, S. W. Digel, E. Do Couto E Silva, P. S. Drell, R. Dubois, D. Dumora, C. Espinoza, C. Farmer, C. Favuzzi, S. J. Fegan, W. B. Focke, P. Fortin, M. Frailis, Y. Fukazawa, S. Funk, P. Fusco, F. Gargano, D. Gasparrini, N. Gehrels, S. Germani, G. Giavitto, B. Giebels, N. Giglietto, F. Giordano, T. Glanzman, G. Godfrey, I. A. Grenier, M. H. Grondin, J. E. Grove, L. Guillemot, S. Guiriec, Y. Hanabata, A. K. Harding, M. Hayashida, E. Hays, R. E. Hughes, M. S. Jackson, G. Jóhannesson, A. S. Johnson, T. J. Johnson, W. N. Johnson, T. Kamae, H. Katagiri, J. Kataoka, J. Katsuta, N. Kawai, M. Kerr, J. Knödseder, M. L. Kocian, M. Kramer, M. Kuss, J. Lande, L. Latronico, M. Lemoine-Goumard, F. Longo, F. Loparco, B. Lott, M. N. Lovellette, P. Lubrano, A. G. Lyne, G. M. Madejski, A. Makeev, M. N. Mazziotta, J. E. McEnery, C. Meurer, P. F. Michelson, W. Mitthumsiri, T. Mizuno, C. Monte, M. E. Monzani, A. Morselli, I. V. Moskalenko, S. Murgia, T. Nakamori, P. L. Nolan, J. P. Noms, A. Noutsos, E. Nuss, T. Ohsugi, N. Omodei, E. Orlando, J. F. Ormes, D. Paneque, D. Parent, V. Pelassa, M. Pepe, M. Pesce-Rollins, F. Piron, T. A. Porter, S. Rainò, R. Rando, M. Razzano, A. Reimer, O. Reimer, T. Reposeur, A. Y. Rodriguez, R. W. Romani, M. Roth, F. Ryde, H. F.W. Sadrozinski, D. Sanchez, A. Sander, P. M. Saz Parkinson, J. D. Scargle, C. Sgrò, E. J. Siskind, D. A. Smith, P. D. Smith, G. Spandre, P. Spinelli, B. W. Stappers, F. W. Stecker, M. S. Strikman, D. J. Suson, H. Tajima, H. Takahashi, T. Takahashi, T. Tanaka, J. B. Thayer, J. G. Thayer, G. Theureau, D. J. Thompson, L. Tibaldo, O. Tibolla, D. F. Torres, G. Tosti, A. Tramacere, Y. Uchiyama, T. L. Usher, V. Vasileiou, C. Venter, N. Vilchez, V. Vitale, A. P. Waite, P. Wang, B. L. Winer, K. S. Wood, R. Yamazaki, T. Ylinen, and M. Ziegler. Gamma-ray emission from the shell of supernova remnant W44 revealed by the Fermi LAT. *Science*, 327(5969):1103–1106, feb 2010.
- [159] A. Wolszczan, J. M. Cordes, and R. J. Dewey. Discovery of a young, 267 millisecond pulsar in the supernova remnant W44. *The Astrophysical Journal*, 372:L99, may 1991.

- [160] A Smith, L R Jones, M G Watson, R Willingale and N Wood, and F D Seward Harvard. X-ray observations of the supernova remnant W44. *Monthly Notice of the Royal Astronomical Society*, 217(99-104):99, 1985.
- [161] J. R. Dickel, H. R. Dickel, and R. M. Crutcher. The supernova remnant W44 and its surroundings. *Publications of the Astronomical Society of the Pacific*, 88:840, dec 1976.
- [162] M. R. Kundu, T. Velusamy, M. R. Kundu, and T. Velusamy. Brightness and polarization structure of four supernova remnants 3C 58, IC 443, W28, and W44 at 2.8 centimeter wavelength. *Astronomy and Astrophysics*, 20:237–244, 1972.
- [163] J. J. Condon, W. D. Cotton, E. W. Greisen, Q. F. Yin, R. A. Perley, G. B. Taylor, and J. J. Broderick. The NRAO VLA Sky Survey. *The Astronomical Journal*, 115(5):1693–1716, may 1998.
- [164] G Castelletti, G Dubner, C Brogan, and N E Kassim. The low-frequency radio emission and spectrum of the extended SNR W44: new VLA observations at 74 and 324 MHz. *A&A*, 471:537–549, 2007.
- [165] Gilles Ferrand and Samar Safi-Harb. A census of high-energy observations of Galactic supernova remnants. *Advances in Space Research*, 49(9):1313–1319, may 2012.
- [166] Hirotugu Akaike. A New Look at the Statistical Model Identification. *IEEE Transactions on Automatic Control*, 19(6):716–723, 1974.
- [167] Giada Peron, Felix Aharonian, Sabrina Casanova, Roberta Zanin, and Carlo Romoli. On the Gamma-Ray Emission of W44 and Its Surroundings. *The Astrophysical Journal Letters*, 896(2), 2020.
- [168] M. Ackermann, M. Ajello, A. Allafort, L. Baldini, J. Ballet, G. Barbiellini, M. G. Baring, D. Bastieri, K. Bechtol, R. Bellazzini, R. D. Blandford, E. D. Bloom, E. Bonamente, A. W. Borgland, E. Bottacini, T. J. Brandt, J. Bregeon, M. Brigida, P. Bruel, R. Buehler, G. Busetto, S. Buson, G. A. Caliandro, R. A. Cameron, P. A. Caraveo, J. M. Casandjian, C. Cecchi, O. Celik, E. Charles, S. Chaty, R. C. G. Chaves, A. Chekhtman, C. C. Cheung, J. Chiang, G. Chiaro, A. N. Cillis, S. Ciprini, R. Claus, J. Cohen-Tanugi, L. R. Cominsky, J. Conrad, S. Corbel, S. Cutini, F. D’Ammando, A. de Angelis, F. de Palma, C. D. Dermer, E. do Couto e Silva, P. S. Drell, A. Drlica-Wagner, L. Falletti, C. Favuzzi, E. C. Ferrara, A. Franckowiak, Y. Fukazawa, S. Funk, P. Fusco, F. Gargano, S. Germani, N. Giglietto, P. Giommi, F. Giordano, M. Giroletti, T. Glanzman, G. Godfrey, I. A. Grenier, M.-H. Grondin, J. E. Grove, S. Guiriec, D. Hadasch, Y. Hanabata, A. K. Harding, M. Hayashida, K. Hayashi, E. Hays, J. W. Hewitt, A. B. Hill, R. E. Hughes, M. S. Jackson, T. Jogler, G. Johannesson, A. S. Johnson, T. Kamae, J. Kataoka, J. Katsuta, J. Knodlseder, M. Kuss, J. Lande, S. Larsson, L. Latronico, M. Lemoine-Goumard, F. Longo, F. Loparco, M. N. Lovellette, P. Lubrano, G. M. Madejski, F. Massaro, M. Mayer, M. N. Mazziotta, J. E. McEnery, J. Mehault, P. F. Michelson, R. P. Mignani, W. Mitthumsiri,

- T. Mizuno, A. A. Moiseev, M. E. Monzani, A. Morselli, I. V. Moskalenko, S. Murgia, T. Nakamori, R. Nemmen, E. Nuss, M. Ohno, T. Ohsugi, N. Omodei, M. Orienti, E. Orlando, J. F. Ormes, D. Paneque, J. S. Perkins, M. Pesce-Rollins, F. Piron, G. Pivato, S. Raino, R. Rando, M. Razzano, S. Razzaque, A. Reimer, O. Reimer, S. Ritz, C. Romoli, M. Sanchez-Conde, A. Schulz, C. Sgro, P. E. Simeon, E. J. Siskind, D. A. Smith, G. Spandre, P. Spinelli, F. W. Stecker, A. W. Strong, D. J. Suson, H. Tajima, H. Takahashi, T. Takahashi, T. Tanaka, J. G. Thayer, J. B. Thayer, D. J. Thompson, S. E. Thorsett, L. Tibaldo, O. Tibolla, M. Tinivella, E. Troja, Y. Uchiyama, T. L. Usher, J. Vandenbroucke, V. Vasileiou, G. Vianello, V. Vitale, A. P. Waite, M. Werner, B. L. Winer, K. S. Wood, M. Wood, R. Yamazaki, Z. Yang, S. Zimmer, Z. Yang, and S. Zimmer. Detection of the Characteristic Pion-Decay Signature in Supernova Remnants. *Science*, 339(6121):807–811, feb 2013.
- [169] M. Cardillo, M. Tavani, A. Giuliani, S. Yoshiike, H. Sano, T. Fukuda, Y. Fukui, G. Castelletti, and G. Dubner. The Supernova Remnant W44: confirmations and challenges for cosmic-ray acceleration. *Astronomy & Astrophysics*, 565(A74), mar 2014.
- [170] L. Ambrogi, R. Zanin, S. Casanova, E. De Oña Wilhelmi, G. Peron, and F. Aharonian. Spectral and morphological study of the gamma radiation of the middle-aged supernova remnant HB 21. *Astronomy and Astrophysics*, 623, 2019.
- [171] George R. Blumenthal and Robert J. Gould. Bremsstrahlung, synchrotron radiation, and compton scattering of high-energy electrons traversing dilute gases. *Reviews of Modern Physics*, 42(2):237–270, 1970.
- [172] E. Haug. Bremsstrahlung and Pair Production in the Field of Free Electrons. *Zeitschrift fur Naturforschung - Section A Journal of Physical Sciences*, 30(9):1099–1113, sep 1975.
- [173] Pasquale Blasi and Elena Amato. Diffusive propagation of cosmic rays from supernova remnants in the Galaxy. II: anisotropy. *Journal of Cosmology and Astroparticle Physics*, 2012(01):011–011, jan 2012.
- [174] Martina Cardillo, Elena Amato, and Pasquale Blasi. The supernova remnant W44: a case of cosmic-Ray reacceleration. *Astronomy & Astrophysics*, 595(A58), apr 2016.
- [175] P. M. Saz Parkinson, H. Xu, P. L. H. Yu, D. Salvetti, M. Marelli, and A. D. Falcone. CLASSIFICATION AND RANKING OF FERMI LAT GAMMA-RAY SOURCES FROM THE 3FGL CATALOG USING MACHINE LEARNING TECHNIQUES . *The Astrophysical Journal*, 820(1):8, mar 2016.
- [176] Yasunobu Uchiyama, Stefan Funk, Hideaki Katagiri, Junichiro Katsuta, Marianne Lemoine-Goumard, Hiroyasu Tajima, Takaaki Tanaka, and Diego F Torres. Fermi large area telescope discovery of GeV gamma-ray emission from the vicinity of SNR W44. *The Astrophysical Journal Letters*, 749(5pp):35, 2012.

- [177] Masumichi Seta, Tetsuo Hasegawa, T. M. Dame, Seiichi Sakamoto, Tomoharu Oka, Toshihiro Handa, Masahiko Hayashi, Jun-Ichi Morino, Kazuo Sorai, and Kumiko S. Usuda. Enhanced CO $J = 2-1 / J = 1-0$ Ratio as a Marker of Supernova Remnant–Molecular Cloud Interactions: The Cases of W44 and IC 443. *The Astrophysical Journal*, 505(1):286–298, sep 1998.
- [178] G Giacinti, M Kachelrieß, and D V Semikoz. Anisotropic Cosmic Ray Diffusion and its Implications for Gamma-Ray Astronomy. *Physical Review D*, 88,2(023010), 2013.
- [179] Ti-Pei Li and Yu-Qian Ma. ANALYSIS METHODS FOR RESULTS IN GAMMA-RAY ASTRONOMY. *The Astrophysical Journal*, 272:317–324, 1983.
- [180] A. M. Hillas. Evolution of ground-based gamma-ray astronomy from the early days to the Cherenkov Telescope Arrays. *Astroparticle Physics*, 43:19–43, 2013.
- [181] Stefan Funk. Ground- and Space-Based Gamma-Ray Astronomy. *Annual Review of Nuclear and Particle Science*, 65(1):245–277, oct 2015.
- [182] Giuseppe Di Sciascio. Ground-based Gamma-Ray Astronomy: An Introduction. In *Journal of Physics: Conference Series*, volume 1263, page 012003. Institute of Physics Publishing, jun 2019.
- [183] Welcome to VERITAS. <<https://veritas.sao.arizona.edu/>> visited on 23.09.2020.
- [184] MAGIC. <<https://www.magic.mpp.mpg.de/>> visited on 23.09.2020.
- [185] German Hermann. The HESS array: a new system of 100 GeV IACTs for stereoscopic observations. In *Proceedings of the XXXII Rencontres de Moriond, Les Arcs, Franc*, 1997.
- [186] H.E.S.S. The High Energy Stereoscopic System. <<https://www.mpi-hd.mpg.de/hfm/HESS/>> visited on 23.09.2020.
- [187] Cherenkov Telescope Array. <<https://www.cta-observatory.org/>> visited on 23.09.2020.
- [188] HAWC: the High-Altitude Water Cherenkov Observatory. <<https://www.hawc-observatory.org/>> visited on 23.09.2020.
- [189] P. Abreu, A. Albert, R. Alfaro, C. Alvarez, R. Arceo, P. Assis, F. Barao, J. Bazo, J. F. Beacom, J. Bellido, S. BenZvi, T. Bretz, C. Brisbois, A. M. Brown, F. Brun, M. Buscemi, K. S. Caballero Mora, P. Camarri, A. Carramiñana, S. Casanova, A. Chiavassa, R. Conceição, G. Cotter, P. Cristofari, S. Dasso, A. De Angelis, M. De Maria, P. Desiati, G. Di Sciascio, J. C. Díaz Vélez, C. Dib, B. Dingus, D. Dorner, M. Doro, C. Duffy, M. DuVernois, R. Engel, M. Fernandez Alonso, H. Fleischhack, P. Fonte, N. Fraija, S. Funk, J. A. García-González, M. M. González, J. A. Goodman, T. Greenshaw, J. P. Harding, A. Haungs, B. Hona, P. Huentemeyer, A. Insolia, A. Jardin-Blicq, V. Joshi, K. Kawata, S. Kunwar, G. La Mura, J. Lapington, J. P. Lenain, R. López-Coto, K. Malone, J. Martinez-Castro, H. Martínez-Huerta, L. Mendes, E. Moreno, M. Mostafá, K. C. Y. Ng,

- M. U. Nisa, F. Peron, A. Pichel, M. Pimenta, E. Prandini, S. Rainò, A. Reisenegger, J. Rodriguez, M. Roth, A. Rovero, E. Ruiz-Velasco, T. Sako, A. Sandoval, M. Santander, K. Satalecka, M. Schneider, H. Schoorlemmer, F. Schüssler, R. C. Shellard, A. Smith, S. Spencer, W. Springer, P. Surajbali, K. Tollefson, B. Tomé, I. Torres, A. Viana, T. Weisgarber, R. Wischnewski, A. Zepeda, B. Zhou, and H. Zhou. The Southern Wide-Field Gamma-Ray Observatory (SWG0): A Next-Generation Ground-Based Survey Instrument for VHE Gamma-Ray Astronomy. jul 2019.
- [190] The Southern Wide-field Gamma-ray Observatory (SWG0). <<https://www.swgo.org/SWGOWiki/doku.php>> visited on 23.09.2020.
- [191] The Large High Altitude Air Shower Observatory. <<http://english.ihep.cas.cn/lhaaso/>> visited on 23.09.2020.
- [192] A. Moiseev, J. Norris, J. Ormes, S. Ritz, and D. Thompson. Anticoincidence Detector for GLAST. In *Bulletin of the American Astronomical Society*, dec 1999.
- [193] B Huber, C Farnier, A Manalaysay, U Straumann, and R Walter. Astrophysics A stacking method to study the gamma-ray emission of source samples based on the co-adding of Fermi-LAT count maps. *A&A*, 547:102, 2012.
- [194] Jan Conrad and Olaf Reimer. Indirect dark matter searches in Gamma- and Cosmic Rays. *Nature Physics*, 13(3):224–231, may 2017.
- [195] Fermi-LAT collaboration. Fermi-LAT Observations of the LIGO event GW150914. *The Astrophysical Journal Letters*, 34(13pp):2, feb 2016.